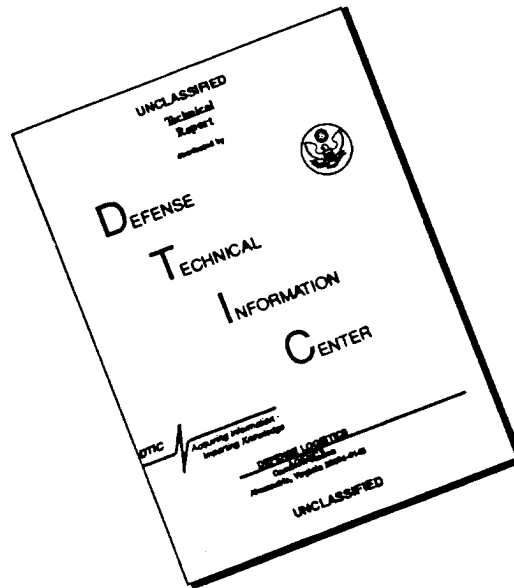


REPORT DOCUMENTATION PAGE			Form Approved OMB No. 0704-0188	
Public reporting burden for this collection of information is estimated to average 1 hour per response, including the time for reviewing instructions, searching existing data sources, gathering and maintaining the data needed, and completing and reviewing the collection of information. Send comments regarding this burden estimate or any other aspect of this collection of information, including suggestions for reducing this burden, to Washington Headquarters Services, Directorate for Information Operations and Reports, 1215 Jefferson Davis Highway, Suite 1204, Arlington, VA 22202-4302, and to the Office of Management and Budget, Paperwork Reduction Project (0704-0188), Washington, DC 20503.				
1. AGENCY USE ONLY (Leave blank)		2. REPORT DATE 8 Dec 95		3. REPORT TYPE AND DATES COVERED
4. TITLE AND SUBTITLE Green's Function Analysis of Pavement Deflections Due to Moving Wheel Loads			5. FUNDING NUMBERS	
6. AUTHOR(S) Richard G. Thuma				
7. PERFORMING ORGANIZATION NAME(S) AND ADDRESS(ES) AFIT Student Attending: University of Washington			8. PERFORMING ORGANIZATION REPORT NUMBER 96-020	
9. SPONSORING/MONITORING AGENCY NAME(S) AND ADDRESS(ES) DEPARTMENT OF THE AIR FORCE AFIT/CI 2950 P STREET, BLDG 125 WRIGHT-PATTERSON AFB OH 45433-7765			10. SPONSORING/MONITORING AGENCY REPORT NUMBER	
11. SUPPLEMENTARY NOTES				
12a. DISTRIBUTION / AVAILABILITY STATEMENT Approved for Public Release IAW AFR 190-1 Distribution Unlimited BRIAN D. GAUTHIER, MSgt, USAF Chief Administration			12b. DISTRIBUTION CODE	
13. ABSTRACT (Maximum 200 words)				
<div style="font-size: 2em; font-weight: bold;">19960531 082</div>				
14. SUBJECT TERMS			15. NUMBER OF PAGES 181	
			16. PRICE CODE	
17. SECURITY CLASSIFICATION OF REPORT	18. SECURITY CLASSIFICATION OF THIS PAGE	19. SECURITY CLASSIFICATION OF ABSTRACT	20. LIMITATION OF ABSTRACT	

DISCLAIMER NOTICE



THIS DOCUMENT IS BEST QUALITY AVAILABLE. THE COPY FURNISHED TO DTIC CONTAINED A SIGNIFICANT NUMBER OF PAGES WHICH DO NOT REPRODUCE LEGIBLY.

GENERAL INSTRUCTIONS FOR COMPLETING SF 298

The Report Documentation Page (RDP) is used in announcing and cataloging reports. It is important that this information be consistent with the rest of the report, particularly the cover and title page. Instructions for filling in each block of the form follow. It is important to *stay within the lines* to meet optical scanning requirements.

Block 1. Agency Use Only (Leave blank).

Block 2. Report Date. Full publication date including day, month, and year, if available (e.g. 1 Jan 88). Must cite at least the year.

Block 3. Type of Report and Dates Covered. State whether report is interim, final, etc. If applicable, enter inclusive report dates (e.g. 10 Jun 87 - 30 Jun 88).

Block 4. Title and Subtitle. A title is taken from the part of the report that provides the most meaningful and complete information. When a report is prepared in more than one volume, repeat the primary title, add volume number, and include subtitle for the specific volume. On classified documents enter the title classification in parentheses.

Block 5. Funding Numbers. To include contract and grant numbers; may include program element number(s), project number(s), task number(s), and work unit number(s). Use the following labels:

C - Contract	PR - Project
G - Grant	TA - Task
PE - Program Element	WU - Work Unit Accession No.

Block 6. Author(s). Name(s) of person(s) responsible for writing the report, performing the research, or credited with the content of the report. If editor or compiler, this should follow the name(s).

Block 7. Performing Organization Name(s) and Address(es). Self-explanatory.

Block 8. Performing Organization Report Number. Enter the unique alphanumeric report number(s) assigned by the organization performing the report.

Block 9. Sponsoring/Monitoring Agency Name(s) and Address(es). Self-explanatory.

Block 10. Sponsoring/Monitoring Agency Report Number. (If known)

Block 11. Supplementary Notes. Enter information not included elsewhere such as: Prepared in cooperation with...; Trans. of...; To be published in.... When a report is revised, include a statement whether the new report supersedes or supplements the older report.

Block 12a. Distribution/Availability Statement. Denotes public availability or limitations. Cite any availability to the public. Enter additional limitations or special markings in all capitals (e.g. NOFORN, REL, ITAR).

DOD - See DoDD 5230.24, "Distribution Statements on Technical Documents."

DOE - See authorities.

NASA - See Handbook NHB 2200.2.

NTIS - Leave blank.

Block 12b. Distribution Code.

DOD - Leave blank.

DOE - Enter DOE distribution categories from the Standard Distribution for Unclassified Scientific and Technical Reports.

NASA - Leave blank.

NTIS - Leave blank.

Block 13. Abstract. Include a brief (*Maximum 200 words*) factual summary of the most significant information contained in the report.

Block 14. Subject Terms. Keywords or phrases identifying major subjects in the report.

Block 15. Number of Pages. Enter the total number of pages.

Block 16. Price Code. Enter appropriate price code (*NTIS only*).

Blocks 17. - 19. Security Classifications. Self-explanatory. Enter U.S. Security Classification in accordance with U.S. Security Regulations (i.e., UNCLASSIFIED). If form contains classified information, stamp classification on the top and bottom of the page.

Block 20. Limitation of Abstract. This block must be completed to assign a limitation to the abstract. Enter either UL (unlimited) or SAR (same as report). An entry in this block is necessary if the abstract is to be limited. If blank, the abstract is assumed to be unlimited.

Green's Function Analysis of
Pavement Deflections due to
Moving Wheel Loads

by

Richard G. Thuma

A thesis submitted in partial fulfillment
of the requirements for the degree of

Master of Science
in
Civil Engineering

University of Washington

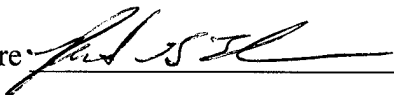
1995

Approved by St. L. Thuma
Chairperson of Supervisory Committee

Program Authorized
to Offer Degree CIVIL ENGINEERING

Date 8 DEC 95

In presenting this thesis in partial fulfillment of the requirements for a Master's degree at the University of Washington, I agree that the Library shall make its copies freely available for inspection. I further agree that extensive copying of this thesis is allowable only for scholarly purposes, consistent with "fair use" as prescribed in the U.S. Copyright Law. Any other reproduction for any purposes or by any means shall not be allowed without my written permission.

Signature 

Date 8 Dec 95

University of Washington

Abstract

Green's Function Analysis of Pavement Deflections
due to Moving Wheel Loads

by Richard G. Thuma

Chairperson of the Supervisory Committee:

Professor Steven L. Kramer
Department of Civil Engineering

Nondestructive pavement deflection testing is commonly used to evaluate the structural capacity of flexible pavements. Different types of tests, characterized by their loading mechanism -- static or dynamic, stationary or moving -- are used for this purpose. For all tests, a pavement deflection model is used to interpret the measured deflections. This thesis presents the conceptual development, validation, and parametric study of a flexible pavement model for predicting deflections caused by a rolling wheel.

The model uses a Green's function approach to compute deflections. The Green's function computes the deflections at a known distance from a disk that is loaded harmonically at a known frequency. The deflections caused by an impulse load are computed using Fourier superposition analysis. The rolling wheel load is modeled as a sequence of impulse loads and the model combines the responses from each impulse to predict a deflection basin that would be seen by an observer moving with the wheel. This process assumes that all materials in the pavement structure behave linear-elastically.

The model was validated by predicting deflections caused by falling weight deflectometer (FWD) tests. Predicted deflections were reasonably close to measured deflections; however, the pavement layer moduli used in the validation were backcalculated using static rather than dynamic models.

The sensitivity of the computed deflection basin to three categories of input parameters -- algorithm, material, and loading -- was investigated by a detailed parametric study. Algorithm variables were studied to determine the values that

produced the most accurate solution in the minimum time. The sensitivity of the basin shape to layer material variables provided insight into which variables can be potentially backcalculated with this model. Loading variables were studied to determine the effect that the wheel speed, load, and tire pressure had on the deflection basin shape. The parametric study revealed that backcalculation of layer moduli or thicknesses may be possible using this model. However, backcalculating both layer modulus and thickness simultaneously will require a very precise definition of the deepest part of the deflection basin. The model may not be practical for use in a backcalculation program until the computation time can be reduced.

TABLE OF CONTENTS

	<i>Page</i>
List of Figures	v
List of Tables	viii
Chapter 1: Introduction	1
1.1 Background	1
1.2 Objectives	3
1.3 Organization	3
Chapter 2: Nondestructive Pavement Deflection Analysis	5
2.1 Static Load	5
2.1.1 General	5
2.1.2 Pavement Deflection Response	6
2.1.3 Testing Devices	8
2.1.3.1 Benkelman Beam	9
2.1.3.2 Traveling Deflectometer	9
2.1.3.3 LaCroix - L.C.P.C. Deflectometer	10
2.1.3.4 Plate Bearing Test	10
2.1.4 Application	11
2.2 Steady State Dynamic Load	11
2.2.1 General	11
2.2.2 Pavement Deflection Response	13
2.2.3 Testing Equipment	14
2.2.3.1 Dynaflect	14
2.2.3.2 Road Rater	14
2.2.4 Application	15
2.3 Transient (Impulse) Dynamic Load	16
2.3.1 General	16
2.3.2 Pavement Deflection Response	17
2.3.3 Testing Equipment	18
2.3.3.1 Dynatest 8000 Falling Weight Deflectometer	18
2.3.3.2 KUAB 2M Falling Weight Deflectometer	19
2.3.4 Application	20
2.4 Transient Surface Wave Analysis	21
2.4.1 General	21
2.4.2 Pavement Deflection Response	23
2.4.3 Testing Equipment	23
2.4.4 Application	25
2.5 Rolling Wheel Load	26
2.5.1 Testing Equipment	26
2.5.1.1 SNRA Rolling Weight Deflectometer	26

	<i>Page</i>
2.5.1.2 UT Rolling Dynamic Deflectometer	27
2.5.2 Application	28
Chapter 3: Flexible Pavement Deflection Prediction Models	30
3.1 Static Models	30
3.2 Dynamic Models	33
3.2.1 Stationary Load Models	33
3.2.1.1 Linear Elastic Dynamic Models	33
3.2.1.2 Viscoelastic Dynamic Models	35
3.2.2 Rolling Load Models	36
Chapter 4: Dynamic Layered Elastic Analysis Using Green's Function	38
4.1 Green's Functions	38
4.2 Dynamic Layered Elastic Model using Green's Functions	39
4.2.1 Frequency Domain Analysis	39
4.2.2 Green's Function Solution	40
4.2.3 FWD Load Representation	42
4.2.4 Rolling Wheel Load Representation	46
4.2.4.1 Loaded Area	47
4.2.4.2 Load Pulse Shape	47
4.2.4.3 Load Pulse Duration	48
4.2.4.4 Load Pulse Spacing	50
Chapter 5: BASIN Conceptual Development	52
5.1 Algorithm Development	52
5.1.1 Simulated Green's Function	52
5.1.2 Case 1: Falling Weight Deflectometer	54
5.1.3 Case 2: Rolling Load Passing a Stationary Point	57
5.1.4 Case 3: Deflection "Snapshot"	58
5.1.5 Case 4: "Snapshot" 3-Dimensional Deflection Basin	62
5.1.6 Case 5: 3-D Basin for Two Parallel Rolling Wheels	63
5.2 Algorithm Modifications for Moving Deflection Sensors	64
5.2.1 BASIN Algorithm	65
5.2.2 <i>Avertime</i> and <i>Timeback</i>	69
5.2.3 Deflection Basin Assembly	70
5.2.4 3-D Basin for Two Parallel Rolling Wheels	71
5.3 BASIN Code Details	72
Chapter 6: BASIN Verification	73
6.1 FWDDROP Program	73
6.2 Comparison to SHRP Test Sections	74
6.3 Comparison to PACCAR Test Sections	77
6.4 Modification of Deflection Time Histories	80

	<i>Page</i>
Chapter 7: Parametric Study	85
7.1 Parametric Study Plan	85
7.1.1 Standard Pavement Section and Standard Loading	85
7.1.2 Structure	86
7.1.3 Data Presentation and Statistical Parameters	88
7.2 Algorithm Variables	92
7.2.1 Layer Discretization	93
7.2.2 Cutoff Frequency	94
7.2.3 Frequency Increment	96
7.2.4 <i>Timeback</i>	100
7.2.5 <i>Avertime</i>	102
7.3 Material Variables	104
7.3.1 Density	104
7.3.2 Poisson's Ratio	106
7.3.3 Modulus	108
7.3.3.1 AC Modulus	108
7.3.3.2 Base Modulus	109
7.3.3.3 Subgrade Modulus	111
7.3.3.4 Stiff Layer Modulus	114
7.3.3.5 Discussion	116
7.3.4 Thickness	116
7.3.4.1 AC Thickness.....	116
7.3.4.2 Base Thickness	118
7.3.4.3 Subgrade Thickness	120
7.3.4.4 Stiff Layer Thickness	120
7.3.4.5 Discussion	123
7.3.5 Combinations of Thickness and Modulus	123
7.3.5.1 AC Thickness/Modulus	124
7.3.5.2 Base Thickness/Modulus	124
7.3.5.3 Discussion	126
7.4 Loading Variables	128
7.4.1 Wheel Load	128
7.4.2 Tire Pressure	130
7.4.3 Vehicle Speed	130
7.4.4 Pulse Duration	132
7.5 Transverse Deflection Basin	136
 Chapter 8: Summary, Conclusions, And Recommendations	 139
8.1 Summary	139
8.2 Conclusions	140
8.3 Recommendations	143

	<i>Page</i>
Bibliography	145
Appendix A: BASIN Code	150
A.1 Primary BASIN Modules	150
A.2 BASIN Input and Output	150
A.3 BASIN Code	151

LIST OF FIGURES

<i>Number</i>	<i>Page</i>
1-1. Typical three-layered flexible pavement cross section	2
2-1. Deflection basin and individual deflections produced by a loaded plate as measured by seven deflection sensors	5
2-2. Schematic representation of the Benkelman Beam	9
2-3. Typical output of force generator used for steady-state dynamic testing	12
2-4. a) Schematic Illustration of the Dynaflect. b) Plan view of the loading and geophone configuration	15
2-5. Schematic illustration of the loading mechanism used by two falling weight deflectometers	19
2-6. General configuration of SASW test	22
2-7. Schematic of CMRP arrangement for SASW testing	24
2-8. Schematic representation of the SNRA Rolling Weight Deflectometer	27
2-9. Schematic representation of the UT Rolling Dynamic Deflectometer	28
3-1. Illustration of an n-layer system subjected to a disk load	31
3-2. Illustration of the properties of a viscoelastic Maxwell model	36
3-3. Static and dynamic deflections resulting from a rolling wheel load	37
4-1. Schematic illustration of Fourier superposition analysis using Green's functions	41
4-2. Typical wheel load applied by a moving truck	42
4-3. Typical load pulses for four different FWD devices	44
4-4. a) Average measured load pulse and functional analogues in the time domain. b) Fourier amplitude spectra for average measured load pulse and functional analogues	45
4-5. Fourier amplitude spectra for average measured load pulse and adjusted haversine approximation	46
4-6. Original and bandwidth-limited haversine load pulses	47
4-7. Illustration of method for combining different load pulse shapes to achieve a common line load	48
4-8. Variation of equivalent principal stress pulse time with vehicle velocity and depth	49
4-9. Illustration of method for using different load pulse duration and amplitude to achieve a common line load	50
4-10. Illustration of method for using different load pulse amplitude and spacing to achieve a common line load	51
5-1. Simulated deflection response caused by a unit impulse load for several distances from the impact site	54

<i>Number</i>	<i>Page</i>
5-2. Simulated impact load function conversion to discrete point loads	55
5-3. Individual deflection responses due to individual impulse loads measured at 10 distance units from the impact site	56
5-4. Time history of deflection for a point 10 distance units from the impact site	56
5-5. a) Time history of deflection measured at several radial distances from the impact site. b) Deflection basin constructed using peak deflections	57
5-6. Deflection basins predicted for several discrete time intervals	59
5-7. Representation of a rolling wheel passing an observation point as a sequence of impulse point loads	60
5-8. Individual impulse load deflection responses for case in which wheel passes (a) directly over observation point ($y=0$), and (b) 30 distance units from observation point ($y=30$)	60
5-9. Time history of deflection for rolling wheel passing directly over ($y=0$) and 30 units ($y=30$) from the observation point	61
5-10. "Snapshot" deflection basin conceptual development illustrating a constant time plane	61
5-11. "Snapshot" deflection basin observed when wheel is directly over $x = 0$ position	62
5-12. Deflection basin observed when a single rolling wheel is directly over the $x=0, y=0$ position	63
5-13. Deflection basin observed when the axle connecting two rolling wheels is directly over the $x=0$ position	64
5-14. Flow chart of the algorithm coded in the computer program BASIN	66
5-15. Method for calculating deflections at sensor location D_T at time T_{10}	68
5-16. Longitudinal deflection basin with deflection sensors located at each data point marker	70
5-17. Single wheel deflection basin computed using BASIN	71
5-18. Double wheel deflection basin computed using BASIN	72
6-1. Typical FWD deflection time histories and construction of "static" deflection basin	74
6-2. Pavement structures for SHRP test sections A and B	75
6-3. Measured and calculated deflection basins for SHRP sections A and B	78
6-4. Pavement structures for PACCAR test site Core 4	79
6-5. Measured and calculated deflection basins for PACCAR Core 4 FWD tests	82
6-6. Measured and calculated deflection basins for PACCAR Core 4 FWD tests when peak load is reduced by 8%	83
6-7. a) Illustration of negative deflections at the beginning and end of the deflection time history calculated by FWDDROP. b) Modified deflection time history	84

<i>Number</i>	<i>Page</i>
7-1. Standard Pavement Section	87
7-2. Example function, $z(x)$, represented by N discrete points	88
7-3. Two functions with identical shapes but different mean values	89
7-4. Two functions with identical means but different standard deviations	90
7-5. Two functions with opposite skewness, one positive and the other negative	91
7-6. A normal distribution ($C_4 = 3$) and two functions with greater and lesser kurtosis	92
7-7. Typical data presentation format	93
7-8. Sensitivity to Layer Discretization	95
7-9. Sensitivity to Cutoff Frequency	97
7-10. Sensitivity to Frequency Increment	99
7-11. Sensitivity to <i>Timeback</i>	101
7-12. Sensitivity to <i>Avetime</i>	103
7-13. Sensitivity to Density	105
7-14. Sensitivity to Poisson's Ratio	107
7-15. Sensitivity to AC Modulus	110
7-16. Sensitivity to Base Modulus	112
7-17. Sensitivity to Subgrade Modulus	113
7-18. Sensitivity to Stiff Layer Modulus	115
7-19. Sensitivity to AC Thickness	117
7-20. Sensitivity to Base Thickness	119
7-21. Sensitivity to Subgrade Thickness	121
7-22. Sensitivity to Stiff Layer Thickness	122
7-23. Sensitivity to AC Thickness/Modulus	125
7-24. Sensitivity to Base Thickness/Modulus	127
7-25. Sensitivity to Wheel Load	129
7-26. Sensitivity to Tire Pressure	131
7-27. Sensitivity to Wheel Speed	133
7-28. Sensitivity to Load Pulse Duration	135
7-29. Longitudinal and Transverse Deflection Basins	137
7-30. Transverse Profile -- Sensitivity to Base Modulus	138

LIST OF TABLES

<i>Number</i>	<i>Page</i>
6-1. Moduli backcalculated from measured deflection basins	76
6-2. Assumed layer properties for SHRP test sections	76
6-3. Comparison of measured and calculated FWD deflections for SHRP test sections	77
6-4. Moduli backcalculated from measured deflection basins	79
6-5. Assumed layer properties for PACCAR Core 4	80
6-6. Comparison of measured and calculated FWD deflections for PACCAR Core 4	81
7-1. AC Thickness/Modulus Combinations	124
7-2. Base Thickness/Modulus Combinations	126

ACKNOWLEDGMENTS

I would like to express my sincere gratitude to Professor Steve Kramer for his insightful guidance, thorough manuscript reviews, and helpful conceptual brainstorming. I also owe a debt to Professor Roger Meier for providing the primary subroutine used in this thesis, along with helpful explanations and programming advice. I would also like to recognize the US Air Force for sponsoring my graduate studies at the University of Washington.

Lastly, I would like to thank my wife and best friend, Mary Angela, for her unwavering patience, love, and support throughout this project.

Chapter 1

INTRODUCTION

1.1 Background

Researchers have recognized for many years that the structural capacity and life expectancy of roadways was related to the load-deflection properties of the pavement system materials. To determine these properties, two basic testing methods can be used -- destructive or non-destructive.

Destructive testing requires removing material from the roadway and then performing laboratory tests on the samples. An obvious disadvantage of this method of testing is the time and cost associated with collecting samples and repairing the damaged pavement. However, there are two very important additional disadvantages. First, samples cut from the roadway and underlying soils are considerably disturbed -- this casts doubt on the transferability of the results of lab tests to the field situation. Second, the roadway is composed of several layers of materials (illustrated in Figure 1-1), each composed of inherently heterogeneous materials. Destructive testing considers only a small sample of the materials, and does not test the interaction between material layers.

Non-Destructive testing (NDT), as the name suggests, does not require sample collection. Instead it indirectly measures material properties *in situ*. Besides the shorter test times and relatively low cost, NDT is superior to destructive testing because it measures a larger volume of material, and tests the way the individual layers interact. An additional advantage to non-destructive testing is that the pavement can be evaluated using the same load that it is designed to resist -- i.e. the pavement can be loaded with a truck.

Several types of non-destructive tests have been developed to measure the deflections caused by an applied load. Static tests apply a constant load to a stationary area and dynamic tests apply a vibrating or impact load to a stationary contact plate. Each test measures the associated static or dynamic deflections using a variety of devices.

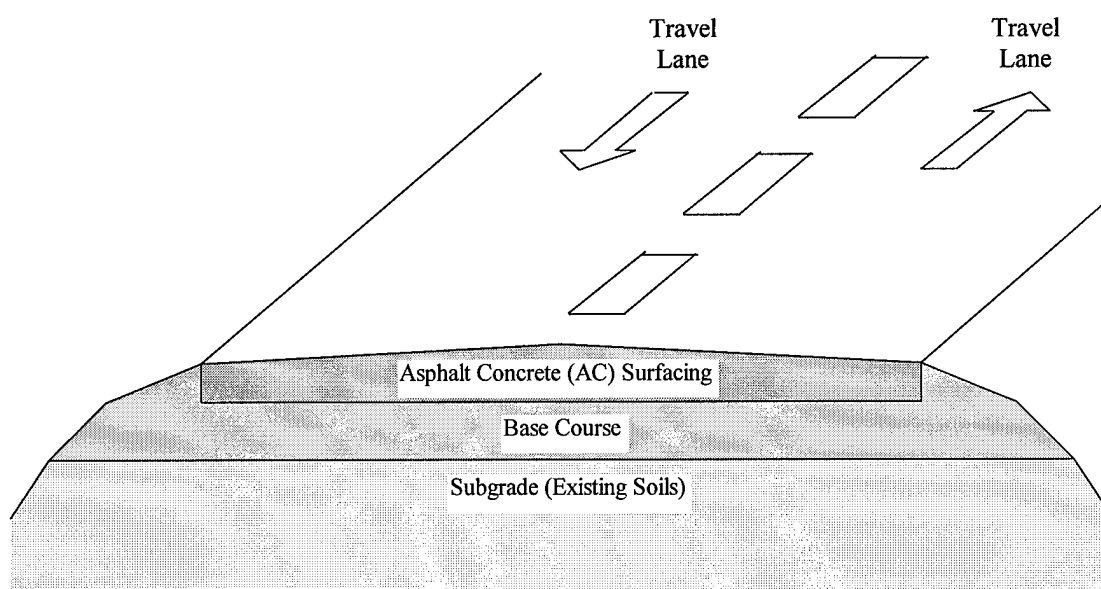


Figure 1-1. Typical three-layered flexible pavement cross section.

Recently a new type of testing device has been developed that measures the deflections caused by a rolling wheel. This type of device has tremendous potential for determining the true dynamic properties of pavement structures because it applies exactly the same load that is applied by highway vehicles. Using this device, a better understanding of the deflection behavior and resulting damage caused by traffic can be developed.

All non-destructive tests require models to interpret the measured deflection data because the material properties cannot be measured directly (i.e. deflection is *not* a material property). Using models, the layer material properties are adjusted until the predicted deflections match the measured deflections. Using a process called *backcalculation*, the layer material properties are adjusted until the deflections predicted by the model match the measured deflections. The properties used to calculate the matching prediction then correspond to the properties of the pavement structure.

Models range in complexity from simple static load formulas to intricate dynamic finite element computer programs. Many static and several dynamic models have been developed to interpret stationary load test deflections. However, only a few models exist that predict deflections caused by a moving load.

1.2 Objectives

The main objective of this research was to develop a model to predict the deflections resulting from a rolling wheel load. To accurately model pavement structures, the model must be capable of considering a multi-layered system. Towards this end, a Green's function approach was selected as the method for dynamic analysis. Also, the model must be capable of predicting the shape of a constantly-moving deflection basin because the sensors that measure the deflections are attached to the moving vehicle.

Because other rolling-wheel models and deflection measurements were not readily available, the model was compared to a different dynamic test -- the falling weight deflectometer. This test applies an impact load to a stationary contact plate. This validation required modification of the primary model to allow for the different loading conditions, but the principal components remained identical.

The sensitivity of the model to the most significant input parameters was determined using a detailed parametric study. The changes in deflection basin shape due to material properties and loading conditions was investigated. Also, the conceptual parameters that influence the computation speed and accuracy were studied to determine the values that produced the best accuracy in the least time.

With a completed model, backcalculation can be used to determine material properties from measured deflections. However, developing a backcalculation scheme was outside the scope of this research. Only the forward model was created and analyzed.

1.3 Organization

The first portion of this thesis describes the development of non-destructive testing and the models used to interpret the tests. The latter portion explains the development and validation of the rolling wheel model. The following paragraphs provide a brief description of each chapter.

Chapter 2 describes the non-destructive tests that have historically been used to evaluate pavements. The testing devices are grouped according to the method by which the load is applied to the pavement: static, steady-state dynamic, transient dynamic, transient surface wave, and rolling wheel. The pavement response produced by each loading scheme and the applications for each test are also described. The analytical models used to interpret the data measured by NDT devices are explained in Chapter 3. Again, the models are grouped by the assumed load type: static, dynamic stationary load, and dynamic rolling load. For each load type, the simplest models are described first, followed by the more complicated models.

Chapter 4 explains the Green's function concept and describes how it was used to develop a solution for the deflections of a layered pavement system subjected to harmonic loading. Chapter 5 provides a detailed conceptual development of an algorithm for calculating the deflection basin caused by a rolling wheel. The simplest case, a stationary transient load, is considered first, followed by additional cases that add incremental levels of complexity. Initially, a simulated deflection response function is employed to easily illustrate the applied concepts. Eventually, the chapter describes how the true Green's function solution was used with this algorithm in the computer program BASIN. The program BASIN was verified by comparing the calculated deflections to falling-weight deflectometer data, as described in Chapter 6. The results of a parametric study of BASIN are presented in Chapter 7. The study shows the influence of the most significant input variables on the deflection basin shape. First, a "standard" pavement section was established, so that all subsequent variations would have a common basis for comparison. Next, each input parameter was systematically adjusted to illustrate its influence on the calculated basin. Finally, Chapter 8 summarizes the findings of this research project, lists the conclusions drawn from this research, and makes recommendations for further study.

The model developed in this research was coded into a computer program called BASIN. The FORTRAN code for BASIN is listed in Appendix A.

Chapter 2

NONDESTRUCTIVE PAVEMENT DEFLECTION ANALYSIS

The first nondestructive pavement testing device, the Travel Gage, was installed by General Electric in 1938 on a California highway. It consisted of holes drilled in the pavement to different depths with calibrated rods inserted in the holes. As a vehicle drove over the instrumented pavement section, technicians observed and manually recorded the deflections (Moore et al., 1978). Although this device performed reasonably well, engineers soon realized that a mobile, non-intrusive pavement testing device would be much more useful for assessing pavement and subgrade stiffness.

As numerous technological and theoretical advances occurred over the next 50 years, engineers developed many different devices for determining the stiffness of a pavement system. These nondestructive devices can be grouped into five broad categories, distinguished by their different loading schemes.

- 1) Static
- 2) Steady-State Dynamic
- 3) Transient Dynamic
- 4) Transient Surface Wave Analysis
- 5) Moving Wheel

This chapter describes the general concepts, loading responses, testing equipment, and applications for each category of pavement testing device.

2.1 Static Load

2.1.1 General

Pavement evaluation systems using stationary or very slowly moving loads fall into the category of static deflection devices. Measurements are taken before and after loading, or at points radially outward from a loaded plate. The primary problem with these systems is establishing a reference point from which to measure the deflection -- the point must be close enough to be convenient, yet far enough away that it is not affected

by the load. Because of this problem, the deflection data obtained by static devices is often questionable. However, because so much data has been collected with these devices, the developed correlations are considered fairly reliable (Moore et al., 1978)

The first static deflection measurement device, the GE Travel Gage, was intrusive, using rods inserted into drilled holes of different depths to measure the deflection of pavement and subgrade layers. To improve data acquisition speed, the rods were outfitted with linear variable differential transformers (LVDTs - an electronic dial gauge). This device was extensively used to measure pavement deflections during the Western Association of State Highway Officials (WASHO) Road Test conducted in southeastern Idaho in 1952. However, the Travel Gage still proved too slow and expensive for widespread use (Moore et al., 1978).

Based on observations at the WASHO Road Test, planners realized a mobile pavement testing device would be needed to evaluate pavement at specific locations while the test progressed. Fortunately, A.C. Benkelman was developing a simple lever-arm device to measure static deflections of flexible pavements. He released this device, dubbed the Benkelman Beam, in 1952. As early as 1954, the California Division of Highways began widespread use of the Benkelman Beam (Moore et al., 1978). Many other agencies followed California's lead, while others chose to improve upon the manually operated, tedious instrument. These versions, using the same concept, included the Traveling Deflectometer and the LaCroix - L.C.P.C. (Laboratoire Central des Ponts et Chaussées) Deflectograph, which greatly improved the data collection speed (Moore et al., 1978).

2.1.2 Pavement Deflection Response

Static loading devices create a static deflection basin, which has a magnitude and shape that is dependent on the stiffness of the pavement system. Deflection basins produced by static testing devices are relatively large (up to 10.2 mm (400 mils)) compared to other testing devices because the loads are large and applied for a long time

(several minutes). (Hoffman and Thomson, 1981). Very slow moving loads (less than 3.2 km/hr (2 mph)) create a moving deflection basin that, for all practical purposes, is identical to a stationary basin. Thus, static devices have two potential methods for determining the shape of the deflection basin.

- 1) A stationary load can be applied and deflections measured directly under and at points radially outward from the loading plate.
- 2) Deflections can be measured periodically at one stationary point, while the load is slowly rolled away.

The deflections obtained from either of these methods are plotted as function of distance from the load, as illustrated in Figure 2-1. Rotating this deflection shape around the center of the load creates the entire static deflection basin. Once the shape of the basin is defined, parameter correlations or backcalculation techniques are used to determine the pavement system properties.

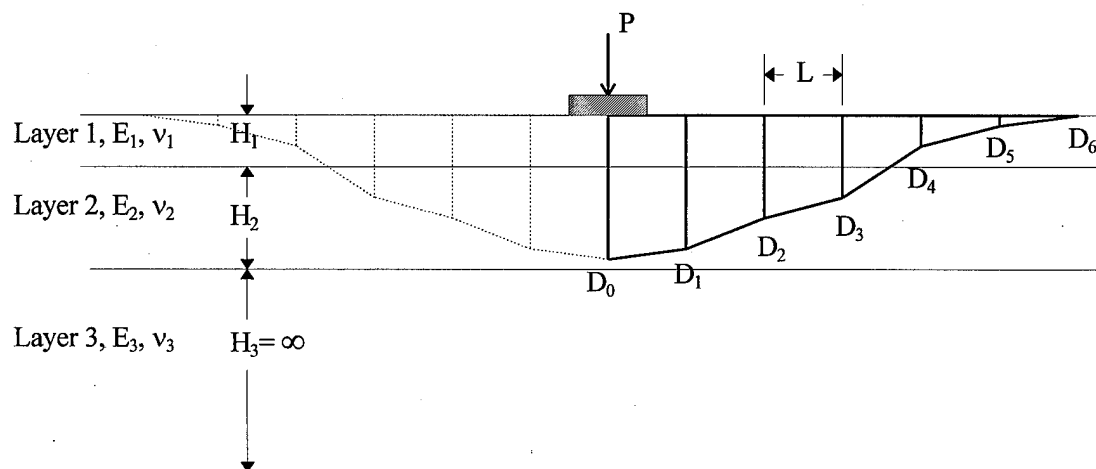


Figure 2-1. Deflection basin and individual deflections produced by a loaded plate as measured by seven deflection sensors.

Correlations directly relate one measurement or index to a pavement property. In pavement analysis, two parameters are commonly used for correlations:

$D(r)$ -- the magnitude of the deflection, D , at a distance, r , from the center of the loading plate. Many correlations between deflections and moduli have been developed, and they generally follow the trend that deflections under and nearby the load plate correlate best to AC layer modulus, deflections in the middle of the basin (between 300 and 900 mm (11.8 and 35.4 in) from the center of the load) correlate best to the base course modulus, and deflections at the edge of the basin relate best to the subgrade modulus.

Area Parameter -- a normalized index equal to the sum of the areas of the trapezoids defined by the deflection measurements divided by the deflection directly under the center of the loading plate. For example, the area parameter from Figure 2-1 would be given by:

$$A = \frac{0.5L}{D_0} (D_0 + 2D_1 + 2D_2 + 2D_3 + 2D_4 + 2D_5 + D_6)$$

Several correlations have been made between the area parameter and pavement layer stiffnesses.

Backcalculation techniques are iterative, require multiple calculations, and use computer programs to quickly solve complicated mathematics. First, a predicted deflection basin is calculated using a model and compared to the measured deflection basin. Next, certain material parameters are adjusted, and finally the predicted deflection basin is recalculated, beginning the next iteration. Iterations continue until the predicted deflection basin matches the measured deflection basin, within a tolerable error. The values of material parameters that were used to produce the matching deflection basin correspond to the actual pavement parameters.

2.1.3 Testing Devices

ASTM D4695-87 (Standard Guide for General Pavement Deflection Measurements) provides guidance for using static deflection devices.

2.1.3.1 Benkelman Beam

A long beam carefully placed between the dual tires of a loaded truck (usually with 80 kN (18,000 lb) rear axle weight) measures the deflected pavement position. As the truck slowly drives away and the pavement rebounds, the beam rotates around a stationary pivot point. The new position represents the undeflected pavement elevation and is compared to the deflected elevation. An observer reads the measurements from a dial gauge that is accurate to $25.4\ \mu\text{m}$ (0.001 in) and then calculates the deflection.

Figure 2-2 illustrates the basic components of the Benkelman Beam.

The Benkelman Beam is simple and inexpensive, but relatively slow. The instrument alone costs only about \$1,000 and an experienced crew can make between 300 and 400 measurements in a day. Of course, traffic must be carefully controlled around the testing crew to ensure their safety.

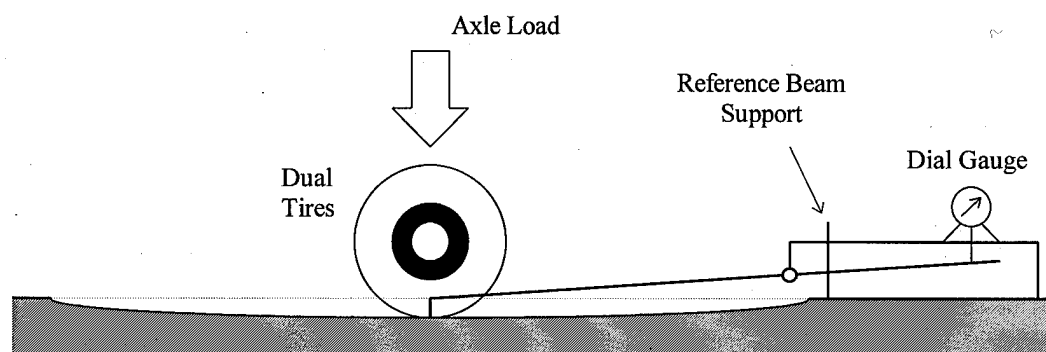


Figure 2-2. Schematic representation of the Benkelman Beam (after Meier, 1995).

2.1.3.2 Traveling Deflectometer

The Traveling Deflectometer is essentially an automated version of the Benkelman Beam and was used by the California Division of Highways. A tractor-trailer outfitted with two lever arms simultaneously measures the deflection between each set of dual tires on its 80 kN (18,000 lb) rear axle. Undeflected measurements are recorded by separate probes located beyond the loaded axle's influence zone. Measurements are

recorded every 6.1 m (20 ft) as the vehicle rolls forward at a creep speed of 0.8 km/hr (0.5 mph).

With this device, 1,500 to 2,000 measurements are possible in a single day (Moore et al., 1978). Also, safety was greatly improved with this device because the operators ride on the vehicle during the test.

2.1.3.3 *LaCroix - L.C.P.C. Deflectograph*

The LaCroix - L.C.P.C. Deflectograph is very similar to the Traveling Deflectometer -- it also is essentially an automated Benkelman Beam. It uses the 116 kN (26,000 lb) rear axle of a truck to load the pavement, and measures deflections with a unique moving beam system. As the truck rolls slowly forward at 1.8 km/hr (1.1 mph), twin measurement beams, each analogous to a Benkelman Beam, are lowered to rest on the pavement surface. The frame supporting the beams slides slowly backwards to keep the probe tips in exactly the same place while the wheels roll forward. The probe tips start about one meter in front of the rear wheels and stay on the pavement until they reach a maximum deflection, slightly behind the rear wheels. Thus, entire deflection basins can be measured and automatically recorded by the Deflectograph. When a test is complete, the beams quickly slide forward to start the testing cycle again (Prandi, 1967).

The LaCroix - L.C.P.C Deflectograph is significantly faster than the Benkelman Beam or the Traveling Deflectometer. Prandi (1967) reported that 7,000 to 8,000 measurements were possible in a single day. However, he added a caveat to this report that speaks to the accuracy of the measurements, "...pavement deformability is better expressed through analysis of numerous deflection measurements, even not very accurate, than by that of a few measurements, even highly accurate."

2.1.3.4 *Plate Bearing Test*

In the plate bearing test, a hydraulic jack reacts against a stationary frame (usually a heavy tractor-trailer) to load a steel plate. This method is very slow (2-3 hours per test)

and used primarily for asphalt overlay thickness design for existing pavement structures. The US Navy procedure for this test uses two separate load plates, 203 and 760 mm (8 and 30 in) diameter, and loads are applied until a 5.1 mm (0.2 in) deflection is observed directly under the load plate (Moore et al., 1978).

2.1.4 Application

Static deflection devices showed promise and filled a valid role during their time, but now have been outdated by technological advances. However, the data relationships developed for static devices still are used today for correlating steady-state and impulsive loading testing to pavement overly design.

Even though static devices were widely used by highway officials, engineers realized that static loading devices had several problematic features. First, deteriorated, loosely bound pavement surfaces are difficult, if not impossible, to test with static devices because the probe tip can move erratically if it rests on a loose stone. Second, a convenient, undeflected reference point for deflection measurements is difficult to find. Stiffer pavements with bound base course materials have wider basins and smaller amplitude deflections, thus, the Deflectograph and Traveling Deflectometer may not record reference points that are truly undeflected. Third, the static loading scheme does not incorporate the dynamic effects of a rolling wheel load.

2.2 **Steady State Dynamic Load**

The next generation of pavement testing devices, steady-state dynamic load, overcame some of the limitations of static testing devices.

2.2.1 General

All steady-state deflection devices cyclically load and unload the pavement to induce a steady-state sinusoidal vibration in the pavement. The dynamic force generator applies a load time history similar to that shown in Figure 2-3 by superimposing the

dynamic load on the static load produced by the weight of the equipment. Note that the dynamic force (peak-to-peak) must be less than twice the static weight of the equipment to ensure continuous contact with the pavement surface.

Steady-state devices represent a significant improvement over static instruments because they overcome the problem of finding a stationary reference point for measuring deflections. Rather than measuring the *absolute* deflection due to the dynamic load, the device measures the amplitude of the *relative* deflection produced by the dynamic load. In other words, an inertial reference system is used and the amplitude of the deflection (peak-to-peak deflection value) can be compared directly to the amplitude of the dynamic force (peak-to-peak force value). Therefore, for a given dynamic force amplitude, a smaller deflection amplitude indicates a stiffer pavement.

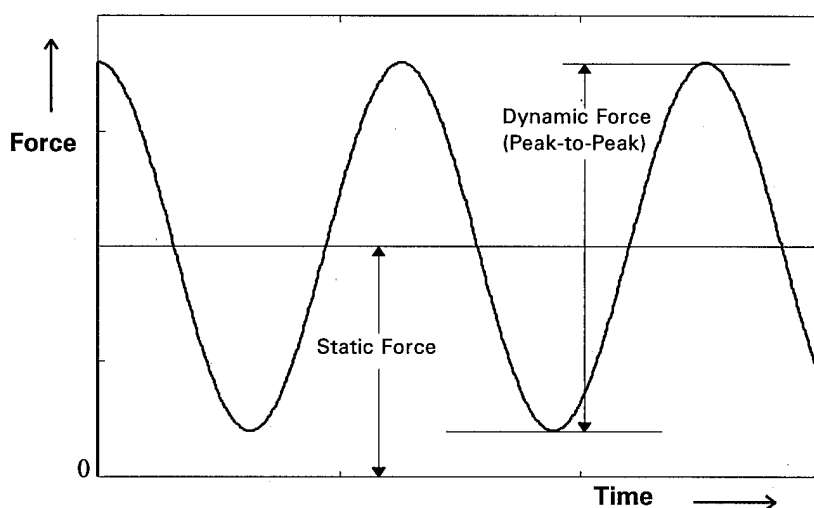


Figure 2-3. Typical output of force generator used for steady-state dynamic testing.

Improvements in deflection measurement systems also make steady-state devices a practical alternative to static systems. With steady-state devices, deflections are measured with electronic displacement, velocity, or acceleration transducers, rather than dial gauges or LVDTs. These inertial motion sensors are essentially single degree of

freedom structures. An internal mass moves within a casing along a particular axis (vertical, for pavement deflection devices). The internal mass displacement, velocity, or acceleration relative to the external case generates an output signal that is processed and recorded by a computer system (Graves and Drnevich, 1993).

Most steady-state devices use velocity transducers (commonly called geophones) and an automatic, electronic integrator to convert the velocity time history to a displacement time history. Velocity transducers with integrators, rather than displacement transducers, are commonly used because the output characteristics of most displacement transducers are heavily frequency *dependent*, whereas velocity outputs are frequency *independent* above a minimum frequency (Moore et al., 1978).

2.2.2 Pavement Deflection Response

In static loading systems, when the load is applied, the pavement deflects proportionally to the applied load; when the load is removed, the pavement returns to the same position (assuming the load is within the elastic range). The same principles apply to dynamic loading. The oscillating load creates a maximum deflection when the maximum load is applied, and the pavement rebounds as the load amplitude reaches a minimum. Therefore, the amplitude of the dynamic deflection is proportional to the dynamic force. In effect, the load on the pavement creates a vibration in the pavement oscillating at the same frequency that the load is applied. The amplitude of the deflection decreases as the distance between the load and the measurement location increases because of material and radiation damping.

The deflection basins measured in a steady-state dynamic test are similar to the deflections created by a static load. However, dynamic deflections are different because the *dynamic stiffness* of the pavement system changes with the driving frequency. The dynamic stiffness has been found to increase as the driving frequency increases. Thus, smaller deflections are observed during higher frequency tests (Moore et al., 1978).

2.2.3 Testing Equipment

ASTM 4695-87 (Standard Guide for General Pavement Deflection Measurements) describes the general procedures for testing pavements with steady-state dynamic devices.

2.2.3.1 *Dynaflect*

The Dynaflect consists of several deflection sensors and a motor that drives two counter-rotating masses, mounted on a two-wheel trailer. The resulting dynamic load is transferred to the pavement through two 101 mm (4 in) wide, 406 mm (16 in) outer-diameter rubber-coated steel wheels spaced 504 mm (20 in) center to center. The resulting pavement contact area is less than 2581 mm^2 (4 in^2). Figure 2-4 illustrates a general schematic of the device and the typical loading configuration.

When the device stops at the test point, the sensors are lowered to the pavement on a beam aligned with the axis of symmetry which passes between the wheels. Geophones spaced 304.8 mm (12 in) apart record the deflections induced by the dynamic force generator. The machine's static load of 8 kN (1,800 lb) is offset by the peak-to-peak dynamic force of 4.4 kN (1,000 lb) applied at a fixed frequency of 8 Hz.

The driver of the towing vehicle completely controls the Dynaflect via remote console. The entire operation at each test site obtains 5 measurements within about two minutes (Moore et al., 1978). Because the device is stationary during testing, traffic must be controlled in the vicinity of the machine.

2.2.3.2 *Road Rater*

Several models of this instrument are available, but they all share certain common features. First, a vibratory load is produced by a steel mass and hydraulically actuated vibrator. The pavement is loaded through two 102 x 1788 mm (4 x 7 in) steel plates spaced 267 mm (10.5 in) center to center, for a total contact area of $36,129 \text{ mm}^2$ (56 in^2).

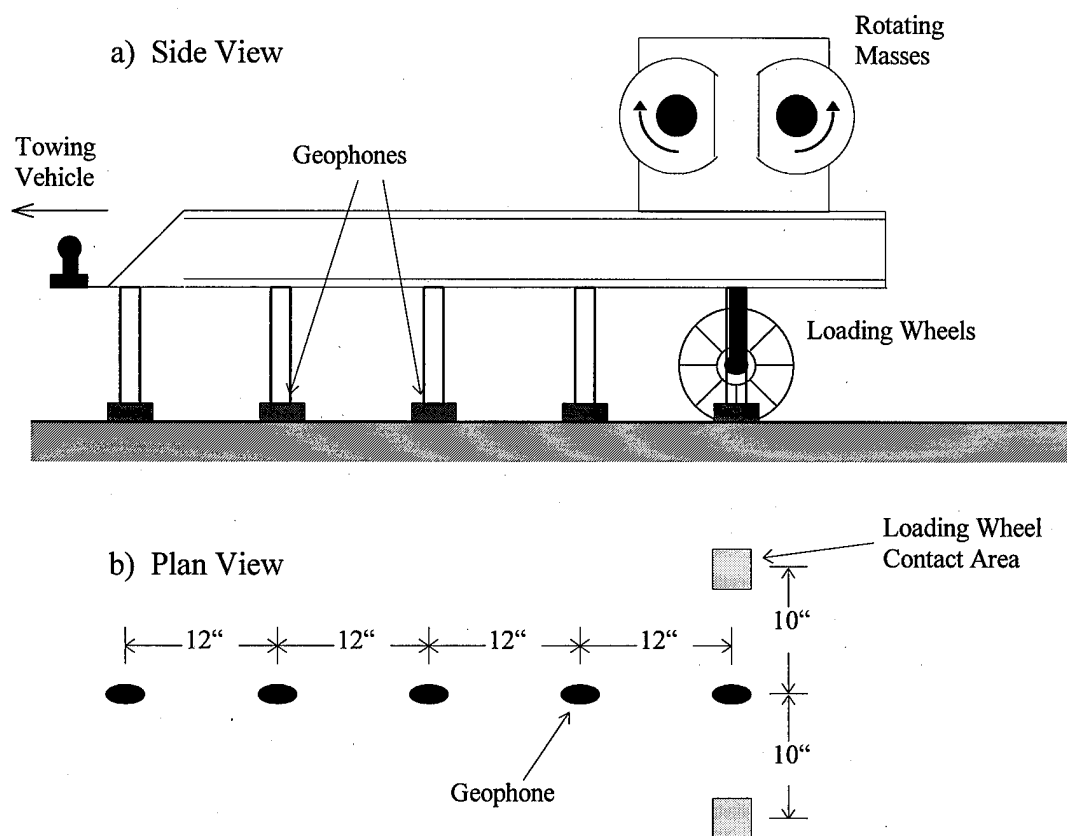


Figure 2-4. a) Schematic Illustration of the Dynaflect. b) Plan view of the loading and geophone configuration.

Normally four geophones, spaced at 305 mm (12 in) along the symmetry axis passing between the load plates, measure the deflections. Like the Dynaflect, these are lowered to the pavement at each test location. Depending on the model, the Road Rater can apply loads ranging between 8 and 22 kN (1,800 and 5,000 lb) at five different frequencies, ranging between 10 and 40 Hz (Moore et al., 1978).

Tests are very fast, requiring less than a minute for one deflection measurement at a preset driving frequency. Like the Dynaflect, the Road Rater is operated by the driver of the towing vehicle.

2.2.4 Application

Steady-state deflection testing devices overcome some of the problems with static devices. The most important advance is the use of an inertial reference system for

measuring deflections. As described in Section 2.2.1, very sensitive and accurate accelerometers or velocity transducers indirectly measure deflections of the pavement surface. Because a stationary local reference is not needed, the devices are much smaller, lighter, and consequently more mobile. All this results in cost savings for highway departments, allowing a smaller crew (1 person) to accomplish more measurements in less time.

Even though steady-state testing devices are a significant improvement over static load devices, there are still problems with the test. First, moving traffic does not load the pavement sinusoidally like steady-state devices. Second, the equipment must be stationary during the test, which requires routing traffic around the equipment. Third, tests are only accomplished at finite locations, usually about every few hundred meters. Therefore, a weak section could go undetected until significant surface distress was recognized.

2.3 Transient (Impulse) Dynamic Load

The next generation of pavement testing devices, falling weight deflectometers, attempt to overcome the single-frequency loading problem associated with steady-state devices by loading the pavement with a single impulse force.

2.3.1 General

All impact load devices, commonly referred to as falling weight deflectometers (FWDs), produce a transient impulse load by dropping a known weight from a known height onto a contact plate of known area and stiffness. Typically, the peak load and the induced vertical deflections are measured at points directly under the load and at different distances from the load.

FWD loading systems are comprised of a force-generating device (falling weight), guide system, loading plates, and load cell. The falling weight is mechanically raised to one of several controlled heights and released. The guides ensure that the weight falls

perpendicular to the pavement surface with negligible friction, and that the weight strikes the plate in a controlled, repeatable manner. Load plates help to uniformly distribute the load over a 305 to 457 mm (12 to 18 in) diameter area. They are generally made of steel with a rubber coating on the bottom, which helps to condition and extend the transient load shape. Additionally, the plates have a small opening in their centers to allow for a deflection measuring device. The force pulse duration lasts between 20 and 60 milliseconds (ms) and can be approximately described by a haversine or half-sine wave. This load shape more closely resembles the action of real traffic than either the static or steady-state devices (Barksdale, 1971).

Deflection measurement sensors are generally mounted on a beam extending from the load plate radially outward along the travel direction. Each particular testing model may have different numbers and spacing of sensors. With some models, the sensor locations may be adjusted, depending on the testing application. The sensors are connected to an onboard computer system that records the peak vertical deflection at each sensor location. Several types of sensors are used, including seismometers, velocity transducers, and accelerometers.

2.3.2 Pavement Deflection Response

When the falling weight strikes the load plate, the surface of the pavement deflects by an amplitude dependent on the stiffness of the entire pavement system. While the deflection is occurring directly under the load plate, a deflection wave front is emanating radially away from the load plate. As a result of radiation and material damping, the amplitude of the pavement deflection decreases as the wave moves farther from the load plate. For a given impulse force, a stiffer pavement will deflect less than a softer pavement. Also, the speed at which the wave propagates away from the load plate is a function of the material stiffness -- waves travel faster in stiffer systems.

As described in the previous section, FWDs have sensors that record the deflection at several points on a line extending outward from the load plate. These

sensors capture a time history of deflection at each point; however, typically only the peak deflection is used for analysis. Plotted together, these peaks form a “static” deflection basin. Close analysis of the time history of deflections shows that the peak deflections do not occur simultaneously at all points. Rather, the peak occurs later at each successive sensor. Thus, the “static” basin never truly exists during an FWD test. This concept is more fully illustrated in Chapter 5.

Once the “static” deflection basin is known, the same procedures used for static and steady-state devices are used to analyze the data and determine layer moduli. That is, correlations to basin measurements or backcalculation techniques are used, as described in Section 2.1.2.

2.3.3 Testing Equipment

ASTM 4694-87 (Standard Test Method for Deflections with a Falling Weight Type Impulse Load Device) describes the general testing procedures, apparatus, and data acquisition systems applicable to transient dynamic load testing devices.

2.3.3.1 *Dynatest 8000 Falling Weight Deflectometer.*

Introduced in the early 80's, this FWD device has the longest service record in the United States. It is trailer mounted and remotely controlled by the driver of the towing vehicle. The impulse load is delivered by dropping a hydraulically raised weight onto a buffer/loading plate system. The loading plate is 300 mm (11.8 in) in diameter and is comprised of a single piece of steel with a rubber pad on the bottom to help distribute the load more evenly. Figure 2-5 illustrates the loading system.

Deflections are measured using 7 geophones located on a raise-lower bar extending towards the towing vehicle from the load plate. An onboard computer records the peak deflection or the entire time history of deflection for each sensor. The load pulse duration is 25 to 30 ms, and the load magnitude can range between 7 and 125 kN (1,574 and 28,103 lb), depending on the drop height.

Up to eight individual drops at 4 different heights can be used in a single test program. Like the steady-state devices, the Dynatest is automated and requires less than two minutes at each test site.

2.3.3.2 KUAB 2M - Falling Weight Deflectometer (Model 8714)

The KUAB 2M, manufactured in Sweden, gives results similar to the Dynatest, but loads and measures the pavement deflections in a very different way. The KUAB uses a two-mass system, consisting of a falling mass and a second mass-buffer system to create the impulse load, as illustrated in Figure 2-5. The two-mass system creates a more reproducible load shape, and also approximately doubles the pulse duration (60 - 70 ms) (Crovetti et al., 1989). The load plate is a 300 mm (11.8 in) diameter steel plate segmented into four quadrants, each with a rubber pad. The four segments are equally loaded, but the segmenting allows the plate to better conform to pavement surface irregularities.

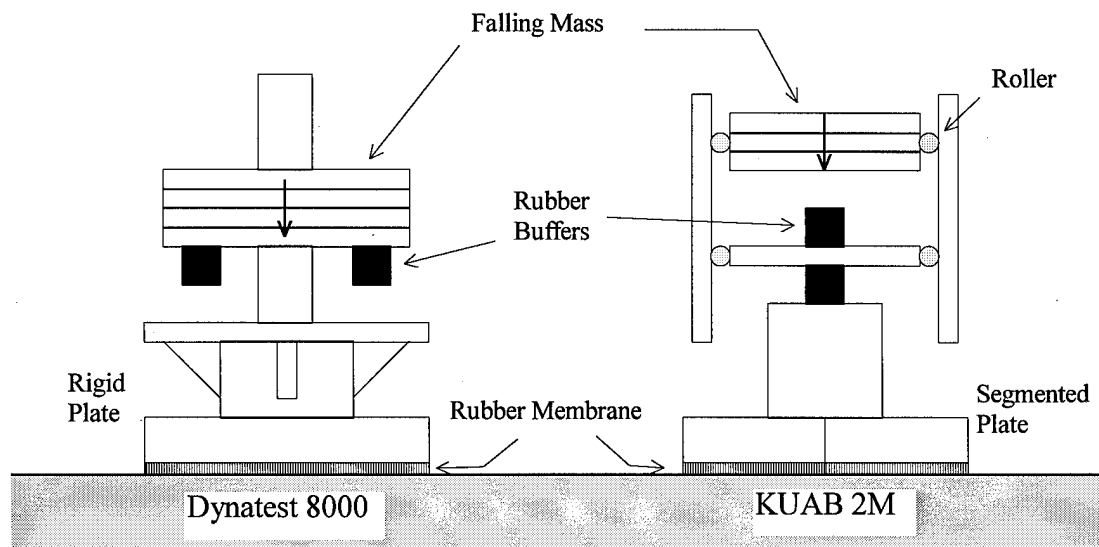


Figure 2-5. Schematic illustration of the loading mechanism used by two falling weight deflectometers (after Crovetti et al., 1995).

Rather than using geophones, the KUAB is equipped with seven seismometers (deflection transducers) to measure the pavement displacements. The sensors are mounted on a raise-lower bar that extends radially away from the towing vehicle.

Like the Dynatest, the KUAB 2M is fully automated, requiring just a few minutes at each test site. Unlike the Dynatest, a virtually unlimited number of drops can be programmed for each height in a testing sequence. Also, the testing device is completely enclosed by a locking metal housing for protection from weather and road grime during transportation.

2.3.4 Application

Falling weight deflectometers are widely used by state highway administrations for pavement evaluation and overlay design. Often, the FWD testing program is used in conjunction with a backcalculation program like EVERCALC, ILLI-PAVE, BISAR, or WESDEF. These programs adjust layer stiffnesses until the predicted deflection basin matches the measured "static" deflection basin. Maintenance decisions and rehabilitation design are based on the layer stiffnesses determined by the FWD testing program.

Some researchers have developed methods for determining layer thickness along with stiffness (Sivaneswaran et al., 1993). Additionally, more work is underway that uses the entire time history of deflection for pavement analysis (Ketchum, 1993; Zaghoul et al., 1994).

Although deflection analysis programs are now well-developed and produce accurate, repeatable results, there are still two principle limitations to FWD testing. First, the FWD must be completely stationary to perform each test. Therefore traffic control is needed to keep traffic flowing around the machine. Second, although the FWD load pulse is very similar to a rolling wheel passing over a stationary point, it is not exactly the same. Coupled with analysis programs that only use peak "static" deflection basins, the true *dynamic* response of the pavement is not well understood. In spite of the

disadvantages of the FWD, it remains far superior to earlier testing devices. As backcalculation models become more refined, results will only improve.

2.4 Transient Surface Wave Analysis

2.4.1 General

A fourth type of nondestructive testing called Spectral Analysis of Surface Waves (SASW) can be used to determine the pavement system layer modulus *and* thickness. Like falling weight deflectometers, SASW uses the results of deflection time histories at discrete points due to an impulse load. However, instead of using deflection *magnitudes*, the SASW method uses the *phase difference* in surface wave records to determine the wave propagation velocity at various depths. When the velocity, V_s , density, ρ , and Poisson's ratio, ν , are known, the material modulus (a.k.a. stiffness), E , can be directly calculated through the following basic relationships,

$$V_s = \sqrt{\frac{G}{\rho}} \Rightarrow G = \rho V_s^2$$

$$E = 2G(1 + \nu) = 2\rho V_s^2(1 + \nu)$$

where G is equal to the shear modulus.

Figure 2-5 schematically illustrates the basic components used in SASW testing. The impulse source, ranging from a tack hammer to a 67 N (15 lb) sledge hammer (depending on the distance to the geophones), impacts the pavement and generates a group of Rayleigh waves (surface waves) emanating from the source at various frequencies. The two vertically oriented receivers record the motion of the pavement as the wave energy moves past them. The spectral analyzer quickly converts the time history output from the receivers into a frequency domain response using a fast-Fourier transformation (FFT). By analyzing the phase difference between the two receivers at each frequency, the variation of Rayleigh wave velocity with wavelength is determined. A plot of the surface wave velocity versus the wavelength is called a dispersion curve.

The dispersion curve is the “raw data” carried out of the field for in-house data reduction (Nazarian and Stokoe, 1984).

Dispersion curves are then converted to meaningful layer stiffness and thickness information by a process known as *inversion*. The earliest and least sophisticated inversion processes simply assumed that the shear wave velocity was equal to 1.1 times the Rayleigh wave velocity at the depth corresponding to one-half to one-third the wavelength (Nazarian and Stokoe, 1984). In recent years, more sophisticated inversion processes have been developed that model the pavement as a laminate of many individual sublayers, each with (potentially) unique properties. Through an iterative process, a shear wave velocity (or stiffness) for each sublayer is assumed, and a theoretical dispersion curve is calculated. The theoretical curve and the measured curve are compared, and then the shear wave velocity profile is adjusted until the two curves match, within a tolerable error.

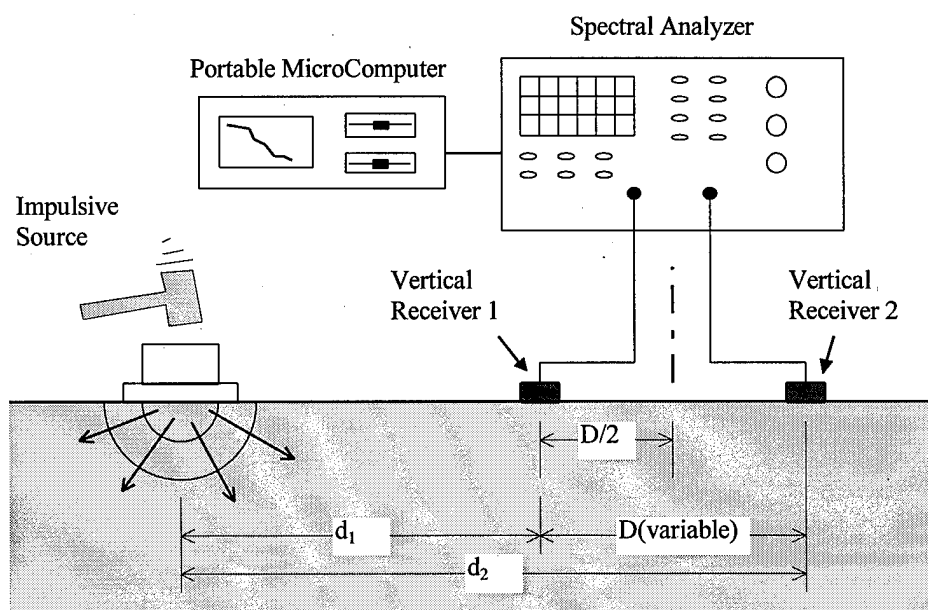


Figure 2-6. General configuration of SASW test (after Nazarian and Stokoe, 1989).

The final shear wave velocity profile is converted to a stiffness profile by assuming a Poisson's ratio and mass density for each layer, and using the formula:

$$E = 2G(1 + \nu) = 2\rho V_s^2(1 + \nu)$$

The stiffness profile is next examined to determine layer thicknesses. The boundary between separate layers is indicated by a sharp contrast in stiffness. Thus, if two adjacent sublayers have very similar stiffnesses, they can be considered as one layer (Nazarian and Stokoe, 1989).

2.4.2 Pavement Deflection Response

As established in the previous section, SASW tests derive all of their information from the propagation of surface waves over a broad range of frequencies. If the SASW test were conducted on a homogeneous, isotropic, elastic halfspace, only one frequency would be needed for testing, because the surface wave velocity would be constant for all frequencies. However, because pavement layer properties vary with depth, the surface wave is dispersive; i.e. its velocity changes with frequency. Thus, to determine the variation of stiffness from the pavement surface down through the subgrade, tests must be conducted using very high (tack hammer) to very low (sledge hammer) impulse frequencies.

In theory, all frequencies should be recorded with a single impact. However, in practice, certain receiver spacings and impulse loadings work best to develop a quality profile. Nazarian and Stokoe (1989) describe a common receiver midpoint (CMRP) array that is most appropriate for analyzing pavement layers. Forward and reverse profiles are conducted with each configuration to reduce data scatter. Figure 2-7 illustrates the source and receiver arrangement for the CMRP array.

2.4.3 Testing Equipment

The field equipment required for SASW testing basically consists of three components: a source, two (or more) receivers, and a recording/analyzing device.

Sources used in SASW testing must be capable of generating surface waves containing a wide range of frequencies. Because small hammers generate predominantly high frequency waves and large hammers generate predominantly low frequency waves, a combination of hammers is often used for the entire series of tests at one site. Extremely high frequency waves (over 20 kHz) must be generated to examine the upper few centimeters of pavement; pulsating crystals have been successfully used for this purpose (Nazarian and Stokoe, 1989). Very small impulse sources can be used when the sensors are close together because the deflection amplitude is not used for SASW testing, only the phase lag between receivers is important.

Receivers are selected depending on the frequency of interest. Accelerometers are better at capturing higher frequency waves (over 500 Hz), and geophones (velocity transducers) work better for lower frequency waves (less than 500 Hz), (Nazarian and Stokoe, 1989).

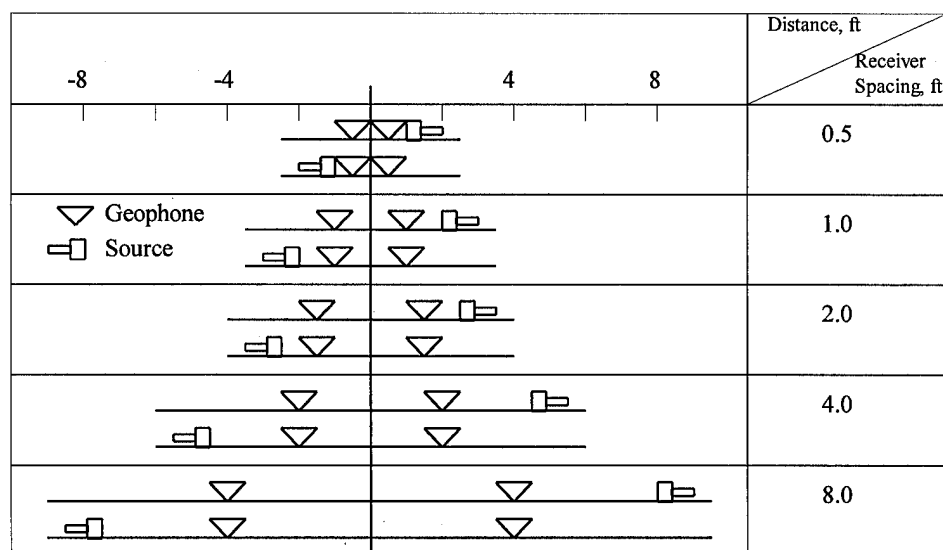


Figure 2-7. Schematic of CMRP arrangement for SASW testing (after Nazarian and Stokoe, 1989).

A spectral analyzer and microcomputer are used to analyze and record the measured data. The spectral analyzer automatically digitizes the time-domain signal, and using a fast-Fourier transform, converts the signal to the frequency domain. Next the cross-power spectrum and coherence functions are generated and used to create a field dispersion curve. The cross-power spectrum is a way to view the surface wave phase lag as a function of frequency. It is used to determine the surface wave velocity and wavelength. The coherence function simply determines the range of frequencies over which the analyzed signal is coherent, i.e. reasonable and accurate (Nazarian and Stokoe, 1989).

Automated SASW testing devices are still in the developmental stage, and as such, single-unit commercial testing devices are not available. Without automation, a team of technicians requires 20 to 40 minutes to run the complete series of tests at one site. Thus, the method is not considered economically feasible for general applications until it can be automated.

2.4.4 Application

The SASW method is not as fast as the previously described nondestructive test methods, but it does offer three distinct advantages over those test methods.

First, layer thicknesses can be determined directly from the testing. With deflection-based testing and analysis (except for a few advanced backcalculation techniques), layer thicknesses are assumed based on construction drawings, or core samples are drilled to determine precise thicknesses.

Second, the variation of moduli *within* the subgrade can be determined. Other tests treat the entire subgrade as a single layer with constant modulus. This plays a particularly important role when there is a rigid layer (bedrock) near the pavement surface. Also, deflection-based testing must assume the depth to the rigid layer, whereas SASW testing can determine the depth and the modulus of the rigid layer (Nazarian and Stokoe, 1989).

Third, the modulus of thin layers at the pavement surface can be accurately determined. Large variations in thin layer stiffness may only slightly change the shape of a deflection basin, but the SASW method can easily locate and determine the modulus of thin layers.

2.5 Rolling Wheel Load

The newest type of device developed for pavement testing loads the pavement with a rolling wheel and uses sensors to continuously measure deflections. Though several loading and measuring schemes exist, one common advantage for all the devices is that a continuous deflection profile is produced. Thus, small weak zones can be easily identified. This section describes the operation and testing of two different rolling deflectometers.

2.5.1 Testing Equipment

Rolling weight deflectometers are still in the developmental stage and are not yet commercially available. However, some prototypes have been constructed. Two models are described here. Each loads the pavement and measures the deflections using very different methods.

2.5.1.1 *SNRA Rolling Weight Deflectometer*

The Swedish National Road Administration (SNRA) began developing a rolling weight deflectometer (RWD) in the 1980's, and built its first prototype in 1991 (Arnberg et al., 1991). The testing device consists of a heavy truck with two transverse laser profilometers. The profilometers were originally developed for measuring surface roughness, but in this case were used to measure deflections.

As illustrated in Figure 2-8, the first profilometer is mounted a few feet behind the lightly loaded front axle. It measures the undeflected shape of the pavement surface. The second profilometer is mounted immediately behind the heavily-loaded rear axle and

measures the deflected shape of the pavement. The difference between the two profiles represents the deflections caused by the loaded axle.

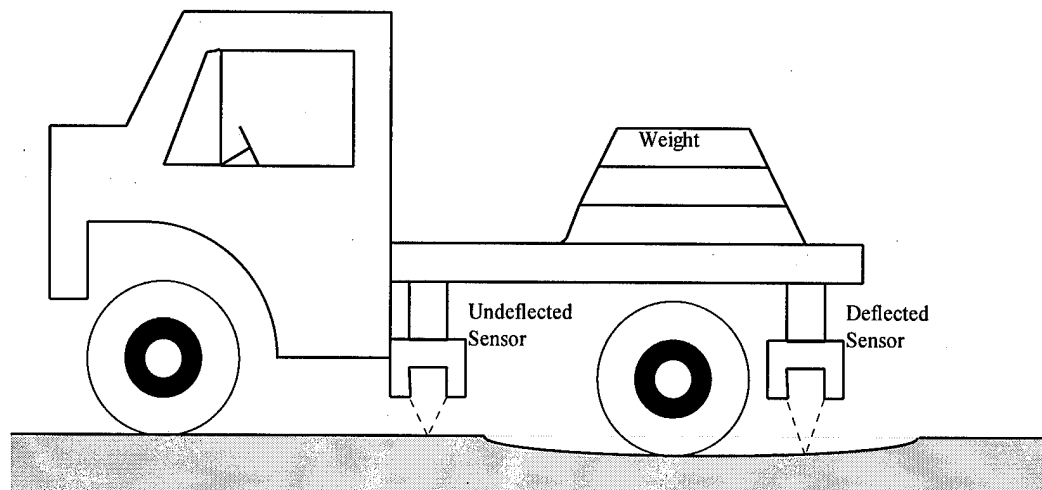


Figure 2-8. Schematic representation of the SNRA Rolling Weight Deflectometer.

Preliminary tests with the prototype indicated that the measured deflections were very repeatable over the same pavement segment. Tests conducted at 10, 30 and 50 km/hr (6, 19, and 31 mph) showed that deflections markedly decreased as the vehicle speed increased. Comparisons between the RWD and the FWD maximum deflections (directly behind the wheel and under the load plate) showed reasonable agreement for wheel velocities of 5 km/hr. Errors were attributed to the differences between the dynamics of the two tests.

2.5.1.2 UT Rolling Dynamic Deflectometer

Bay et al. (1995) describe a rolling dynamic deflectometer (RDD) constructed at the University of Texas at Austin that applies a dynamic load to the pavement through two wheels mounted midway between the front and rear axles (Figure 2-9). The load is applied by a servo-hydraulic vibrator and can generate dynamic vertical forces as large as 310 kN (70,000 lb). The servo-hydraulic vibrator can generate a variety of dynamic

loading functions, including transient (like the FWD) and steady-state (ranging from 5 to 100 Hz). The test can be conducted at speeds between 4 and 6 km/hr (2 and 4 mph).

The resulting deflections are measured by an isolated pair of wheels resting on the pavement directly between the loading wheels. An accelerometer records the vertical motion of the wheels to generate a continuous motion profile. After some data processing, a continuous record of pavement flexibility can be constructed.

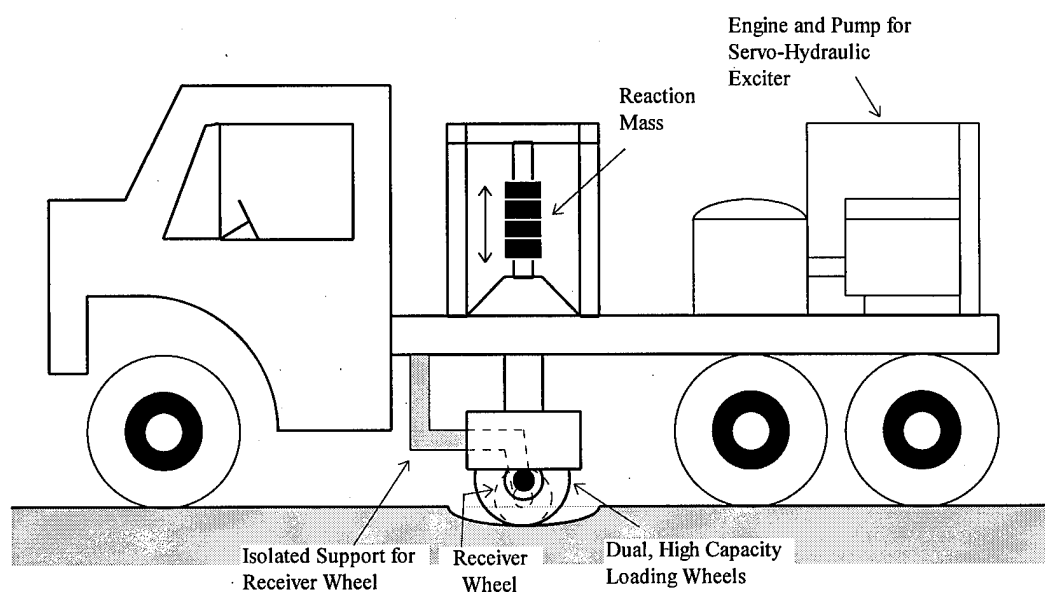


Figure 2-9. Schematic representation of the UT Rolling Dynamic Deflectometer (after Bay et al., 1995).

Tests have been completed with the RDD on eight flexible pavement sections. The results showed that the test is particularly good for identifying weak segments within a generally sound pavement section. Comparisons between the RDD and FWD found that the tests show similar deflection to load trends, but that more work is necessary to fully understand the relationship between the two tests (Bay et al., 1995).

2.5.2 Application

Rolling deflectometers show real promise for future use in pavement analysis. Three aspects stand out as significant advantages of rolling load testing. First, the tests are conducted while in motion, so traffic control around the equipment is easier, and user (highway travelers) costs are lower. In the case of the SNRA device, high speed testing (up to 90 km/hr (56 mph)) may make the tests completely transparent to the user. Second, the testing generates a continuous pavement profile. This helps to identify weak segments of the road that may be missed by conventional stationary tests. Third, for the SNRA Rolling Weight Deflectometer the applied load exactly matches traffic loading. This solves a problem that has plagued all of the other testing devices.

However, there are still several significant problems to overcome before rolling deflectometers will be fully operational. First, the measurement system must be improved to ensure accurate measurements at reasonable speeds. The RDD sensor wheel will likely not perform well at even moderate speeds, and the laser sensors used by the RWD can be adversely effected by moisture on the pavement or a coarse, open-grained surface. Also, accurately defining the undeflected datum is difficult because of small movements in the beam to which the sensors are attached. A precisely defined datum is essential because the amplitude of the measured deflections is very small (< 1 mm).

Second, dynamic interpretation models for rolling load tests are not well-developed. As previously described, the dynamic aspects of FWD tests are frequently ignored so that backcalculation can be accomplished more quickly. Rolling loads add an extra level of complexity to the stationary dynamic load model, and cause computation times to increase even more. At this time, models that accurately predict the deflection basin caused by a rolling wheel on a layered pavement system do not exist.

Chapter 3

FLEXIBLE PAVEMENT DEFLECTION MODELS

Pavement deflection models attempt to answer the question: *What is the deflection (or stress or strain) at location A, when a load is applied at location B?* Many possibilities exist for both the locations and types of loads that may be of interest. For example, a load could be located at the surface or within a pavement layer, and the response of interest could be horizontal, vertical, or rotational deflections. Also, applied loads could be static or dynamic over time, horizontal, vertical, or torsional in direction, and applied to a disk, ring, or square plate.

Ideally, the deflection model would be developed to match the loading conditions exactly. Inevitably, certain assumptions must be made to simplify the model and facilitate easier (or more rapid) calculations. For example, as mentioned in Chapter 2, static deflection models are routinely used to interpret data measured by dynamic tests. Unfavorable consequences may result from this type of oversimplification. This chapter describes some flexible pavement deflection models that have been developed, and emphasizes the inherent assumptions of these models.

3.1 Static Models

Static deflection models predict the response resulting from a static load applied to a known area on a given medium. The level of complexity of these models is determined by the number of layers in the loaded medium, the stress-strain characteristics of the materials in the medium (linear elastic or non-linear elastic), and the type of interface conditions between individual layers (frictionless or fully-frictional).

In 1885, Boussinesq developed the first solutions for deflections due to a point load applied to the surface of a homogeneous linear elastic halfspace. His solutions were extended to include deflections due to loaded areas, such as disks, by integrating over the loaded area.

The next advancement in static deflections occurred in 1943, when Burmister published his solution for displacements in a two-layered system (a finite layer over a

homogeneous halfspace). This allowed pavement analysts to model the asphalt layer separately from the underlying base and subgrade. Burmister later refined his solution to allow for a frictionless (1945a) or fully-frictional (1945b) interface between layers, and for a three-layered system (1945c). At that point, pavement analysts could finally separate a pavement system into its three primary layers: asphalt concrete, base course, and subgrade.

Linear elastic static loading models, such as Burmister's, make the following assumptions about layered systems (after Huang, 1993). A generalized pavement profile is illustrated in Figure 3-1.

1. Each layer is homogeneous, isotropic, and linearly elastic with modulus, E , and Poisson's ratio, ν .
2. The material is weightless and infinite in areal extent.
3. Each layer has a finite thickness, h , but the lowest layer is infinite in thickness.
4. A uniform pressure, q , is applied on the surface of the pavement over a circular area of radius a .
5. Continuity equations are satisfied at layer interfaces, as indicated by the same vertical stress, shear stress, vertical displacement, and radial displacement.

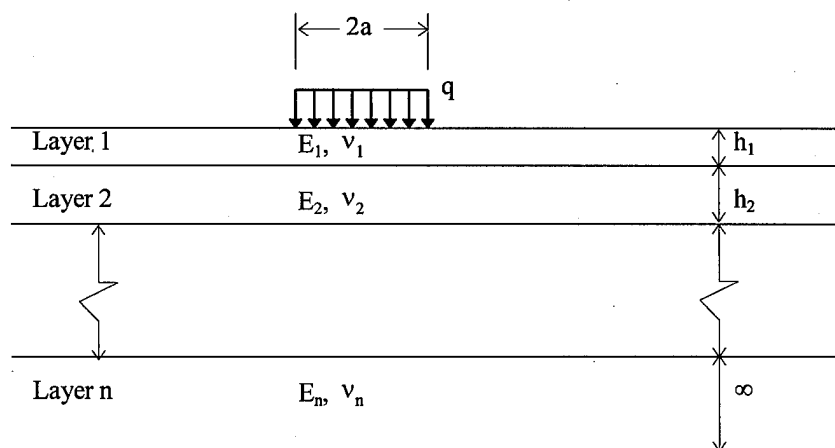


Figure 3-1. Illustration of an n-layer system subjected to a disk load (after Huang, 1993).

The first assumption, which states that all materials are linear elastic, is a very important feature of these models. The *linear* aspect allows the use of superposition to calculate deflections caused by multiple loads. For example, the deflection at the midpoint between two equally loaded tires is equal to twice the magnitude of deflection at the same distance from a single tire. The *elastic* portion of the assumption recognizes that moving traffic loads cause small deformations that are recoverable, even though subgrade soils do not behave elastically when subjected to large, stationary loads (Huang, 1993).

These assumptions can be applied to a multi-layered system, and with the use of computers, programs have been developed that quickly solve for stresses, strains, and displacements on the surface and within the pavement system (Huang, 1993). ELSYM5, KENLAYER, WESLEA, BISAR, and EVERSTRESS all use layered linear elastic theory to solve the static load problem.

Non-linear elastic models recognize that pavement system materials, especially subgrade soils, do not have a constant modulus as stresses and strains increase. Non-linear models require knowledge of a soil's constitutive relationship (Huang, 1993), which, in the simplest case, relates the stiffness of a soil element to its state of stress. When a pavement system is modeled as a combination of many small elements, a constitutive relationship allows the moduli to be adjusted for each element within a soil layer, depending on the overburden and applied stress.

Chang et al. (1992) studied the potential for non-linear behavior in the FWD test. By varying the applied loads at a single site, the deflection behavior was obtained. Chang et al. determined that non-linearities were especially pronounced where the subgrade was soft or the asphalt pavement was relatively thin. In these cases, non-linear effects increased peak deflections by as much as 50% under very heavy FWD loads (88.96 kN (20,000 lb)). However, deflections more than 3 ft away from the load plate were nearly unchanged.

Several computer programs have been developed to model the non-linear behavior of multi-layered systems. MICH-PAVE, developed at Michigan State University, and

ILLI-PAVE, developed at the University of Illinois, both use finite element methods to calculate stresses, strains, and deflections due to static loads on non-linear pavement systems.

3.2 Dynamic Models

Many pavement analysts use static models to interpret the data obtained from dynamic tests, such as the FWD or Road Rater. Although this practice is common, certain conditions can result in gross misinterpretation of the data. For example, Roesset and Shao (1985) concluded that a static interpretation of Dynaflect (steady-state dynamic load) deflections, when the soil is underlain by a stiff layer (bedrock) at depths of less than 60 feet, can result in substantial errors (up to 70%) in pavement layer moduli. The errors were attributed to dynamic amplifications at certain loading frequencies. Dynamic effects are not as pronounced in FWD tests because the impact load excites a broad range of frequencies. However, the AC moduli still could be underpredicted by as much as 40% when the FWD dynamic response is not considered.

This section describes dynamic deflection models that use a variety of mathematical techniques. First, models that consider a dynamic load applied at one location are explained. Next, moving load models are described.

3.2.1 Stationary Load Models

In this thesis, dynamic stationary load models refer to those in which the load is applied at the same location on a pavement throughout the duration of loading. Dynamic steady-state and FWD tests both fall into this category.

3.2.1.1 Linear-Elastic Dynamic Models

Determining the response of a soil deposit to dynamic loading, whether caused by explosions, moving traffic, or earthquakes, falls into the mathematical realm of wave propagation. In 1904, Lamb first published the solution for waves passing through an elastic halfspace (Meier, 1995). Thomson (1950) was the first to develop the solution for

waves passing through a *layered* halfspace. Thomson's solution used matrices that linearly related stresses at the top of a layer to the stresses at the bottom, and ensured that particle velocities at the bottom of one layer were identical to those at the top of the underlying layer. Using Thomson's method, the stresses at the top or bottom of any layer could be related to the stresses at the surface.

Haskell (1953) used Thomson's matrix formulation to generate the phase velocity dispersion equations for elastic *surface* waves (Rayleigh and Love waves) through a multi-layered halfspace. Haskell also corrected an error in Thomson's derivation, thus his results produced what is now called the Haskell-Thomson transfer matrix method (Meier, 1995).

Kausel and Roesset (1981) used the Haskell-Thomson transfer matrix approach to derive layer stiffness matrices that relate applied loads to displacements. The stiffness matrix solution is not more general than the Haskell-Thomson transfer matrix approach, but it is more efficient for numerical integration. When layer thicknesses are small compared to the wavelengths of interest, the transcendental functions which govern vertical displacements can be linearized. Algebraic functions then replace the transcendental functions, and the eigenvalue problems for wave propagation can be solved by standard techniques. This results in significant gains in computational efficiency.

Using this stiffness matrix approach, Kausel and Peek (1982) developed an explicit, closed-form solution for functions (Green's functions - described in Chapter 4) that relate displacements in a layered strata to unit harmonic loads. Solutions were developed for several loading schemes including vertical disk loads, horizontal point loads, torsional ring loads, and other permutations of load direction and areas. Kausel created a computer program called PUNCH, that uses this method of calculating the Green functions. PUNCH has been used by several researchers to develop dynamic pavement deflection models.

Davies and Mamlouk (1985) studied deflection basins generated by dynamic steady-state testing devices, and concluded that the basins were substantially different

than those produced by static loads. The application of static deflection analyses applied to dynamically produced basins may yield misleading results if the operating frequency is close to the resonant frequency of the pavement system. Other researches have studied the influence of a rigid layer (bedrock) at a shallow depth (less than 60 ft) on deflection basins. Roesset and Shao (1985) showed that static analysis of the basin produced by steady-state (Dynalect) and transient (FWD) dynamic loads can lead to large errors in backcalculated layer moduli.

Sanchez-Salinero (1987) used PUNCH to model waves produced during seismic testing of soils. After conducting a series of parametric studies, he developed rules for discretizing a layered system to yield the most accurate solution.

Ketchum (1993) developed a dynamic model that uses PUNCH to interpret FWD tests on airport pavements. He focused on the effects of a frozen layer at shallow depth on the dynamic response of pavements, and was able to formulate a backcalculation procedure to determine layer moduli. Ketchum found that pavements could exhibit a significant resonant amplification at certain frequencies when a rigid layer is at a shallow depth.

To generate dynamic deflection basins for training a neural network backcalculation scheme, Meier (1995) used Sanchez-Salinero's version of PUNCH. He optimized the code to calculate only vertical deflections due to a vertical disk load, and added a subroutine that automatically discretized the pavement layers into properly-sized sublayers.

3.2.1.2 *Viscoelastic Dynamic Models*

Asphalt concrete is considered a viscoelastic material. That is, the stress in the asphalt is a function of the strain *and* the strain rate. Viscoelastic materials are often represented in models by a linked combination of a linear spring and dashpot -- the stress in the spring is directly proportional to the strain, whereas the stress in the dashpot is proportional to the strain rate. For example, the Maxwell model, illustrated in Figure 3-2, is represented by a spring and dashpot in series. For a constant applied stress, an

instantaneous elastic extension of the spring occurs. At the same time, the dashpot begins to extend, and over a period of time the strain will steadily increase (Haddad, 1995).

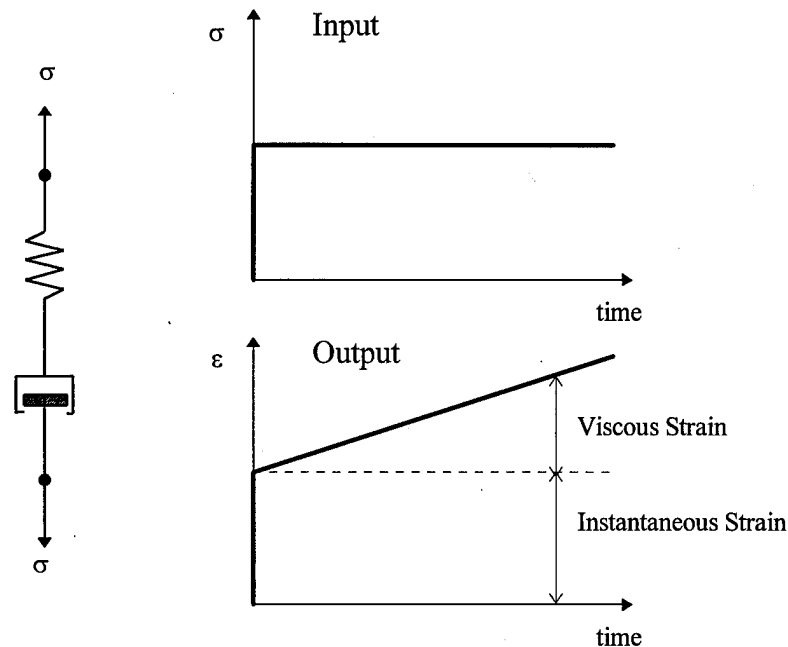


Figure 3-2. Illustration of the properties of a viscoelastic Maxwell model (after Haddad, 1995).

Because FWD and moving wheel loads are inherently time-dependent loads, it is logical to build a viscoelastic model to predict deflections. For example, KENLAYER has the option to consider dynamic loads by assigning viscoelastic properties to each layer (Huang, 1993). SAPSI, developed at the University of California at Berkeley, uses the finite element method with viscoelastic properties to calculate deflection responses resulting from multiple dynamic surface loads (Chatti et al., 1995).

3.2.2 Rolling Load Models

Relatively few models have been created to predict the displacements from a moving load on a pavement system. Huang (1993) describes viscoelastic models using

KENLAYER and VESYS to predict the time history of deflection at a single location as the wheel passes over it. For these models, a series of individual loads are applied to the point at each time increment. The amplitude of each point load increases and decreases following the pattern of a haversine. The duration of the combined pulse is dependent on the speed of the vehicle and the tire contact area.

An alternative approach that is particularly applicable to railroads is to treat the asphalt surface layer as a beam fully supported by an elastic or viscoelastic foundation. Achenbach and Sun (1965) used a viscoelastic model to study the dynamic response of a beam resulting from a rapidly moving load. Holder and Michalopoulos (1977) investigated the response of a beam supported by a Winkler-type elastic foundation with inertia (i.e. not massless) and damping subjected to a moving load. Steady-state solutions for beam deflections were developed; that is, the deflections an observer moving with the load would see.

Trochanis et al. (1987) predicted the beam-foundation contact pressure, beam deflection, and bending moment resulting from a moving, oscillating load (train wheel set) on a fully-supported beam. The system was modeled as an infinitely long beam supported by an arbitrary linear-elastic, damped foundation. The model showed that for a moving load, the maximum deflection occurs slightly behind the wheel, as illustrated in Figure 3-3.

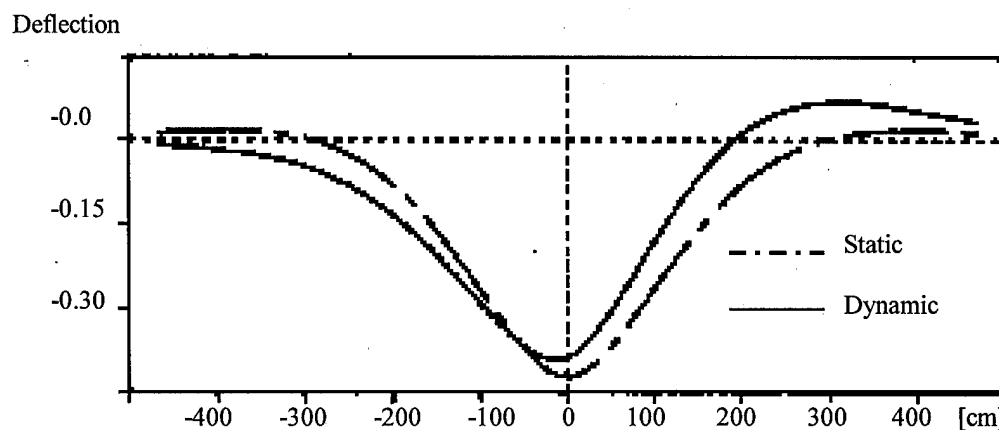


Figure 3-3. Static and dynamic deflections resulting from a rolling wheel load (Trochanis et al., 1987).

Chapter 4

DYNAMIC LAYERED ELASTIC ANALYSIS USING GREEN'S FUNCTIONS

The previous chapter described a number of different types of pavement deflection models. This chapter will focus on one particular type -- a dynamic layered elastic model. In this research, a dynamic layered elastic model was developed using the Green's function approach. This chapter describes the Green's function concept, applications, and the specific solutions developed for this project.

4.1 Green's Functions

A Green's function is a mathematical tool that can be used to find solutions to many boundary value problems associated with either ordinary or partial differential equations. The Green's function concept was first introduced by G. Green in 1828, but its use as a practical analysis tool did not begin to develop until the middle of this century (Roach, 1970). The Green's function itself is unique for each problem and set of boundary conditions. However, once the Green's function is determined, it reduces the solution to an integral equation with boundary conditions, rather than a differential equation. For numerical analysis, the integral form is easier to solve than the differential equation (Roach, 1970).

The Green's function approach has been applied to many practical applications in engineering. For example, Roach (1970) used Green's functions to solve boundary value problems associated with the wave equation and the diffusion equation. Trim (1990) described the use of Green's functions to find the displacement in a horizontal, taut string that is fixed at one end while the other end is moved harmonically in the vertical direction.

Hartzell (1978) described a Green's function approach for predicting earthquake ground motion. An earthquake was modeled as a series of point ruptures on a fault zone. A total earthquake motion was produced by superimposing the phase-delayed ground motion resulting from each point rupture. Hartzell scaled previously recorded aftershocks (small tremors) to serve as the response at each point source -- these small motions are

empirical Green's functions. The Green's function method of dividing a large problem into the sum of smaller, easier to solve problems is a common feature of Green's function analyses, and was employed in this thesis.

4.2 Dynamic Layered Elastic Model using Green's Functions

In this research, the Green's function can be viewed as a simple transfer function, $G(\omega_i, R)$, that relates displacements, $U(\omega_i, R)$, to load, $P(\omega_i)$.

$$U(\omega_i, R) = G(\omega_i, R) * P(\omega_i)$$

Combining the displacements at all frequencies produces the desired displacement time history.

$$U(t) = \sum_{i=-\infty}^{+\infty} G(\omega_i, R) * P_i(\omega_i)$$

This formulation was used to build a pavement deflection model, which was coded into the computer program BASIN.

The following sections describe the manner in which the Green's functions approach was applied in BASIN. First, conversion from the time domain to the frequency domain for the analysis of transient loads and responses is described. Next, the generalized method for calculating the elastodynamic Green's functions is explained. Finally, the last sections illustrate the schemes used to represent both FWD and rolling wheel loads.

4.2.1 Frequency Domain Analysis

As mentioned in Chapter 3, the Green's functions solved by Kausel and Peek (1982) describe the harmonic deflections produced by steady-state harmonic unit loads. To use these Green's functions for calculating deflections resulting from transient loads, the transient load must be represented in the frequency domain as a combination of harmonic loads of different amplitude, phase, and frequency. This transformation and combination approach is commonly known as Fourier superposition analysis.

Figure 4-1 illustrates a general schematic for analysis in the frequency domain. In the first step, the load time history is discretized into individual points spaced at a constant time interval. The discretized loading is then decomposed into the sum of a series of simple harmonic loads using a discrete Fourier transform. The Green's functions are then solved to determine the amplitude and phase of harmonic displacement resulting from a unit load at each frequency. Next, the Green's functions are multiplied by the Fourier series of the loading to determine the Fourier series of the pavement deflection. Finally, the sum of the harmonic responses are transformed back into the time domain by an inverse discrete Fourier transform. This method of superimposing the harmonic responses is only valid for linear-elastic materials.

4.2.2 Green's Function Solution

As described previously, an explicit, closed-form solution for the Green's functions corresponding to dynamic loads acting on layered strata was used to build the pavement deflection model BASIN. This section very briefly summarizes the general solution process. The complete derivation can be found in Kausel and Peek (1982). Additionally, an excellent overview is given by Meier (1995).

The solution developed by Kausel and Peek (1982) uses the following steps to solve for harmonic displacements in a layered strata. First, the stiffness matrix for each layer must be computed. Each stiffness matrix is a function of the material properties and thickness of the layer. Additionally, the equation for the stiffness matrix is dependent on the loading frequency and wave number. The wave number is obtained by a spatial Fourier transformation of the loading function (this is analogous to a time-dependent function transformed into the frequency domain) and is used to include the distance between the loaded area and the observation point as part of the solution. A global stiffness matrix, \mathbf{K} , is obtained by overlapping the individual layer matrices at their layer interfaces. The global stiffness matrix relates the displacements, $\bar{\mathbf{U}}$, to the loads, $\bar{\mathbf{P}}$, i.e.

$$\bar{\mathbf{P}} = \mathbf{K}\bar{\mathbf{U}}$$

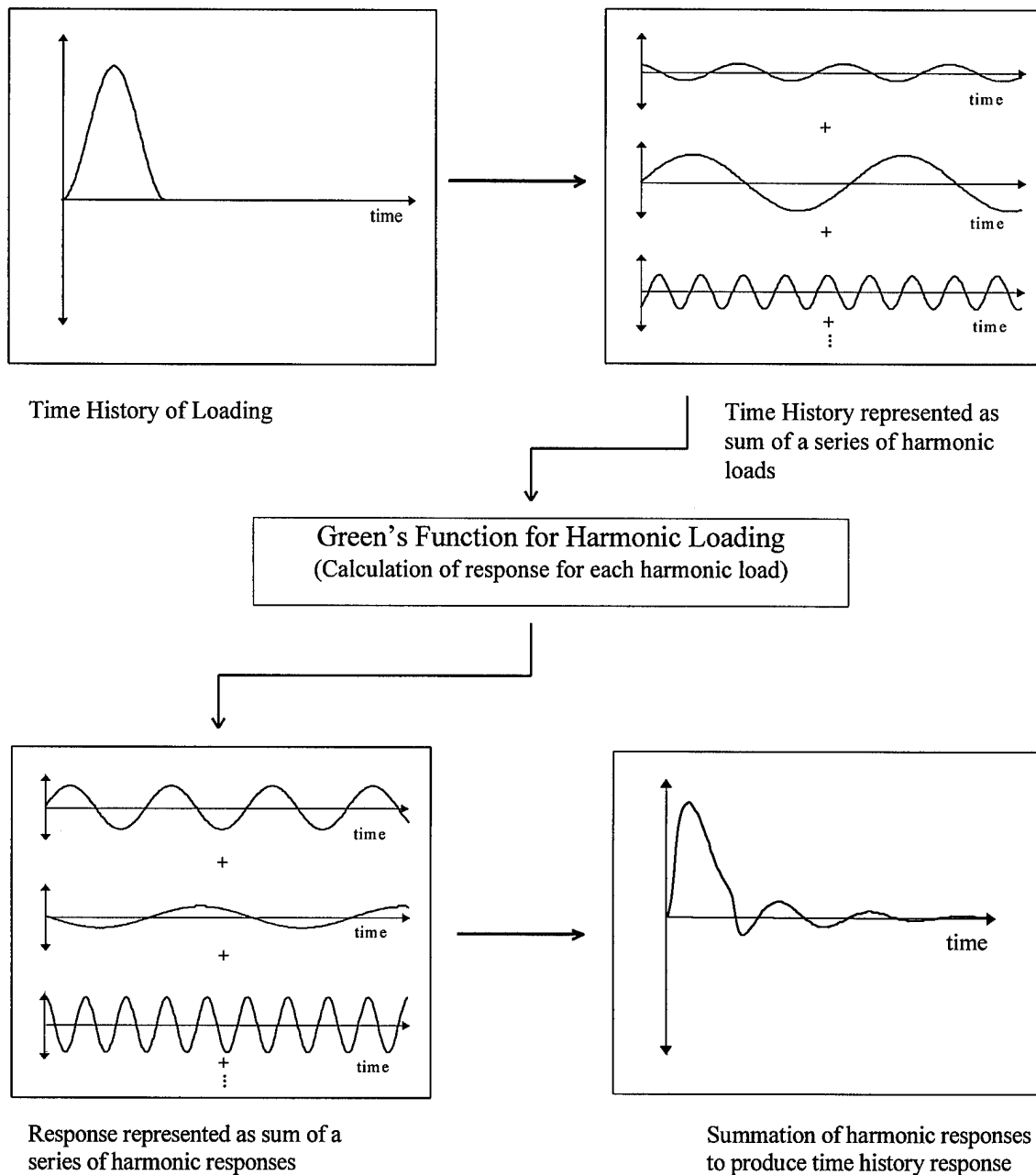


Figure 4-1. Schematic illustration of Fourier superposition analysis using Green's functions (after Kramer, 1996).

By formally inverting the stiffness matrix, an expression that solves directly for the displacements is found,

$$\bar{\mathbf{U}} = \mathbf{K}^{-1}\bar{\mathbf{P}} = \mathbf{F}\bar{\mathbf{P}}$$

where, $\mathbf{F} = \mathbf{K}^{-1}$, represents the flexibility matrix. After the flexibility matrix is established, it is multiplied by the loading vector to calculate the displacements.

Kausel and Peek (1982) developed solutions for the displacements produced by several types of loading. Displacements, in cylindrical coordinates, are calculated in the vertical, radial, and tangential directions. Loads can be applied horizontally or vertically to a disk, ring or point; additionally, torsional and rocking loads are solved.

4.2.3 FWD Load Representation

The load pulse produced by an FWD was developed to approximate the deflection pulse produced by a moving truck load (Hoffman and Thomson, 1982). Barksdale (1971) reported the actual load pulse caused by a moving wheel closely resembled a haversine, illustrated in Figure 4-2. Example pulses from several FWD devices are shown in Figure 4-3. The shape and duration of the pulse are controlled by the mass, height of drop, and buffer system stiffness.

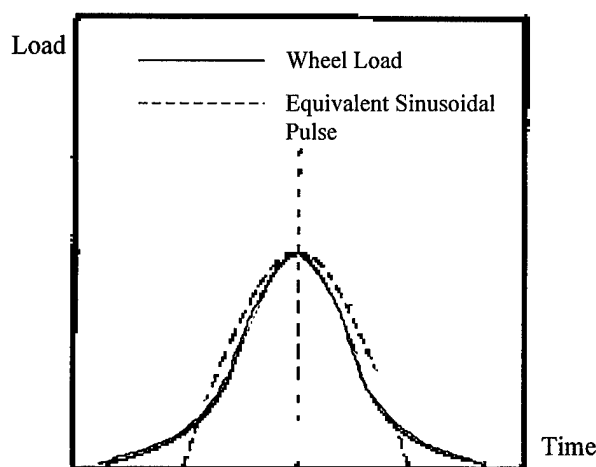


Figure 4-2. Typical wheel load applied by a moving truck (Barksdale, 1971).

For dynamic analysis of pavement systems, it is computationally easier to model the load as a smooth function. The level of agreement between these functions and the “real” load shapes are most easily distinguished when the loads are represented in the

frequency domain. Figure 4-4 shows time-domain loading and the Fourier amplitude spectrum for a triangle, haversine and real pulse, all with equal peak amplitude and duration. Because of its sharp peak and straight sides, the triangular pulse has more energy in the 100 to 200 Hz range than the haversine or measured pulse (Meier, 1995). Huang (1993) and Ong et al. (1991) suggested that the ideal approximating shape is a haversine -- that shape was used for all analyses in this project. There is an additional benefit to using a haversine rather than a triangular pulse in this project. Because the haversine function has less high frequency energy than the triangular wave, a smaller number of discrete frequencies are necessary to accurately define the load. The upper bound of the range of frequencies used to characterize the loading is called the *cutoff frequency* -- i.e. energy at frequencies higher than the cutoff is neglected. The range of frequencies between 0 Hz (static) and the cutoff frequency is also known as the bandwidth. Because GREEN calculates a solution for each frequency of interest, a lower cutoff frequency requires less computation time to determine the response to the haversine loading.

Meier (1995) showed that a haversine constructed to match impulse and duration of a measured pulse also matched over the range of 0-75 Hz in the frequency domain (Figure 4-5). Differences are apparent at frequencies above 75 Hz, but the amplitudes are very small relative to those at lower frequencies.

Because computational times for GREEN increase in direct proportion to the number of frequencies needed to represent the loading pulse, it is desirable to minimize the cutoff frequency and maximize the increment between frequencies. To examine the effects of limiting the cutoff frequency, a FFT was performed on a 1024-point time record with a 30 msec (60 point) haversine pulse at the beginning. The 30 msec duration was selected as typical for FWD tests. The total frequency range for this record was 0 to 996.45 Hz, with 511 discrete frequencies spaced at 1.95 Hz. To limit computation time the cutoff frequency was set at 76.05 Hz, therefore only the first 40 discrete frequencies were used. An inverse FFT on the cutoff (or bandwidth-limited) spectrum was then used to convert the record back to the time domain. Figure 4-6 shows that there is virtually no

difference between the original and bandwidth-limited pulses. Meier (1995) produced similar results using frequencies below 75.47 Hz with a 2.36 Hz interval. Section 7.2.2 describes the sensitivity of the deflection basin to the cutoff frequency and shows that this bandwidth is acceptable for accurately calculating deflection basins.

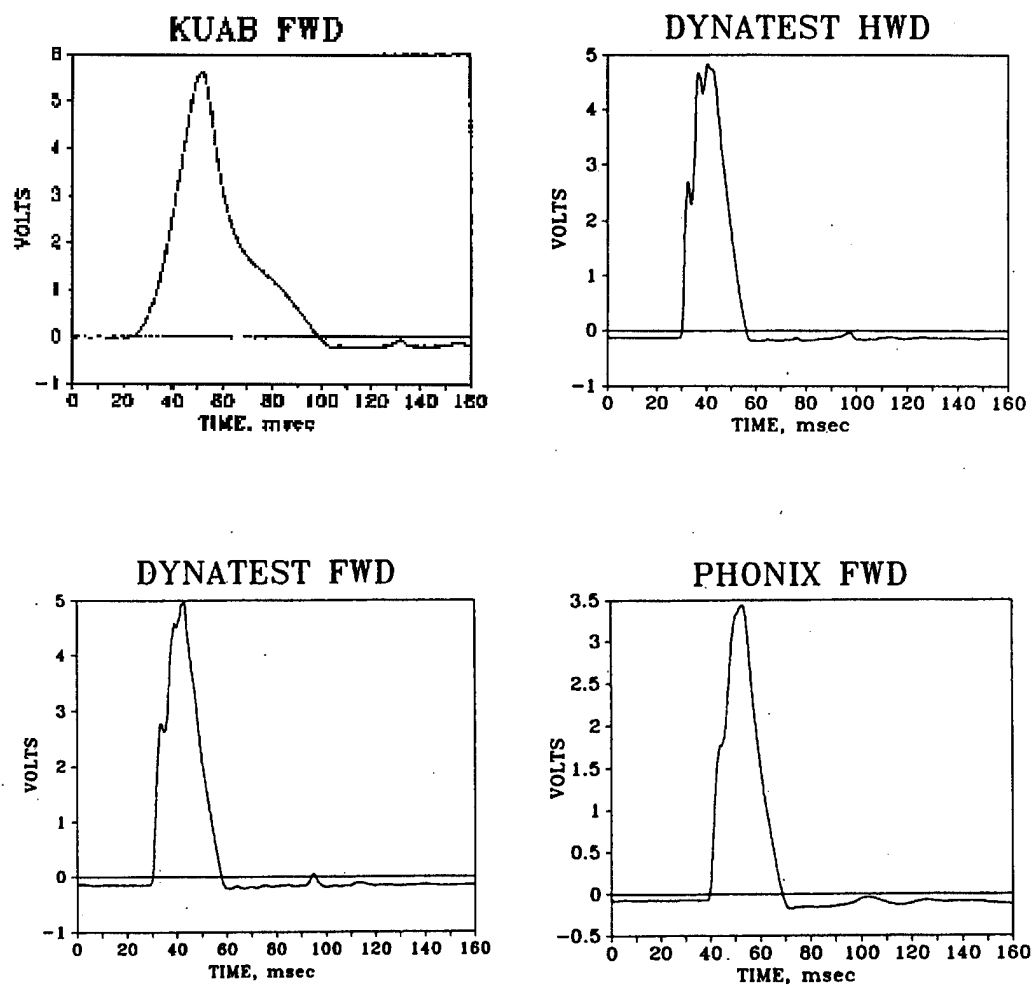


Figure 4-3. Typical load pulses for four different FWD devices (Bentson et al., 1989).

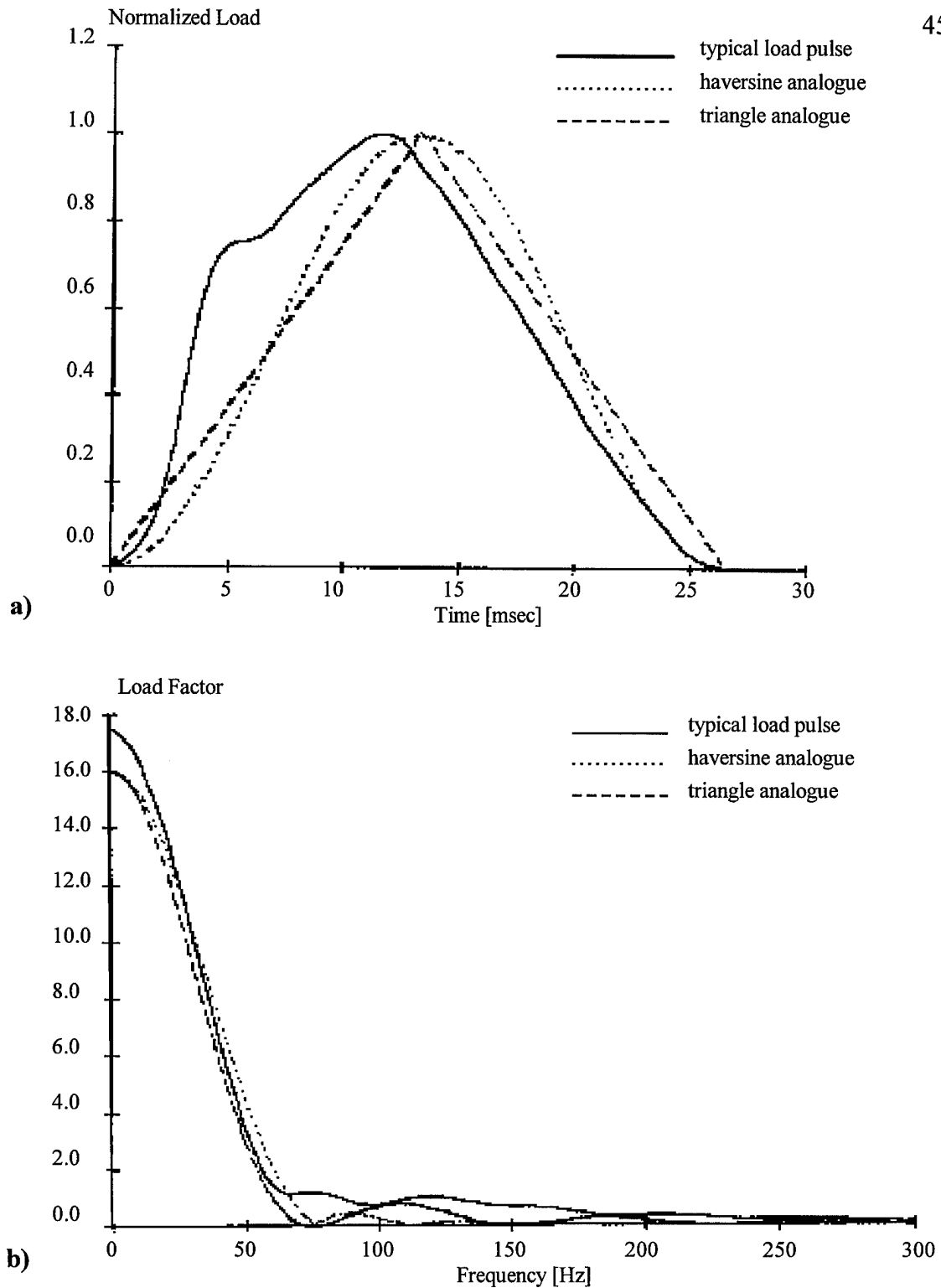


Figure 4-4. a) Average measured load pulse and functional analogues in the time domain. b) Fourier amplitude spectra for average measured load pulse and functional analogues (Meier, 1995).

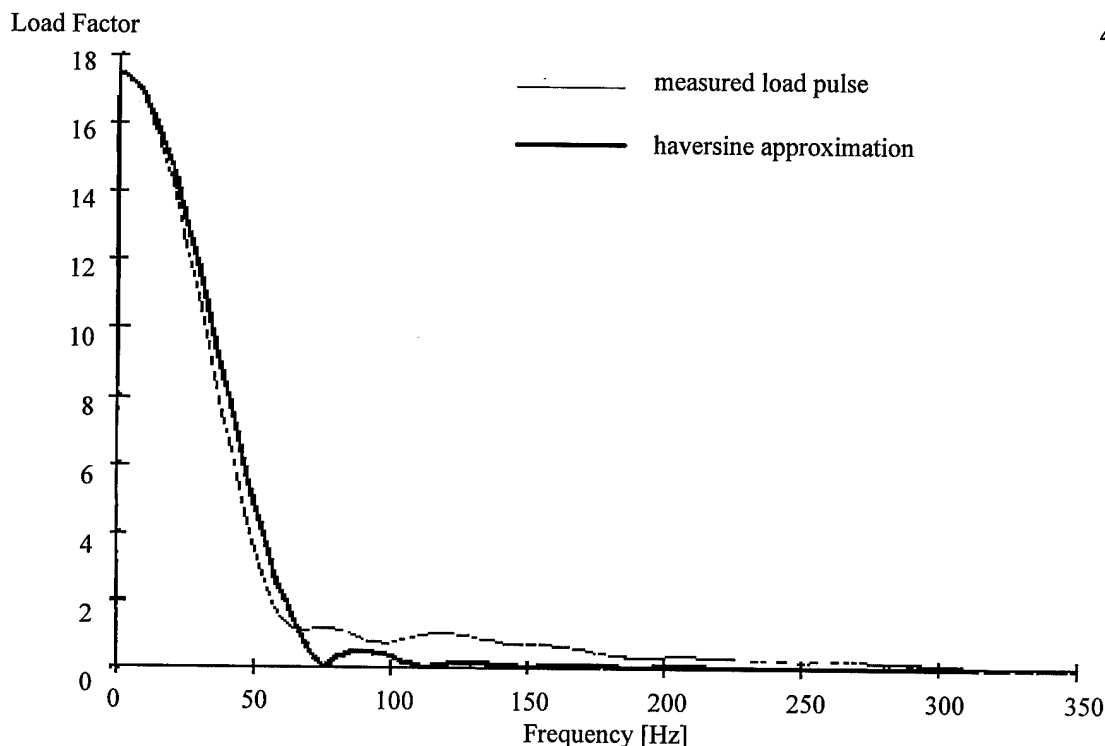


Figure 4-5. Fourier amplitude spectra for average measured load pulse and adjusted haversine approximation (Meier, 1995).

4.2.4 Rolling Wheel Load Representation

To model the load applied by a rolling wheel, it is necessary to develop a method that can approximate a moving load applied over time and space. Ideally, the load would be represented by a sequence of infinitesimally-spaced point loads. However, this is computationally impossible. Instead the line load can be achieved by discretizing the load into a series of pulses, such that the combination of pulses approximates the desired load in time and space.

Four components of the individual pulses must be considered to develop the rolling wheel representation: the area on which the load is applied, the shape of individual load pulses, the duration of each pulse, and the spacing between each pulse.

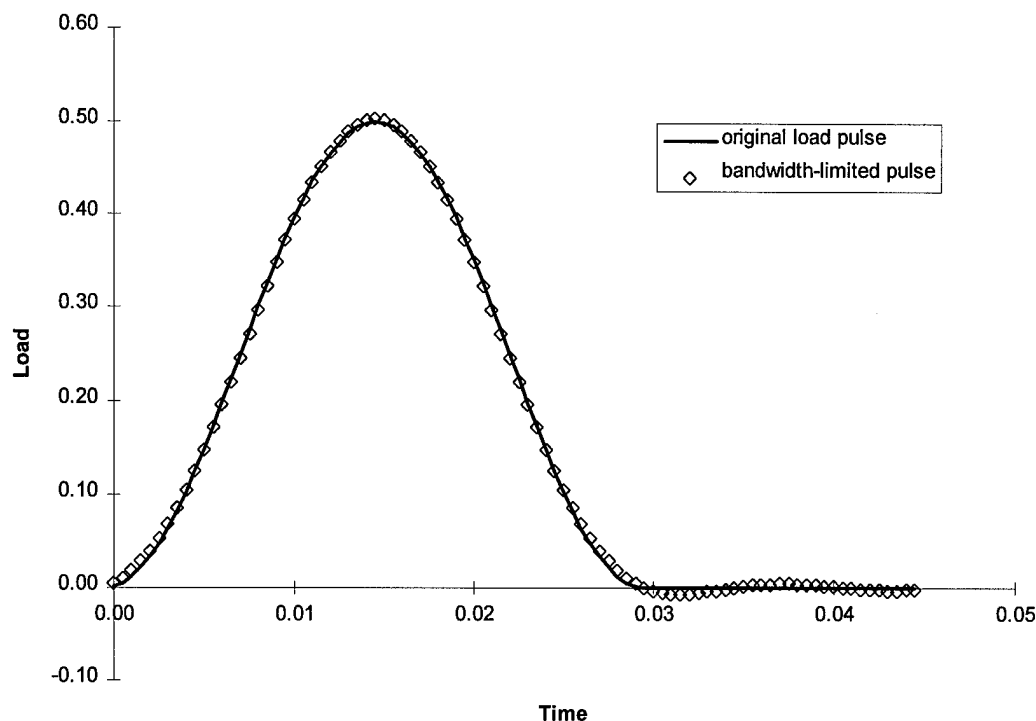


Figure 4-6. Original and bandwidth-limited haversine load pulses (after Meier, 1995).

4.2.4.1 Loaded Area

The loaded area was modeled as a circle with a radius that is a function of the tire pressure and applied load. For example, a radial tire inflated to 620.6 kPa (90 psi) carrying a load of 30,000 N (6,745 lb) has a contact area of 48,387 mm² (75 in²). A circular disk with this area would have a radius of 120 mm (4.7 in).

4.2.4.2 Load Pulse Shape

Figure 4-7 illustrates the manner in which symmetrical load pulses can be applied in succession to approximate a moving point load of constant amplitude. In this figure, each individual pulse has a small amplitude with a 0.1 sec duration, and is represented by a dashed line. The bold line above the individual pulses is calculated by summing the load contribution of each pulse at each time increment. From this figure, it is clear that a simple, symmetrical function is most desirable for modeling the load pulse. For reasons

previously described, a haversine was selected as the standard load pulse shape for modeling moving loads.

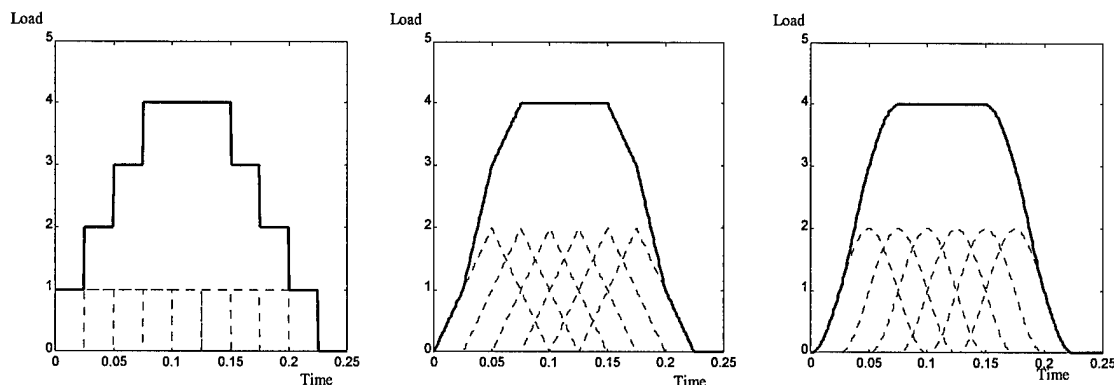


Figure 4-7. Illustration of method for combining different load pulse shapes to achieve a common line load.

4.2.4.3 Load Pulse Duration

The duration of the load pulse from a moving wheel influences the nature of the pavement deflections. Two alternatives were examined in the selection of an appropriate load pulse duration.

Barksdale (1971) developed a chart for approximating the duration of applied load for trucks moving at several speeds, ranging from 1 to 45 mph, illustrated in Figure 4-8. The charts were derived from an elastic finite element model using linear elastic elements. Barksdale's chart was generalized to calculate stress pulse times at all depths beneath a pavement surface. However, for this project, only the pulse duration at the pavement surface is of interest. For a vehicle speed of 50 km/hr (31 mph), Barksdale predicts a 30 msec pulse duration.

Alternatively, the duration could be decided by the length of time that the tire is in contact with one point on the pavement surface at a specific speed. Continuing with the example begun in Section 4.2.4.1, if the wheel were rolling at 50 km/hr = 13.89 m/s, then the time that the tire is in contact with any given point can be calculated as follows.

$$t = \frac{\text{Diameter}}{\text{Velocity}} = \frac{0.24\text{m}}{13.89 \frac{\text{m}}{\text{sec}}} = 0.0173 \text{sec} = 17.3 \text{msec}$$

With this scheme the pulse duration changes when the speed, tire pressure, or load changes.

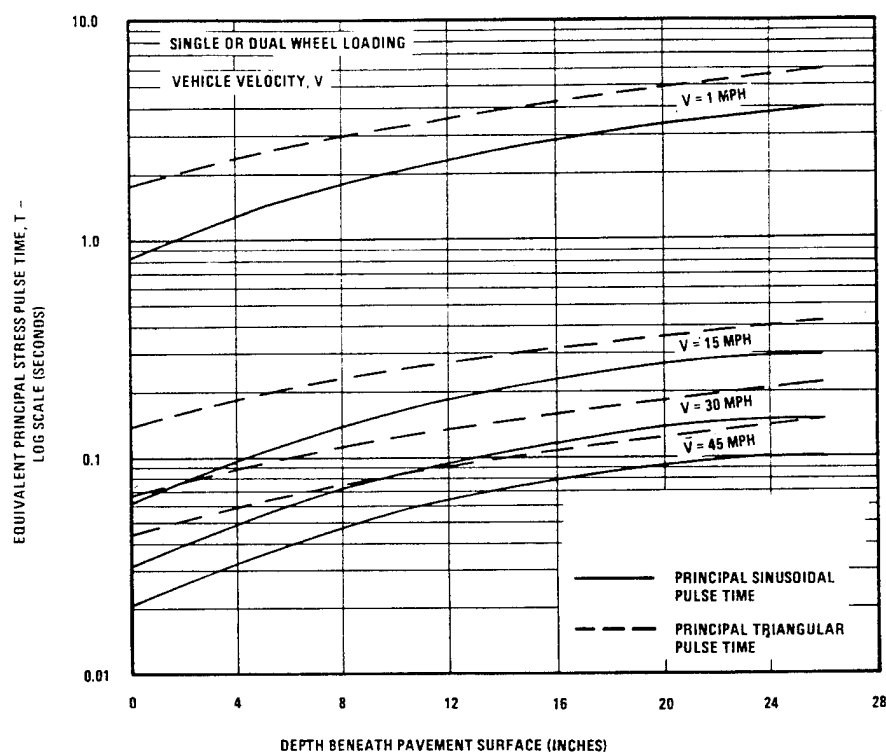


Figure 4-8. Variation of equivalent principal stress pulse time with vehicle velocity and depth (Barksdale, 1971).

For the prototype model which only allows constant load and velocity, the pulse durations reported by Barksdale (1971) are used. Improved algorithms that allow variable load and velocity could conceivably use a scheme to automatically calculate the pulse duration based on the tire contact duration.

For the selected pulse duration, a constant line load can be achieved by adjusting the amplitude of each individual pulse, as illustrated by Figure 4-9.

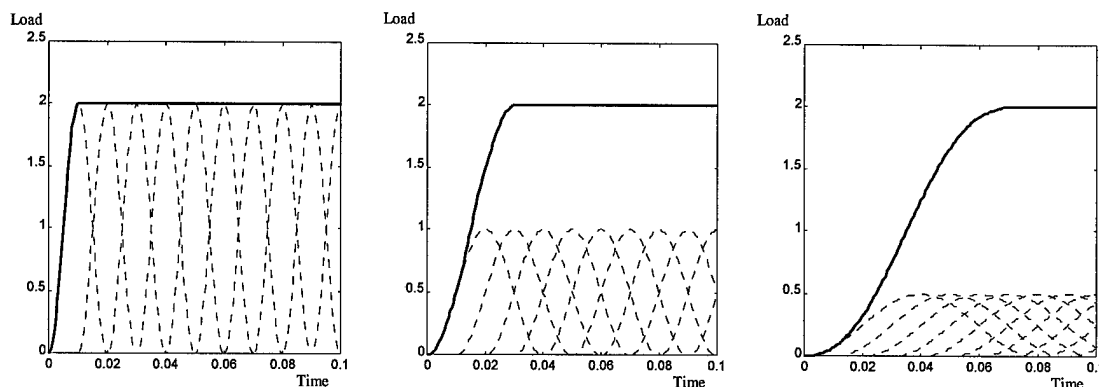


Figure 4-9. Illustration of method for using different load pulse duration and amplitude to achieve a common line load.

4.2.4.4 Load Pulse Spacing

The final component of the rolling load model is the spacing between individual load pulses. The same line load can be achieved with different spacing between pulses of the same duration, but different magnitude, as illustrated by Figure 4-9. Individual load pulses are represented by thin, dashed lines. The bold line illustrates the total applied load, and is equal to the sum of the pulses at each time increment. In each case, the amplitude of an individual pulse is calculated using the following formula:

$$\text{Pulse Amplitude} = \text{Line Load Magnitude} * \frac{2 * \text{Pulse Spacing}}{\text{Pulse Duration}}$$

To improve required computation time, a minimum number of pulses are desirable. However, the spacing between pulses has a significant impact on the calculated deflections. Increasing the load pulse spacing necessarily increased the distance traveled by the wheel between load pulses. Therefore, deflection responses from more widely-spaced pulses contribute to the total deflection. As the load pulse spacing increases, the model less closely approximates a moving wheel as a sequence of infinitesimally-spaced point loads. Chapter 5 more completely describes this concept,

and Chapter 7 contains the details of a parametric study that determined the optimum spacing between load pulses.

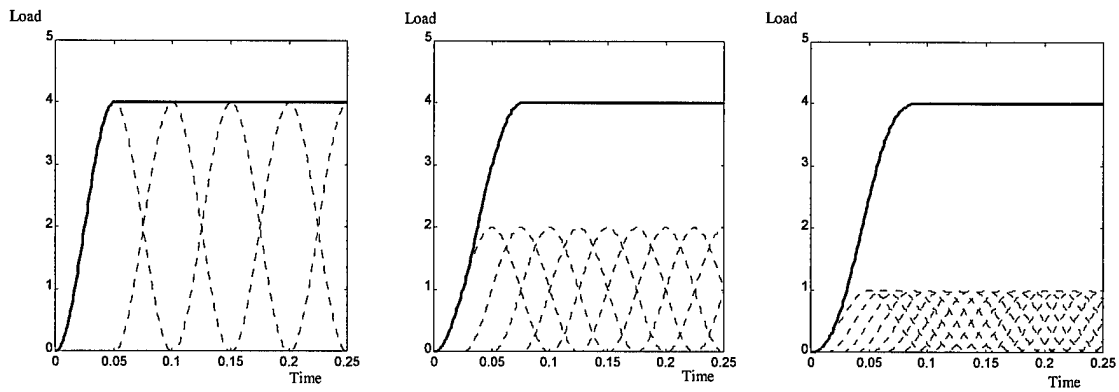


Figure 4-10. Illustration of method for using different load pulse amplitude and spacing to achieve a common line load.

Chapter 5

BASIN CONCEPTUAL DEVELOPMENT

This chapter describes an approach developed to compute deflection basins using Green's functions. Initially, a simple, simulated deflection response function was used in place of the Green's function to develop the logic process for deflection basin calculations. After the basic logic had been developed and verified, the complex-valued Green's function response solved by Kausel and Peek (1982) was used to compute deflection basins for layered elastic systems. This final program was coded in the program BASIN.

5.1 Algorithm Development

The algorithm for computing deflection basins was developed by working through several loading/observation scenarios -- from simple FWD loading to complex, dual rolling wheel loading. Initially, a simple deflection response function was developed to simulate the time history of deflection due to a unit impulse load at a given distance from an observation point. This simple function was used to develop the logic for computing observation point deflections caused by time-varying loads from both stationary and moving sources. This section presents the general concepts used to compute deflections using a Green's function approach.

5.1.1 Simulated Green's Function

A simulated Green's function response to a unit impulse load was developed as a function of time and distance from the impact point. The function was designed so that the deflections observed at nearby observation points would arrive quickly and with large amplitude. Responses farther from the load would arrive later and with smaller amplitude to simulate the effects of radiation and material damping. Additionally, a small amplitude, low frequency, transient vibrating response was included in the simulated deflection response. This generates a small rebound (positive deflection) after the initial deflection at small measurement distances from the load.

The function developed for the simulated deflection, $D(R, T)$, was manipulated to produce a plausible response shape (i.e. coefficients were added and adjusted until the shape looked reasonable). The deflection, D , is a function of time, T , and distance, R , and is of the form:

$$D(R, T) = e^{-1.5T} * C * (a * b + e^{-KT} * A \sin(\omega T))$$

where:
$$C = e^{-R/50} * \frac{1}{1 + \frac{R}{40}}$$

$$a = 1 - \frac{1}{\left[1 + \left(\frac{T}{p}\right)^m\right]^{0.5}} \quad \text{with} \quad p = 0.001 + \left(\frac{R}{V_s}\right) * 300$$

$$m = 25$$

$$V_s = 48000$$

$$b = \frac{1}{\left[1 + \left(\frac{T}{q}\right)^n\right]^{0.5}} \quad \text{with} \quad q = 0.2 + \left(\frac{R}{V_s} + R^{jV_s}\right) * 500$$

$$n = 45$$

$$j = \frac{1.1}{1 + \frac{R}{80}}$$

$$K = 1.5 \quad ; \text{ Rate of decay of vibrating response}$$

$$A = \frac{1.5}{10 + R} \quad ; \text{ Amplitude of vibrating response}$$

$$\omega = 10 \quad ; \text{ Frequency of vibrating response}$$

Figure 5-1 illustrates the simulated time history of deflection measured at several distances from the load. Units have deliberately been omitted from all the figures in this section to emphasize that these are simulated responses.

The simulated response function was used while developing the logic required for prediction of observation point deflections under a variety of loading conditions. First, this function was used to compute deflection basins produced by falling weight deflectometer (FWD) tests -- a case in which the load varies with time but not position (i.e. the load is stationary) and the observation point is stationary. Next, the Green's function approach was applied to the case of a single moving load of constant amplitude and velocity and passing by a stationary observation point. Finally, this approach was extended to predict the shape of a deflection basin that could be measured by deflection sensors moving *with* the load.

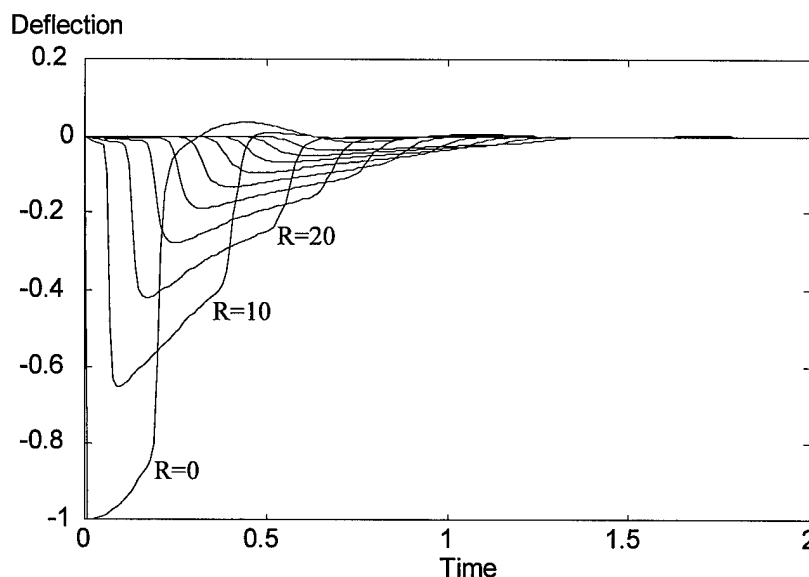


Figure 5-1. Simulated deflection response caused by a unit impulse load for several distances from the impact site.

5.1.2 Case 1: Falling Weight Deflectometer

As described in Chapter 2, commonly only the *peak* deflections at each sensor are recorded in a FWD test. Alternatively, the system could record the *time history* of deflection at each sensor to capture the *dynamic* effects of the load.

Case 1 models a FWD test to determine the time history of deflection at several sensors located at different distances from the load. Figure 5-2 shows the arbitrary shape

of the load used in this process. The continuous actual loading curve was approximated by a series of point loads, P , separated by an equal time step, Δt . Each of these point loads was assigned an impulse value, $I(i) = P(i) * \Delta t$, that was multiplied by the simulated deflection response for that distance. Figure 5-3 shows the response at R(10) due to each impulse; the response due to the point load $P(i)$ (from Figure 5-2) is highlighted. To find the total response, the principle of superposition was used to combine the deflections at each time step. The resulting total response at this sensor is shown in Figure 5-4.

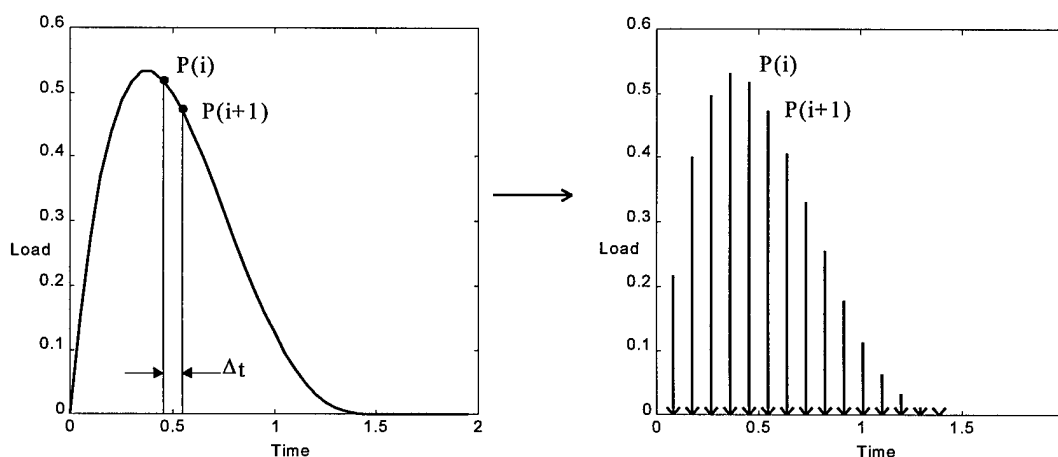


Figure 5-2. Simulated impact load function conversion to discrete point loads.

This process was repeated for each measurement distance. Figure 5-5a shows the time history of deflection at several distances. Using the peak values from each of the curves, the deflection basin measured by a typical FWD was created (Figure 5-5b). Note that the peaks did not occur simultaneously, even though most current interpretation techniques for FWD data assume that the maxima *do* occur simultaneously. The farther the measurement point was from the loading point, the later the peak deflection occurred. Figure 5-6 illustrates the manner in which the shape of the deflection basin changes with time by plotting the basin measured at 6 discrete times after the impact occurs. In each image, the thickest solid line represents the basing shape at the stated time value. The progressively thinner dashed lines represent the basin shapes at previous time increments.

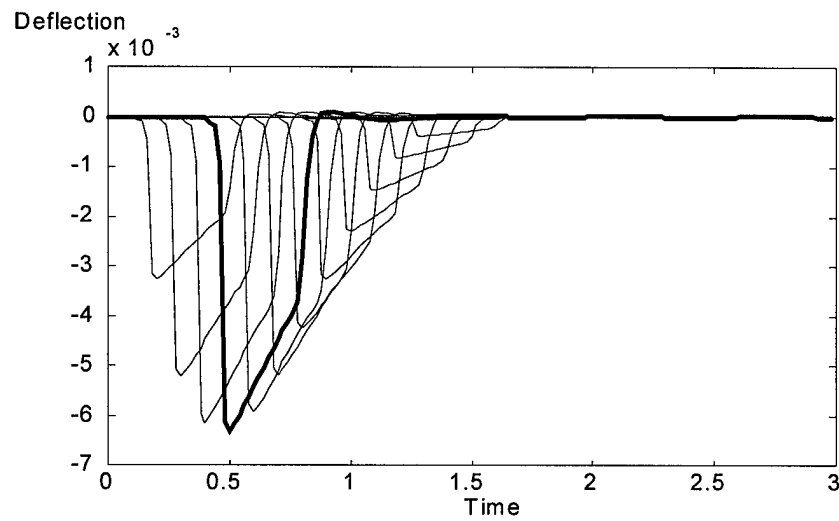


Figure 5-3. Individual deflection responses due to individual impulse loads measured at 10 distance units from the impact site.

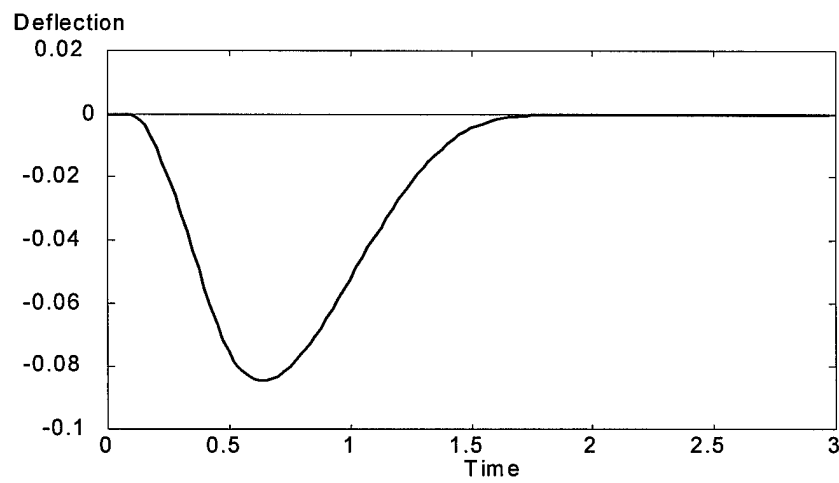


Figure 5-4. Time history of deflection for a point 10 distance units from the impact site.

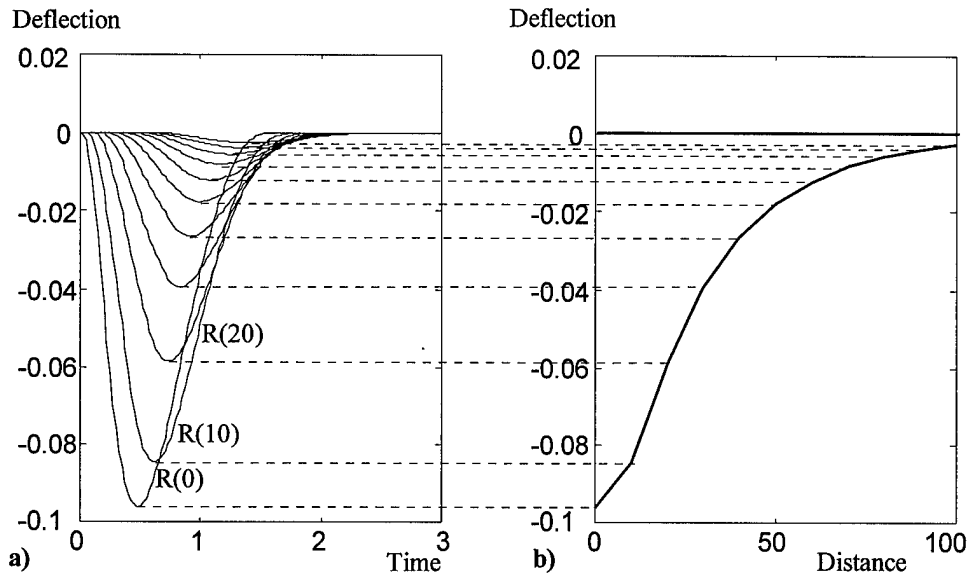


Figure 5-5. a) Time history of deflection measured at several radial distances from the impact site. b) Deflection basin constructed using peak deflections.

5.1.3 Case 2: Rolling Load Passing a Stationary Point

This case models a loaded wheel passing a stationary observation point. The purpose of this case was to develop the logic for prediction of the time history of deflection at the observation point due to the rolling load. Figure 5-7 illustrates the manner in which the problem of a continuous, moving load was discretized as a series of impulsive loads. Each point load, P , is separated in time by Δt , and in space by Δx . The relationship between Δt and Δx is a function of the load velocity, V : $\Delta x = V\Delta t$. For this case, the load and velocity were assumed to remain constant throughout the period of interest. Therefore, each impulse had equal magnitude, $I = P \cdot \Delta t$, and was applied at equal spacing, Δx .

The same procedure used in Case 1 to sum the individual responses applies to this case. However, in contrast to Case 1, each time history of deflection produced by each impulsive load has a different shape because it is applied at different distances from the observation point. Figure 5-8 illustrates the individual responses due to each impulse for two cases, one in which the wheel passed directly over the observation point (located at $x=0, y=0$), and the other, in which the wheel traveled a parallel path offset by 30 units in the y -direction (as in Figure 5-7). The time scale was adjusted so that at time = 0, the

wheel is at $x=0$, which is directly over, or closest to, the observation point. The highlighted individual deflections are caused by the point load applied at $x=0$, when the wheel is closest to the observation point. As described in Case 1, the resulting overall time history of deflection for each case was computed using superposition, as shown in Figure 5-9.

5.1.4 Case 3: Deflection “Snapshot”

Building upon the results of Case 2, this case considered the deflections at a particular instant in time along a line parallel to the wheel path. Such deflections could be measured by a series of observation points aligned along the wheel path, if the deflections were all recorded simultaneously. In this sense, the deflections can be thought of as describing a “snapshot” of the deflection basin produced by a moving load. The same deflection basin would also be recorded by a string of observation points that moved with the wheel; as such, this case is more applicable to rolling wheel deflectometers than either of the preceding cases.

The snapshot deflection basin was developed through the following process. First, a time history deflection response was created in the same manner used in Case 2. Second, this time history was shifted in time by Δt to represent the time history of deflection that would be observed at $(x+\Delta x, y)$. It should be noted that this is only valid when the material properties at $(x+\Delta x, y)$ are the same as at (x, y) . In other words, an observation point at $(x+\Delta x, y)$ would experience the same time history of deflection as an observation point at (x, y) , except that the response would start Δt later. Figure 5-10 illustrates this process for several observation points using the time history for $y=30$ from Figure 5-9.

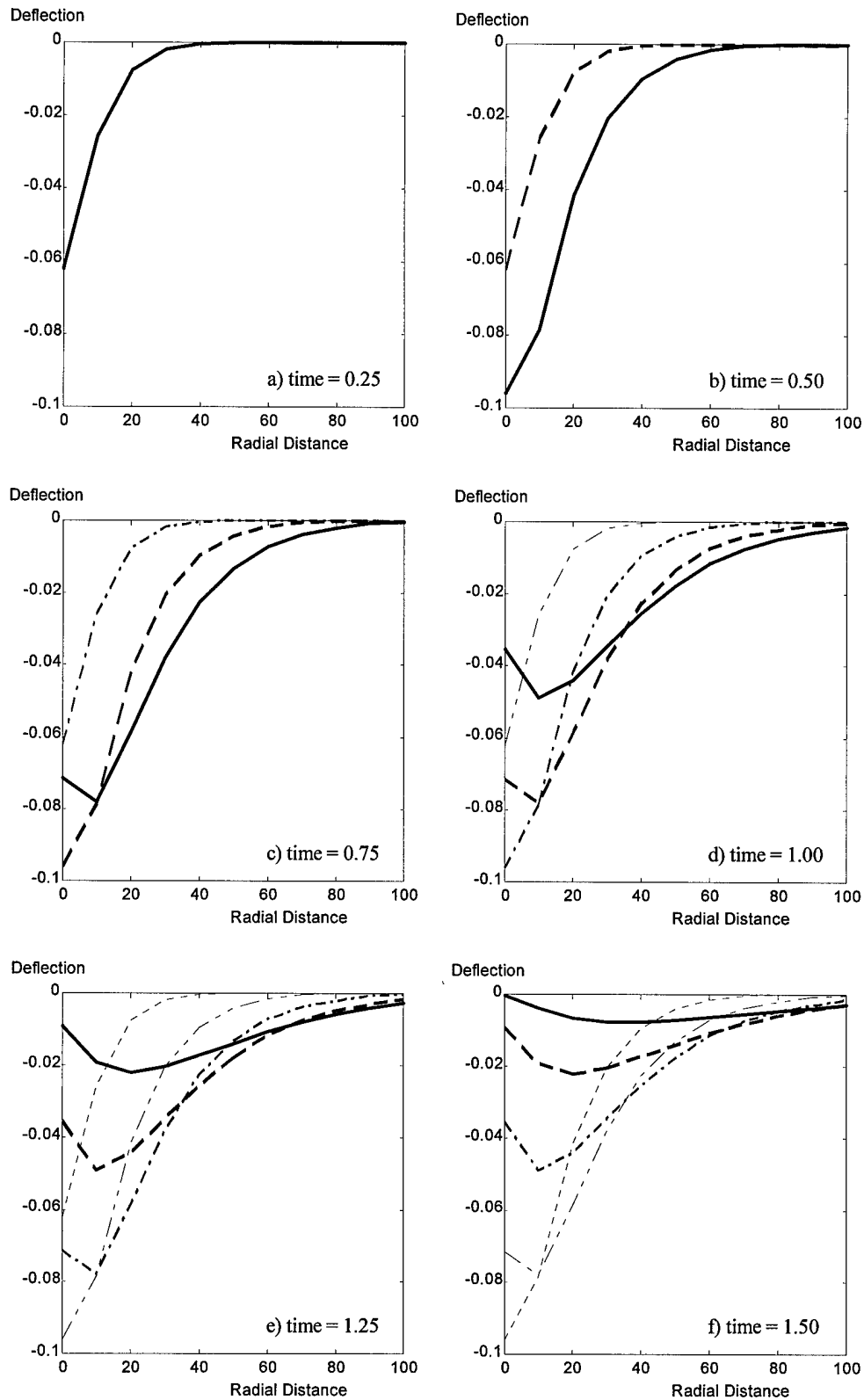


Figure 5-6. Deflection basins predicted for several discrete time intervals.

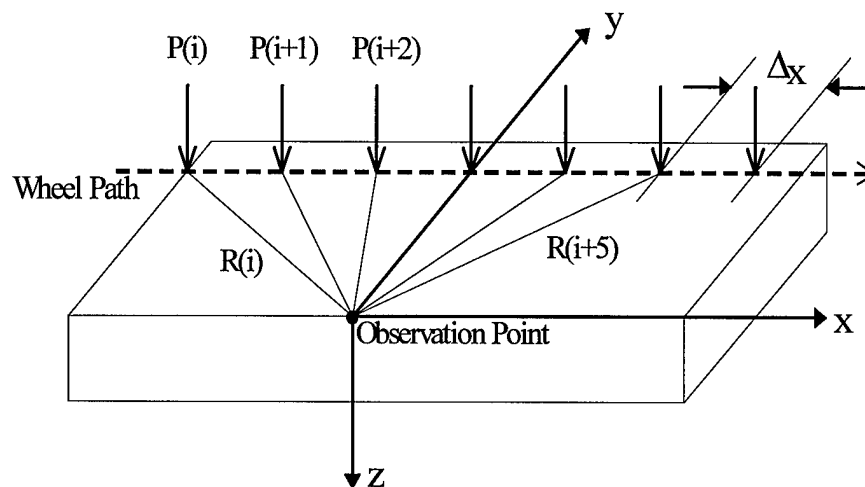


Figure 5-7. Representation of a rolling wheel passing an observation point as a sequence of impulse point loads.

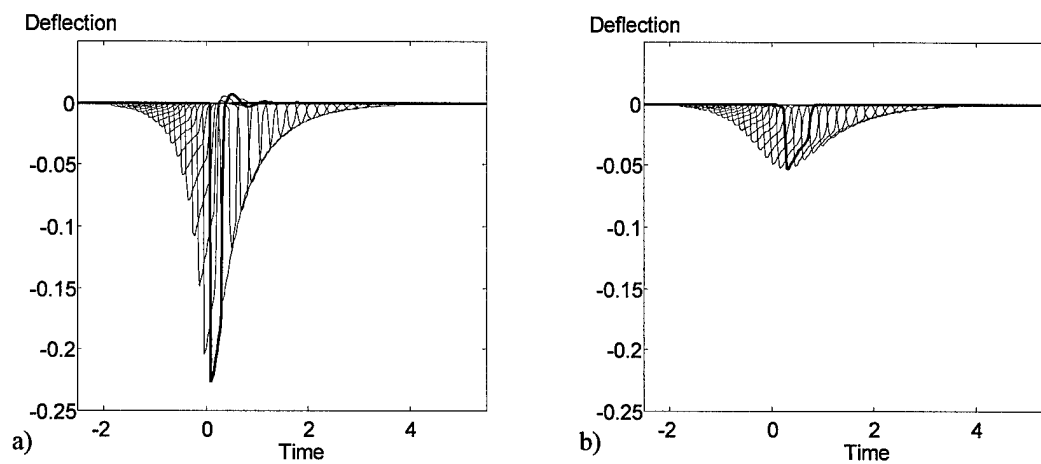


Figure 5-8. Individual impulse load deflection responses for case in which wheel passes (a) directly over observation point ($y=0$), and (b) 30 distance units from observation point ($y=30$).

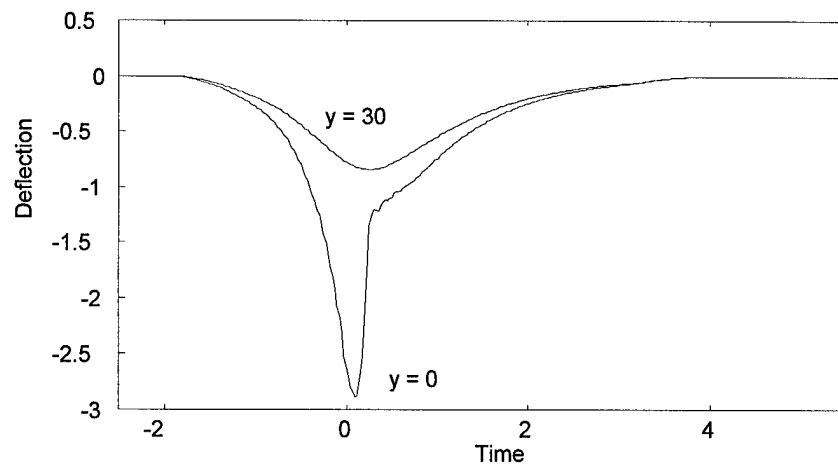


Figure 5-9. Time history of deflection for rolling wheel passing directly over ($y=0$) and 30 units ($y=30$) from the observation point.

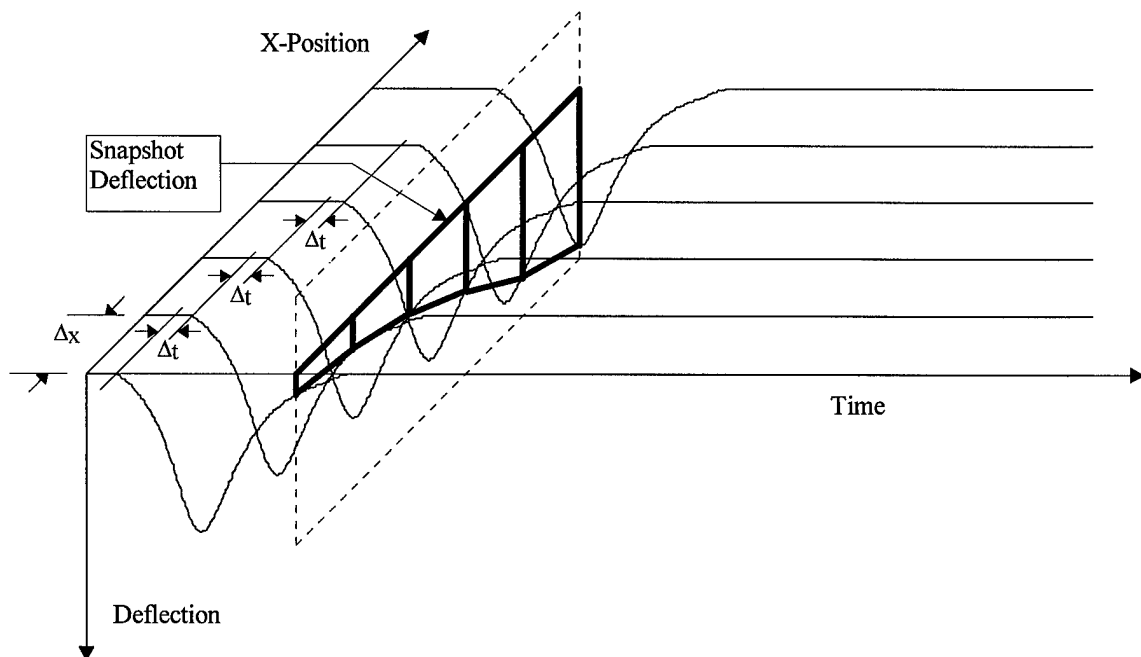


Figure 5-10. "Snapshot" deflection basin conceptual development illustrating a constant time plane.

A "snapshot" can be created by choosing a constant time value and finding the corresponding deflection at each position. In Figure 5-10, the dashed-line vertical plane represents the constant time slice for which the snapshot was calculated. Figure 5-11

shows the resulting snapshots for $y=30$ and $y=0$ when the response calculated in Case 2 (Figure 5-9) was shifted and cut as described above. At the instant these “snapshots” were calculated, the wheel was directly over the $x=0$ position. Note that the peak deflection occurred slightly behind the position of the wheel for both cases and that the peak deflection for $y=30$ occurred farther behind the wheel than for the $y=0$ case.

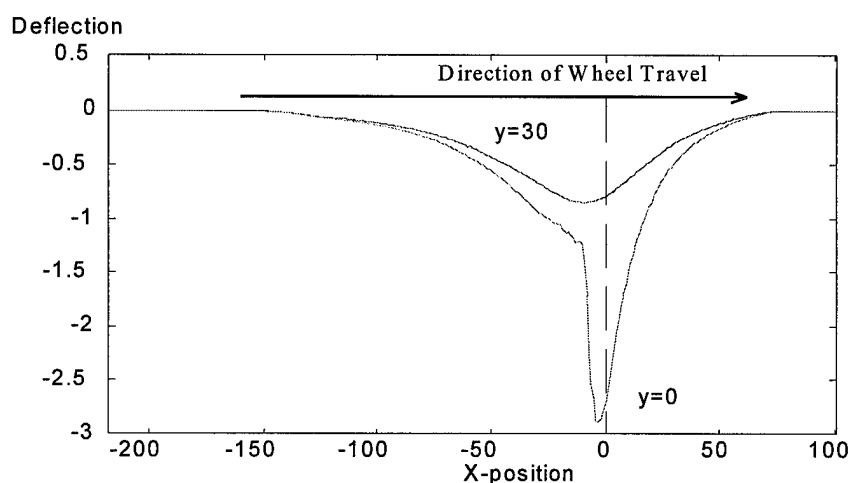


Figure 5-11. “Snapshot” deflection basin observed when wheel is directly over $x = 0$ position.

For this simplified case which has constant velocity and load, the shape of the “snapshot” is the reverse image of the time history of deflection for a stationary observation point, but with an important difference -- the scale on the x-axis measures distance, not time. When loads and velocities are changing with time, this mirror image effect will not occur because the position scale will not transform at a constant rate.

5.1.5 Case 4: “Snapshot” 3-Dimensional Deflection Basin

The “snapshot” deflection basin along a single line parallel to the wheel path was developed in Case 3. Case 4 creates a three-dimensional deflection *basin* by extending the calculations of Case 3 to several different parallel slices at different distances from the wheel path. Plotting these snapshots together in three-dimensional space illustrates the

shape of the basin that travels with the moving wheel load (Figure 5-12). At the instant this basin was calculated, the load was located at $x=0$ and $y=0$.

5.1.6 Case 5: 3-D Basin for Two Parallel Rolling Wheels

This final case models two wheels traveling along parallel paths -- i.e. a loaded axle. For this case, the principle of superposition was applied. Assuming the second wheel applied the same load as the first, it would produce an identical deflection basin. Therefore a copy of the single wheel basin can be shifted away from the x -axis by a distance equal to the wheel spacing, and superimposed on the original basin. Summing the two basins creates the two-wheel deflection basin illustrated in Figure 5-13.

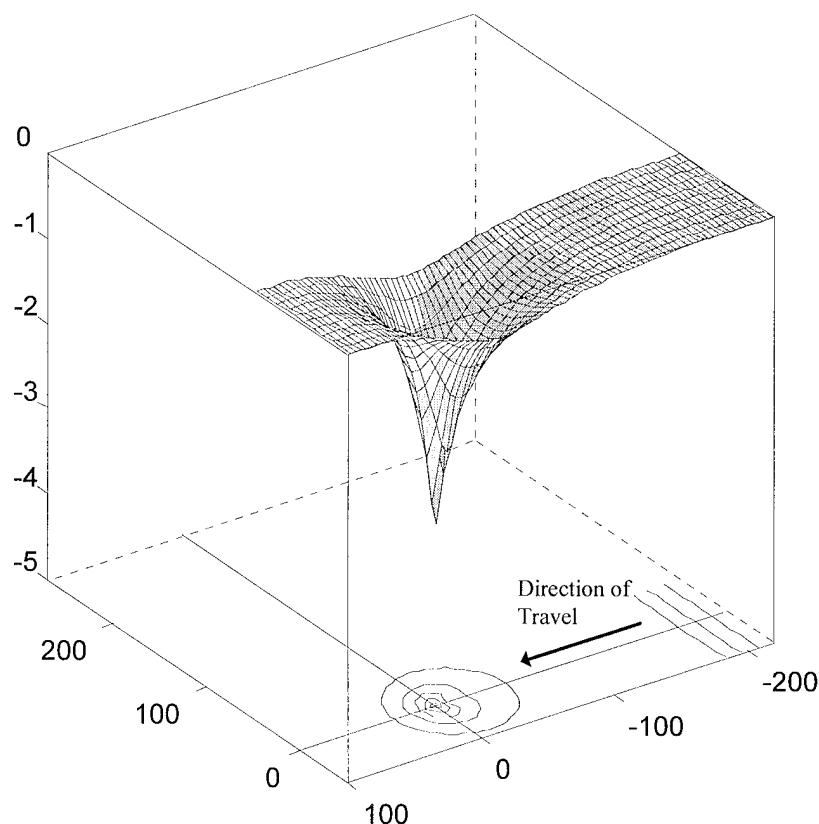


Figure 5-12. Deflection basin observed when a single rolling wheel is directly over the $x=0$, $y=0$ position.

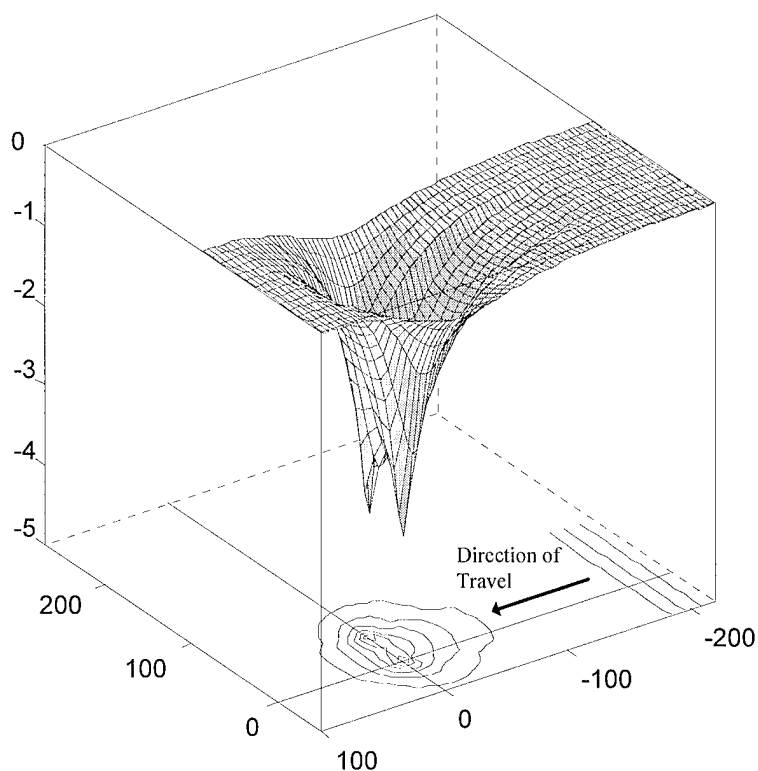


Figure 5-13. Deflection basin observed when the axle connecting two rolling wheels is directly over the $x=0$ position.

5.2 Algorithm Modifications for Moving Deflection Sensors

The previous section described calculating the entire deflection basin produced by a rolling wheel at every space increment along the direction of travel. However, rolling weight deflectometers have three important differences from the idealized cases modeled in Section 5.1.

First, rolling weight deflectometers (or any other pavement testing device) only measure deflections at several discrete points. Therefore, only deflections at the measurement sensors need to be calculated. This significantly reduces the required computation time.

Second, Case 3 (Section 5.1.4) assumed that the deflection sensors were stationary when the “snapshot” was measured. However, the deflection sensors on a rolling weight

deflectometer move *with* the load. This has important implications for determining the applied loads that contribute to the deflection at the time of measurement.

Third, the previous section was based on the ideal assumption that the wheel rolled at constant velocity and applied a constant load. In reality, rolling weight deflectometers neither move at a constant velocity or apply a constant load. Therefore, the model must base its calculations on the velocity and load recorded by the rolling weight deflectometer over the testing time.

The following sections describe the algorithm developed to model a rolling weight deflectometer. This algorithm was coded in the computer program BASIN.

5.2.1 BASIN Algorithm

A new computer program, called BASIN, was developed to compute the deflections using the load and velocity of the rolling weight deflectometer. The flow chart in Figure 5-14 illustrates the BASIN algorithm, which is further described below. To simplify the explanation, only a single wheel load is considered, rather than a two-wheeled axle.

First, data collected by the rolling weight deflectometer is loaded into the program. This data consists of the velocity and load applied by the wheel, and the deflection sensor measurements at each time increment. Also, the initial coordinates of the wheel (x_0 , y_0) and the location of the deflection sensors relative to the wheel are loaded into BASIN. Because BASIN is a forward model, not a backcalculation tool, the deflection measurements are not used. However, when a backcalculation system is completed, measured deflections could be loaded in the algorithm at this point.

Next, BASIN calculates the position of the wheel at each time increment. When the wheel location is known at all times, calculation of the position of the deflection sensors at all times by adding or subtracting the relative offset of the sensors from the wheel location is straightforward.

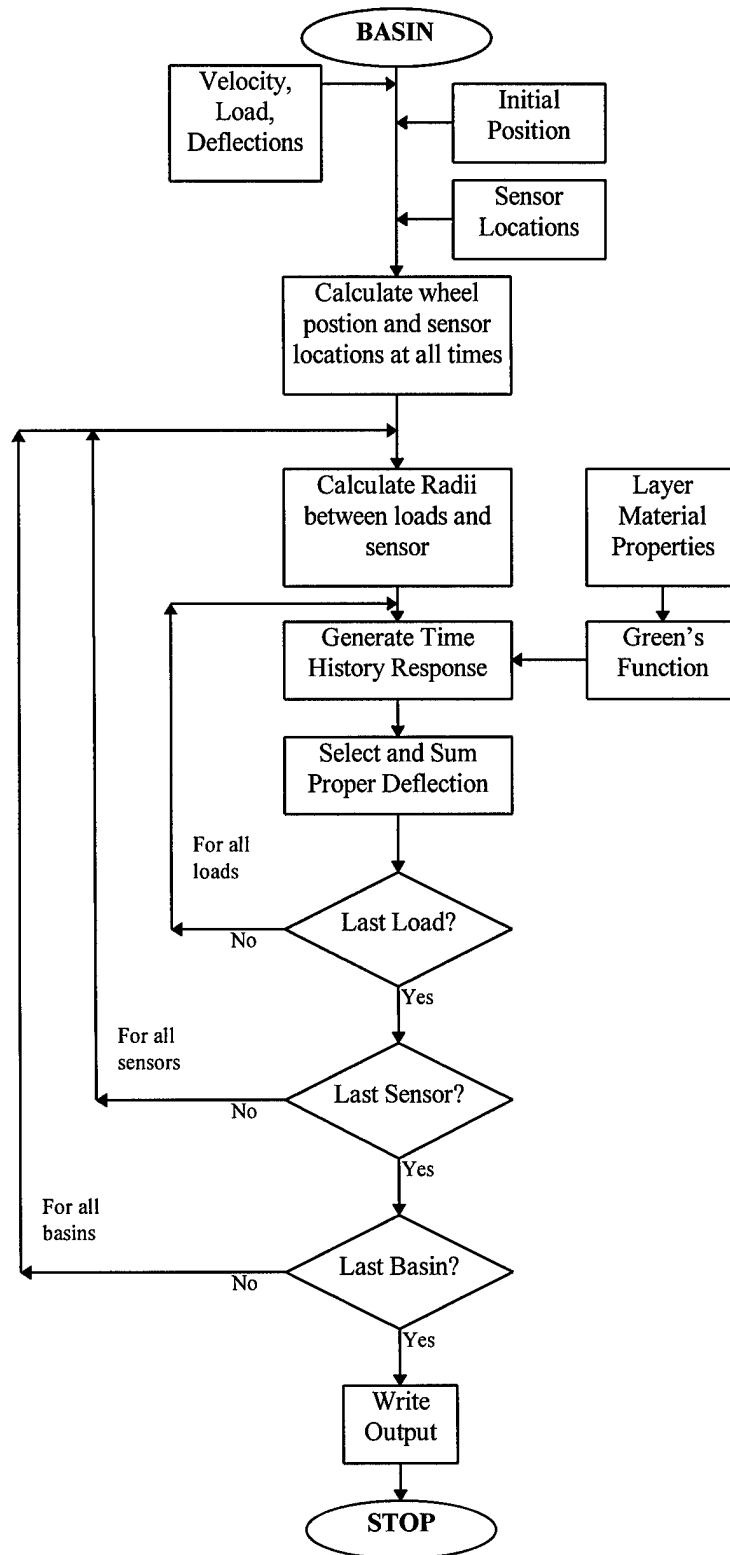


Figure 5-14. Flow chart of the algorithm coded in the computer program BASIN.

For each deflection sensor, there are numerous load pulses that contribute to the deflection measured at a given time. Each of these pulses is applied at a different distance from the deflection sensor; therefore, BASIN next calculates all the radii for the applied load pulses. Figure 5-8 illustrated this concept.

Next, the time history deflection response for each load pulse is computed by BASIN. The response is generated using the Green's functions described in Chapter 4. The Green's function uses the material properties of the layered system, which are supplied from an input file, to calculate the deflection response.

After the deflection time history for each load pulse is known, the proper contribution to the measured deflection must be selected. This is a key step that was not necessary for the idealized cases modeled previously. In Section 5.1.3 (Case 2), the entire time history of deflection due to each applied load (at each radius) was calculated. Then all time histories were superimposed to create an overall time history of deflection for a single observation point. However, because the time of deflection measurement is known, only one deflection value from each time record is actually needed. Therefore, BASIN selects the proper deflection contribution from each load pulse and combines all contributions to calculate the total deflection.

Figure 5-15 and the following explanation help clarify this important concept.

When pulse P_0 occurs at time T_0 , the wheel is at position (x_0, y_0) . The wheel rolls forward until time T_{10} , applying a new load pulse at each time step. At time T_{10} , the wheel is at location (x_{10}, y_{10}) , and the deflection sensor is at $(x_{def_{10}}, y_{def_{10}})$. The radius between P_0 and the deflection sensor is:

$$r_{10} = \sqrt{(x_{def_{10}} - x_0)^2 + (y_{def_{10}} - y_0)^2}$$

P_0 generates a response, $D_0(r_{10})$, that starts at time t_0 and lasts through time t_{20} , where the t time scale is relative only to each load pulse, and the T scale represents absolute time. Only the deflection at time t_{10} contributes to the

total deflection measured by the deflection sensor. Similarly, P_1 creates a response and contributes $D_1(r_9, t_9)$ at time T_{10} . Obviously, only pulses occurring prior to the measurement time can influence the measured deflection, so the last pulse that must be considered is P_9 . Therefore the total deflection measured by the sensor at time T_{10} is:

$$D_T(T_{10}) = D_0(r_{10}, t_{10}) + D_1(r_9, t_9) + D_2(r_8, t_8) + \dots + D_8(r_2, t_2) + D_9(r_1, t_1)$$

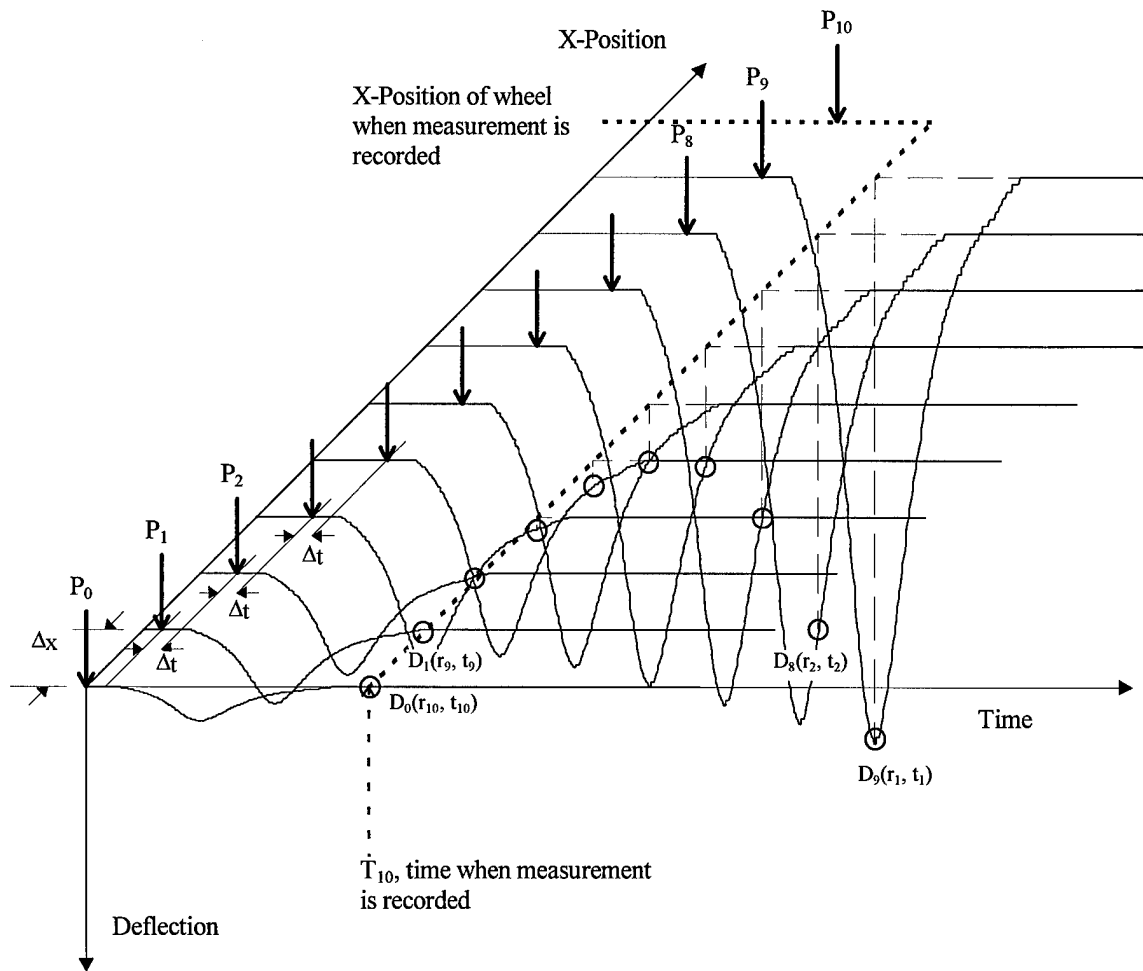


Figure 5-15. Method for calculating deflections at sensor location D_T at time T_{10} . For simplification of the illustration, haversine load pulses are represented by vertical arrows.

After the last load pulse is considered, BASIN repeats the identical process for the next deflection sensor. An entirely new set of radii and responses must be calculated because each sensor location is different. When the total deflection for the final sensor has been calculated, BASIN moves to the next set of measured deflections and calculates the basin measured at the next time increment. For this thesis, the load, velocity, and material properties were assumed to be constant throughout. Therefore, only one basin was calculated because all others would be identical.

5.2.2 *Avetime and Timeback*

To limit the number of required computations, two questions must be answered regarding the load pulses. First, *how far apart (in time and space) should the load pulses occur?* Second, *how far back (in time and space) should loads be considered to have an influence on the measured deflection?* Ideally loads would be placed infinitesimally close and all previous loads would be considered. However, this is computationally impractical. Two parameters were created to quantify these two issues: *avetime* and *timeback*.

Avetime represents the time increment between each load pulse. For the idealized cases analyzed in Section 5.1, point loads were assumed to be applied at every time (and space) increment. When the transition to the real Green's function solution was made, haversine load pulses were applied such that they overlapped to produce a constant line load. Section 4.2.4.4 first addressed this issue and showed that different combinations of spacing and pulse amplitude could produce the same line load in time. The best spacing between load pulses was only suitably determined through a parametric study. Section 7.2.5 describes the manner in which the predicted deflection basin changes as the spacing is varied.

Timeback represents the period of time over which load pulses are considered to influence the calculated deflections. This has a significant influence on the computation time because the number of load pulses increase in direct proportion to *timeback*. By examining time history deflections predicted by FWDDROP, it becomes clear that for an

average load pulse duration of 30 msec, all responses are negligible after 200 msec.

Section 7.2.4 examines this parameter in greater detail to determine its influence on the deflection basin shape.

5.2.3 Deflection Basin Assembly

When the deflection at each measurement location is known, the data can be assembled and plotted to show the approximate shape of the deflection basin. Two- or three-dimensional images can be created, depending on the location of the deflection sensors. Figure 5-16 illustrates a longitudinal deflection basin computed by BASIN. The data point markers show the location of the deflection sensors on a line directly under the wheel path. Note that more sensors were located at points of high curvature to more accurately define the basin.

Using the method described for the Case 4 idealized model (Section 5.1.5), three-dimensional basins can be constructed using BASIN. Figure 5-17 illustrates such a basin.

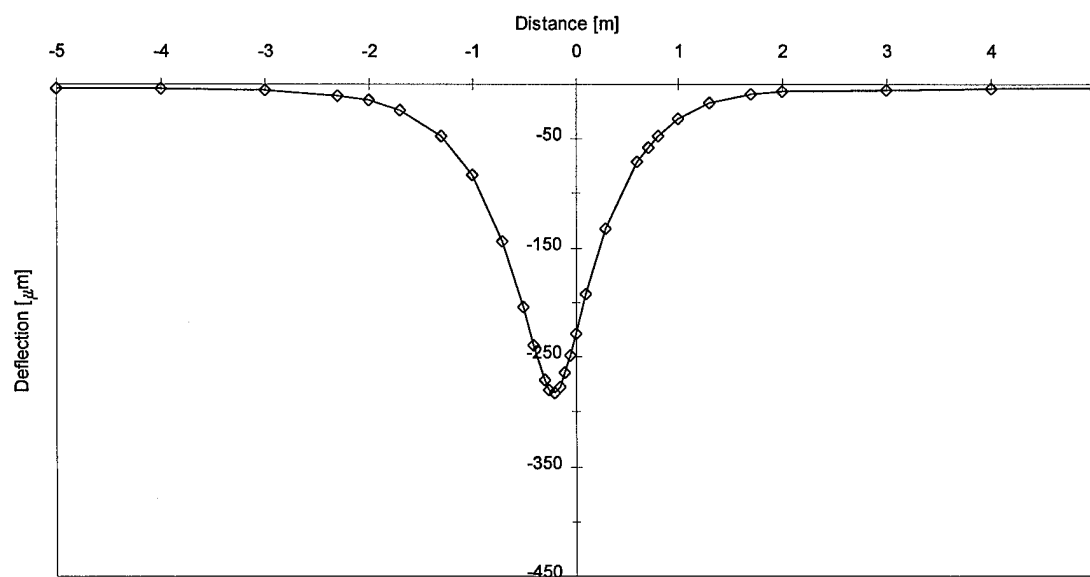


Figure 5-16. Longitudinal deflection basin with deflection sensors located at each data point marker.

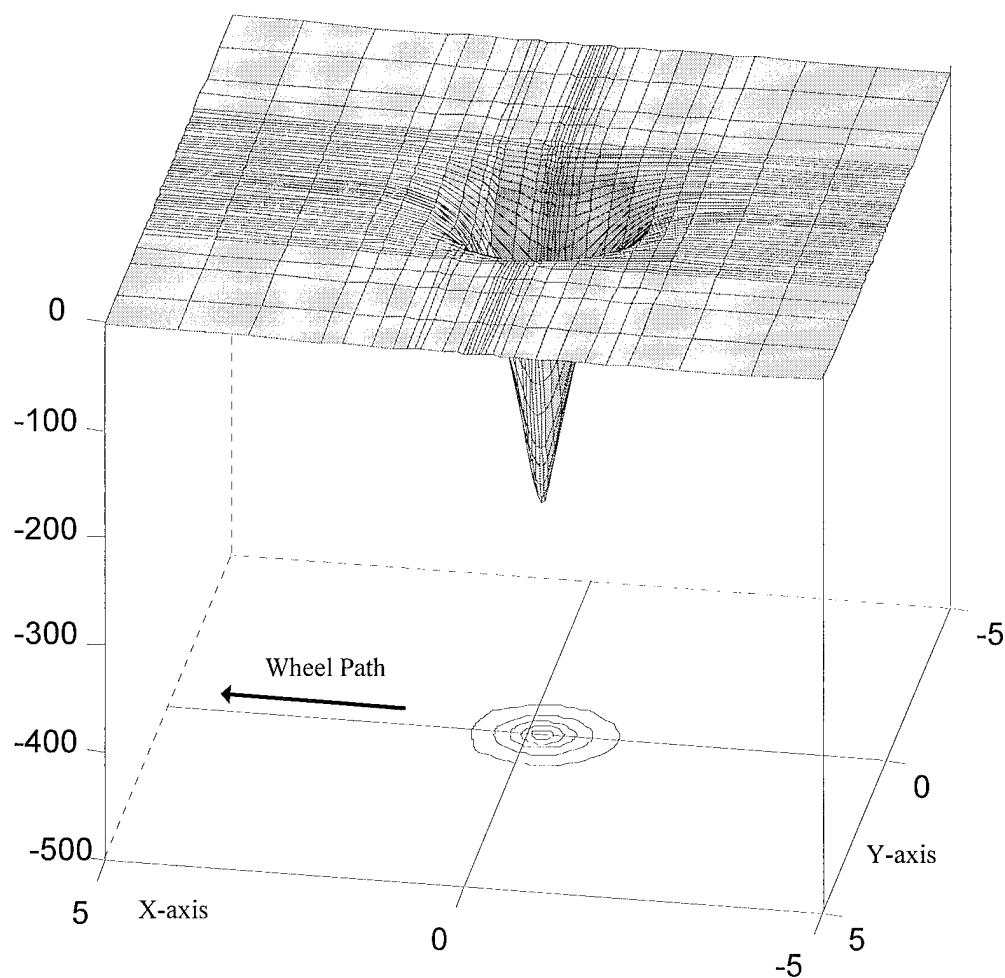


Figure 5-17. Single wheel deflection basin computed using BASIN.

5.2.4 3-D Basin for Two Parallel Rolling Wheels

The deflection basin created by two parallel rolling wheels, each with identical load, can be constructed using superposition. As described in Case 5 (Section 5.1.6), a two-wheel basin is created when a copy of the one-wheel basin is shifted in the transverse direction by a distance equal to the wheel spacing, and then superimposed on the original basin. Figure 5-18 illustrates the result of this process.

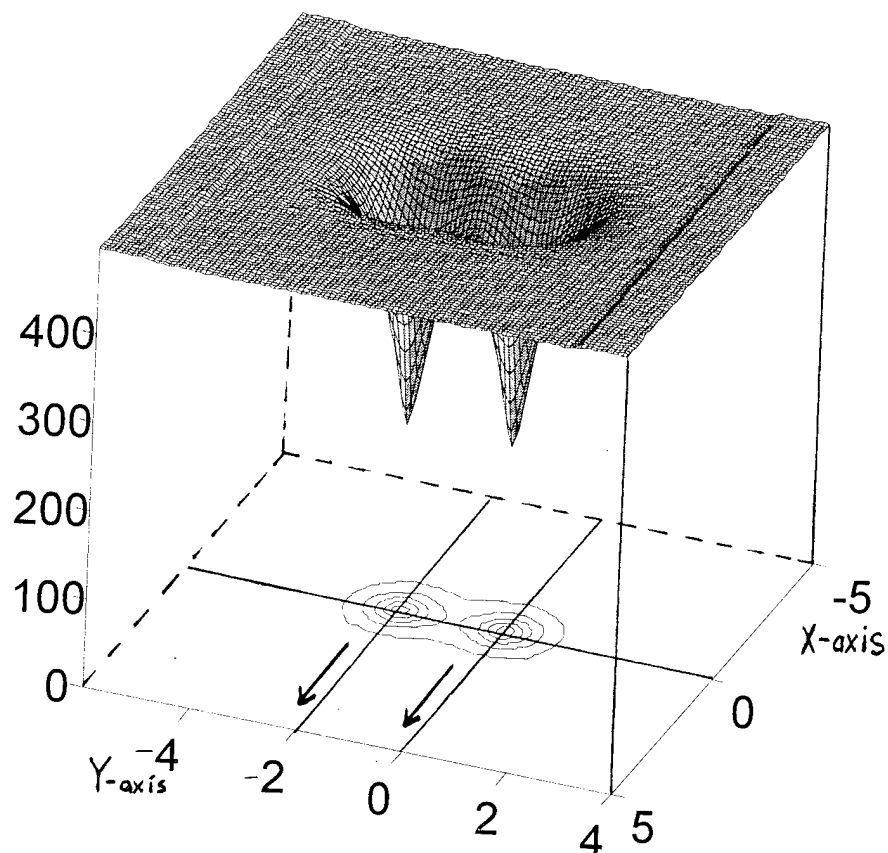


Figure 5-18. Double wheel deflection basin computed using BASIN.

5.4 BASIN Code Details

The idealized cases examined in Section 5.1 were programmed using MATLAB because of the user-friendly syntax and enhanced graphics capabilities. However, when the complex Green's function was used, the program was converted to MS-FORTRAN. The entire code is listed in Appendix A.

Chapter 6

PAVEMENT DEFLECTION MODEL VERIFICATION

To test the accuracy of BASIN, the program was compared to other pavement models. Data from dynamic moving wheel models was not available for comparison, therefore BASIN was checked against static pavement deflection models. To make this comparison, BASIN was modified to calculate the deflections that would be produced by a FWD test. Using moduli that were backcalculated from static models, the deflections from the new program, FWDDROP, were compared to deflections measured by FWD tests.

6.1 FWDDROP Program

To create a program that would predict the pavement deflections produced by a falling weight deflectometer, the BASIN program was modified to compute the time history of deflection at a several fixed locations resulting from a transient load applied over a known area at a known location. Several distinct, yet simple, changes were required to accomplish the modification. These changes resulted in a new computer program, FWDDROP. The steps required to develop FWDDROP are described in the following paragraphs.

First, BASIN's data input module was scaled down because the input data required for an FWD model is less comprehensive than that required for the RWD model. For FWDDROP, only the following items need to be known. (Units for the program can be either metric or US, as long as they are consistent.)

Pavement system parameters - variables needed to define the geometry and material properties of each layer of the pavement profile (thickness, shear wave velocity, mass density, Poisson's ratio, and damping ratio).

Load - the peak load applied by the FWD.

Load Duration - the period of time over which the impulse load is applied.

Load Area - the size of the FWD loading plate.

Sensor Locations - the locations of the FWD deflection sensors (geophones).

Second, the BASIN modules that determine the location of the wheel and deflection sensors were removed because the load plate and the sensors are stationary throughout the test. Third, the program was changed so that only one load pulse is applied to the pavement, rather than the multiple pulses used to model a moving load. This modification required removal of the loop that calculated the response from each pulse. The coding in BASIN that characterizes the load as a haversine was retained in FWDDROP; however, any load shape (or an actual load time history) could be used in FWDDROP. Finally, the output data module was modified to save the entire time history of deflection at each sensor location.

With the modifications complete, FWDDROP was a fully functional dynamic linear-elastic pavement deflection model. Figure 6-1 illustrates the deflection time histories produced by FWDDROP and shows how a “static” deflection basin can be produced by selecting the peak value from each deflection time history, then plotting deflection as a function of distance from the center of the load plate.

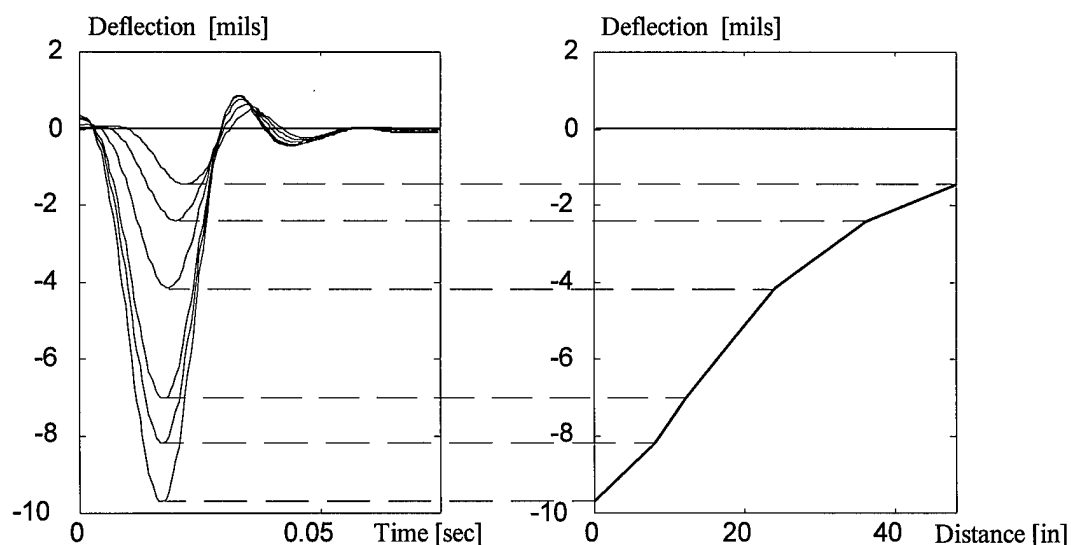


Figure 6-1. Typical FWD deflection time histories and construction of “static” deflection basin.

6.2 Comparison to SHRP Test Sections

Deflections calculated by FWDDROP were compared to deflections reported by Meier (1995) for the two Strategic Highway Research Program (SHRP) pavement sections illustrated in Figure 6-2. Meier used three static, layered elastic pavement backcalculation programs to determine the moduli of the SHRP pavement layers, as listed in Table 6-1. The first set of moduli was backcalculated using Meier's artificial neural network algorithm which he coded in an extremely fast basin-matching program. The second set of moduli were determined using Modulus 4.0, SHRP's database-searching, basin-matching program (Rada, Richter, and Jordahl, 1994). The last set of moduli were backcalculated by WESDEF, an iterative program that uses a layered elastic pavement model that allows variable frictional properties on layer interfaces (Van Cauwelaert et al., 1989). Considerable scatter (5%) exists in the AC layer moduli for both sections, even though all analyses were performed with static load models.

SHRP Section A		SHRP Section B	
Asphalt Concrete	4.95 in =0.126 m	Asphalt Concrete	4.20 in =0.107 m
Crushed Limestone Base	13.4 in =0.340 m	Uncrushed Gravel Base	5.00 in =0.127 m
.....		Sand Subgrade	∞
Soil/Aggregate Subbase	12.0 in =0.305 m		
Sand Subgrade	∞		

Figure 6-2. Pavement structures for SHRP test sections A and B (after Meier, 1995).

Because all the parameters of the pavement system and the loading time history were not available, some values were estimated from the best available information. Estimated values of mass density, Poisson's ratio, and damping ratio for each layer of the pavement system are listed in Table 6-2. Mass densities were based on suggested values

reported by Yoder and Witczak (1975). Poisson's ratios were taken as those assumed by Meier (1995) for his backcalculations. The damping ratio was assumed to be 5% for all materials. Sensitivity calculations showed that errors in the assumed density or damping ratio had almost no effect on the calculated deflection basins.

Table 6-1. Moduli backcalculated from measured deflection basins (Meier, 1995). [1 ksi = 6.895 MPa]

SHRP Section	Pavement Layer	Backcalculated Moduli (ksi)		
		Neural Network	Modulus 4.0	WESDEF
A	Asphalt	1294	1250	1317
	Base*	42	41	42
	Subgrade	32	30	31
B	Asphalt	855	921	918
	Base	53	56	46
	Subgrade	27	27	27

*Combination of crushed limestone base and soil/aggregate subbase

Table 6-2. Assumed layer properties for SHRP test sections.
[1 lb/ft³ = 16.018 kg/m³]

SHRP Section	Pavement Layer	Density [lb/ft ³]	Poisson's Ratio	Damping Ratio
A & B	Asphalt	150.00	0.325	0.05
	Base	130.00	0.35	0.05
	Subgrade	120.00	0.35	0.05

The load pulse was modeled as a haversine with duration of 26.5 msec as suggested by Meier (1995). Meier found that differences between the shape of an actual load pulse and a haversine required that the peak of the haversine be increased by a factor of 1.09 to achieve the same total impulse. Therefore, the peak of the haversine applied in FWDDROP was 9% greater than the actual measured load.

Deflection basins were calculated using each set of moduli for both pavement sections, and the error between the measured and calculated deflections was determined. Table 6-3 presents the results of the calculations. Figure 6-3 shows the measured deflection basins and the basins predicted by FWDDROP using Meier's neural network backcalculated moduli. The agreement between the deflection basins is very good, particularly when all of the assumptions that went into the dynamic model are considered. It should be noted that the moduli used by FWDDROP were backcalculated using *static* pavement deflection models, and the true *dynamic* modulus of each layer is unknown.

Table 6-3. Comparison of measured and calculated FWD deflections for SHRP test sections.
[1 mil = 25.4 μ m]

Section	Layer Moduli	Measured	Deflections [mils] at radius [in]						
Load [lbs]			0	8	12	18	24	36	60
A 10006	Model	Measured	9.47	7.43	6.31	4.9	3.82	2.48	1.24
	Neural Network	Calculated	9.28	7.47	6.26	4.78	3.72	2.47	1.48
		error (%)	-2.0	0.6	-0.8	-2.4	-2.7	-0.3	19.0
	Modulus 4.0	Calculated	9.63	7.76	6.51	4.98	3.89	2.61	1.56
		error (%)	1.6	4.4	3.1	1.7	1.9	5.1	26.0
	WESDEF	Calculated	9.31	7.52	6.32	4.85	3.78	2.53	1.52
error (%)		-1.7	1.2	0.1	-1.1	-0.9	2.1	22.2	
B 9596		Measured	12.21	9.43	7.65	5.72	4.32	2.62	1.36
	Neural Network	Calculated	12.46	9.64	7.89	5.92	4.57	2.99	1.72
		error (%)	2.0	2.2	3.2	3.4	5.7	13.9	26.7
	Modulus 4.0	Calculated	12.14	9.47	7.80	5.89	4.56	2.99	1.72
		error (%)	-0.6	0.4	1.9	3.0	5.5	14.0	26.6
	WESDEF	Calculated	12.56	9.77	7.99	5.97	4.59	2.99	1.72
error (%)		2.9	3.6	4.5	4.4	6.2	13.9	26.8	

6.3 Comparison to PACCAR Test Section

An additional pavement section was used to further evaluate the accuracy of FWDDROP. A heavily instrumented asphalt concrete pavement section located at PACCAR Inc.'s Technical Center in Mount Vernon, WA, was extensively tested and analyzed by Winters (1993). Data collected from 130 FWD (WSDOT's Dynatest 8000) tests at 61 locations on a 12.2 m (40 ft) pavement section were analyzed using

EVERCALC 3.3 (a static, layered elastic backcalculation program) to determine layer moduli.

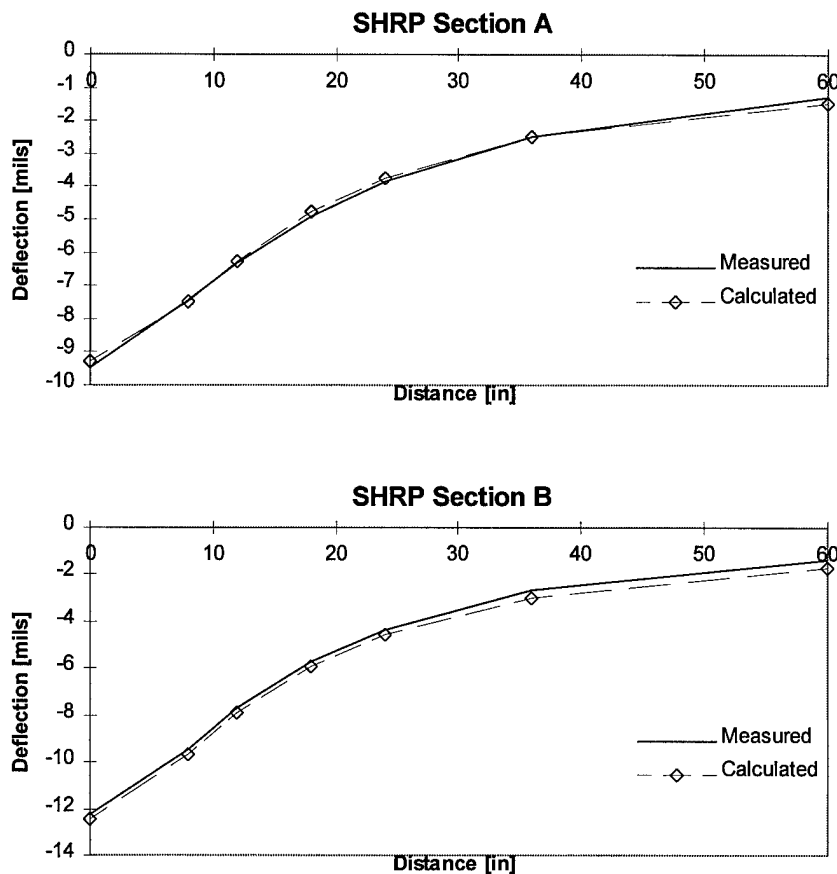


Figure 6-3. Measured and calculated deflection basins for SHRP sections A and B.
[1 mil = 25.4 μm]

Measured deflections from three FWD tests were compared with FWDDROP calculations. All three tests were conducted at the site identified as Core 4, where layer thicknesses had been determined from a drilled core, illustrated in Figure 6-4. Winters backcalculated the moduli of the AC, base, and subgrade for each test, as shown in Table 6-4. One significant difference between the PACCAR profile and the SHRP sites is that the material below the groundwater table was modeled as a stiff layer. Using

EVERCALC, Winters determined that the modulus of the stiff layer was 40 ksi (275.8 MPa). Other researchers agree that a fully saturated soil layer should be modeled as a stiff layer for backcalculation purposes (Newcomb et al., 1995).

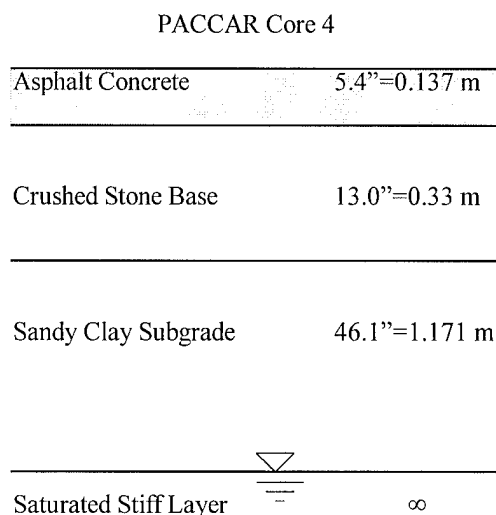


Figure 6-4. Pavement structures for PACCAR test site Core 4.

Table 6-4. Moduli backcalculated from measured deflection basins.
[1 ksi = 6.895 MPa]

PACCAR Core 4	FWD Load (lb)	Backcalculated Moduli (ksi)		
		Asphalt	Base	Subgrade
1	14039	654.794	11.42	9.542
2	10631	678.106	11.634	10.14
3	5045	731.217	10.688	13.185

Winters reported the assumed Poisson's ratios used for his backcalculations, but the densities and damping ratios were not known. These values were again assumed as described in Section 6.2, and are listed in Table 6-5.

The load pulse was modeled as a 30 msec haversine, which is consistent with the duration reported by Chatti et al. (1995) for WSDOT's Dynatest 8000. The reported load

pulse for WSDOT's FWD very closely resembled a haversine, therefore no adjustments to match the total impulse were required.

Table 6-5. Assumed layer properties for PACCAR Core 4.
[1 lb/ft³ = 16.018 kg/m³]

PACCAR Core 4	Pavement Layer	Density [lb/ft ³]	Poisson's Ratio	Damping Ratio
1,2,3	Asphalt	150.00	0.350	0.05
	Base	130.00	0.40	0.05
	Subgrade	110.00	0.45	0.05
	Stiff	120.00	0.35	0.05

Table 6-6 lists the measured and predicted deflections and errors, and Figure 6-5 illustrates the deflection basins. The predicted deflections do not agree with the measured deflections as closely as they did for the SHRP pavement sections; however, the shape of the calculated basin is virtually parallel to that of the measured basin. It would appear that the basins would match very closely if the peak load was reduced. However, Figure 6-6 illustrates that an 8% reduction in load changes the deflections differently at each distance from the load; therefore, the calculated basin loses its parallel match to the measured basin. The discrepancies between the basins can be possibly attributed to the dynamic interaction of the stiff layer. As described in Chapter 3, stiff layers at shallow depths can profoundly affect the measured deflections, which can result in significant errors from backcalculation programs that use static loading models.

6.4 Modification of Deflection Time Histories

During analysis of the deflection time histories, a problem was encountered with the deflections at the very beginning and end of the time record. Figure 6-7a indicates that the initial pavement deflection is positive at the time of FWD impact. This implies that the pavement has moved before loading has been applied. Also, the deflections at the very end of the time record become positive, again implying that the pavement begins to deflect again, long after the deflections due to the loading have ceased. Presumably,

these spurious deflections are due to a basic assumption in a Fourier transformation -- the motion transformed into the frequency domain is periodic (i.e., the motion begins again immediately after the last point of the time record). It is also possible that the spurious deflections may result in part from the Green's function assumption that the response varies linearly between the top and the bottom of each sublayer.

Table 6-6. Comparison of measured and calculated FWD deflections for PACCAR Core 4.
[1 mil = 25.4 μm]

Test	Load [lbs]		Deflections [mils] at radius [in]					
			0	8	12	24	36	48
1	14039	Measured	29.20	24.06	20.58	11.66	6.04	3.17
		Calculated	31.18	26.42	22.97	14.08	8.37	5.16
		error (%)	6.8	9.8	11.6	20.8	38.6	62.8
2	10631	Measured	21.39	17.57	15.04	8.52	4.41	2.33
		Calculated	22.64	19.21	16.67	10.18	6.03	3.71
		error (%)	5.9	9.4	10.9	19.5	36.8	59.4
3	5045	Measured	9.29	7.62	6.44	3.56	1.81	0.96
		Calculated	9.70	8.15	7.02	4.14	2.36	1.43
		error (%)	4.4	7.0	9.0	16.2	30.5	49.1

Input parameters were systematically varied to determine which affected this problem. The thickness of the layers of the pavement system appeared to have the greatest influence, but the spurious deflections could not be completely removed by reducing the thickness of individual layers.

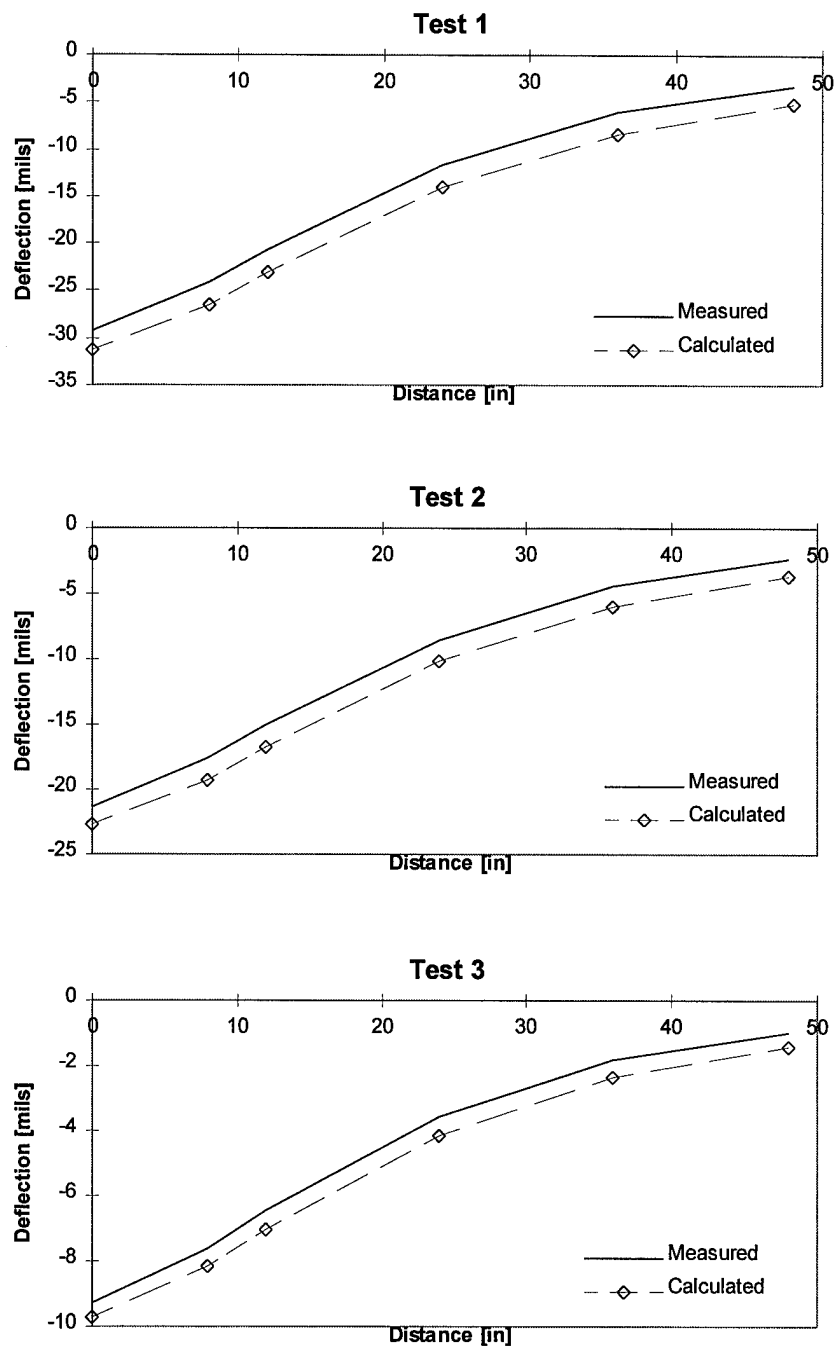


Figure 6-5. Measured and calculated deflection basins for PACCAR Core 4 FWD tests. [1 mil = 25.4 μm]

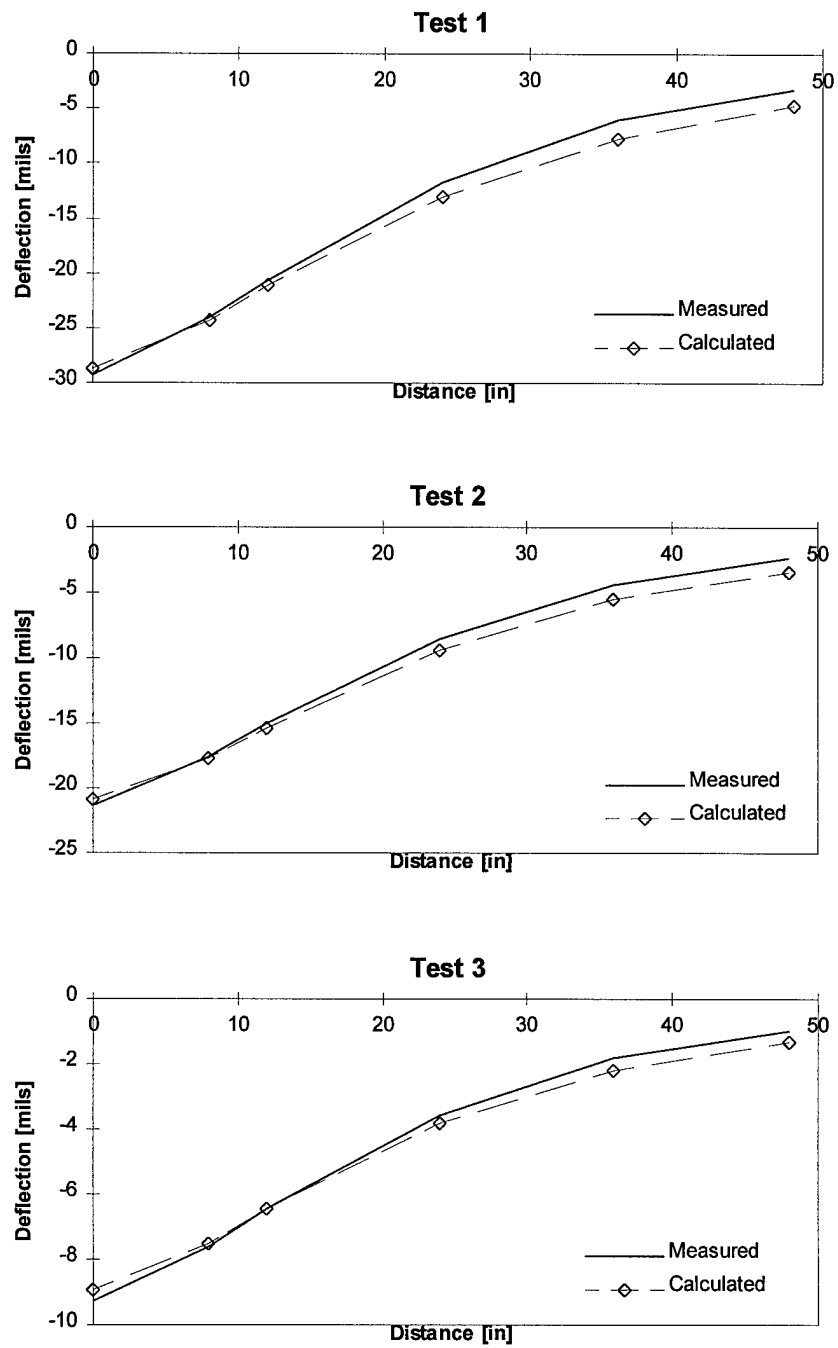


Figure 6-6. Measured and calculated deflection basins for PACCAR Core 4 FWD tests when peak load is reduced by 8%. [1 mil = 25.4 μm]

A correction procedure was developed to eliminate the computed spurious deflections. A simple "tripwire" code loop was added to FWDDROP (and BASIN) to process the calculated time history of deflection. From the beginning of the time record, the deflection is set to 0.0 until the first negative deflection occurs. From that time until the middle of the time record, the deflections are not modified. By the middle of the time record, pavement deflections are negligible, so the deflections were set to 0.0 for the remainder of the loading period. Figure 6-7b illustrates the modified time history of deflection calculated for the same sensor used in Figure 6-7a. The peak deflections calculated by FWDDROP remain absolutely unchanged by this modification. Also, comparisons between deflection basins calculated by BASIN using the modified and unmodified deflection records revealed only very minor differences.

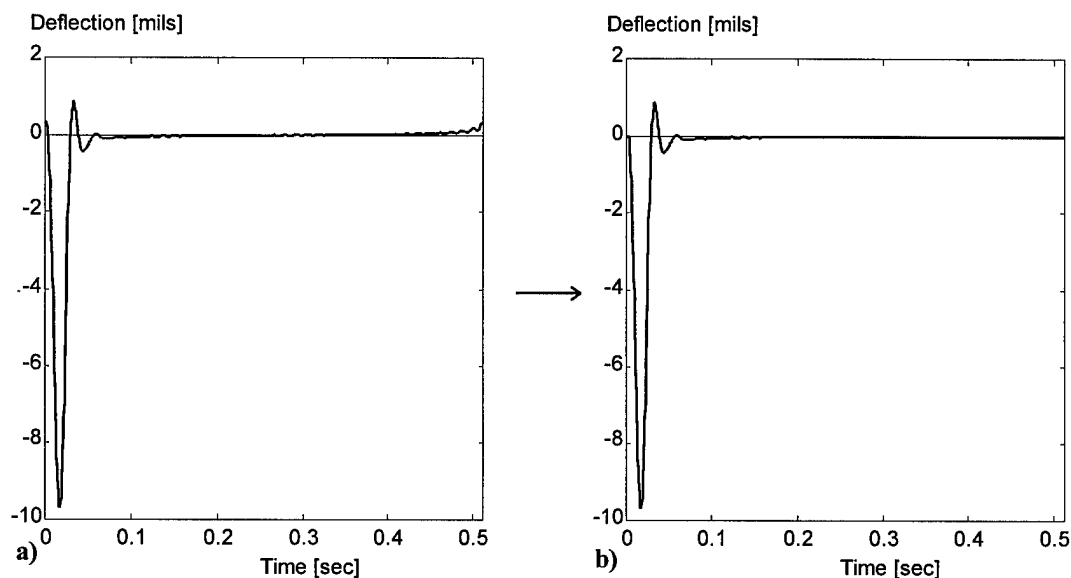


Figure 6-7. a) Illustration of negative deflections at the beginning and end of the deflection time history calculated by FWDDROP. b) Modified deflection time history.

Chapter 7

PARAMETRIC STUDY

The sensitivity of the calculated deflection basin to a variety of input parameters was investigated by a detailed parametric study. The parametric study involved systematic perturbation of each input variable and evaluation of the resulting changes in calculated deflections. This chapter describes the plan, execution, and results of the study.

7.1 Parametric Study Plan

A detailed, logical plan of action for the parametric study was prepared before calculations began. First, a standard pavement section and standard loading were selected for use throughout the study. Next, the BASIN inputs were grouped into three categories of variables according to their role in the calculations: algorithm variables, pavement system variables, and loading variables. Last, a method was developed for quantitatively describing and comparing the calculated deflection basins. Each of these aspects of the plan are described in the following sections.

7.1.1 Standard Pavement Section and Standard Loading

A pavement section was selected to establish a standard deflection basin that would serve as a common starting point for all sensitivity analyses. To keep the basin consistent, a standard loading scheme was also designated.

A 12.2 m (40 ft) section of pavement at PACCAR Inc.'s Technical Center in Mt. Vernon, WA, was selected as the standard pavement section for two primary reasons. First, it is a very typical heavy-traffic flexible pavement structure -- the thickness and properties of the asphalt, base, and subgrade layers are very typical of those commonly used throughout Washington state. Second, the sections had been extensively analyzed by Winters (1993); consequently, the layer thicknesses and moduli were well-established from core samples and backcalculations of over one hundred FWD tests.

Figure 7-1 illustrates the profile of the PACCAR test section. The pavement structure consists of 137 mm (5.4 in) of asphalt on 330 mm (13.0 in) of crushed stone base. The subgrade material is a medium stiff sandy clay. The groundwater table was measured at the time of FWD testing and found at an average depth of 1.637 m (64.4 in) below the pavement surface. The modulus of each layer was determined from the average of 130 FWD analyses using EVERCALC 3.3. As described in Chapter 6, Winters modeled the saturated soil below the ground water table as a stiff layer with a modulus of 275.8 MPa (40 ksi). The density of each layer was assumed based on suggested values, and the Poisson's ratios were set equal to the values used by Winters (1993) for backcalculation. A damping ratio of 5% was assigned to each layer.

In addition to the standard pavement section, a standard load was also selected. The standard wheel load was set equal to the load applied by the left front wheel of a Peterbuilt truck, model PB359. The standard tire pressure was selected at 90 psi, which is a typical operating pressure for large trucks in the United States. This combination of load and tire pressure results in a standard loaded radius of 0.112 m (4.4 in). As explained in Chapter 4, the standard load pulse has a haversine shape with a duration of 30 msec. This duration corresponds to a standard travel speed of 50 km/hr = 13.89 m/sec (31 mph).

7.1.2 Structure

The input variables of BASIN were grouped into three categories: algorithm variables, pavement system variables, and loading variables.

Algorithm variables result from the concepts and mathematics used in BASIN. They include the time increment, frequency interval, frequency range, layer discretization, spacing between load pulses, and the number of pulses behind the wheel that are considered in the deflection calculations. These parameters were evaluated first because they influence the speed and accuracy of the deflection calculations. The algorithm variables were adjusted to find values that produce high accuracy with minimal computational effort.

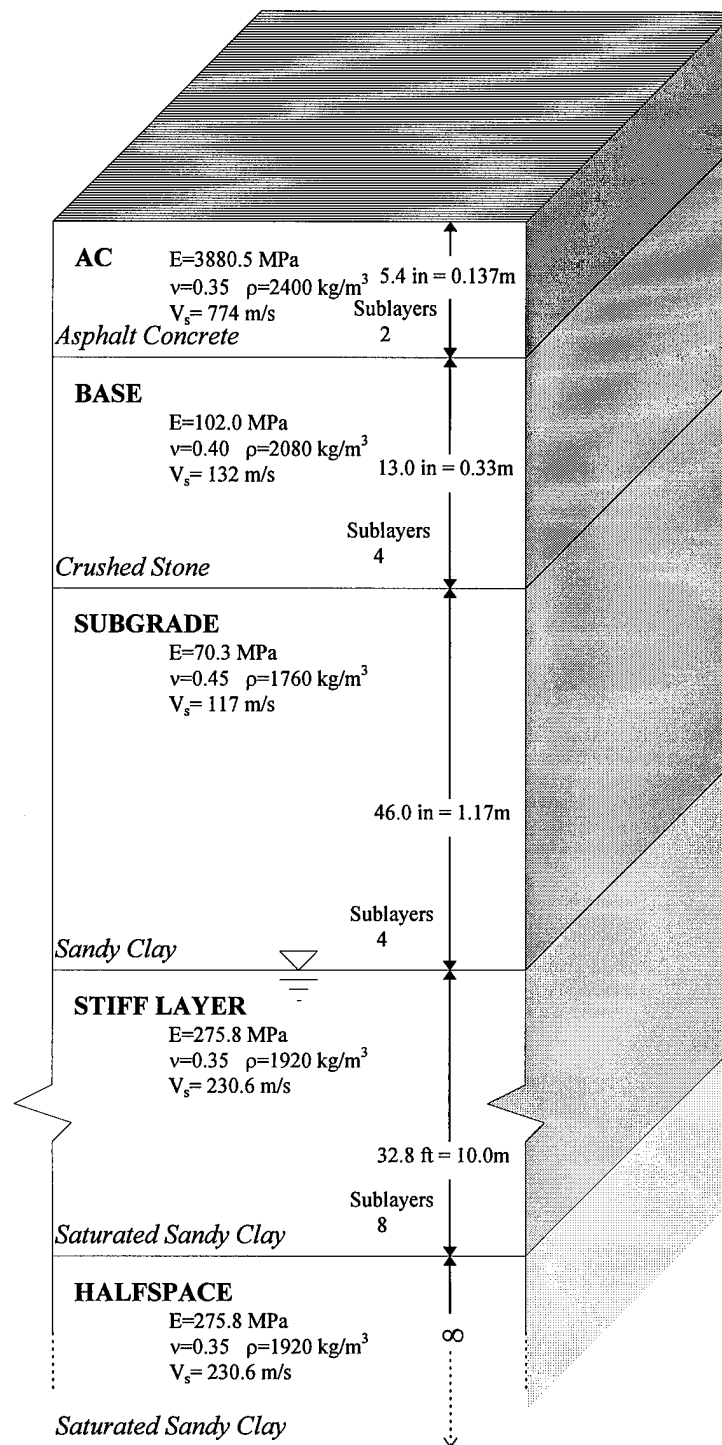


Figure 7-1. Standard Pavement Section.

Pavement system variables describe the pavement structure that supports the wheel load. They include the thickness, modulus, density, Poisson's ratio, and damping ratio of each layer. In typical static pavement analyses, all except the layer moduli are assumed. However, because BASIN's dynamic analysis may be more sensitive to the other parameters, each of these variables were studied separately.

Loading variables characterize the magnitude and type of load applied to the pavement. They include the magnitude, pulse duration, vehicle speed, and tire pressure. These parameters are purely functions of the loading mechanism; however, it is important to understand their effects on the basin shape because the sensitivity of the deflection basin to the loading variables may help determine the optimum loading conditions and the best locations for deflection sensors.

7.1.3 Data Presentation and Statistical Parameters

Because the sensitivity of deflection basins to parameter variations is not easily described in qualitative terms, a quantitative approach was developed. For this purpose, the shape of the deflection basin was described by a series of coefficients related to the moments of the deflection basin. Description of distributed parameters by moments is frequently used, most commonly in the area of statistics. If the deflection basin is considered analogous to a probability density function, the mean, standard deviation, coefficient of skewness, and coefficient of kurtosis can be calculated. These parameters are most easily described and understood by referring to Figure 7-2.

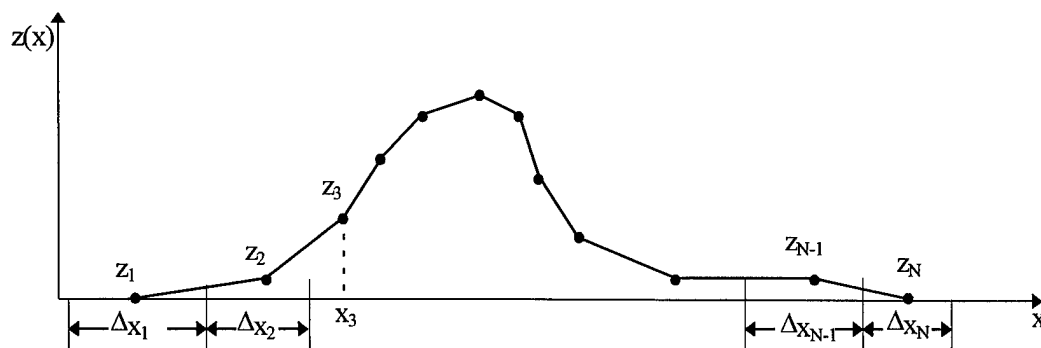


Figure 7-2. Example function, $z(x)$, represented by N discrete points.

The area under the function can be calculated using the following formula:

$$\text{Area} = \sum_{i=1}^N z_i \Delta x_i$$

Next, a function, $f(x)$, analogous to the probability density function, can be calculated for all x_i to show the likelihood that a randomly sampled value of z will be at x .

$$f_i = \frac{z_i \Delta x_i}{\text{Area}}$$

After f_i is determined for all N terms, several statistical parameters can be calculated.

Mean, \bar{x} : the mean, average, or expected value of the function is calculated as:

$$\bar{x} = \sum_{i=1}^N x_i f_i$$

Figure 7-3 shows how the mean for two identical functions can be different, depending on the location of the distribution on the x axis.

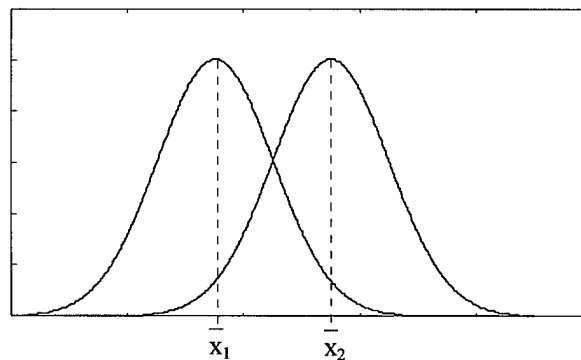


Figure 7-3. Two functions with identical shapes but different mean values.

Standard Deviation, σ : the standard deviation is a measure of the spread of the function about the mean and is related to the variance, V , or *second moment about the mean*, μ_2 . The standard deviation is equal to the square root of the variance, and is calculated in the following manner.

$$V = \mu_2 = \sum_{i=1}^N f_i (x_i - \bar{x})^2$$

$$\sigma = \sqrt{V}$$

Because the standard deviation has the same units as x , its actual value is only meaningful when the units of x are known. Figure 7-4 illustrates two functions centered about the same mean, but with different distributions -- one broad (large σ), one narrow (small σ).

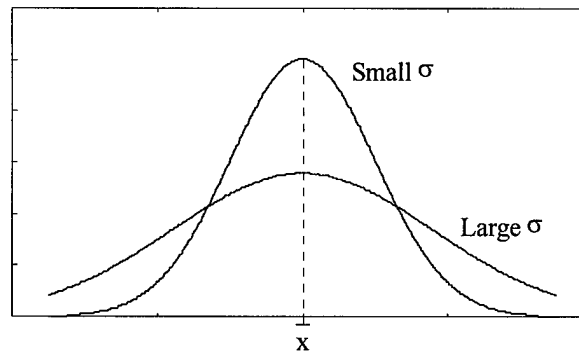


Figure 7-4. Two functions with identical means but different standard deviations.

Coefficient of Skewness, C_3 : The coefficient of skewness provides a quantitative measure of the symmetry of the function about its mean value. The coefficient of skewness is calculated from the *third moment about the mean*, μ_3 . To render the coefficient of skewness independent of scale, the third moment is divided by cube of the standard deviation.

$$\mu_3 = \sum_{i=1}^N f_i (x_i - \bar{x})^3$$

$$C_3 = \frac{\mu_3}{\sigma^3}$$

Skewness can be either positive, negative, or zero. If more than half of the function is greater than the mean, the function is negatively skewed. If the majority of the function is less than the mean, the function is positively skewed

(Walker and Lev, 1969), as illustrated in Figure 7-5. A symmetric function has zero skewness.

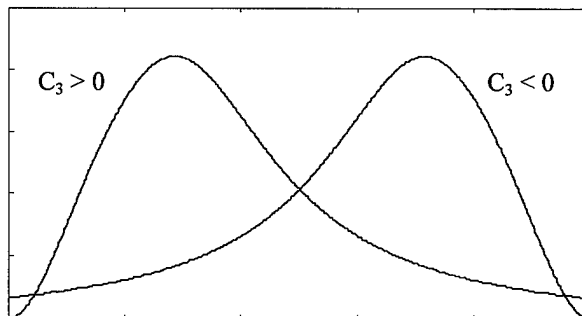


Figure 7-5. Two functions with opposite skewness, one positive and the other negative.

Coefficient of Kurtosis, C_4 : Kurtosis is a measure of the peakedness of a function calculated from the *fourth moment about the mean*, μ_4 . The dimensionless coefficient of kurtosis is equal to the fourth moment divided by the fourth power of the standard deviation.

$$\mu_4 = \sum_{i=1}^N f_i (x_i - \bar{x})^4$$

$$C_4 = \frac{\mu_4}{\sigma^4}$$

Kurtosis describes the arch of the distribution, and is usually compared to a normal distribution with a variance equal to the variance of the distribution of interest. The coefficient of kurtosis of a normal distribution is always equal to 3. Therefore, if the peak of the studied function is higher than the normal distribution peak, C_4 is greater than 3. If the function is flatter on top and with a lower peak than a normal distribution, C_4 is less than 3 (Sachs, 1982). Kurtosis is illustrated in Figure 7-6.

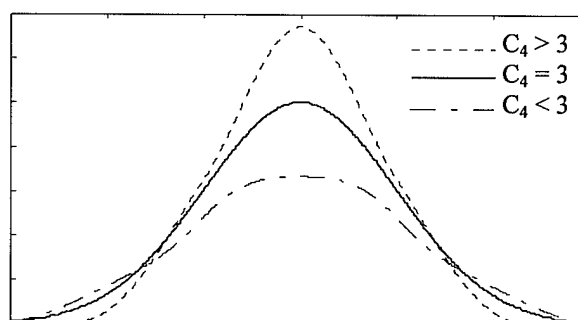


Figure 7-6. A normal distribution ($C_4 = 3$) and two functions with greater and lesser kurtosis.

The results of each parameter study are illustrated with the sequence of figures shown in Figure 7-7. Figure 7-7a shows the longitudinal deflection basin for each of the parameters of interest. Longitudinal, rather than transverse, basins were computed throughout this study because they were expected to reveal more information about dynamic deflection behavior. In all deflection basin figures, the loaded wheel is located at the zero position coordinate and moving from left to right. Figure 7-7b shows how the peak deflection varies for each parameter value. Figure 7-7c illustrates the mean and standard deviation of each deflection basin. The coefficient of skewness is plotted in Figure 7-7d, and the coefficient of kurtosis is illustrated in Figure 7-7e. In Figure 7-7a, the standard deflection basin is always printed using a bold line. In Figures 7-7b through 7-7e, the standard value is designated by a solid data point marker.

7.2 Algorithm Variables

The algorithm variables are the basic limits used when BASIN computes the deflection basins. They can have a profound impact on the accuracy of the results and the computation time required to achieve them. These parameters were investigated first to find the values that maximized accuracy while minimizing computation time.

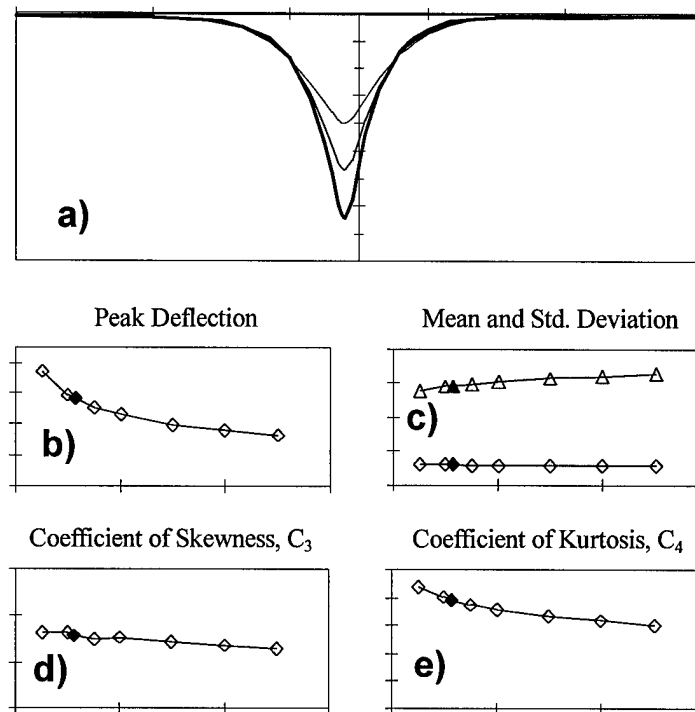


Figure 7-7. Typical data presentation format.

7.2.1 Layer Discretization

The Green's function calculation scheme developed by Kausel and applied in PUNCH relies on the individual layers being sufficiently thin that a linear response within a layer closely approximates the actual response. Thus, if layers are too thick, the response may be in error.

To determine the best layering scheme for the standard pavement section, the number of sublayers in each of the four layers was initially set to one. Then the number of sublayers was systematically increased until there were a total of 40 sublayers in the entire pavement system. A total of six layering schemes were tested.

As the number of sublayers was increased, the basin converged to a constant shape (Figure 7-8a). The basin shape appeared to have converged when the sublayers totaled 14 sublayers ($2_{AC} + 4_{Base} + 4_{Subgrade} + 4_{Stiff}$); no further change was visible as the number of

sublayers exceeded the standard. The remainder of the analyses were performed with a standard scheme consisting of 18 sublayers ($2_{AC} + 4_{Base} + 4_{Subgrade} + 8_{Stiff}$).

The peak deflections (Figure 7-8b) increased by 16% when the sublayers were doubled from the initial setting, but only increased by 4% with further increases. The mean (Figure 7-8c) remained nearly constant for all layering combinations. The standard deviation decreased initially by 7%, but remained constant for combinations with more than 14 layers. The coefficient of skewness (Figure 7-8d) also increased initially, but then leveled out, indicating that the basin is slightly deeper behind the mean (relative to the direction of travel). The coefficient of kurtosis (Figure 7-8e) increased by 10% with the first increase in layers, but then quickly became nearly constant when more than about 10 layers were used. The coefficient of kurtosis indicates that the shape of the deflection basin was more sharply peaked than the shape of a normal probability distribution.

This analysis shows that the accuracy of the deflection basin is not improved by increasing the number of layers above the standard scheme. Based on this observation and the significant increase in computation time associated with more layers, the standard layering scheme was deemed acceptable and used for the remainder of the analyses.

7.2.2 Cutoff Frequency

As described in Section 4.2.3, the loading function is represented by a bandwidth-limited discrete Fourier series. Increasing the cutoff frequency used to characterize the load improves the accuracy of the representation, but also increases the required computation time.

To determine the best cutoff frequency for all other analyses, six specified cutoff frequencies were examined, each with a frequency increment of 1.95 Hz. The smallest cutoff frequency was 37.05 Hz and the largest was 154.05 Hz.

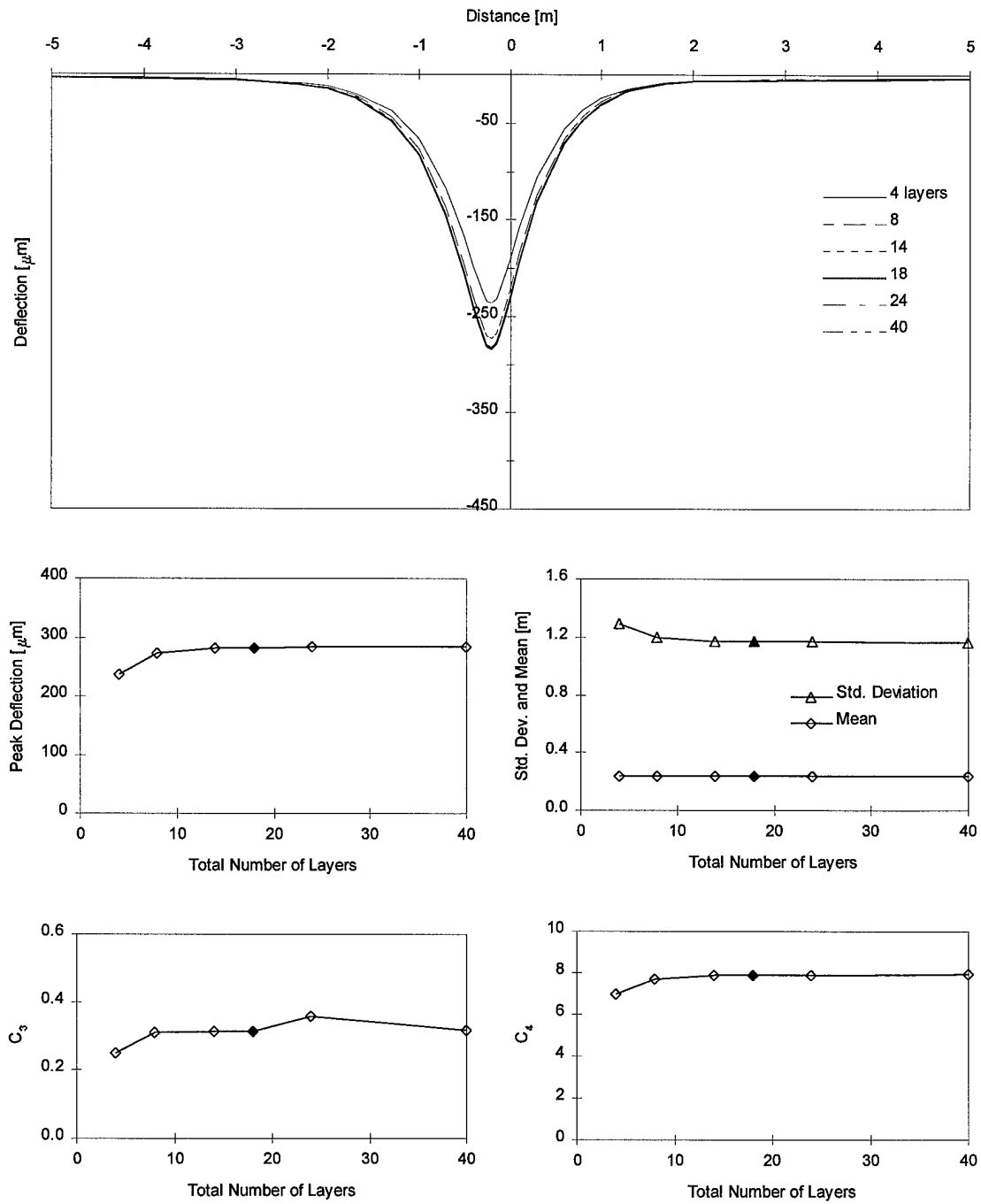


Figure 7-8. Sensitivity to Layer Discretization.

Figure 7-9 illustrates the calculated basins for all cutoff frequencies. The lowest cutoff frequency (37.05 Hz) resulted in a slightly deeper and wider basin than higher cutoff frequencies. Virtually no change was recognizable when the cutoff frequency was increased above 76.05 Hz.

The peak deflection decreased by 2% when the cutoff frequency was increased from 36 to 56 Hz, but remained constant thereafter. The mean was constant for all cutoff frequencies. The standard deviation was essentially constant at 1.17 until the cutoff frequency exceeded 76 Hz, and then jumped by 8% to 1.25 and remained constant thereafter. The coefficient of skewness slowly decreased by 10% as the cutoff frequency increased from 37 to 154 Hz. The coefficient of kurtosis also decreased by about 12% overall, including an 8% drop when the cutoff frequency increased from 76.05 to 95.55 Hz.

This analysis showed that using all but the smallest cutoff frequency produces approximately the same deflection basin. Although the coefficient of skewness and kurtosis change slightly as the cutoff frequency was increased, unless they are used for backcalculation purposes, a bandwidth of 56 or 76 Hz appears to be acceptable. For this study, 76.05 Hz was selected as the standard cutoff frequency and used for the remainder of the calculations.

7.2.3 Frequency Increment

The frequency increment, Δf , used in a discrete Fourier transformation is determined by the number of discrete points, N , and the time increment, Δt , between each point in the loading function. These values are related in the following manner:

$$\Delta f = \frac{2\pi}{N * \Delta t}$$

Thus, the frequency increment can be increased by decreasing the time increment with the total number of points held constant or by decreasing the total number of points with the time increment held constant. Increasing the frequency increment decreases computation time, but may increase error in the calculated deflection basins.

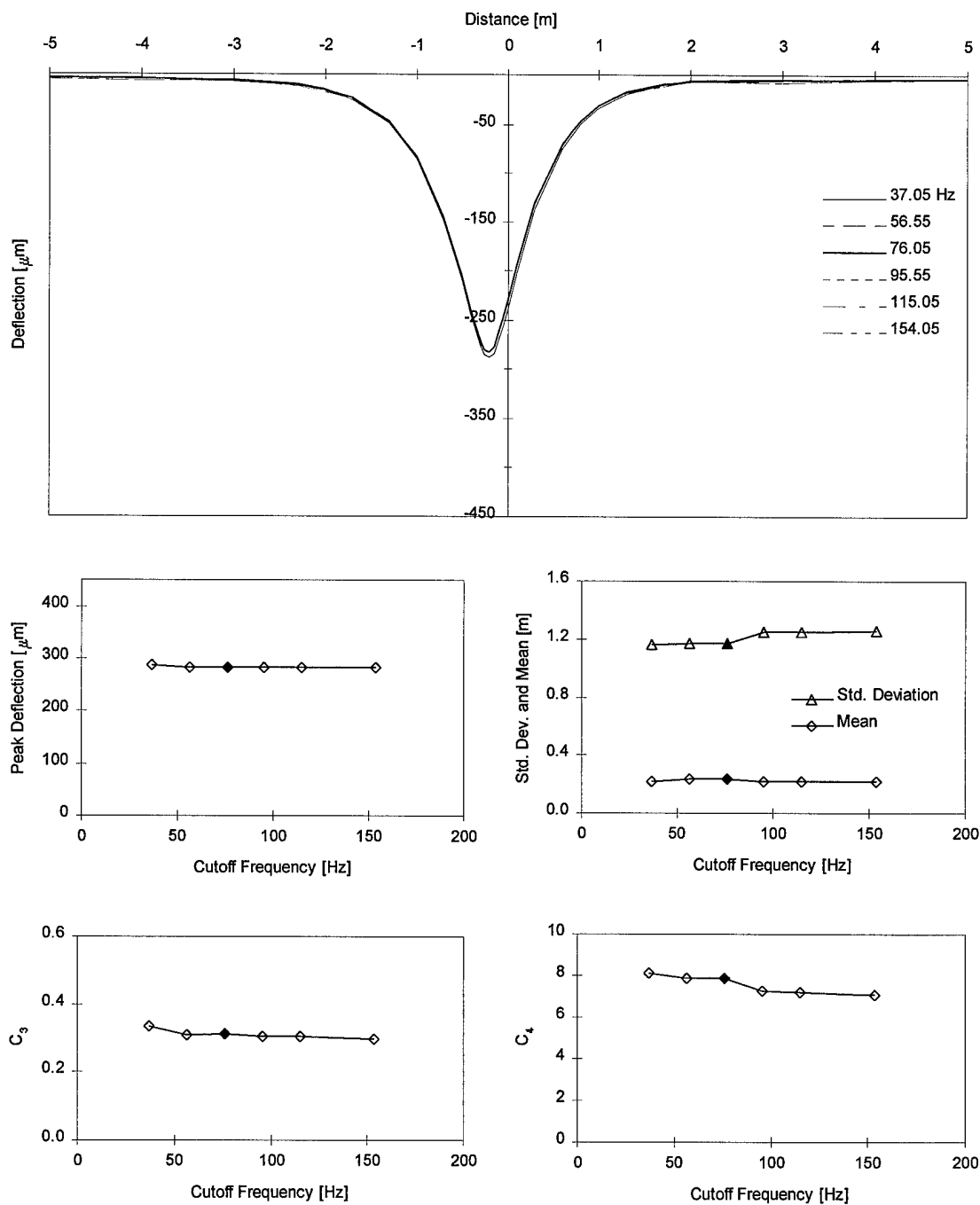


Figure 7-9. Sensitivity to Cutoff Frequency.

To determine the best frequency increment, three combinations of Δf and Δt were used, while N was held constant at 1024.

$$\Delta t = 0.00025 \Rightarrow \Delta f = 3.906$$

$$\Delta t = 0.0005 \Rightarrow \Delta f = 1.95$$

$$\Delta t = 0.001 \Rightarrow \Delta f = 0.977$$

Figure 7-10 presents the results for each of these frequency increments. The only visible difference occurred when the frequency increment was 3.906 Hz. For this case, the basin was slightly shallower than the other basins at a distance 1 to 2 m behind the wheel. Frequency increments of 1.95 and 0.977 Hz produced virtually identical basins.

The peak deflection for each frequency increment was identical. The mean variation showed a slight, but consistent downward trend; the mean decreased by 8% when the standard frequency increment doubled and increased by 8% when the increment was halved. The standard deviation increased only slightly as the frequency increment was increased. The coefficient of skewness was largest for the standard increment, and reduced by about 30% for the other two increments. The coefficient of kurtosis was lowest for the standard increment and increased by only 4% and 1% for the minimum and maximum increments.

Even though the basins did not change visibly for these different frequency increments, the statistical parameters show that small changes did occur. The minimum frequency increment should produce the most accurate solution because the loading is most accurately represented. However, the calculation time is inversely proportional to the frequency increment, i.e. it doubles each time the frequency increment is halved. Therefore, the middle increment (1.95 Hz) was selected as the standard because it appeared to produce adequate accuracy in a reasonable computation time.

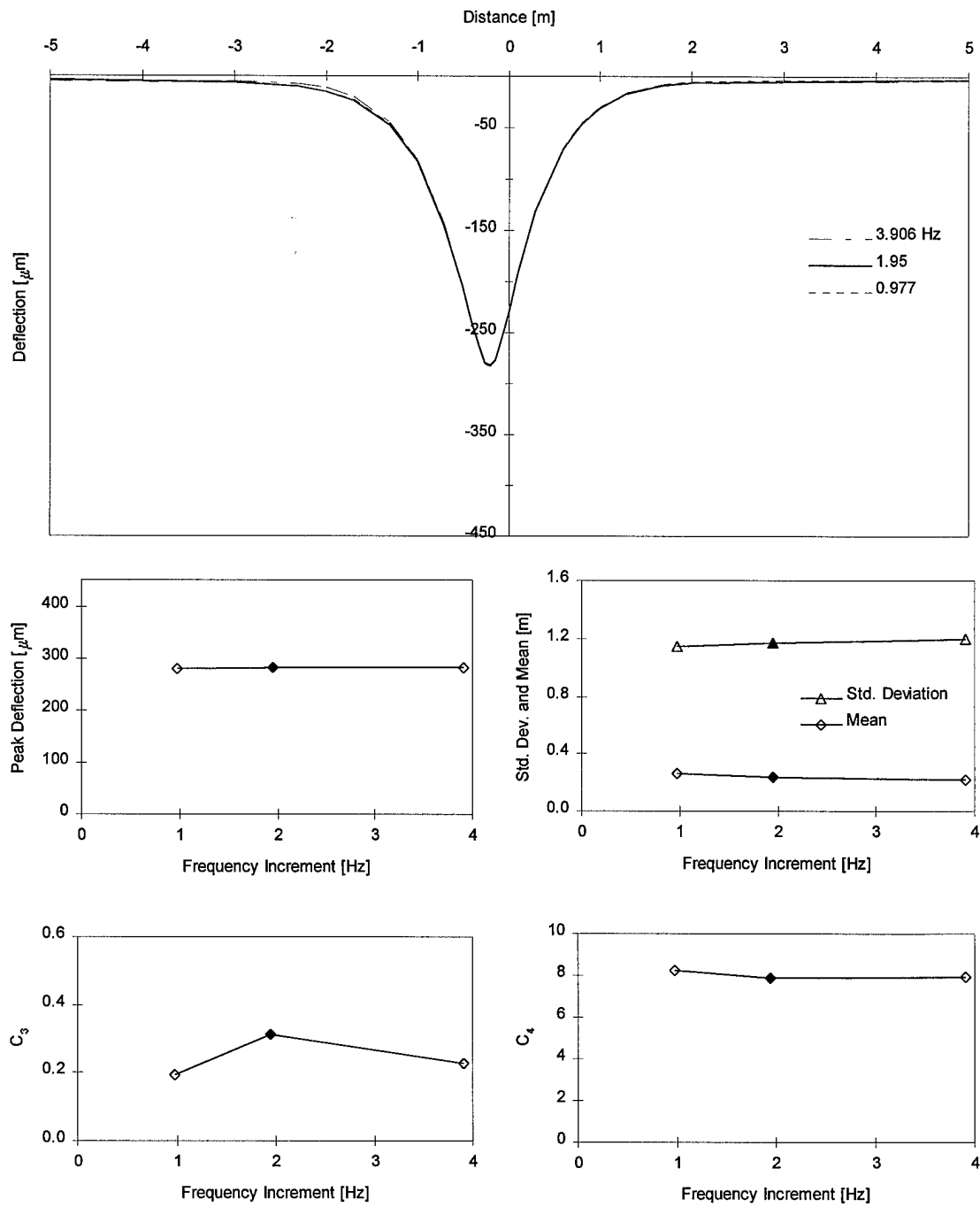


Figure 7-10. Sensitivity to Frequency Increment.

7.2.4 *Timeback*

The variable *timeback* designates how far back in time (and space) the load pulses are considered in deflection calculations. An appropriate value for *timeback* could be selected by closely examining the deflection time histories for load pulses at various distances and determining when the response has ceased. Alternately, the value of *timeback* could be adjusted to determine the actual influence on rolling-wheel deflection basins. Like the other parameters examined in this section, *timeback* has a strong influence on the required computation time -- the number of load pulses for which a response must be calculated is directly proportional to *timeback*.

Deflection basins using four different values of *timeback* were calculated, ranging from 0.10 to 0.25 seconds. For the standard vehicle speed of 50 km/hr = 13.89 m/s (31 mph), these *timeback* values correspond to distances of 1.39 to 3.47 m (4.6 to 11.4 ft).

Figure 7-11 illustrates the calculated basins for all *timeback* values. The only discernible change in the basins appeared at distances between 1 and 3 m (3.3 and 9.8 ft) behind the wheel. The basin became very slightly deeper in this zone as *timeback* was increased from 0.15 to 0.20 sec. No visible change was observed when *timeback* was extended to 0.25 sec.

The peak deflection was constant for all values of *timeback*. The mean increased very slightly as *timeback* was increased, and the standard deviation decreased by 3% when *timeback* was doubled from 0.10 to 0.20. The coefficient of skewness was largest when *timeback* was equal to 0.15, then dropped by 12% as *timeback* increased to 0.25. The coefficient of kurtosis increased by only 1.5% when *timeback* was doubled from 0.1 to 0.2 sec.

This analysis shows that the deflection basin did not change visibly as *timeback* is increased beyond 0.2 sec. The standard deviation and mean did change slightly as *timeback* was increased. Additionally, the computation time increased by about 50% when *timeback* was increased from 0.20 to 0.25 msec. Therefore, the standard value for *timeback* was set at 0.20 seconds and used for the remainder of the analyses.

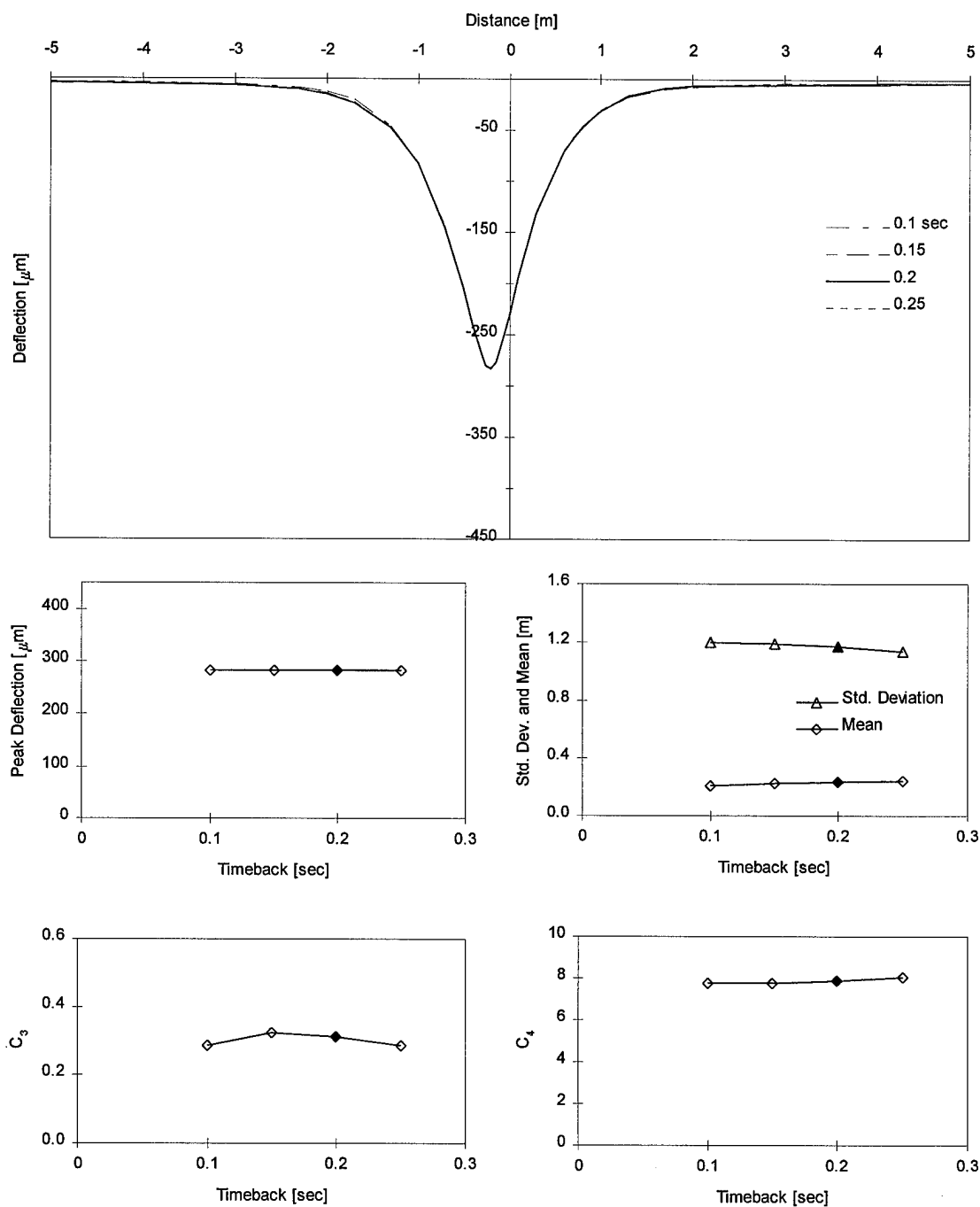


Figure 7-11. Sensitivity to *Timeback*.

7.2.5 *Avetime*

The parameter *avetime* represents the time step between each discrete load pulse. Because the response to each pulse must be computed separately, the number of pulses, N , considered within *timeback* has a significant influence on the required computation time. *Avetime* and *timeback* are related in the following manner.

$$N = \frac{\text{timeback}}{\text{avetime}}$$

To determine the best time increment between load pulses, four different values of *avetime* were analyzed, ranging from 0.5 to 4.0 msec. For the standard vehicle speed of 50 km/hr = 13.89 m/s (31 mph), these *avetime* values correspond to distances of 7 to 56 mm (0.3 to 2.2 in).

Figure 7-12 illustrates the calculated basins for all values of *avetime*. When *avetime* was equal to 4 msec, the basin was shifted slightly forward of the other three basins, however, the peak deflection was nearly identical to the others.

The peak deflection for the three smallest values of *avetime* was nearly identical, and when *avetime* was increased from 1 to 4 msec, the peak decreased by only 0.7%. The mean was constant for the two smallest values of *avetime*, but decreased by 8% as *avetime* was increased to 2 and 4 msec. The coefficient of skewness showed a slightly downward trend, decreasing a total of 20% from the minimum to maximum *avetime*. The coefficient of kurtosis was nearly constant for all *avetime*.

In general, the basin shapes and the statistical parameters converged to constant values as *avetime* was decreased. The computation time tripled when *avetime* was changed from 1.0 to 0.5 msec, with no significant improvement in accuracy. Therefore, the standard *avetime* value was set at 1 msec and used for the remainder of the analyses.

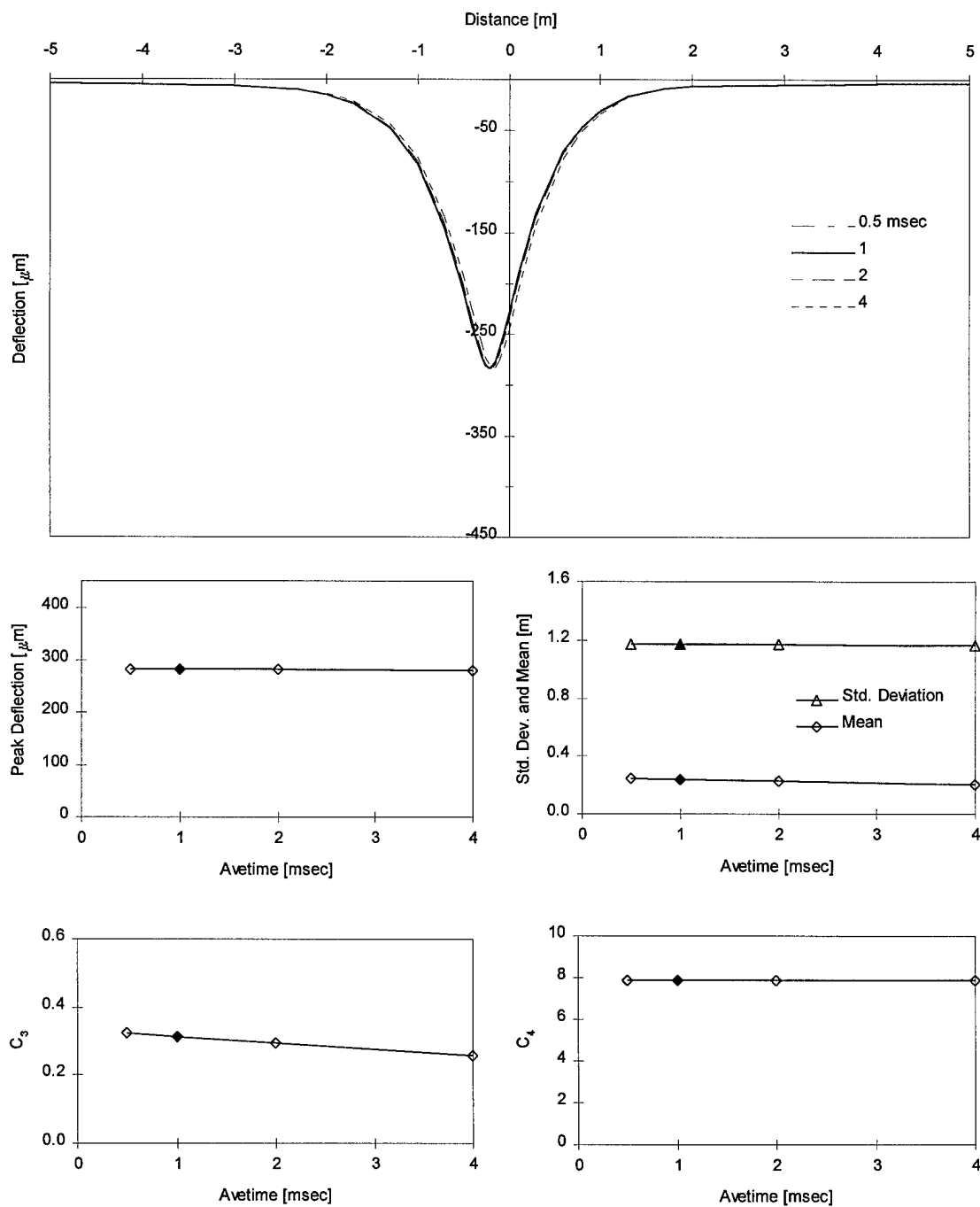


Figure 7-12. Sensitivity to *Avetime*.

7.3 Material Variables

The material variables describe the physical characteristics of the pavement structure. They are the properties that pavement tests are designed to determine because they can provide an indication of the strength and life expectancy of a pavement system. Current backcalculation schemes can only determine one or two types of these variables, so the others must be assumed or measured. Typically, the density, Poisson's ratio, and thickness of each layer are predetermined and the modulus is backcalculated. This section describes the deflection basin sensitivity to each of these material variables.

7.3.1 Density

The density of each pavement layer is most strongly related to the type and gradation of the material in each layer. AC layers have the highest densities because they are primarily composed of crushed stone aggregate with the voids between aggregate particles filled with asphalt cement. Subgrade layers generally have a lower density because they are often composed of fine-grained soil with very little aggregate. The gravel mixtures used in base course materials usually produce a density somewhere between the AC and subgrade.

Three density schemes were selected for testing and applied to all material layers: 10% less than standard, standard, and 10% greater than standard. Material layer densities can usually be estimated within a 10 or 20% error, so the limited range of densities was reasonable.

Figure 7-13 illustrates the calculated basins for all density combinations. There was no visible change in the deflection basins for either offset combination of densities.

The peak deflection for both offset density combinations was 0.4% less than that of the standard densities. The mean and standard deviation were essentially constant for all density combinations. The coefficient of skewness increased by 3% from the standard for both of the other density combinations. The coefficient of kurtosis decreased by only 0.4% from the lowest to the highest density combination.

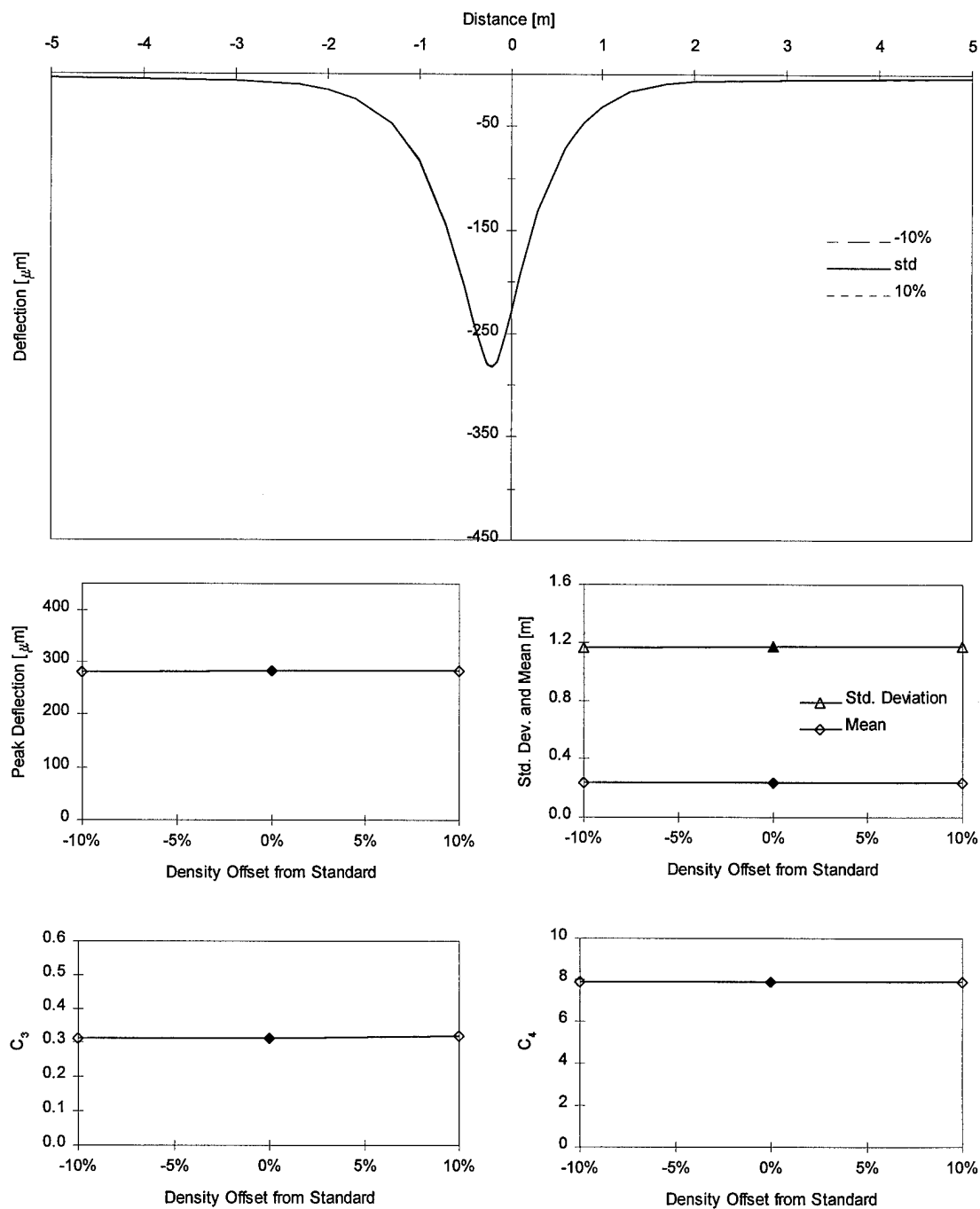


Figure 7-13. Sensitivity to Density.

This analysis shows that the deflection basin is extremely insensitive to the density of the material layers. Therefore, even if the densities are slightly in error, the predicted deflection basins will still be accurate.

7.3.2 Poisson's Ratio

Poisson's ratio relates the amount of lateral strain to the axial strain resulting from loading in the axial direction. Poisson's ratio, ν , also relates Young's modulus, E , to shear modulus, G , in an isotropic linear elastic material in the following manner.

$$G = \frac{E}{2(1 + \nu)}$$

Five combinations of Poisson's ratio in the layers were tested, as listed below.

Layer	1	2	3	4	5
AC	0.325	0.35	0.35	0.35	0.35
Base	0.35	0.35	0.40	0.40	0.40
Subgrade	0.35	0.35	0.40	0.45	0.45
Stiff Layer	0.35	0.35	0.40	0.35	0.45

The Poisson's ratio for each layer is usually estimated for backcalculation, but there is considerable range in the values that are commonly used. The values listed above were selected to represent typical values used for pavement deflection backcalculation.

Combination 4 was selected as the standard setting.

Figure 7-14 illustrates the calculated basins for all Poisson's ratio combinations. There was very little visible change in the basins; however, close examination reveals that the first three combinations resulted in slightly deeper and wider deflection basins. There was no visible difference between Combinations 4 and 5.

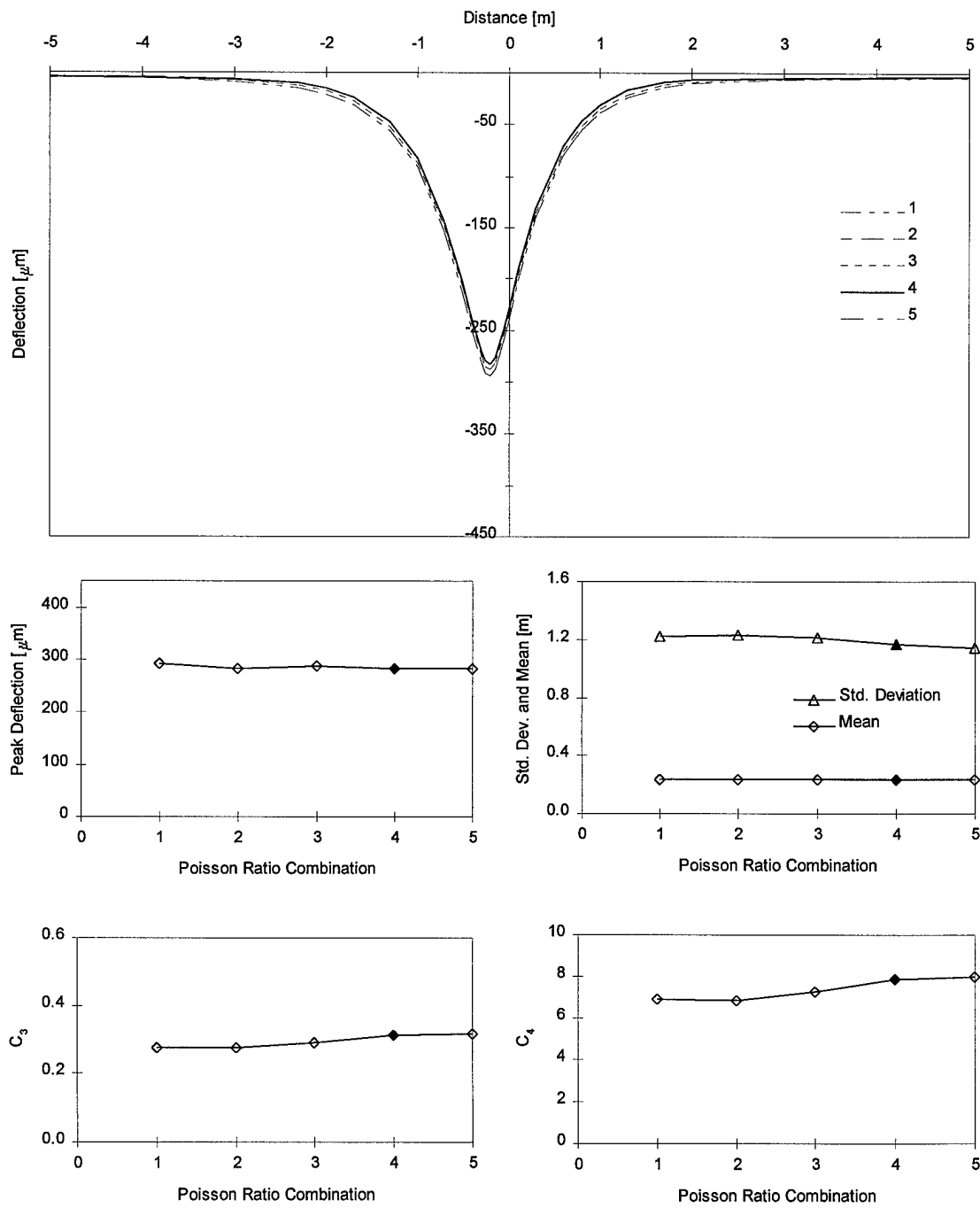


Figure 7-14. Sensitivity to Poisson's Ratio.

The peak deflection for Combination 1 was 4% greater than that of the standard, but all other combinations were within 2% of the standard. The mean was nearly constant for all combinations and Combination 2 produced the largest difference in standard deviation -- 6% greater than the standard. The coefficient of skewness was 12% less than the standard for Combinations 1 and 2, but closer to standard for Combinations 3 and 5, at 7% less and 1% greater, respectively. The coefficient of kurtosis was more than 12% less than standard for Combinations 1 and 2, and again, Combinations 3 and 5 were closer to standard.

This analysis shows that the deflection basin is fairly insensitive to the Poisson's ratio of the each layer. The tested range covered the extremes of assumed values, yet none of the parameters was more than 14% different than the standard. This indicates that Poisson's ratios should be carefully estimated but large errors will not result if the selected values are slightly in error.

7.3.3 Modulus

The modulus (or stiffness) of a material relates applied stress to resulting strain. In pavement testing and analysis, the modulus of each layer strongly influences the deflections produced by a wheel load. Large deflections result from large strains which ultimately cause the pavement materials to weaken and deteriorate. This section describes the deflection basin sensitivity to the modulus of each pavement layer.

7.3.3.1 *AC Modulus*

The modulus of the AC layer was assigned eight values between 250 and 2500 ksi (1724 and 17238 MPa), with the standard AC modulus set at 562.8 ksi (620.6 MPa). AC moduli can exceed 1000 ksi (6895 MPa) at asphalt temperatures below 10° C (50° F). At the other end of the scale, an AC modulus of 250 ksi can correspond to a distressed or a very warm pavement (>27° C (80° F)).

Figure 7-15 illustrates the deflection behavior calculated for each AC modulus.

The majority of the changes in the basin occurred within 0.8 m (2.6 ft) of the peak deflection, and deflections farther from the peak changed very little over the entire range of AC moduli. The basin became very pointed when the AC modulus was small, and much more rounded when the AC was extremely large. Close observation of the area about 1 m ahead and behind the peak showed that the deflections increased in this zone as the AC stiffness increased, resulting in a wider deflection basin.

The peak deflection decreased by 20% when the modulus was doubled from the initial value, and subsequent doublings resulted in 22% and 23% reductions from the previous value. The mean was nearly constant over the entire range of moduli, while the standard deviation steadily increased as the AC modulus increased, registering an 18% increase from the smallest to largest values. The coefficient of skewness slowly decreased by about 20% over the range of moduli, indicating that the deflection basin became more symmetric with increasing AC modulus. The coefficient of kurtosis rapidly decreased as the modulus increased, which should be expected from observing the relative peakedness of the basins.

7.3.3.2 *Base Modulus*

The modulus of the base layer was varied between 5 and 50 ksi (35 and 345 MPa), with the standard layer modulus set at 14.8 ksi (102 MPa). A base modulus of 5 ksi corresponds to a relatively soft fine-grained soil and a modulus of 50 ksi may be achieved with a well-graded, well-compacted crushed stone mixture. Most base course materials have a modulus between 12 and 30 ksi (83 and 207 MPa).

Figure 7-16 illustrates the deflection behavior calculated for each base modulus value. The base course modulus influenced deflections within about 1.2 m (3.9 ft) of the peak deflection. Almost no change in the basins was visible outside this zone.

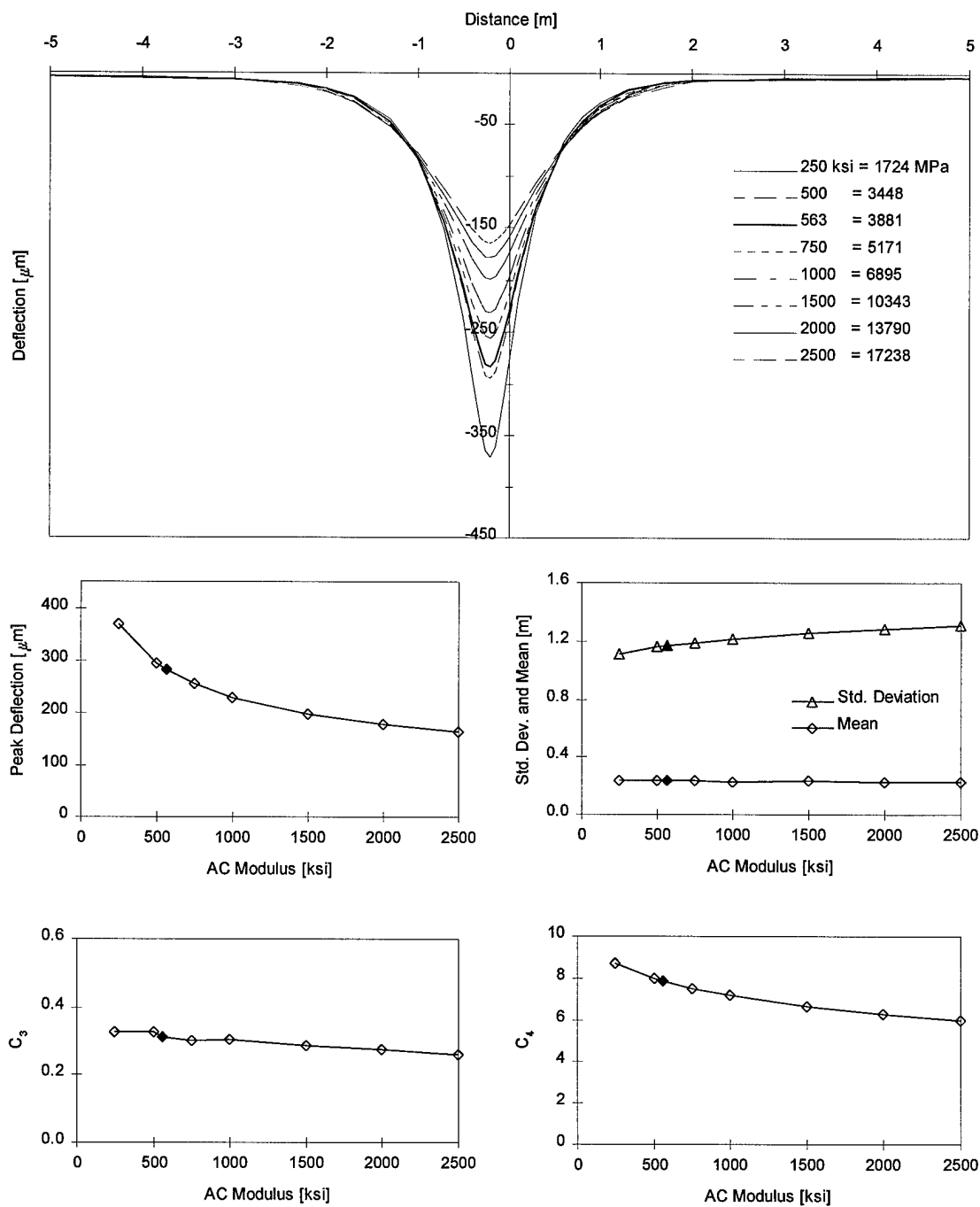


Figure 7-15. Sensitivity to AC Modulus.

The peak deflection increased by 20% when the base modulus was reduced from the standard by 65%. The peak deflection decreased by 28% when the base modulus was increased from the standard to the maximum. The mean value was essentially constant for all base moduli, while the standard deviation increased by 20% from the minimum to maximum modulus tested. The coefficient of skewness slowly decreased by 15% over the range of moduli, indicating that the deflection basin becomes more symmetric as the modulus increases. The coefficient of kurtosis increased by 18% from the standard to the minimum, but only decreased by 19% from the standard to the maximum modulus.

7.3.3.3 *Subgrade Modulus*

The modulus of the subgrade layer was varied between 3 and 25 ksi (21 and 173 MPa), with the standard layer modulus set at 10.2 ksi (70.2 MPa). A subgrade modulus of 3 ksi corresponds to a very soft clay or very loose sand, and a modulus of 25 ksi to a very dense well-graded soil. The range of subgrade moduli typically encountered is highly dependent on the local soil conditions. Desirable subgrades for highway construction generally have moduli greater than about 12 ksi (83 MPa).

Figure 7-17 illustrates the deflection behavior calculated for each value of subgrade modulus. The subgrade modulus influences deflections over a wide area of the pavement, stretching nearly 2 m (6.6 ft) in either direction from the wheel. The general shape of the basin stayed fairly consistent in the upper range of moduli. Heaving (positive deflections) was predicted about 3 m (9.8 ft) behind the wheel for very weak moduli of 3 ksi (21 MPa) or less.

The peak deflection rapidly decreased as the modulus increased from the minimum to the standard. Above the standard, the peak deflections decreased nearly

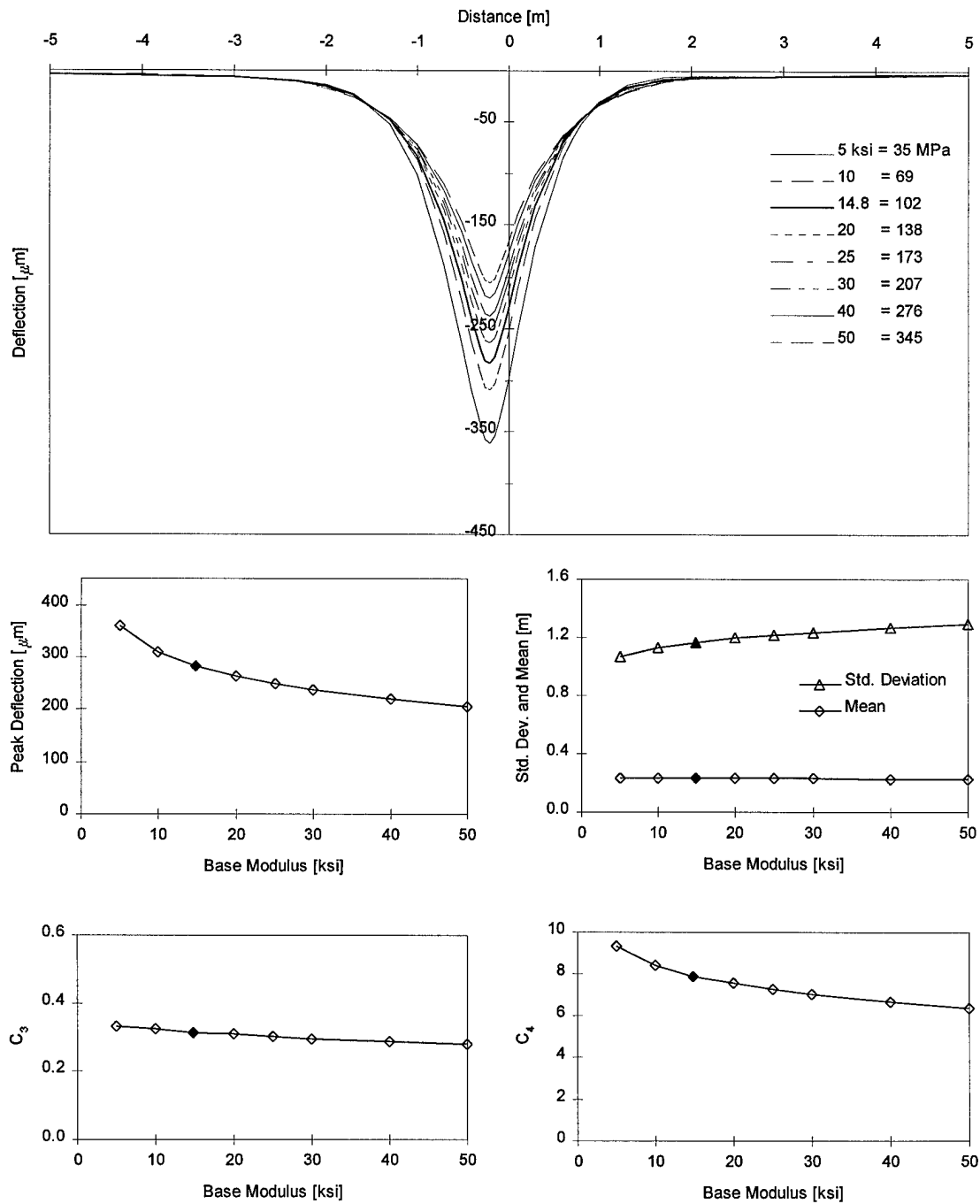


Figure 7-16. Sensitivity to Base Modulus.

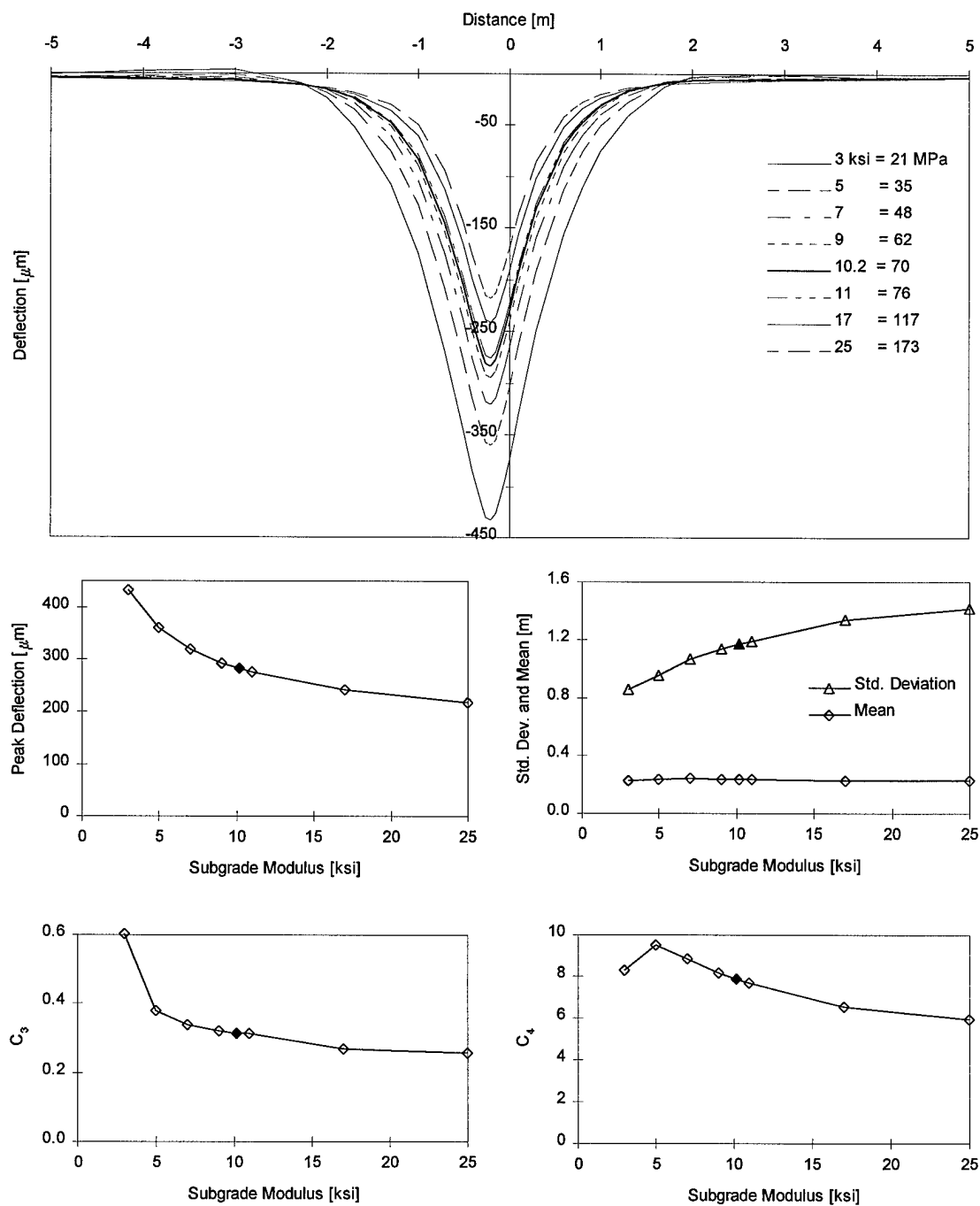


Figure 7-17. Sensitivity to Subgrade Modulus.

linearly, declining about 4 μm for every 1 ksi increase in modulus. The mean increased slightly over the 3 to 10 ksi range, but then became constant as the modulus increased. The standard deviation increased by 20 % when the modulus was doubled from 5 to 10 ksi, but then increased less rapidly from the standard to the maximum modulus. The coefficient of skewness sharply dropped by nearly 40% when the subgrade modulus was increased from 3 to 5 ksi; thereafter, it decreased slowly over the middle range of moduli. The coefficient of kurtosis posted a 15% gain when the modulus increases from 3 to 5, but steadily decreased as the modulus rose to 25 ksi.

7.3.3.4 *Stiff Layer Modulus*

The modulus of the stiff layer was varied between 5 and 1000 ksi, with the standard modulus set at 40 ksi. A modulus of 5 ksi corresponds to a soft clay or very loose sand deposit -- not exactly a "stiff" layer, but thick deposits of these materials do exist. Moduli approaching 1000 ksi may represent bedrock or a frozen groundwater layer.

Figure 7-18 illustrates the deflection behavior calculated for each stiff layer modulus. The stiff layer modulus had a wider influence on the deflection basin than any other layer modulus. Visible deflections extended beyond 5 meters from the wheel when the modulus was equal to 5 and 10 ksi. As the stiff layer modulus was increased above 25 ksi, the basins began to converge to a consistent shape. Heave was predicted about 1.5m in front of the wheel and 2m behind the wheel when the modulus reached 1000 ksi.

The peak deflection initially decreased rapidly by 14% when the modulus was doubled from 5 to 10 ksi; above 25 ksi, the decrease was nearly linear. The mean noticeably increased as the modulus increased from 5 to 40 ksi, and then leveled out thereafter. The standard deviation was very sensitive to the stiff layer modulus, decreasing by 65% over the range from 5 to 75 ksi. The coefficient of skewness steadily increased over the range of moduli examined. The coefficient of kurtosis rapidly increased as the modulus increased, gaining 245% from the minimum to the maximum modulus examined.

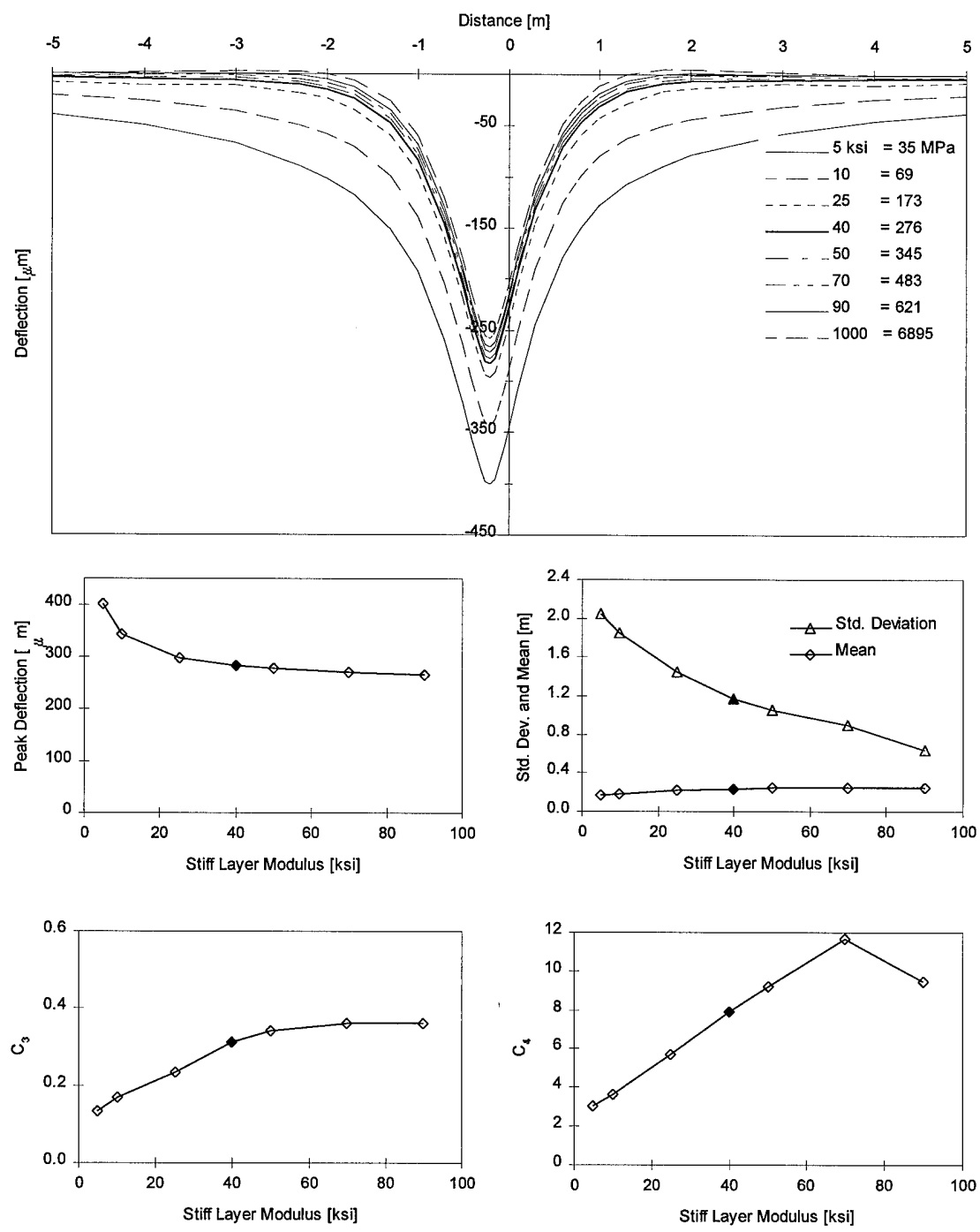


Figure 7-18. Sensitivity to Stiff Layer Modulus.

7.3.3.5 Discussion

The deflection basin produced by a rolling wheel is very sensitive to the modulus of each material layer. As expected, the modulus of the deeper material layers influenced a wider zone of the deflection basin. Very soft subgrade and stiff layers produce such a wide deflection basin that they may be very difficult to measure because the undeflected reference measurement could easily be inside the deflection basin. Overall, the peak deflection and the standard deviation are the most consistently sensitive statistical parameters for each layer modulus.

7.3.4 Thickness

The thickness of each pavement layer is a key design decision when constructing new pavements. For pavement testing and analysis, the thickness is an important input for parameter backcalculation of layer moduli. Typically, the layer thickness is determined from drilled cores, construction specifications, or occasionally field tests. The sensitivity of the dynamic deflection basin to layer thickness may be such that the layer thicknesses can be backcalculated with the layer moduli. This section investigates the deflection basin sensitivity to the thickness of each layer.

7.3.4.1 AC Thickness

The thickness of the AC layer was varied between 50 and 600 mm (2 and 24 in), with the standard layer thickness at 137 mm (5.4 in). AC layers as thin as 50 mm may be used for a temporary road, and 600 mm of asphalt could be specified for a cargo aircraft runway. Many highway AC layers are between 150 and 300 mm (5.9 and 11.8 in) thick.

Figure 7-19 illustrates the computed deflection behavior for each AC thickness. The largest changes in the basin occurred within 0.8 m (2.6 ft) of the peak deflection, where the deflections decreased as the AC thickness increased. However, the deflections outside this zone actually *increased* as the AC thickness increased. At large thicknesses, the basin began to show a distinctive rounded peak within 0.2 m (0.7 ft) of the peak deflection; beyond the wheel contact area, the basin became very broad.

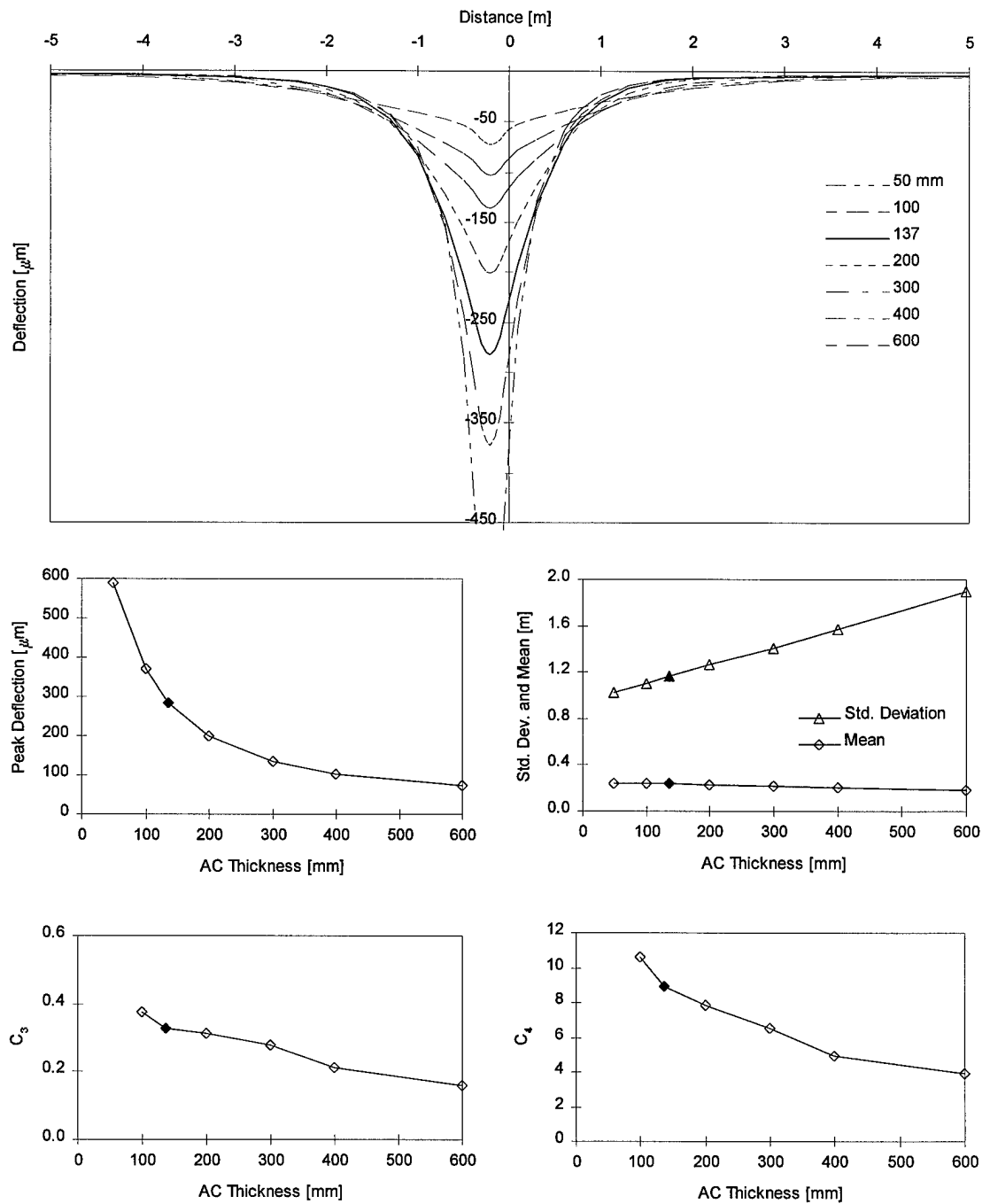


Figure 7-19. Sensitivity to AC Thickness.

The peak deflection decreased rapidly as the thickness increased from 50 to 200 mm, but then decreased by 64% when the thickness was tripled from 200 to 600 mm. The mean decreased slightly from the minimum to maximum thickness, while the standard deviation increased nearly linearly with increasing AC thickness. The coefficient of skewness decreased by about 0.06 for every 100 mm increase in thickness. In a manner consistent with the shapes of the basins, the coefficient of kurtosis rapidly decreased as the thickness increased.

7.3.4.2 *Base Thickness*

The thickness of the base layer was varied between 200 and 800 mm (8 and 31.5 in), with the standard layer thickness at 330 mm (13 in). A 200 mm thickness can be used when the subgrade is fairly competent, while a thickness of 800 mm might be required when the subgrade is weak or soft. Typical base thicknesses range from 150 to 600 mm (6 to 24 in).

Figure 7-20 illustrates the deflection behavior calculated for each base thickness. The only visible changes in the deflection basins occurred in the zones 1 to 2 m (3.3 to 6.6 ft) ahead and behind the peak deflections. Very small changes were also observed at the peak of the basin.

The peak deflection was nearly constant, only decreasing 3% over the entire range of thicknesses studied. The mean was also nearly constant; the standard deviation was constant for thicknesses between 200 and 600 mm, but then jumped by 9% when the thickness was increased from 600 to 800 mm. The coefficient of skewness was nearly constant, with a slight dip observed for the 400 mm thickness. The coefficient of kurtosis decreased nearly linearly by 0.056 for every 100 mm increase in thickness.

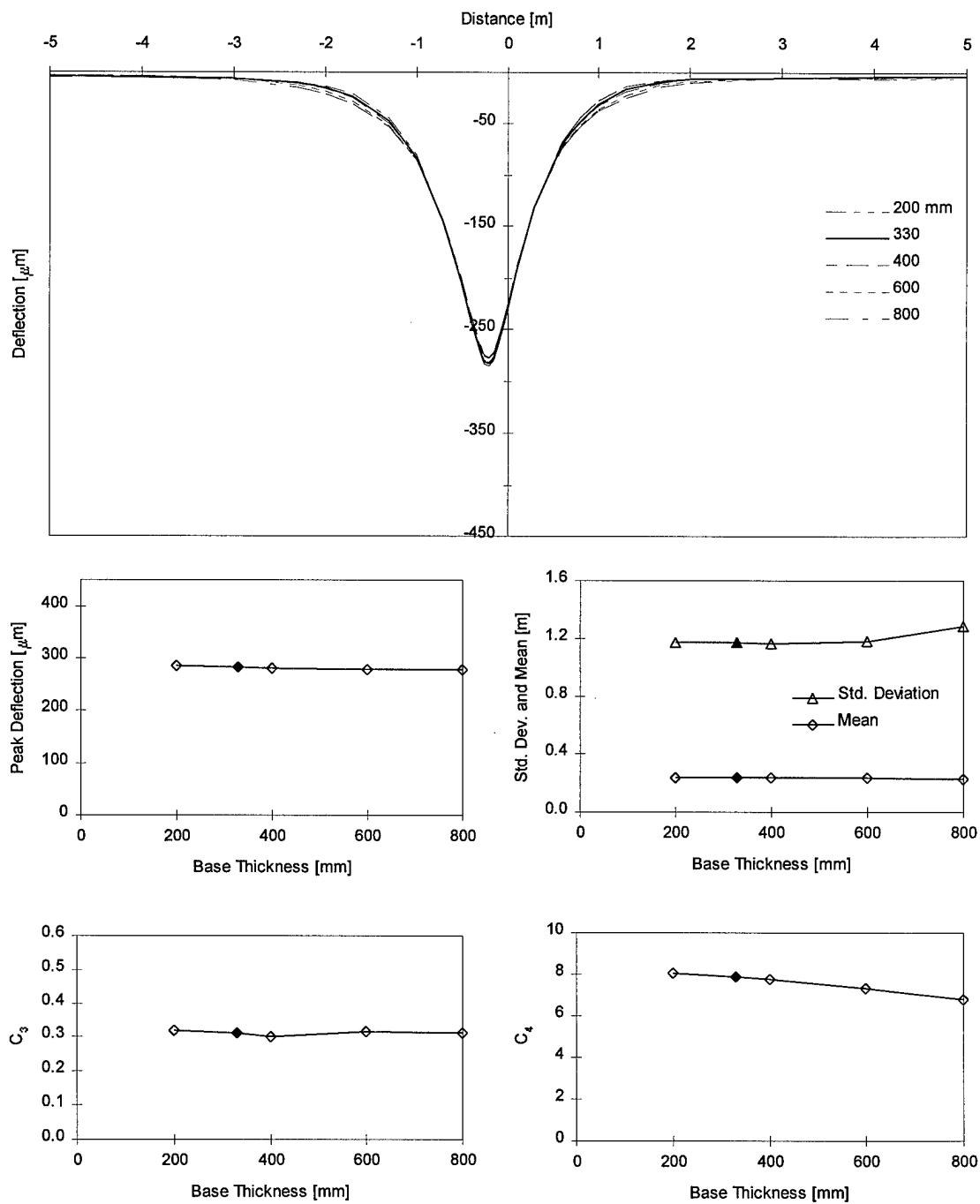


Figure 7-20. Sensitivity to Base Thickness.

7.3.4.3 *Subgrade Thickness*

The thickness of the subgrade layer was varied between 0.5 and 2.0 m (20 and 79 in), with the standard layer thickness at 1.17 m (46 in). The subgrade thickness of an actual pavement system depends on the local site conditions. The bottom of the subgrade is defined by the top of the stiff layer; therefore, the thickness is entirely determined by the depth to bedrock or the ground water table.

Figure 7-21 illustrates the deflection behavior calculated for each subgrade thickness. As the subgrade thickness increased, the deflection basin became wider and deeper, because the underlying stiff layer was deeper below the pavement surface.

The peak deflection decreased by 10% when the thickness was halved from 1.0 to 0.5 m, and increased by 10% when the thickness was doubled from 1.0 to 2.0 m. The mean was also nearly constant over the range of thicknesses; the standard deviation decreased by 10% when the thickness was halved from 1.0 to 0.5 m, but decreased by only 7.5% when the thickness doubled from 1.0 to 2.0 m. The coefficient of skewness was largest for the standard thickness, and decreased by 32% when the thickness was increased to 2.0 m. The coefficient of kurtosis showed the same trend as the skewness, with the standard thickness exhibiting the largest kurtosis.

7.3.4.4 *Stiff Layer Thickness*

The thickness of the stiff layer was varied between 5 and 40 m (16.4 and 131 ft), with the standard layer thickness at 10 m (33 ft). Because the material below the stiff layer is modeled as a halfspace with the same properties as the stiff layer, the thickness of the subgrade only needs to be large enough to ensure an accurate solution.

Figure 7-22 illustrates the deflection behavior calculated for each stiff layer thickness. Only the basin calculated for a stiff layer 5 m thick was visibly different than the other basins.

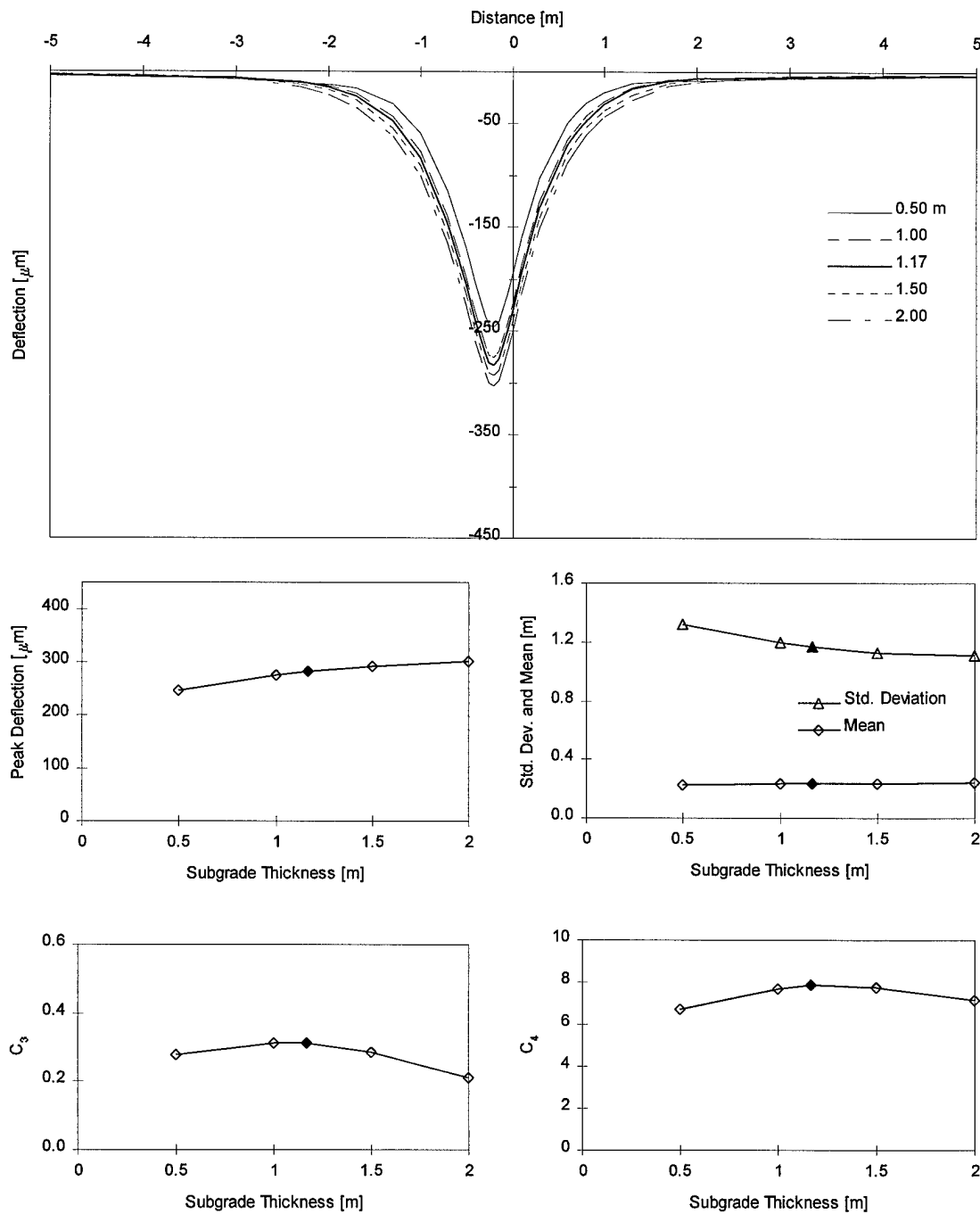


Figure 7-21. Sensitivity to Subgrade Thickness.

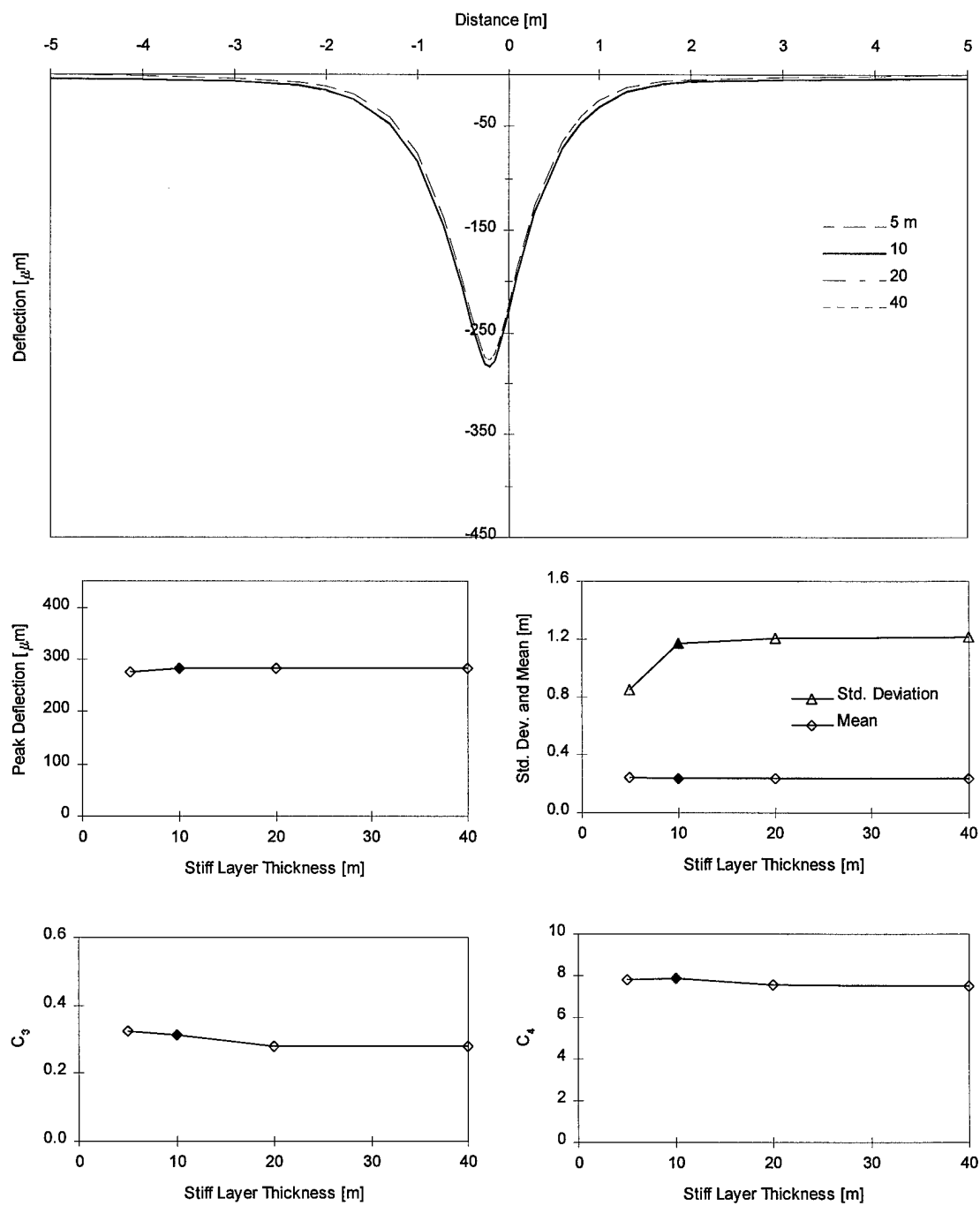


Figure 7-22. Sensitivity to Stiff Layer Thickness.

The peak deflection for the 5 m layer was 2.5% less than the deflection for the standard (and all other) thickness. The mean was constant for all cases; the standard deviation was 30% less than that of the standard when the stiff layer thickness was 5 m, and only increased 3% above standard when the stiff layer thickness was increased to 40 m. The coefficient of skewness decreased by 13% when the thickness was increased from 5 to 20 m, but was constant for thicker layers. The coefficient of kurtosis was largest for the standard thickness, and decreased by 5% when the thickness was increased to 40 m.

7.3.4.5 Discussion

The deflection basin produced by a rolling wheel is very sensitive to the thickness of the AC layer, and somewhat sensitive to the thickness of the subgrade layer. However, the base thickness had very little influence on the deflection basin. The standard deviation and coefficient of kurtosis were very sensitive to the AC thickness, but not to the thicknesses of the other layers. The standard stiff layer thickness of 10 m was shown to be an acceptable choice because the basin shape did not visibly change as the thickness was increased.

7.3.5 Combinations of Thickness and Modulus

Most pavement backcalculation programs cannot determine both the thickness and modulus of each layer. Generally the thickness is measured or assumed, and the modulus is backcalculated. This section examines the sensitivity of the deflection basin to both modulus *and* thickness.

The static backcalculation program EVERCALC 4.0 was used to determine the moduli of pavement layers for given input thicknesses. By specifying the same static deflection basin while adjusting the thickness of only one layer, the modulus of all of the layers was backcalculated. With this scheme, a stiff, thin layer and a soft, thick layer would produce identical static deflection basins. In all cases, the stiff layer was held constant at 1.64 m (64.4 in) below the pavement surface.

7.3.5.1 AC Thickness/Modulus

Five combinations of AC thickness and modulus, listed in Table 7-1, were examined. The modulus of the base and subgrade layers was adjusted for each case to produce identical static deflection basins.

Table 7-1. AC Thickness/Modulus Combinations.

	-50%	-25%	Standard	10%	20%
AC Thickness [mm]	69	103	137	171	206
AC Modulus [MPa]	15.1	4.7	2.2	1.3	0.9

Figure 7-23 illustrates the deflection behavior calculated for each AC thickness/modulus combination. The only visible changes in the deflection basin were observed within about 0.2 m (0.7 ft) of the peak deflection. In this zone, the peak deflection increased with increasing AC thickness.

The peak deflection steadily increased as the AC thickness increased, gaining 17% from the minimum to the maximum thickness. The mean and standard deviation did not change appreciable over the range of thicknesses. The coefficient of skewness increased slightly with AC thickness, gaining 6% from the minimum to maximum thickness. The coefficient of kurtosis was nearly constant for all but the thinnest AC, which was 2.7% less than the standard.

7.3.5.1 Base Thickness/Modulus

Five combinations of base thickness and modulus, listed in Table 7-2, were examined. The modulus of the AC and subgrade layers was adjusted for each case so that the static deflection basin remained constant.

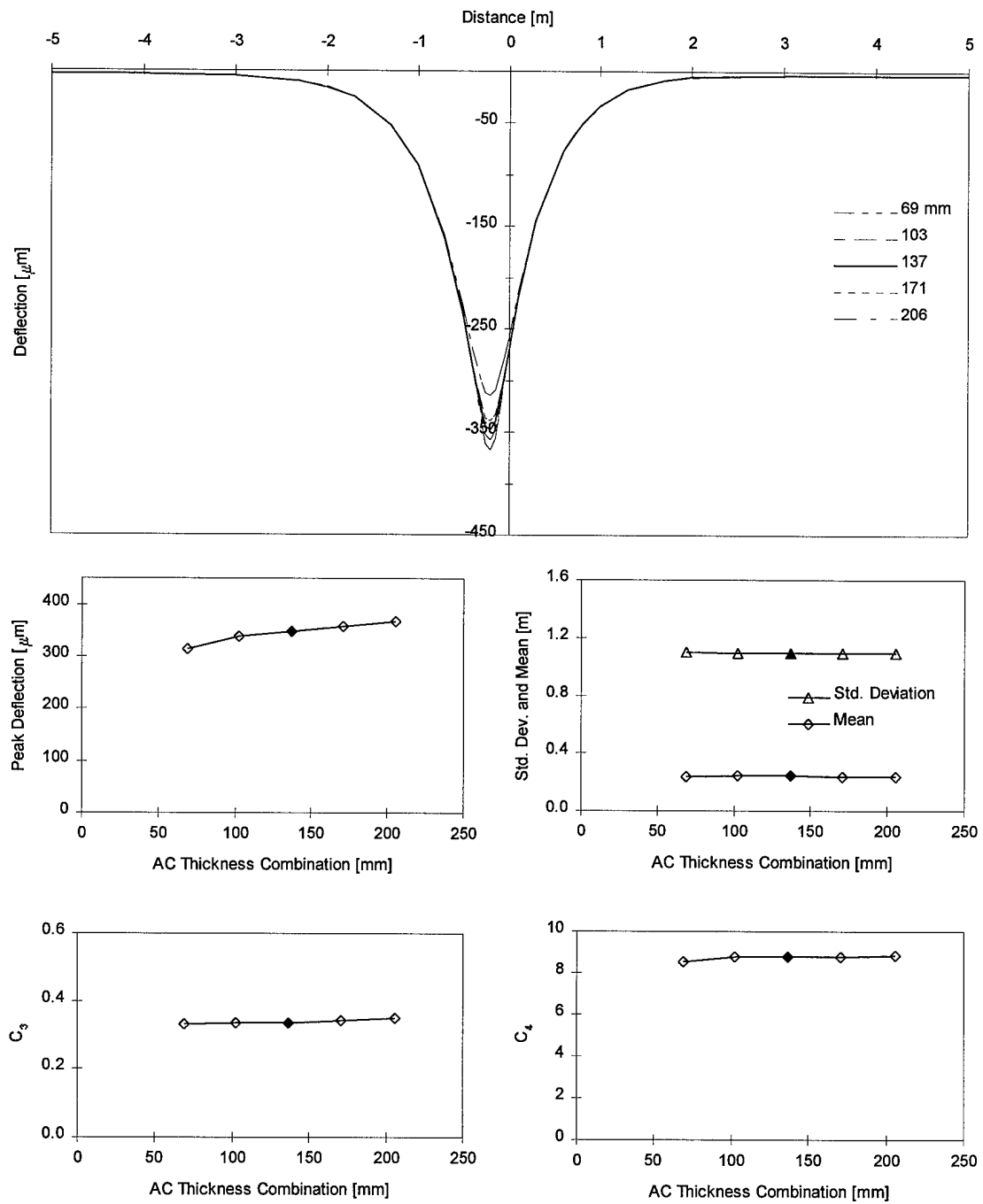


Figure 7-23. Sensitivity to AC Thickness/Modulus.

Table 7-2. Base Thickness/Modulus Combinations.

	-50%	-25%	Standard	10%	20%
Base Thickness [mm]	165	247	330	413	495
Base Modulus [MPa]	0.343	0.162	0.106	0.101	0.092

Figure 7-24 illustrates the deflection behavior calculated for each base thickness/modulus combination. In this case, the deflections only changed significantly within 0.1 m (3.9 in) of the peak. As the base thickness increased, the peak deflection decreased, most significantly when the base was 50% thinner than the standard.

The peak deflection was non-linearly related to the base thickness. The peak deflection for the thinnest base was 7% greater than the standard, but the peak deflection for the thickest base was only 2% less than the standard. The mean and standard deviations were nearly constant for all thickness/modulus combinations. The coefficient of skewness decreased slightly as the base thickness increased, declining only 5% overall. The coefficient of kurtosis also decreased over the range of base thickness/modulus combinations, declining only 4% overall.

7.3.5.2 Discussion

The changes in deflection basins for both analyses were surprisingly small, considering the wide range of thicknesses used. The AC and base layer showed opposite trends for the peak deflection, skewness, and kurtosis change with thickness. For the AC layer, all three parameters increased as the AC thickness increased. For the base layer, all three parameters decreased as the base thickness increased. However, the absolute changes in basins were so small that it appears that backcalculating both the modulus and thickness may be difficult. The results suggest that any attempt at simultaneous backcalculation of modulus and layer thickness will require accurate definition of the deepest part of the deflection basin.

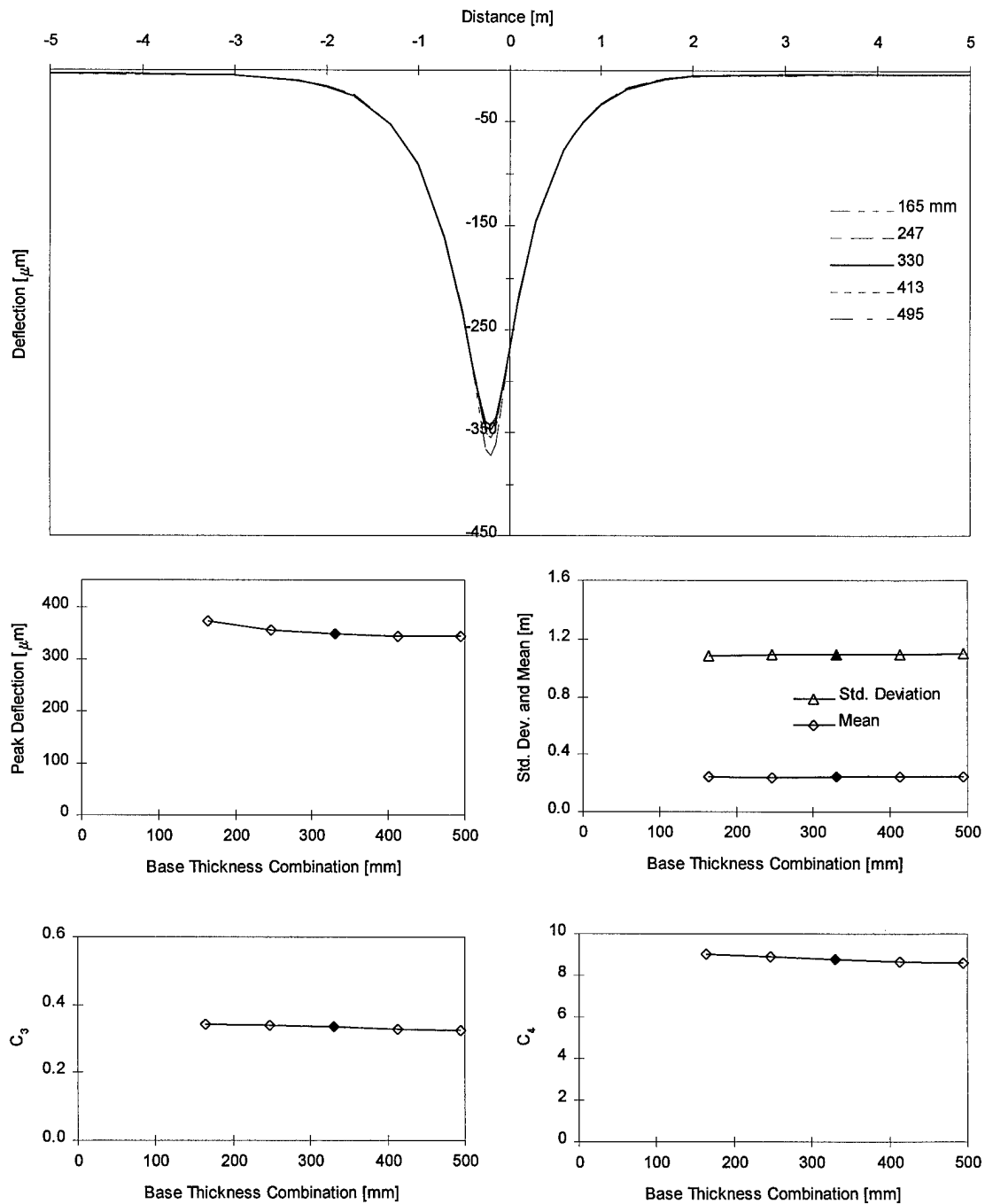


Figure 7-24. Sensitivity to Base Thickness/Modulus.

7.4 Loading Variables

The loading variables are a function of the vehicle speed, weight, and tire pressure. The deflection basin sensitivity to these parameters may help determine the operating conditions that would provide the most useful information about the pavement. Additionally, the optimum location for deflection sensors might be determined from by examining these parameters.

7.4.1 Wheel Load

The wheel load was varied between 3,000 and 11,000 lb (13,344 and 48,928 N), with the standard layer thickness at 5,540 lb (24,642 N). The tire pressure was held constant at 90.0 psi (620.6 kPa); therefore, the loaded area was adjusted so that constant stress was applied for all loads. A 3,000 lb load corresponds to a lightly loaded panel truck, and an 11,000 lb load represents an overloaded wheel (9,000 lb is the limit in most states).

Figure 7-25 illustrates the computed deflection behavior for each wheel load. As the load increased, the basin became consistently deeper and wider.

The peak deflection linearly gained about 50 μm with each 1,000 lb increase in wheel load. The mean was constant for all loads, and the standard deviation was nearly constant as well, gaining only 0.9% from the minimum to maximum load. The coefficient of skewness was also nearly constant, and the coefficient of kurtosis showed a slightly decreasing trend as the load increased.

The deflection basin behavior as the load increased was exactly as would be expected for a linear-elastic analysis. When the load is doubled, the deflections at all locations double. This is confirmed by consistency of all the statistical parameters.

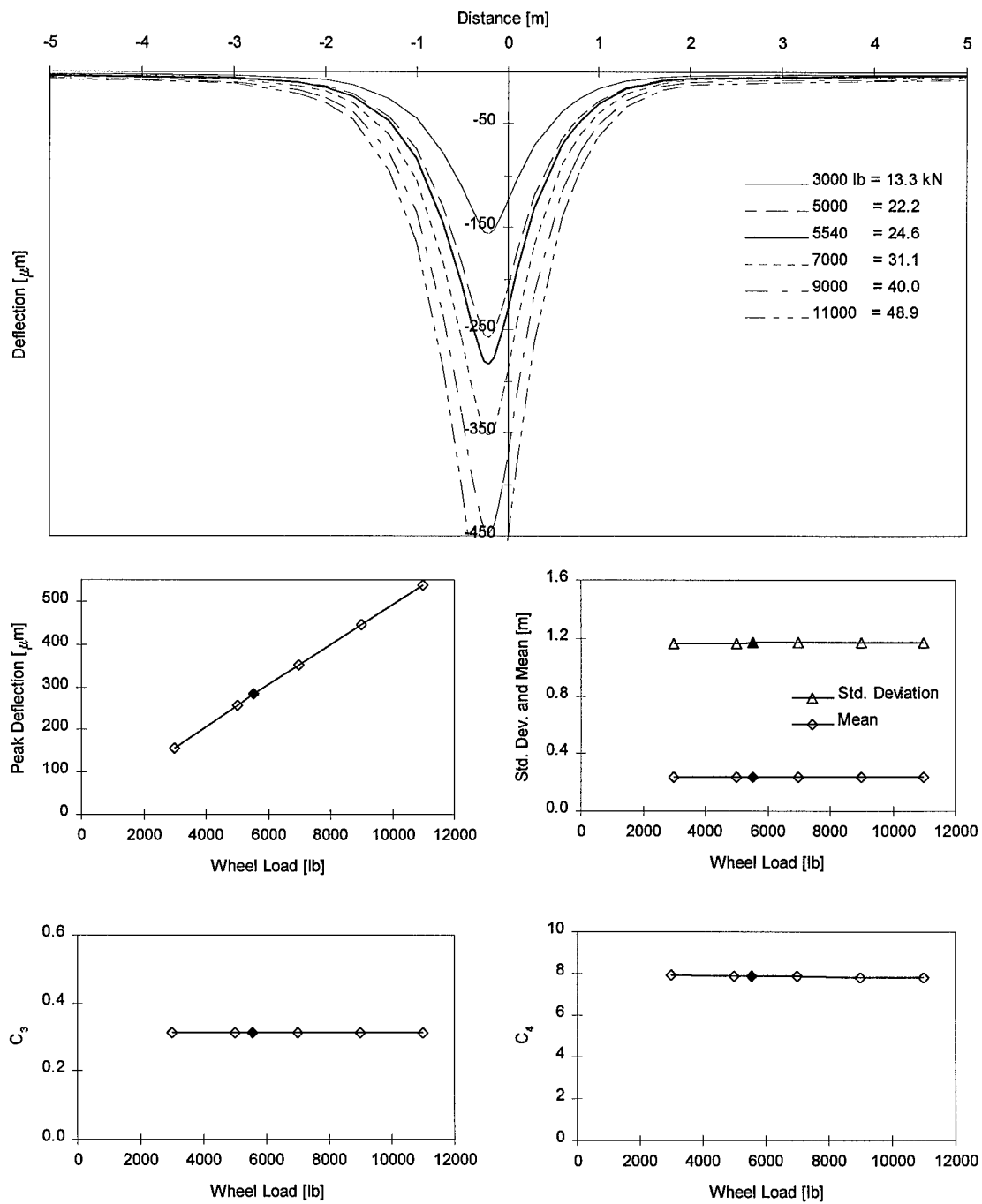


Figure 7-25. Sensitivity to Wheel Load.

7.4.2 Tire Pressure

Four tire pressures were examined, ranging from 30 to 120 psi (207 to 827 kPa). The standard value of 90.0 psi (620.6 kPa) is a typical pressure for heavy trucks. Lower truck tire pressures are occasionally used when heavy loads are carried across weak pavement structures, such as temporary gravel roads. Higher tire pressures are used because they improve gas mileage at high speeds. In each case examined in this study, a constant wheel load was applied and the load radius was adjusted accordingly.

Figure 7-26 illustrates the deflection behavior calculated for each tire pressure. As the load increased, the basin became slightly deeper, but only the area within about 0.2 m (7.9 in) of the peak deflection changed. This zone of change may reflect the size of the load radius. The radius of the loaded area was 0.195 m (7.7 in) at 30 psi (207 kPa), but reduced to 0.097 m (3.8 in) at 120 psi (827 kPa). These radii correspond to the areas of the basins that actually change with the tire pressure.

The peak deflection decreased by 6% when the tire pressure was doubled from 30 to 60 psi, but only increased by 3% when the pressure was doubled again. The standard deviation decreased slightly as the pressure increased, but the mean remained essentially constant. The skewness also was constant for all the tire pressures. The coefficient of kurtosis very slightly increased as the tire pressure was increased, reflecting the smaller contact area at higher tire pressures.

The deflection basin was not very sensitive to tire pressure. However, this analysis does show that higher pressures produce larger deflections directly under the loaded area, supporting the use of low tire pressures on weak roads.

7.4.3 Vehicle Speed

The wheel speed was varied between 10 and 90 km/hr (6 and 56 mph). The speed was adjusted by spacing the same load pulses further apart. In this manner, the same loading was applied over time for all speeds, but the loading was significantly changed over space.

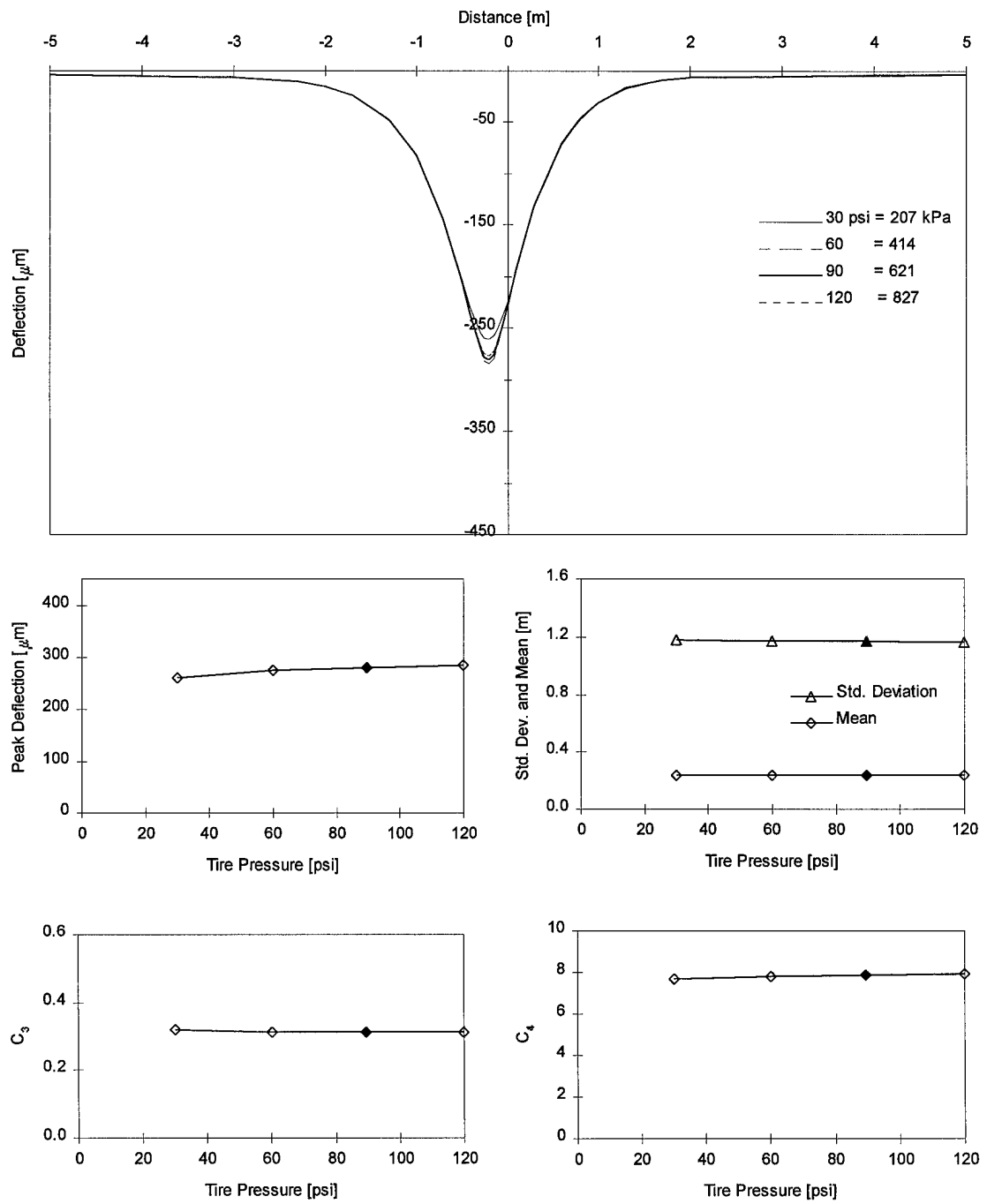


Figure 7-26. Sensitivity to Tire Pressure.

Figure 7-27 illustrates the computed deflection behavior for each wheel speed. As the velocity increased, the peak deflection steadily reduced and the location of the peak moved steadily farther behind the wheel. At the slowest speed, the basin was nearly symmetrical underneath the wheel.

The peak deflection linearly decreased by 11 μm for each 10 km/hr increase in speed. The mean was directly proportional to the speed, increasing (moving farther behind the wheel) 100 mm for each 10 km/hr increase. The standard deviation increased slightly with speed, showing a larger increase per interval at higher speeds. The coefficient of skewness increased in a very non-linear fashion. Initially, the coefficient of skewness was only 0.08, indicating the basin was nearly symmetric about the mean. As the speed increased, the coefficient of skewness increased, but less with each increment, eventually leveling off at about 0.35. The coefficient of kurtosis steadily decreased about 0.2 for each incremental increase in speed.

For this variable, the statistical parameters are very useful for identifying the nuances of the deflection basin changes. The linear changes in mean and peak deflection reflect the manner in which the vehicle velocity influences the load pulses over space (described in Chapter 4). The coefficient of skewness shows that as the speed increases, the basin becomes less symmetric. Notice that if the skewness curve were extended to zero vehicle velocity, it would pass very nearly through zero, indicating the static basin is perfectly symmetric.

7.4.4 Pulse Duration

As described in Chapter 4, the standard pulse duration of 30 msec was selected because it has commonly been used by previous researchers, and because it closely approximates the load duration for an FWD test. Chapter 4 also showed that a constant line load could be applied using any duration pulse, as long as the amplitude of the pulse was adjusted accordingly. This section examines how the load pulse selection can influence the calculated deflections.

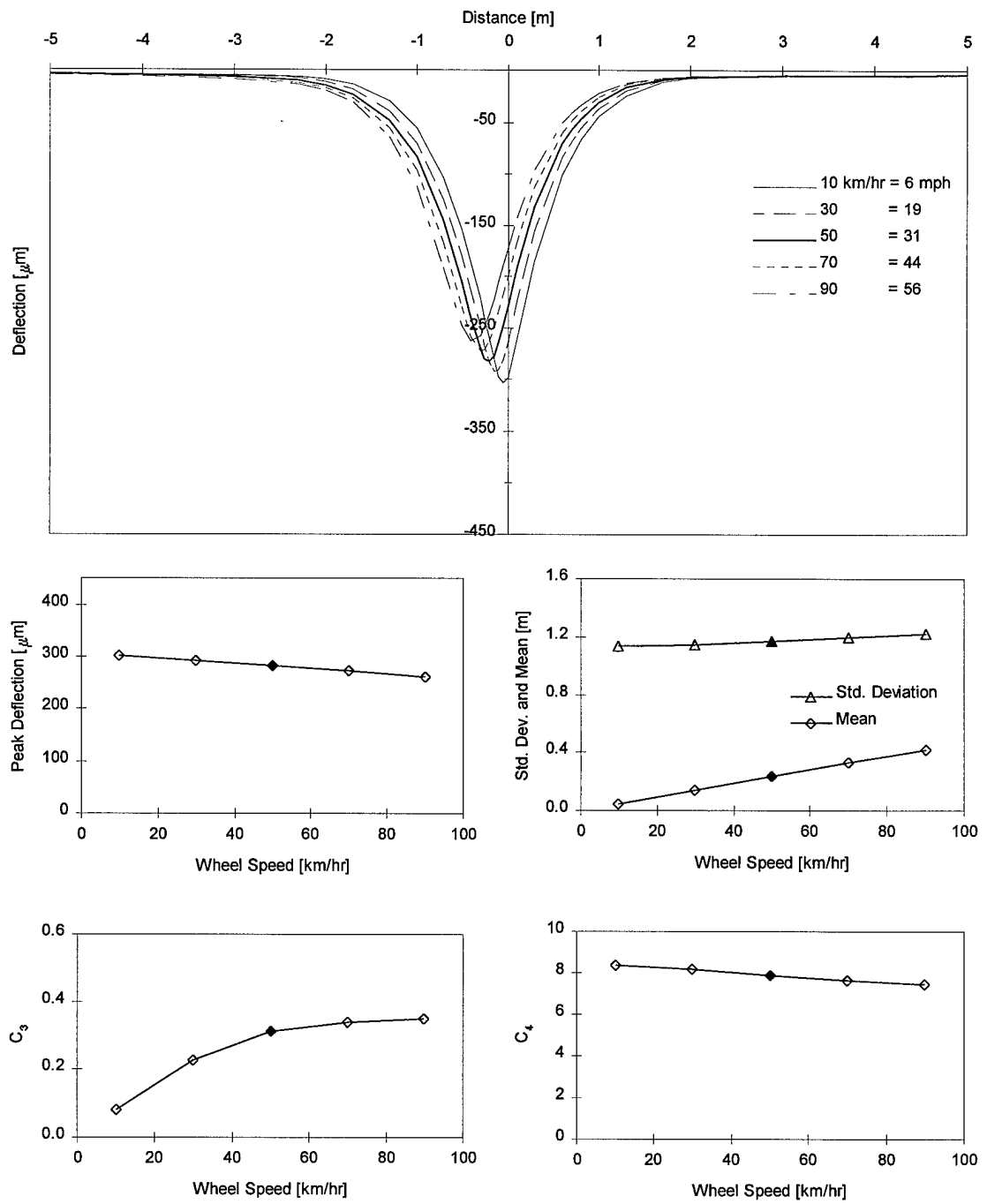


Figure 7-27. Sensitivity to Wheel Speed.

Five different load pulses were examined, ranging between 10 and 50 msec. Based on Barksdale's (1971) analysis, a 10 msec pulse corresponds to a wheel velocity of over 75 km/hr (47 mph), and a wheel traveling at 5 km/hr (3 mph) would produce a 50 msec pulse. However, the wheel velocity was held constant for these analyses -- only the pulse duration was adjusted.

Figure 7-28 illustrates the computed deflection behavior for each pulse duration. The basin became deeper and moved farther behind the wheel as the pulse duration increased.

The peak deflection consistently decreased by 10 μm for each incremental change in pulse duration. The mean consistently increased (moved farther behind the wheel) as the pulse duration was increased and the standard deviation increased the most at the longest pulse durations. The coefficient of skewness increased almost linearly from 0.12 to 0.47 over the range of pulse durations. The coefficient of kurtosis was nearly constant for the three shortest durations, and then reduced by 7.5% as the duration increased from 30 to 50 msec, reflecting the flatter peaks of the longer duration basins.

This analysis clearly shows that the deflection basin is sensitive to the pulse duration. It seems that the appropriate duration should be selected as a function of the vehicle speed. However, when this is done, the resulting deflections do not match the trend illustrated in the previous examination of wheel speed. This phenomenon can be attributed to the manner in which the dynamic response due to a load pulse is used in BASIN. Shorter duration, larger amplitude pulses at the smallest radii have a greater contribution to the total deflection than longer duration, smaller amplitude load pulses applied at the same distances.

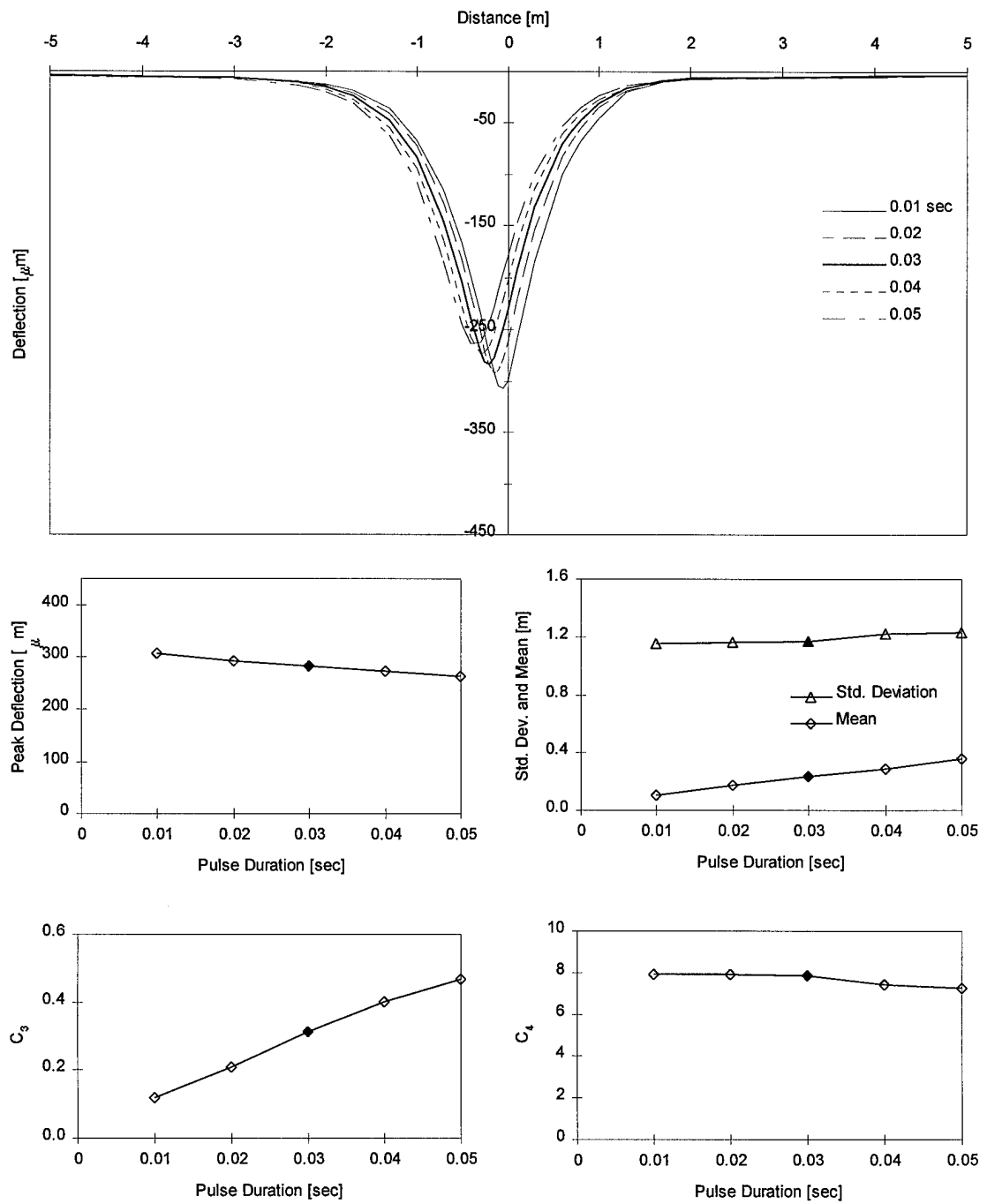


Figure 7-28. Sensitivity to Load Pulse Duration.

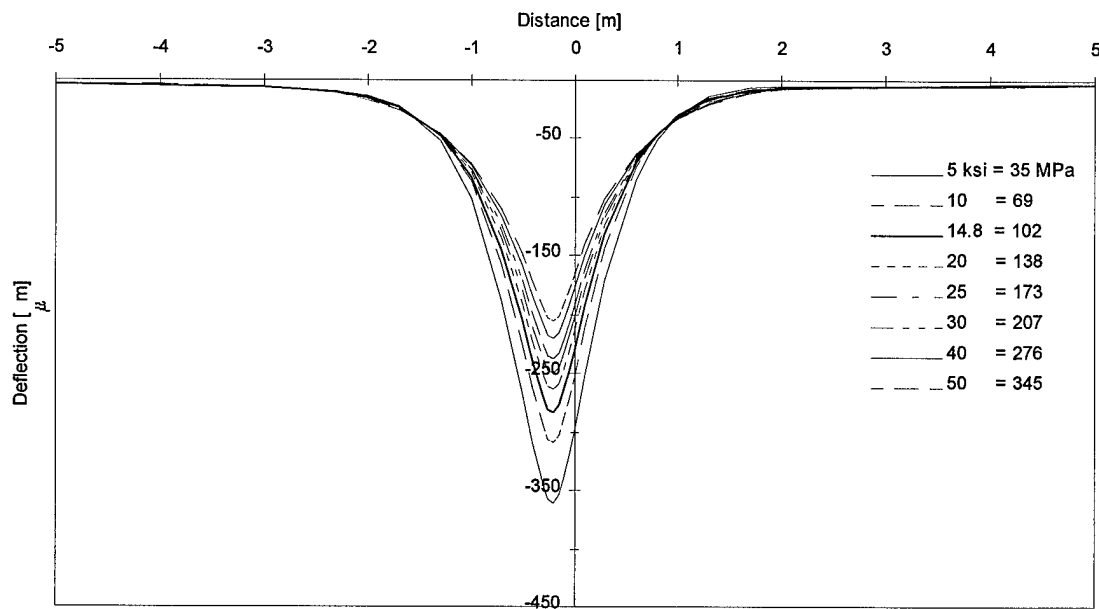
7.5 Transverse Deflection Profile

All of the previous results were based on longitudinal deflection basins, which show the pavement deflections along the direction of travel. However, the basin produced by a moving wheel load is clearly three-dimensional. This section examines the deflections in the transverse direction (perpendicular to the direction of travel) for one parameter, base modulus. The deflection basin at a transverse plane intersecting the wheel path 0.2 m (7.9 in) behind the wheel was calculated for each value of the base modulus. This plane was selected to ensure the peak deflection for the entire basin was included.

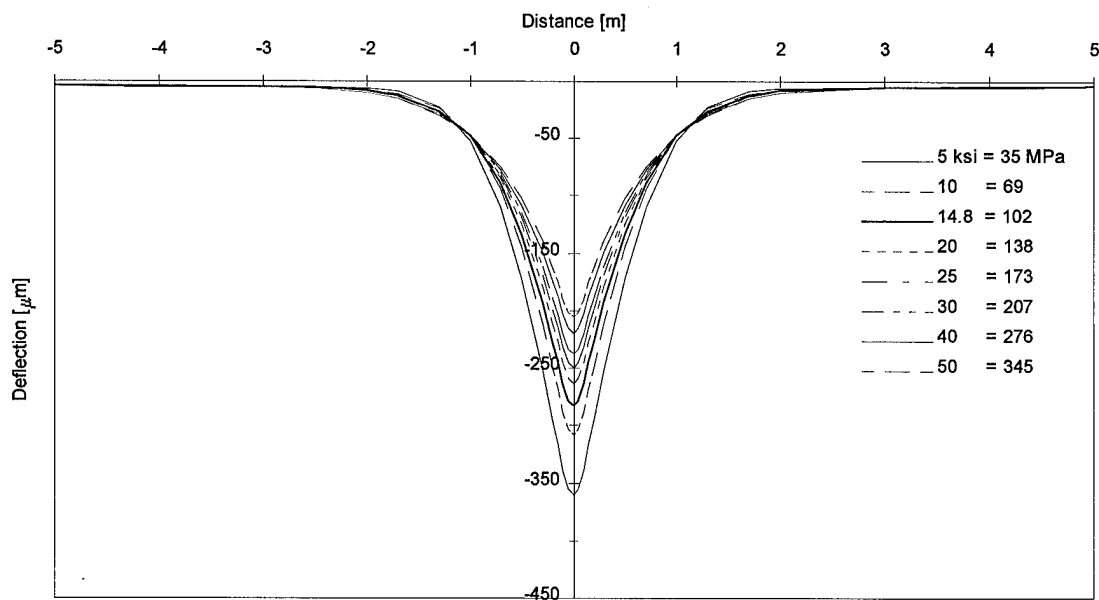
The base moduli were varied over the same range used in the longitudinal analysis, from 5 to 50 ksi (35 to 345 MPa). Figure 7-29 illustrates the differences in the longitudinal and transverse deflection profiles.

The basins were perfectly symmetric about the peak deflection, as would be expected for the transverse profile. The peak deflection and width of the basins appeared to be nearly identical to the longitudinal profiles.

As illustrated in Figure 7-30, the peak deflection increased by 20% when the base modulus was reduced from the standard to the minimum. As the base modulus increased from the standard to the maximum, the peak deflection decreased almost linearly, of 2 μm for every 1 ksi increase in modulus. The mean was essentially zero for all base moduli, and the standard deviation steadily increased as the base modulus increased. The coefficient of skewness was nearly zero for all base moduli, confirming that the basins were symmetrical about the mean. The coefficient of kurtosis decreased in a non-linear manner. When the modulus was decreased from the standard to the minimum, the kurtosis increased 20%, but when the modulus was increased from the standard by an equal increment, the kurtosis decreased by only 11%.



a) Longitudinal Deflection Basins



b) Transverse Deflection Basin

Figure 7-29. Longitudinal and Transverse Deflection Basins.

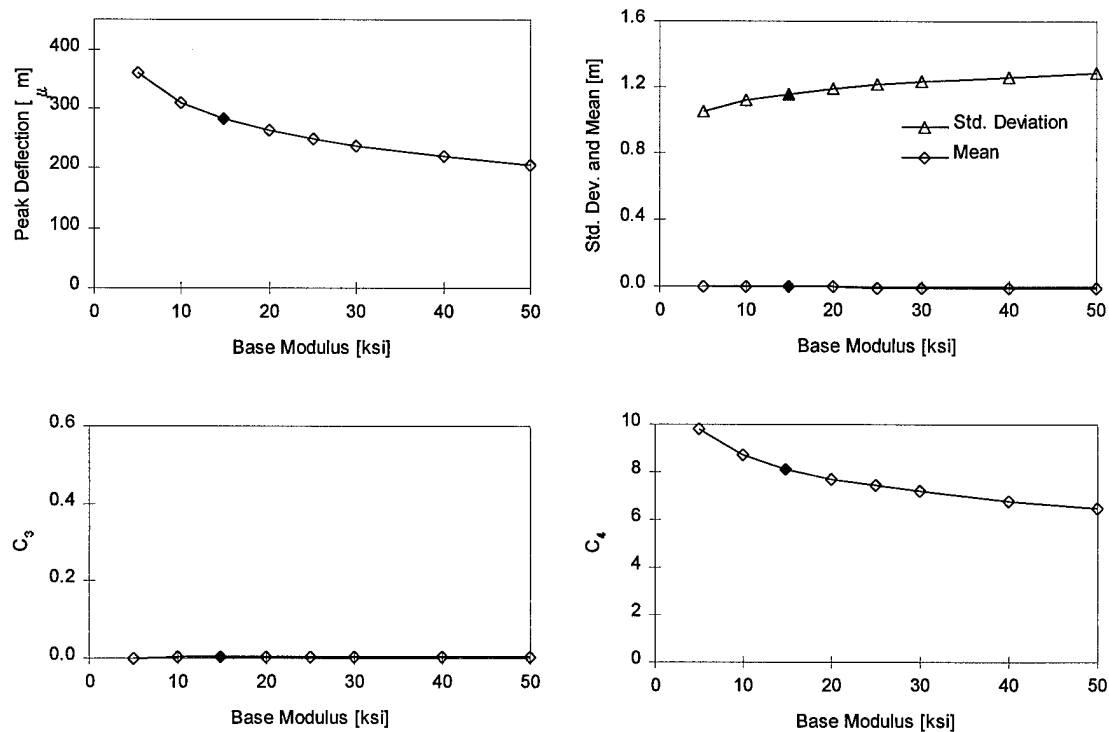


Figure 7-30. Transverse Profile -- Sensitivity to Base Modulus.

The transverse basins behave similarly to the longitudinal basins, except that the skewness is removed. The peak deflections, standard deviations, and coefficient of kurtosis are nearly identical for the transverse and longitudinal profiles -- the small differences are likely caused by the skewness of the longitudinal basins.

Chapter 8

SUMMARY, CONCLUSIONS, AND RECOMMENDATIONS

8.1 Summary

This thesis presented the background, conceptual development, and implementation of a mathematical model for predicting pavement deflections caused by a moving wheel load. The development of this model was described in the preceding chapters.

Chapter 2 described a variety of existing nondestructive tests that are used for pavement analysis. Static, dynamic, surface wave, and rolling wheel testing devices and their historical applications were reviewed.

Chapter 3 presented several types of pavement deflection models. First, the simplest models, static linear elastic, were described. Next, models that can characterize the pavement system as composed of non-linear elastic or viscoelastic materials were described. Finally, dynamic models used for predicting transient stationary and moving load deflections were explained.

In Chapter 4, the Green's function method of solution was applied to dynamic layered elastic analysis. The Green's functions used in this model computed the vertical deflections at the surface of a pavement system resulting from a unit harmonic load applied over a circular area. The calculated response was a function of the frequency, layer material properties, and distance from the applied load. Fourier superposition analysis in combination with the Green's function solution was used to predict the dynamic pavement deflection response. Details of the loading representation for a FWD impulse and rolling wheel were described.

The conceptual development of the computer program BASIN was described in Chapter 5. For convenience, a simulated deflection response function was initially used while the bookkeeping methods were developed. This initial development described the modeling of five increasingly complex load and observation scenarios. The last portion of the chapter described the modifications required to insert the complex-valued Green's functions into the program BASIN.

The results of the deflection model validation were presented in Chapter 6. The rolling load model was modified to determine dynamic deflections caused by a falling weight deflectometer so that predicted and measured deflections could be directly compared.

The results of a detailed parametric study of BASIN were presented in Chapter 7. Significant input variables were systematically adjusted to determine the sensitivity of the deflection basin to each variable. Both layer material properties and loading parameters were investigated.

8.2 Conclusions

A number of conclusions were developed from the results of the parametric study using the new pavement deflection model, coded in the computer program BASIN. The conclusions are organized according to their variable category.

Algorithm Considerations

Algorithm variables were examined to determine the values that produced the best accuracy with the least computation time. Several significant results are listed below.

1. The thickness of the sublayers used to discretize the pavement must be sufficiently thin to produce an accurate result. The parametric study showed that the solution converges to a constant deflection basin shape, beyond which thinner layers will not produce a more accurate result.
2. The deflection basin shape does not change appreciably when the cutoff frequency used to characterize the load is larger than 95 Hz.
3. The spacing between individual load pulses must be less than or equal to 1 msec to guarantee an accurate solution.

Material Considerations

The material variables were studied to determine how their values changed the basin shape. The sensitivity of the basin shape to each variable may provide clues about which material parameters can be backcalculated.

4. The shape of the predicted deflection basin was insensitive to material density. None of the statistical parameters were changed by increasing or decreasing the density from the standard case.
5. The deflection basin shape was relatively insensitive to the Poisson's ratio of each layer. Of the statistical parameters, skewness and kurtosis were affected most by the Poisson's ratio, while the peak deflection and standard deviation were virtually independent of the Poisson's ratio.
6. The deflection basin shape was very sensitive to the AC modulus. As expected, the peak deflection changed more dramatically than the other indicators. Surprisingly, the coefficient of kurtosis was more sensitive to the AC modulus than the standard deviation. As a result, there may be more potential for correlating AC modulus to kurtosis than standard deviation. This can be explained by the manner in which the basins changed -- almost all of the change occurred very close to the peak deflection. Therefore, the spread of the basin was not changed as much as its peak.
7. The deflection basin shape was very sensitive to the base modulus. Like the AC modulus, the coefficient of kurtosis appeared to be more sensitive to the base modulus than the standard deviation.
8. The deflection basin shape was extremely sensitive to the subgrade modulus. Both the peak and the width of the basin changed significantly with the subgrade modulus. In this case, the standard deviation was more sensitive to the subgrade modulus than the other statistical parameters.
9. The deflection basin shape was extremely sensitive to the stiff layer modulus. Unlike the other moduli tested, the standard deviation of the basin rapidly *decreased* as the stiff layer modulus *increased*. The coefficients of skewness and kurtosis were also very sensitive to the stiff layer modulus.
10. The deflection basin changed dramatically as the AC thickness changed. Peak deflections increased rapidly as the AC became thinner. The standard deviation decreased linearly as the AC thickness decreased. Very thick AC layers (greater than 300 mm) resulted in very broad deflection basins with small dips near the peak deflection.
11. The deflection basin shape was very insensitive to the thickness of the base layer. Almost no changes in the statistical parameters or the general shape of the basin were observed for different base layer thicknesses.
12. The deflection basin shape was somewhat sensitive to the subgrade thickness. Unlike the behavior determined for the AC and base thickness, the peak

deflection *increased* as the subgrade thickness *increased*. This behavior can be explained by examining the stiffness of each layer. The subgrade is softer than all the other layers. Therefore, it logically follows that a thicker soft layer would result in larger deflections.

13. Only very small changes in the deflection basin result from combined variations of the thickness and modulus of the AC or base layers. The variations in moduli were backcalculated using static models, but unexpectedly, the dynamic analysis used by BASIN did not compute significantly different basins. These results suggest that attempts to simultaneously backcalculate moduli and layer thickness will require very accurate measurement of the deepest part of the deflection basin.

Loading Considerations

Loading variables were studied to determine their effects on the deflection basin shape. The sensitivity of the deflection basin shape to each of these parameters may provide clues about the optimum operating conditions for a rolling wheel deflectometer.

14. The deflection basin peak was linearly related to the applied wheel load. The other statistical parameters were constant for all applied loads. This is a direct result of the assumed linear-elastic stress-strain behavior of the pavement materials.
15. Only the deepest portion of the deflection basin was sensitive to the tire pressure. Low tire pressures resulted in lower peak deflections, but outside the tire contact zone, the basin was virtually identical to that produced by higher pressure tires.
16. The wheel speed has a significant effect on the deflection basin. Both the peak deflection and the mean were directly proportional to the speed. In fact, wheel speed was the only parameter that influenced the mean. The skewness also was significantly affected by wheel speed. At creep speeds, the basin was nearly symmetric; however, as the speed increased the skewness of the basin became positive.
17. The pulse duration selected for the analysis has a significant impact on the shape and location of the deflection basin. Short pulses produced deeper, more-symmetrical basins with mean values closer to the wheel. Long pulses have the opposite effect. The method in which the relationship between load pulses duration, load pulse spacing, and wheel speed should be applied in BASIN is not yet clearly understood. Computations completed using load

pulses corresponding to the wheel speed produced illogical, inconclusive results.

The final analysis of the parametric study compared longitudinal to transverse deflection profiles. These results may begin to show the advantages of one measurement profile over the other.

18. Transverse deflection profiles can show similar trends to longitudinal profiles; however, the skewness of the function is removed in the transverse profile -- i.e. the basin is perfectly symmetric. Transverse profiles may be better for backcalculation because the absence of changes in skewness would help clarify trends in the other statistical parameters. However, if transverse profiles are measured, the distance between the transverse profile and the peak longitudinal deflection must be accurately determined so that the relative depth of deflection is understood. Also, parameters that produce changes in skewness would not be backcalculated as accurately because the transverse profiles cannot recognize these changes.

8.3 Recommendations for Further Study

The forward model for predicting pavement deflections caused by a moving wheel load is just one component of a much larger problem. For the model to be of practical value for backcalculating pavement properties, several areas require further study.

1. The relationship between load pulse duration, vehicle speed, and load pulse spacing should be further investigated. A clear understanding of these parameters is required to implement the model properly.
2. Only a limited number of deflection sensors can be used to measure pavement deflections. Therefore, it is important to maximize the information obtained from each sensor. The optimum location of each sensor should be determined based on the sensitivity of the deflection basin to expected material parameters and the most probable operating speed and load. If possible, sensors should be located to allow an accurate definition of the peak deflection zone, because this area may be most sensitive to thickness *and* modulus.
3. The statistical parameters used to characterize the deflection basins in the parametric study may prove useful for very rapid direct correlations with layer modulus and thickness. The application of these parameters to FWD deflection basins may help develop new correlations for stationary tests too.

4. The Green's function solution developed by Kausel and Peek (1982) is capable of calculating vertical *or* horizontal displacements within the pavement structure. The program BASIN could be modified to calculate deflections at critical locations in the pavement structure (i.e. horizontal deflections at the bottom of the AC layer). From this information, dynamic pavement damage models could be developed to predict the life expectancy of a pavement structure.
5. The FORTRAN program BASIN required about 70 minutes to compute deflections at 30 locations using a 486/66 MHz microcomputer with 8 Mb RAM. This computation time is much too long for practical application of the model. However, the modified program FWDDROP can calculate the time history deflection for seven sensor locations in only 1.5 minutes. Therefore, this model may have some current practical value for backcalculation. As computer processing speeds increase, the required computation times will undoubtedly decrease.
6. When deflection measurements from rolling weight deflectometers are available, the accuracy of the model should be verified.

BIBLIOGRAPHY

- Achenbach, J.D. and Sun, C. (1965). "Dynamic Response of Beam on Viscoelastic Subgrade." *Journal of Engineering Mechanics*, ASCE, Vol. 91, No. 5, pp. 61-76.
- Arnberg, P.W., Holen, Å., and Magnusson, G. (1991). "The High-Speed Road Deflection Tester." Presented at the Strategic Highway Research Program and Traffic Safety on Two Continents, Gothenburg, Sweden, Sep 18-20, 1991, 13 pp.
- ASTM D4694-87 (1995). "Standard Test Method for Deflections with a Falling-Weight-Type Impulse Load Device," *1995 Annual Book of ASTM Standards: Road and Paving Materials; Paving Management Technologies*, Section 4, Vol. 04.03, American Society for Testing and Materials.
- ASTM D4695-87 (1995). "Standard Guide for General Pavement Deflection Measurements," *1995 Annual Book of ASTM Standards: Road and Paving Materials; Paving Management Technologies*, Section 4, Vol. 04.03, American Society for Testing and Materials.
- Barksdale, R.D. (1971). "Compressive Stress Pulse Times in Flexible Pavements for Use in Dynamic Testing," In *Highway Research Record 345*, Highway Research Board, Washington, D.C., pp. 32-44.
- Bay, J.A., Stokoe, K.H. II, and Jackson, J.D., (1995). "Development and Preliminary Investigation of Rolling Dynamic Deflectometer." In *Transportation Research Record 1473*, Transportation Research Board, National Research Council, Washington, D.C., pp. 43-54.
- Bentson, R.A., Nazarian, S., and Harrison, J.A. (1989). "Reliability Testing of Seven Nondestructive pavement Testing Devices." *Nondestructive Testing of Pavements and Backcalculation of Moduli, ASTM STP 1026*, A.J. Bush III and G.Y. Baladi, Eds., American Society for Testing and Materials, Philadelphia, pp. 41-58.
- Burmister, D.M. (1943). "The theory of stresses and displacements in layered systems and applications to the design of airport runways," *Proceedings of the 23rd Annual Meeting of the Highway Research Board*, Vol. 23, pp. 126-144.
- Burmister, D.M. (1945a). "The general theory of stresses and displacements in layered soil systems, I," *Journal of Applied Physics*, Vol. 16, pp. 89-94.
- Burmister, D.M. (1945b). "The general theory of stresses and displacements in layered soil systems, II," *Journal of Applied Physics*, Vol. 16, pp. 126-127.

- Burmister, D.M. (1945c). "The general theory of stresses and displacements in layered soil systems, III," *Journal of Applied Physics*, Vol. 16, pp. 296-302.
- Chang, D., Roesset, J.M., and Stokoe, K.H. III (1992). "Nonlinear Effects in Falling Weight Deflectometer Tests." In *Transportation Research Record 1355*, Transportation Research Board, National Research Council, Washington, D.C., pp. 1-7.
- Chatti, K., Yun, K.K., Kim, H.B., and Utamsingh, R. (1995). "PACCAR Full-Scale Pavement Tests." Final Report to The University of California - Berkeley and The California Department of Transportation, Michigan State University, East Lansing, MI, 105 pp.
- Crovetti, J.A., Shahin, M.Y. and Touma, B.E. (1989). "Comparison of Two Falling Weight Deflectometer Devices, Dynatest 8000 and KUAB 2M-FWD." *Nondestructive Testing of Pavements and Backcalculation of Moduli, ASTM STP 1026*, A.J. Bush III and G.Y. Baladi, Eds., American Society for Testing and Materials, Philadelphia, pp. 59-69.
- Davies, T.G. and Mamlouk, M.S. (1985). "Theoretical Response of Multilayer Pavement Systems to Dynamic Nondestructive Testing." In *Transportation Research Record 1022*, Transportation Research Board, National Research Council, Washington, D.C., pp. 1-7.
- Graves, R.C. and Drnevich, V.P. (1993). "Calculating Pavement Deflections with Velocity Transducers." In *Transportation Research Record 1293*, Transportation Research Board, National Research Council, Washington, D.C., pp. 12-23.
- Haddad, Y.M. (1995). *Viscoelasticity of Engineering Materials*. Chapman and Hall, London. 378 pp.
- Hartzell, S.H. (1978). "Earthquake Aftershocks as Green's Functions." *Geophysical Research Letters*, Vol. 5, No. 1, pp. 1-3.
- Haskell, N.A. (1953). "The Dispersion of Surface Waves on Multilayered Media." *Bulletin of the Seismological Society of America*, Vol. 43, No. 1, pp. 17-34.
- Hoffman, M.S. and Thomson, M.R. (1981). "Mechanistic Interpretation of Nondestructive Pavement Testing Deflections." Report for Project IHR-508, Illinois Cooperative Highway and Transportation Research Program, University of Illinois, Champaign, IL. 249 pp.

- Hoffman, M.S. and Thomson, M.R. (1982). "Comparative Study of Selected Nondestructive Testing Devices." In *Transportation Research Record 852*, Transportation Research Board, National Research Council, Washington, D.C., pp. 32-41.
- Holder, B.W. and Michalopoulos, C.D. (1977). "Response of a Beam on an Inertial Foundation to a Traveling Load." *AIAA Journal*, American Institute of Aeronautics and Astronautics, Vol. 15, No. 8, pp. 1111-1115.
- Huang, Y. H. (1993). *Pavement Analysis and Design*, Prentice-Hall, Inc., Englewood Cliffs, NJ, 805 pp.
- Kausel, E. and Peek, R. (1982). "Dynamic Loads in the Interior of a Layered Stratum: An Explicit Solution." *Bulletin of the Seismological Society of America*, Vol. 72, No. 5, pp. 1459-1481.
- Kausel, E. and Roesset, J.M. (1981). "Stiffness Matrices for Layered Soils." *Bulletin of the Seismological Society of America*, Vol. 71, No. 6, pp. 1743-1761.
- Ketchum, Stephen A. (1993). "Dynamic Response Measurements and Identification Analysis of a Pavement During Falling-Weight Deflectometer Experiments." In *Transportation Research Record 1415*, Transportation Research Board, National Research Council, Washington, D.C., pp. 78-87.
- Kramer, S.L. (1996). *Geotechnical Earthquake Engineering*, Prentice-Hall, Inc., Englewood Cliffs, NJ, 652 pp. In Press.
- Meier, R.W. (1995). "Backcalculation of Flexible Pavement Moduli from Falling Weight Deflectometer Data Using Artificial Neural Networks." Ph.D. Thesis, Georgia Institute of Technology, Atlanta, GA, 239 pp.
- Moore, W.M., Hanson, D.I., and Hall, J.W. (1978). "An Introduction to Nondestructive Structural Evaluation of Pavements." *Transportation Research Circular 189*, Transportation Research Board, National Academy of Sciences, Washington, D.C., January, 33 pp.
- Nazarian, S. and Stokoe, K.H. II (1984). "Nondestructive Testing of Pavements Using Surface Waves." In *Transportation Research Record 993*, Transportation Research Board, National Research Council, Washington, D.C., pp. 67-79.
- Nazarian, S. and Stokoe, K.H. II (1989). "Nondestructive Evaluation of Pavements by Surface Wave Methods." *Nondestructive Testing of Pavements and Backcalculation of Moduli, ASTM STP 1026*, A.J. Bush III and G.Y. Baladi, Eds., American Society for Testing and Materials, Philadelphia, pp. 119-137.

- Newcomb, D.E., Van Ceusen, D.A., Jiang, Y., and Mahoney, J.P. (1995). "Considerations of Saturated soil Conditions in Backcalculation of Pavement Layer Moduli," In *Transportation Research Record 1473*, Transportation Research Board, National Research Council, Washington, D.C., pp. 63-71.
- Ong, C.L., Newcomb, D.E., and Siddharthan, R. (1991). "Comparison of Dynamic and Static Backcalculation Moduli fro Three-Layer Pavements." In *Transportation Research Record 1293*, Transportation Research Board, National Research Council, Washington, D.C., pp. 86-92.
- Prandi, E. (1967). "The LaCroix - L.C.P.C. Deflectograph." *Proceedings*, International Conference on Structural Design of Asphalt Pavements, University of Michigan, Ann Arbor, MI, USA. pp. 1059-1068.
- Press, W.H., Teukolsky, S.A., Vetterling, W.T., and Flannery, B.P., (1992). *Numerical Recipes in FORTRAN, 2nd Ed.*, Cambridge University Press, Cambridge, pp. 490-508.
- Rada, G.R., Richter, C.A., and Jordahl, P. (1994). "SHRP's Layer Moduli Backcalculation Procedure," *Nondestructive Testing of Pavements and Backcalculation of Moduli, Second Volume, ASTM STP 1198*, H.L. Von Quintas, A.J. Bush III and G.Y. Baladi, Eds., American Society for Testing and Materials, Philadelphia, pp. 38-52.
- Roach, G.F. (1970). *Green's Functions: Introductory Theory with Applications*. Van Nostrand Reinhold Co., London, Great Britain, 279 pp.
- Roesset, J.M. and Shao, K. (1985). "Dynamic Interpretation of Dynaflect and FWD Tests." In *Transportation Research Record 1022*, Transportation Research Board, National Research Council, Washington, D.C., pp. 7-16.
- Sachs, L. (1982). *Applied Statistics: A Handbook of Techniques*. Springer-Verlag, New York, 706 pp.
- Sanchez-Salinerio, I. (1987). "Analytical Investigation of Seismic Methods Used for Engineering Applications." Ph.D. Dissertation, The University of Texas, Austin, TX, 400 pp.
- Sivaneswaran, N., Kramer, S.L., and Mahoney, J.P. (1993). "Advanced Backcalculation Using a Nonlinear Least Squares Optimization Technique." In *Transportation Research Record 1293*, Transportation Research Board, National Research Council, Washington, D.C., pp. 93-102.

- Thomson, W.T. (1950). "Transmission of Elastic Waves through a Stratified Solid Medium." *Journal of Applied Physics*, Vol. 21, No. 2, pp. 89-93.
- Trim, D.W. (1990). *Applied Partial Differential Equations*. PWS-Kent Publishing Co., Boston, MA, 485 pp.
- Trochanis, A.M., Chelliah, R., and Bielak, J. (1987). "Unified Approach for Beams on Elastic Foundations under Moving Loads." *Journal of Geotechnical Engineering*, ASCE, Vol. 113, No. 8, pp. 879-895.
- Van Cauwelaert, F.J., Alexander, D.R., White, T.D., and Barker, W.R. (1989). "Multilayer Elastic Program for Backcalculating Layer Moduli in Pavement Evaluation," *Nondestructive Testing of Pavements and Backcalculation of Moduli, ASTM STP 1026*, A.J. Bush III and G.Y. Baladi, Eds., American Society for Testing and Materials, Philadelphia, pp. 171-188.
- Walker, H.M. and Lev, J. (1969). *Elementary Statistical Methods, 3rd Ed.* Holt, Rinehart, and Winston, Inc., New York, 432 pp.
- Winters, B.C. (1993). *The PACCAR Pavement Test Section - Instrumentation and Validation*. M.S. Thesis, University of Washington, Seattle, WA. 223 pp.
- Yoder, E.J., and Witczak, M.W. (1975). *Principals of Pavement Design, 2nd Edition*. John Wiley & Sons, Inc., New York. 711 pp.
- Zaghloul, S.M., White, T.D., Drnevich, V.P., and Coree, B. (1994). "Dynamic Analysis of FWD Loading and Pavement Response Using a Three-Dimensional Finite Element Program." *Nondestructive Testing of Pavements and Backcalculation of Moduli, Second Volume, ASTM STP 1198*, H.L. Von Quintas, A.J. Bush III and G.Y. Baladi, Eds., American Society for Testing and Materials, Philadelphia, pp. 125-138.

Appendix A

BASIN CODE

A.1 Primary BASIN Modules

BASIN is comprised of a primary module and three main subroutines. The primary module controls the order of the program execution and performs basic “bookkeeping” functions. The LOADDAT subroutine reads the loading and velocity information recorded by the rolling weight deflectometer. Also, *avetime*, *timeback*, and other parameters used to characterize individual load pulses are loaded into the program. The subroutine GREEN was generously provided by Professor Roger Meier. This subroutine calculates the Green’s function response for all frequencies within a specified bandwidth. LOADTIME is called by GREEN after the response at each frequency is known. Subroutine LOADTIME performs Fourier superposition analysis to create the time history of deflection for each load pulse. Within LOADTIME, the subroutine FFT is called to complete forward and inverse Fast Fourier Transforms. The subroutine FFT was taken directly from Press et al. (1989). Finally, LOADTIME selects the proper deflection from each time history and calculates the total deflection at each deflection sensor location.

A.2 BASIN Input and Output

BASIN uses four input files.

<i>pulse.dat</i>	This file contains the time increment, <i>avetime</i> , <i>timeback</i> , pulse duration, total load amplitude, and wheel speed.
<i>rwd.dat</i>	This file contains a simulated list of output data measured by a rolling weight deflectometer. <i>rwd.dat</i> is created using the program CRE8DAT.

- input.dat* This file is used by GREEN and contains the material layer properties, loaded radius, and frequency information. See the subroutine *data* in GREEN for formatting details.
- sense.dat* The initial location of the wheel and the locations of all deflection sensors are listed in this file.

BASIN writes the output to one file -- *output.out*. The output file first lists the basin number and the time and location of the wheel when the calculation was made. Next, the coordinates for each deflection sensor and the deflection at that sensor is listed.

A.3 BASIN Code

```

program BASIN
c
c -----
c This program computes deflection resulting from a rolling wheel load.
c BASIN uses Green's functions that determine the steady-state response
c for a unit vibrating disk load. The green's functions are computed
c in the subroutine GREEN, written by Roger Meier, with minor modifications
c for this purpose.
c NOTE: When compiling on MS FORTRAN Powerstation, two warnings will be
c given that could not be removed. However, they do not prevent
c program execution. They are both in line 1059 and read:
c warning F4016: LOVE : formal argument E : type mismatch
c warning F4016: LOVE : formal argument V : type mismatch
c -----
implicit real*8 (a-h,o-z)
parameter (iout=16,isense=25)
parameter (ntimemax=201,nmbkmax=201,nbasnmax=ntimemax-nmbkmax+1,
1 nterms=1024,ndefmax=40)

parameter(itim=86)
integer*2 ihr,imin,isec,ihun
real*8 dt,time(ntimemax),velo(ntimemax),pleft(ntimemax),
1 pright(ntimemax)
real*8 def1(ntimemax),def2(ntimemax),def3(ntimemax)
real*8 xinit,yinit
real*8 xd(ndefmax),yd(ndefmax)
real*8 xwheel(ntimemax)
real*8 xobserv(nbasnmax,ndefmax)
real*8 yobserv(ndefmax)
real*8 radius(nmbkmax,ndefmax)

```

```

real*8 findef(nbasnmax,ndefmax),calcddef(ndefmax)
real*8 avetime, pulseamp,totalamp

c-----Start timer
  open (itim,file='timer.out',status='new')
  call gettim(ihr,imin,isec,ihun)
  write(itim,*) ihr,':',imin,':',isec

  open (isense,file='sense.dat',status='old')
  open (iout,file = 'output.out', status = 'new')

c-----Load input data from RWD
  call LOADAT (dt,ntime,avetime,timeback,numback,nbasin,
    1          fwda,fwdb,totalamp,pulseamp,
    2          time,velo,pleft,pright,
    3          def1,def2,def3,
    4          ntimemax)
c
c-----Read in basic location paramaters
c  xinit = initial x position of wheel
c  yinit = initial y position of wheel
c  xd(i) = x position of deflection sensor i
c  yd(i) = y position of deflection sensor i
c-----
  read(isense,*) xinit,yinit,ndef
  do i=1,ndef
    read(isense,*) xd(i),yd(i)
  end do
  close(isense)

c-----Calculate the position of the wheel at all times
c  Assume the wheel moves in the +x direction
c
  xwheel(1)=xinit
  do i=2,ntime+1
    xwheel(i)=xwheel(i-1) + velo(i-1)*avetime
  end do

c-----Numback specifies how far backwards in time the program should look for
c  calculating a response.
c  Units for numback are in terms of the number of data points,
c
c-----By default, the first point at which we can calculate a basin is at
c  xwheel(numback).
c
c-----Establish the observation point coordinates for all nbasins.
  do jdef=1,ndef
    yobserv(jdef)=yd(jdef)
  end do
  do i=1,nbasin
    mtemp=numback + (i-1)
    do jdef=1,ndef
      xobserv(i,jdef)=xwheel(mtemp)+xd(jdef)
    end do
  end do

```



```

        end do
    end do
    write(*,*) 'Observation point coordinates established'

    do jbasin=1,nbasin
c-----Calculate matrix containing all radii [numback x ndef]
        do jdef=1,ndef
            do iback=1,numback
                radius(iback,jdef)=dsqrt((xwheel(iback+jbasin-1)-
1                  xobserv(jbasin,jdef))**2 +
2                  yobserv(jdef)**2)
            end do
        end do
        write(*,*) 'Radius matrix established'
c
c-----Call GREEN to calculate the time history response
c    for each radii.
c
        call GREEN(radius,calcdef,dt,
1          avetime,numback,ndef,
2          fwda,fwdb,pulseamp)

        write(*,*) 'THRs complete'
c-----Transfer the calcdef variable to a permanent findef variable
        do jdef=1,ndef
            findef(jbasin,jdef)=calcdef(jdef)
        end do

c-----Print the results in the output file
        write(iout,*) 'Basin #',jbasin
        write(iout,'(2e14.6)') time(jbasin-1+numback+1),
1          xwheel(jbasin-1+numback+1)
        do jdef=1,ndef
            write(iout,'(3e14.6)') xd(jdef),yd(jdef),findef(jbasin,jdef)
        end do
        write(iout,*) ' '
        write(*,*) 'Basin #',jbasin,' complete'
    end do

c-----Stop timer
    call gettim(ihr,imin,iseq,ihun)
    write(itim,*) ihr,':',imin,':',iseq
    close(itim)
    close(iout)

    stop
    end

c
    subroutine LOADAT (dt,ntime,avetime,timeback,numback,nbasin,
1          fwda,fwdb,totalamp,pulseamp,

```

```

2      time,velo,pleft,pright,
3      def1,def2,def3,
4      ntimemax)
c-----
c  Subroutine LOADAT
c  This routine first loads several basic parameters used throughout
c  the main program.  These are in 2 input data files/
c
c  pulse.dat
c  dt = time increment
c  avetime = time spacing between load pulses
c  timeback = span of time used to determine the load pulses used
c  fwda = start of load pulse (should always be zero)
c  fwdb = end of load pulse
c  totalamp = total line load applied by the wheel
c
c  Next, This routine loads data from the RWD into the program.
c  For model development, this data was created by using the
c  program CRE8DAT.
c  Data should be in seven columns of real numbers in the order:
c
c  rwd.dat
c  Time Velocity Left Wheel Right Wheel Deflect Deflect Deflect
c           Load      Load      1      2      3
c
c  Total number of terms to be loaded is specified by ntime.
c-----
c
c  implicit real*8 (a-h,o-z)
c  parameter(idat=14,loadinp=10)
c
c  real*8 dt,time(ntimemax),velo(ntimemax),pleft(ntimemax),
1  pright(ntimemax)
c  real*8 def1(ntimemax),def2(ntimemax),def3(ntimemax)
c  real*8 avetime,totalamp,pulseamp
c  real*8 dummy
c  open(loadinp,file='pulse.dat',status='old')
c  read(loadinp,*) dt,avetime,timeback
c  read(loadinp,*) fwda,fwdb,totalamp
c
c  ntime=timeback/avetime
c  numback = timeback/avetime
c  dummy=(fwdb-fwda)/2
c  pulseamp = totalamp/(dummy/avetime)
c  nbasin = ntime-numback+1
c
c  open(idat,file='rwd.dat',status='old')
c  do i=1,ntime+1
c      read (idat,*) time(i),velo(i),pleft(i),pright(i),
1  def1(i), def2(i), def3(i)
c  end do
c
c  close(loadinp)

```

```

close(idat)
return
end

c
c
c
c
c
c
  subroutine LOADTIME(dt,uz,nfreq,calcdef,
1      avetime,numback,ndef,
2      fwda,fwdb,pulseamp)
c-----
c  This routine creates an impulse load shape and converts it to
c  the frequency domain using an FFT. Next, it multiplies the
c  load times the green's function response for each frequency.
c  Finally, an inverse FFT of the result is used to produce a
c  time history response (thr).
c-----
  parameter(nterms=1024,nterms2=2*nterms)
  parameter(nmbkmax=201,ndefmax=40,maxfr=40)
  parameter(pi=3.1415926535898)
c  parameter(ibug=86)
  implicit real*8 (a-h,o-z)
  real*8 fwda,fwdb,pulseamp
  real*8 dt,fwdtime
  real*8 avetime
  real*8 pload(nterms),pdata(nterms2),data(nterms2)
  real*8 fdata(nterms2),tdata(nterms2),rdata(nterms2)
  real*8 thr(nterms)
  real*8 tdef(ndefmax),deflec(nmbkmax),calcdef(ndefmax)
  complex*16 uz(maxfr,nmbkmax,ndefmax)
  complex*16 fload(nterms),truncp(nterms),eye
  complex*16 fresp(nterms),grnresp(nterms),static

  eye=cdsqrt(-1)

c----Create loading shape in time domain based on input parameters
  do i=1,nterms
    fwdtime=(i-1)*dt
    if(fwdtime.gt.fwda.and.fwdtime.lt.fwdb) then
      pload(i)=0.5*pulseamp*cos((fwdtime-fwda)*2*pi/
1      (fwdb-fwda)+pi)+pulseamp*0.5
    else
      pload(i)=0.0
    endif
  end do

c----Stack the string of numbers into a single string of alternating
c  real and imaginary values
  do i=1,nterms
    pdata(1+(i-1)*2)=pload(i)

```

```

        pdata(2+(i-1)*2)=0.0
    end do

c-----Convert to frequency domain using FFT function
    isign=1
    data=pdata
    call FFT(data,nterms,isign)
    fdata=data

c/RGT Added to fix reversed sign of phase angle
    do i=1,nterms
        fdata(2+(i-1)*2)=-fdata(2+(i-1)*2)
    end do
c/RGT
c-----Reassemble fload into complex number format
    do i=1,nterms
        fload(i)=fdata(1+(i-1)*2)+eye*fdata(2+(i-1)*2)
    end do

c-----Truncate the frequencies to use fewer to define the load
    write(*,*) 'nfreq=',nfreq
    do i=1,nfreq
        truncp(i)=fload(i)
    end do
    do i=nfreq+1,nterms-(nfreq-1)
        truncp(i)=0
    end do
    do i=nterms,nterms-(nfreq-2),-1
        truncp(i)=fload(i)
    end do
    write(*,*) 'Entering main LOADTIME loop'
c-----Convert uz into double-sided, green's function string

    do jdef=1,ndef
        tdef(jdef)=0.0d0
        do iback=1,numback
            static=uz(1,iback,jdef)
            grnresp(1)=dreal(static)
            do i=2,nfreq
                grnresp(i)=uz(i,iback,jdef)
            end do
            do i=nfreq+1,(nterms-(nfreq-1))
                grnresp(i)=0.0d0
            end do
            ncount=2
            do i=nterms,(nterms-(nfreq-2)),-1
                ntemp=i-nterms+ncount
                grnresp(i)=dreal(uz(ntemp,iback,jdef))-
1                eye*dimag(uz(ntemp,iback,jdef))
                ncount=ncount+2
            end do

c-----Multiply the green's function by the load in the frequency domain

```

```

do i=1,nterms
  fresp(i)=truncp(i)*grnresp(i)
end do

c-----Restack the response data into proper format for inverse FFT evaluation
do i=1,nterms
  rdata(1+(i-1)*2)=dreal(fresp(i))
  rdata(2+(i-1)*2)=-dimag(fresp(i))
end do

c-----Convert back to the time domain using an inverse FFT
isign=-1
data=rdata
call FFT(data,nterms,isign)
tdata=data

c-----Unstack tdata into a string of real time values, thr,
c   neglecting the imaginary part of the string.
do i=1,nterms
  thr(i)=tdata(1+(i-1)*2)
end do
c/RGT---If thr values at small and large times are less than zero, set to zero.
ntrip=0
do i=1,512
  if(ntrip.eq.0) then
    if(thr(i).lt.0.0) then
      thr(i)=0.0d0
    else
      ntrip=1
    end if
  else
    continue
  end if
end do
do i=513,nterms
  thr(i)=0.0d0
end do
c/RGT -----

c----- Select the proper deflections and sum them
ntemp=(numback-iback+1)*(avetime/dt)+1
deflec(iback)=thr(ntemp)
tdef(jdef)=tdef(jdef)+deflec(iback)

c-----close the numback loop
end do
calcdef(jdef)=tdef(jdef)
c-----close the ndef loop
end do

c   close(ibug)
return

```

end

```
subroutine FFT(data,nterms,isign)
```

```
c-----
c  This function takes the FFT or IFFT of the string of complex
c  numbers, data, which contains nn complex terms.  If isign = 1,
c  and FFT is performed, if isign = -1, an IFFT is performed.
c  Data must be packed such that data(1) is the real portion
c  of the first input term and data(2) is the imaginary portion.
c  Copied from "Numerical Recipes" by ???
c-----
```

```
integer*4 isign,nterms
real*8 data(nterms*2)
integer*4 i,istep,j,m,mmax,n
real*8 tempi,temp
real*8 theta,wi,wpi,wpr,wr,wtemp
n=2*nterms
j=1
do i=1,n,2
  if(j.gt.i)then
    tempr=data(j)
    tempi=data(j+1)
    data(j)=data(i)
    data(j+1)=data(i+1)
    data(i)=tempr
    data(i+1)=tempi
  end if
  m=n/2
1  if((m.ge.2).and.(j.gt.m)) then
    j=j-m
    m=m/2
    goto 1
  end if
  j=j+m
end do
mmax=2
2  if (n.gt.mmax) then
    istep=2*mmax
    theta=6.28318530717959d0/(isign*mmax)
    wpr=-2.d0*sin(0.5d0*theta)**2
    wpi=sin(theta)
    wr=1.d0
    wi=0.d0
    do m=1,mmax,2
      do i=m,n,istep
        j=i+mmax
        tempr=sngl(wr)*data(j)-sngl(wi)*data(j+1)
        tempi=sngl(wr)*data(j+1)+sngl(wi)*data(j)
        data(j)=data(i)-tempr
        data(j+1)=data(i+1)-tempi
```

```

        data(i)=data(i)+tempr
        data(i+1)=data(i+1)+tempi
    end do
    wtemp=wr
    wr=wr*wpr-wi*wpi+wr
    wi=(wi*wpr)+(wtemp*wpi)+wi
end do
mmax=istep
goto 2
end if

c/RGT Add normalizing term for inverse transform
if(isign.eq.-1) then
    do i=1,nterms
        data(1+(i-1)*2)=data(1+(i-1)*2)/nterms
    end do
else
    continue
end if
c/RGT

return
end

subroutine GREEN(radius,calcdef,dt,
1          avetime,numback,ndef,
2          fwda,fwdb,pulseamp)
c
c -----
c/RGT
c  Obtained from Roger Meier
c/RGT
c  this is a modified version of ignacio sanchez-salinaro's program
c  to find the green's function solutions to elastodynamic problems
c  -----
c  - the program and subroutine banners have been cleaned up
c  - the file code it=17 has been moved to the parameter statement
c  - the temporary files have been eliminated (they're never used)
c  - the inputs for the load have been moved to subroutine data
c  - the fixed file code it replaces the variable file code loadt
c  - frequency has been added to the output to file code io
c  - frequency has been removed from the output to file code it
c  - all output moved from the subroutines into the main program
c  - added close statements for all of the input/output file codes
c  - subroutine hankel replaced with eduardo kausel's version
c  - subroutine jbessel replaced with eduardo kausel's version
c  - added code to automatically create the nodes w/in each layer
c  - added array ns to specify the number of segments per layer
c  - added an exhaustive input data definition section

```

```

c - collapsed the input read statements into implicit do-loops
c - removed references to loading cases that are not supported
c - added loads to the displacement calculations for line loads
c - reformatted subroutine displac to enhance its readability
c - moved all i/o from remaining subroutines to main program
c - removed all debugging i/o that had been commented out
c - added comment statements to subroutines data and echo
c - removed subroutine line (which was never called anywhere)
c - moved four and rr into subroutine boupra as parameters
c - eliminated cs and cp arrays (never used except for halfspace)
c - moved cs and cp calculations for halfspace into hspace
c - moved call to subroutine boupra inside frequency do-loop
c - eliminated temporary variables used inside frequency do-loop
c -----
c see subroutine data for a description of the required input data
c -----

```

```

implicit real*8 (a-h,o-z)
parameter (nterms=1024,mlay=5,msub=40,statfr=0.01,
1      mdim=msub+1,mdim2=2*mdim,mdim3=3*mdim,
2      pi=3.1415926535898,pi2=6.2831853071796)
parameter(nmbkmax=201,ndefmax=40,maxfr=40)
parameter(in=12)
real*8 rock
integer*4 layer(mdim),jfreq
integer*4 iwk(mdim3)
real*8 h(mdim)
real*8 th(mlay),ns(mlay),vs(mlay),rro(mlay),anu(mlay),damp(mlay)
real*8 ml1(mdim),ml2(mdim),mr1(mdim2),mr2(mdim2)
real*8 load
real*8 dt,radius(nmbkmax,ndefmax)
real*8 avetime,fwda,fwdb,pulseamp
real*8 calcdef(ndefmax)
real*8 holdofr
complex*16 lame(mlay,3)
complex*16 al1(mdim),al2(mdim),gl1(mdim),gl2(mdim)
complex*16 dl1(mdim),dr1(mdim),dr2(mdim),dr3(mdim)
complex*16 er1(mdim),er2(mdim),tr1(mdim),tr2(mdim)
complex*16 qr1(mdim),qr2(mdim),pr1(mdim),pr2(mdim)
complex*16 ar1(mdim2),ar2(mdim2),br1(mdim2),br2(mdim2)
complex*16 gr1(mdim2),gr2(mdim2)
complex*16 bl1(mdim),bl2(100)
complex*16 wk1(mdim3),wk2(mdim2),wk3(mdim2),wk4(mdim2)
complex*16 wk5(mdim2),wk6(mdim2),wk7(mdim2),wk8(mdim2)
complex*16 cr1(mdim2),cr2(mdim2)
complex*16 er(mdim2),vr(mdim2,mdim2),wk(mdim2,4)
complex*16 uz1,uz(maxfr,nmbkmax,ndefmax)

```

```

open(in,file='input.dat',status='old')

```

```

call data (th,ns,vs,rro,anu,damp,lame,
1      nfreq,ofr,dfr,ifr,rock,

```



```

2      r,load,loadt,il,id,
3      ndist,odist,ddist,idist,
4      nlay,
5      mlay,in)
c/RGT-Statfr is the smallest frequency calculated -- used to approximate
c  the solution for a static load.
  holdofr=ofr
  ofr=statfr
c/RGT-----
  call sublay (layer,h,
1      th,ns,vs,
2      nfreq,ofr,dfr,ifr,rock,
3      nlay,nsb,nodes,nodes2,
4      mlay,mdim)

  fr = ofr
  do jfreq = 1,nfreq
    om = fr*pi2
    oms = om*om
    call boupra (al1,al2,gl1,gl2,ml1,ml2,ar1,ar2,br1,br2,
1      gr1,gr2,mr1,mr2,dl1,dr1,dr2,dr3,er1,er2,
2      tr1,tr2,qr1,qr2,pr1,pr2,
3      layer,h,
4      rro,lame,
5      nsub,
6      mlay,mdim,mdim2)
    call hspace (al1,al2,gl1,gl2,ml2,ar1,ar2,br1,br2,
1      gr1,gr2,mr2,dr2,dr3,er2,
2      tr2,qr2,pr2,
3      om,rock,
4      layer,
5      lame,vs,anu,damp,
6      nodes,nodes2,
7      mlay,mdim,mdim2)
    call prelove (bl1,bl2,gl1,gl2,ml1,ml2,
1      oms,
2      nodes,
3      mdim)
    call love (bl1,bl2,al1,al2,
1      el,vl,
2      wk1,wk2,wk3,wk4,wk5,
3      iwk,nodes,
4      mdim,mdim2,mdim3,99)
    call prerayl (cr1,cr2,gr1,gr2,mr1,mr2,
1      oms,
2      nodes,
3      mdim2)
    call raylgh (ar1,ar2,br1,br2,cr1,cr2,
1      er,vr,
2      wk,wk1,wk2,wk3,wk4,wk5,wk6,wk7,wk8,
3      iwk,nodes2,
4      mdim2,mdim3,99)
  do jdef=1,ndef

```

c/RGT-----Start loop to calculate response for all radii at this frequency

```
do iback=1,numback
  dist=radius(iback,jdef)
```

c/RGT-----

```
  call displac (uz1,
1      er,vr,
2      r,load,loadt,il,id,
3      dist,
4      nodes2,
5      mdim2,pi)
  uz(jfreq,iback,jdef)=uz1
```

```
end do
```

```
end do
```

```
write(*,*) 'frequency =',fr,'complete'
```

c/RGT---Revert back to the original starting frequency when statfr

c is completed

```
if(jfreq.eq.1) ofr=holdofr
```

c/RGT-----

```
if (ifr.eq.0) then
  fr = ofr + dfr*jfreq
else
  fr = ofr + dfr*2**(jfreq-1)
end if
```

```
end do
```

c

c/RGT-Subroutine to apply load shape and do FFT conversions

```
write(*,*) 'All frequencies complete. Entering Loadtime'
```

```
call LOADTIME(dt,uz,nfreq,calcdef,
```

```
1      avetime,numback,ndef,
```

```
2      fwda,fwdb,pulseamp)
```

C/RGT-----

```
go to 100
```

```
99 write (*,*) 'problems with eigenvalues at fr = ',fr
```

```
100 continue
```

```
close(in)
```

```
return
```

```
end
```

c

c

c

c

c

```
subroutine data (th,ns,vs,rro,anu,damp,lame,
```

```
1      nfreq,ofr,dfr,ifr,rock,
```

```
2      r,load,loadt,il,id,
```

```
3      ndist,odist,ddist,idist,
```

```
4      nlay,
```

```

5      mlay,in)
c      -----
c      input data
c
c      read (in,*) nlay,rock
c      nlay ..... number of material layers
c      rock ..... bottom boundary condition
c      '1' = half-space
c      '0' = rigid
c      read (in,*) (th(i),ns(i),vs(i),rro(i),anu(i),damp(i),i=1,nlay)
c      th(i) ..... total thickness of layer i
c      ns(i) ..... number of segments in layer i
c      vs(i) ..... shear wave velocity in layer i
c      rro(i) ..... mass density in layer i
c      anu(i) ..... poisson's ratio in layer i
c      damp(i) ..... fraction of damping in layer i
c      read (in,*) r,load,loadt,il,id
c      r ..... radius of applied load
c      load ..... magnitude of applied load
c      = force for point loads
c      = force per length for line loads
c      = force per area for area loads
c      loadt ..... type of applied load:
c      1 = point load vertical
c      3 = disk load vertical
c      il ..... node where load applied
c      id ..... node where displacements output
c      read (in,*) ndist,odist,ddist,idist
c      ndist ..... number of output locations
c      odist ..... starting output location
c      ddist ..... output location intervals
c      idist ..... type of progression
c      0 = arithmetic
c      1 = geometric
c      read (in,*) nfreq,ofr,dfr,ifr
c      nfreq ..... number of frequencies
c      ofr ..... starting frequency
c      dfr ..... frequency interval
c      ifr ..... type of progression
c      0 = arithmetic
c      1 = geometric
c      -----
c      implicit real*8 (a-h,o-z)
c      real*8 rock
c      real*8 th(mlay),ns(mlay),vs(mlay),rro(mlay),anu(mlay),damp(mlay)
c      real*8 load
c      complex*16 lame(mlay,3)
c      complex*16 gg,ee
c
c      read material layer data
c
c      read (in,*) nlay, rock
c      write (*,*) 'read nlay '

```

```

do i = 1,nlay
  read (in,*) th(i),ns(i),vs(i),rro(i),anu(i),damp(i)
  gg = rro(i)*vs(i)*vs(i)*dcmplx(1.0d0,2.0d0*damp(i))
  ee = 2.0d0*gg*(1.0d0+anu(i))
  lame(i,1) = ee
  lame(i,2) = gg
  lame(i,3) = 2.0d0*anu(i)*gg/(1.0d0-2.0d0*anu(i))
end do

```

c read applied load data

```

read (in,*) r,load,loadt,il,id

```

c read output location data

```

read (in,*) ndist,odist,ddist,idist

```

c read frequency data

```

read (in,*) nfreq,ofr,dfr,ifr

```

```

return

```

```

end

```

```

subroutine sublay (layer,h,
1      th,ns,vs,
2      nfreq,ofr,dfr,ifr,rock,
3      nlay,nsub,nodes,nodes2,
4      mlay,mdim)

```

```

implicit real*8 (a-h,o-z)
real*8 rock
integer*4 layer(mdim)
real*8 h(mdim)
real*8 th(mlay),ns(mlay),vs(mlay)

```

c compute minimum and maximum frequencies

```

frmin = ofr
if (ifr.eq.0) then
  frmax = ofr + dfr*(nfreq-1)
else
  frmax = ofr + dfr*2**(nfreq-2)
end if

```

```

print *, 'minimum frequency specified = ',frmin
print *, 'maximum frequency specified = ',frmax

```

c compute minimum and maximum wavelengths

```

wavmin = wavlen(th,vs,nlay,mlay,frmax)
wavmax = wavlen(th,vs,nlay,mlay,frmin)

print *, 'minimum Rayleigh wavelength = ',wavmin

```

```
print *, 'maximum Rayleigh wavelength = ', wavmax
```

- c generate sublayers within each material layer

```

nsub = 0
do lay = 1, nlay
  dz = th(lay)/ns(lay)
  do j = 1, ns(lay)
    nsub = nsub + 1
    h(nsub) = dz
    layer(nsub) = lay
  end do
end do

```

- c add another sublayer for the transmitting boundary

```

nodes = nsub
if (rock.eq.1) then
  nodes = nodes + 1
  layer(nodes) = nlay
endif
nodes2 = nodes*2

```

```

return
end

```

```
function wavlen (th, vs, nlay, mlay, fr)
```

- c
c -----
c computes approximate wavelength of dispersed Rayleigh wave
c -----
c

```

implicit real*8 (a-h, o-z)
real*8 th(mlay), vs(mlay)

```

```
w(z) = 1.0 - 1.36765*exp(-2.2281*z) + 0.36765*exp(-5.6137*z)
```

```

guess = vs(nlay)/fr
1 above = 0.0
depth = 0.0
speed = 0.0
do i = 1, nlay
  depth = depth + th(i)
  below = w(depth/guess)
  speed = speed + vs(i)*(below - above)
  above = below
end do
if (above.lt.1.0) speed = speed + vs(nlay)*(1.0 - above)
wavlen = speed/fr
if (abs(wavlen - guess).lt.0.15) return
guess = wavlen
go to 1

```

```

end

subroutine displac (uz1,
1      er,vr,
2      r,load,loadt,il,id,
3      dist,
4      nodes2,
5      mdim2,pi)
c
c -----
c computes displacements using Green's function
c -----
c
implicit real*8 (a-h,o-z)
real*8 load
complex*16 er(mdim2),vr(mdim2,mdim2)
complex*16 uz1
complex*16 ev,zr,zd
complex*16 h0d,h1d,h0r,h1r,j0d,j1d,j0r,j1r,ilr
complex*16 vzd,vzl
complex*16 pihi

c vertical point load

if(loadt.eq.1) then
uz1=(0.0d0,0.0d0)
do l=1,nodes2
ev=er(l)
zd=ev*dist
call hankel (zd,h0d,h1d,2)
vzd=vr(2*id,l)
vzl=vr(2*il,l)
uz1 = uz1 + vzd*vzl*h0d
end do
uz1 = uz1*load/(0.0d0,4.0d0)
endif

c vertical disk load

if(loadt.eq.3) then
uz1=(0.0d0,0.0d0)
pihi=pi/(0.0d0,2.0d0)
do l=1,nodes2
ev=er(l)
zr=ev*r
zd=ev*dist
if(dist.lt.r) then
call hankel (zr,h0r,h1r,2)
call bessell (zd,j0d,j1d)
ilr=pihi*j0d*h1r/ev - 1.0d0/r/ev/ev
else
call hankel (zd,h0d,h1d,2)

```

```

      call bessel (zr,j0r,j1r)
      ilr=pihi*j1r*h0d/ev
    endif
    vzd=vr(2*id,l)
    vzl=vr(2*il,l)
    uzl = uzl + vzd*vzl*ilr
  end do
  uzl = uzl*load*r
endif

return
end

```

c

c

```

      subroutine boupra (al1,al2,gl1,gl2,ml1,ml2,ar1,ar2,br1,br2,
1          gr1,gr2,mr1,mr2,dl1,dr1,dr2,dr3,er1,er2,
2          tr1,tr2,qr1,qr2,pr1,pr2,
3          layer,
4          h,rro,lame,
5          nsub,
6          mlay,mdim,mdim2)

```

c

c

c -----
 c generates boundary layer matrices (a,b,g,m,e,d,n,l,q)
 c -----

c

c

```

      implicit real*8 (a-h,o-z)
      parameter (four=1.0d0,rr=1.0d0)
      integer*4 layer(mdim)
      real*8 h(mdim)
      real*8 rro(mlay)
      real*8 ml1(mdim),ml2(mdim),mr1(mdim2),mr2(mdim2)
      complex*16 lame(mlay,3)
      complex*16 al1(mdim),al2(mdim),gl1(mdim),gl2(mdim)
      complex*16 ar1(mdim2),ar2(mdim2),br1(mdim2),br2(mdim2)
      complex*16 gr1(mdim2),gr2(mdim2),dl1(mdim),dr1(mdim)
      complex*16 dr2(mdim),dr3(mdim),er1(mdim2),er2(mdim2)
      complex*16 tr1(mdim),tr2(mdim),qr1(mdim),qr2(mdim)
      complex*16 pr1(mdim),pr2(mdim)
      complex*16 con,con1

```

```

      al1(1)=0.0d0
      gl1(1)=0.0d0
      ml1(1)=0.0d0
      ar1(1)=0.0d0
      ar1(2)=0.0d0
      br1(1)=0.0d0
      br1(2)=0.0d0
      gr1(1)=0.0d0
      gr1(2)=0.0d0
      mr1(1)=0.0d0

```

```

mr1(2)=0.0d0
er1(1)=0.0d0
dr1(1)=0.0d0
dl1(1)=0.0d0
tr1(1)=0.0d0
qr1(1)=0.0d0
pr1(1)=0.0d0

do i=1,nsup
  k=2*i
  j=layer(i)
  con=h(i)*lame(j,2)/3.
  con1=h(i)*(2.*lame(j,2)+lame(j,3))/3.
  al1(i)=al1(i)+con
  al1(i+1)=con
  al2(i)=0.5*con
  ar1(k-1)=ar1(k-1)+con1
  ar1(k)=ar1(k)+con
  ar1(k+1)=con1
  ar1(k+2)=con
  ar2(k-1)=0.5*con1
  ar2(k)=0.5*con
  con1=lame(j,2)*h(i)/(3.*rr)
  con=2.*con1
  er1(i)=er1(i)+con
  er1(i+1)=con
  er2(i)=con1
  con=con1*four
  con1=0.5*con
  tr1(i)=tr1(i)+con
  tr1(i+1)=con
  tr2(i)=con1
  con1=2.*con/rr
  con=2.*con1
  qr1(i)=qr1(i)+con
  qr1(i+1)=con
  qr2(i)=con1
  con=lame(j,3)*0.5
  con1=lame(j,2)*0.5
  dr1(i)=dr1(i)+con
  dr1(i+1)=-con
  dr2(i)=con1
  dr3(i)=con
  dl1(i)=dl1(i)-con1
  dl1(i+1)=con1
  con=four*lame(j,2)*0.5/rr
  pr1(i)=pr1(i)+con
  pr1(i+1)=-con
  pr2(i)=con
  con=lame(j,2)/h(i)
  con1=(2.*lame(j,2)+lame(j,3))/h(i)
  gl1(i)=gl1(i)+con
  gl1(i+1)=con

```



```

gl2(i)=-con
gr1(k-1)=gr1(k-1)+con
gr1(k)=gr1(k)+con1
gr1(k+1)=con
gr1(k+2)=con1
gr2(k-1)=-con
gr2(k)=-con1
cons=rro(j)*h(i)/3.
ml1(i)=ml1(i)+cons
ml1(i+1)=cons
ml2(i)=0.5*cons
mr1(k-1)=mr1(k-1)+cons
mr1(k)=mr1(k)+cons
mr1(k+1)=cons
mr1(k+2)=cons
mr2(k-1)=0.5*cons
mr2(k)=0.5*cons
con=0.5*(lame(j,2)-lame(j,3))
con1=0.5*(lame(j,2)+lame(j,3))
br1(k-1)=br1(k-1)+con
br1(k)=-con1
br1(k+1)=-con
br2(k-1)=con1
br2(k)=0.
end do
return
end

```

```

subroutine hspace (al1,al2,gl1,gl2,ml2,ar1,ar2,br1,br2,
1      gr1,gr2,mr2,dr2,dr3,er2,
2      tr2,qr2,pr2,
3      om,rock,
4      layer,
5      lame,vs,anu,damp,
6      nodes,nodes2,
7      mlay,mdim,mdim2)
implicit real*8 (a-h,o-z)
real*8 rock
integer*4 layer(mdim)
real*8 vs(mlay),anu(mlay),damp(mlay)
real*8 ml2(mdim),mr2(mdim2)
complex*16 lame(mlay,3)
complex*16 al1(mdim),al2(mdim),gl1(mdim),gl2(mdim)
complex*16 dr2(mdim),dr3(mdim)
complex*16 er2(mdim),tr2(mdim)
complex*16 qr2(mdim),pr2(mdim)
complex*16 ar1(mdim2),ar2(mdim2),br1(mdim2),br2(mdim2)
complex*16 gr1(mdim2),gr2(mdim2)
complex*16 cp,cs,cpcs,coef

```

```

c
c -----
c calculates half-space contribution (transmitting boundary)
c -----

```

c

```

if(rock.eq.1) then
  j = layer(nodes)
  cs = vs(j)*cdsqrt(dcmplx(1.0d0,2.0d0*damp(j)))
  cp = cs*dsqrt((2.0d0-2.0d0*anu(j))/(1.0d0-2.0d0*anu(j)))
  cpcs = cp/cs
  coef = (0.0d0,1.0d0)*lame(j,2)*cs/2.0d0/om
  al1(nodes) = al1(nodes) - coef
  ar1(nodes2-1) = ar1(nodes2-1) + coef*(1.0d0-2.0d0*cpcs)
  ar1(nodes2) = ar1(nodes2) + coef*cpcs*cpcs*(cpcs-2.0d0)
  coef = (0.0d0,1.0d0)*lame(j,2)*om/cs
  gl1(nodes) = gl1(nodes) + coef
  gr1(nodes2-1) = gr1(nodes2-1) + coef
  gr1(nodes2) = gr1(nodes2) + coef*cpcs
  coef = lame(j,2)*(cpcs-2.0d0)
  br1(nodes2-1) = br1(nodes2-1) - coef
endif

```

```

al2(nodes)=0.
gl2(nodes)=0.
ml2(nodes)=0.
ar2(nodes2-1)=0.
ar2(nodes2)=0.
br1(nodes2)=0.
br2(nodes2-2)=0.
br2(nodes2-1)=0.
br2(nodes2)=0.
gr2(nodes2-1)=0.
gr2(nodes2)=0.
mr2(nodes2-1)=0.
mr2(nodes2)=0.
er2(nodes)=0.
dr2(nodes)=0.
dr3(nodes)=0.
tr2(nodes)=0.
qr2(nodes)=0.
pr2(nodes)=0.

```

```

return
end

```

```

subroutine prelove (bl1,bl2,gl1,gl2,ml1,ml2,

```

```

1      oms,
2      nodes,
3      mdim)

```

```

implicit real*8 (a-h,o-z)
real*8 ml1(mdim),ml2(mdim)
complex*16 bl1(mdim),bl2(100),gl1(mdim),gl2(mdim)

```

```

do i = 1,nodes
  bl1(i) = oms*ml1(i) - gl1(i)
  bl2(i) = oms*ml2(i) - gl2(i)

```

```

end do

return
end

subroutine love (a1,a2,b1,b2,
1      e,v,
2      b22,p,q,r,w,
3      int,n,
4      mdim,mdim2,mdim3,*)
c
c -----
c solves eigenvalue problem for love waves
c -----
c
implicit real*8 (a-h,o-z)
integer*4 int(mdim3)
complex*16 c,d,ev,s,x,y,z
complex*16 a1(mdim),a2(mdim),b1(mdim),b2(mdim)
complex*16 b22(mdim3),e(mdim),p(mdim2),q(mdim2),r(mdim2)
complex*16 w(mdim2),v(mdim,mdim)
data tau/1.0d-7/,eps/1.0d-9/

tol=cdabs(a1(1))*1.0d-20
n1=n-1
n2=n-2
do 20 j=1,n
20 b22(j)=b2(j)*2.0d0
t=0.0d0
ev=t
c search for root of determinant by newton method
do 500 nv=1,n
nv1=nv-1
tp=1.
it=0
nit=0
ev=ev*.999
go to 108
105 ev=ev*(1.+tau)
tp=0.
108 it=it+1
if(it.lt.100) go to 109
write (*,*) ' failure to converge in 100 newton steps'
return 1
109 d=0.
if(nv1.eq.0.0d0) go to 115
do 110 j=1,nv1
c=ev-e(j)
t=dabs(dreal(c))+dabs(dimag(c))
if(t.lt.tau*(dabs(dreal(e(j)))+dabs(dimag(e(j))))) go to 105
110 d=d-1./c
115 x=a1(1)-ev*b1(1)
if(dabs(dreal(x))+dabs(dimag(x)).lt.tol) x=tol

```

```

y=-b1(1)/x
d=d+y
do 120 j=2,n
i=j-1
z=a2(i)-ev*b2(i)
c=z/x
x=a1(j)-ev*b1(j)-z*c
if(dabs(dreal(x))+dabs(dimag(x)).lt.tol) x=tol
y=(-b1(j)+(b22(i)+z*y)*c)/x
120 d=d+y
d=-1./d
ev=ev+d
c=d/ev
t=dabs(dreal(c))+dabs(dimag(c))
if(t.gt.eps) go to 108
if(nit.eq.1) go to 200
nit=1
tp=t
go to 108
200 continue
e(nv)=ev
c  compute eigenvector by inverse iteration
do 210 j=1,n
210 w(j)=1.
c  reduction of matrix
x=a1(1)-ev*b1(1)
y=a2(1)-ev*b2(1)
r(1)=y
do 250 i=1,n1
j=i+1
c=a1(j)-ev*b1(j)
s=r(i)
r(j)=a2(j)-ev*b2(j)
t=dabs(dreal(x))+dabs(dimag(x))
if(t.ge.dabs(dreal(s))+dabs(dimag(s))) go to 230
p(i)=1./s
q(i)=c
int(i) = 1
z=-x*p(i)
x=y+z*c
y=z*r(j)
go to 250
230 if(t.lt.tol) x=tol
p(i)=1./x
q(i)=y
int(i) = 0
z=-s*p(i)
x=c+z*y
y=r(j)
250 v(i,nv)=z
if(dabs(dreal(x))+dabs(dimag(x)).lt.tol) x=tol
niter=0
300 niter=niter+1

```

```

c      reduction of vector
      do 330 i=1,n1
        z=v(i,nv)
        if(int(i).eq.1) go to 320
        w(i+1)=w(i+1)+z*w(i)
        go to 330
320 y=w(i)
    w(i)=w(i+1)
    w(i+1)=y+z*w(i)
330 continue
c      back substitution
    w(n)=w(n)/x
    w(n1)=(w(n1)-q(n1)*w(n))*p(n1)
    do 350 l=2,n1
      i=n-l
      y=w(i)-q(i)*w(i+1)
      if(int(i).eq.1) y=y-r(i+1)*w(i+2)
350 w(i)=y*p(i)
      if(niter.lt.2) go to 300
c      normalize eigenvector
    cons=cdabs(w(1))
    do 1 j=2,n
      1 if(cons.lt.cdabs(w(j))) cons=cdabs(w(j))
    cons=1./cons
    do 2 j=1,n
      2 w(j)=w(j)*cons
    c=w(1)*(b1(1)*w(1)+b2(1)*w(2))
    do 420 j=2,n1
      420 c=c+w(j)*(b2(j-1)*w(j-1)+b1(j)*w(j)+b2(j)*w(j+1))
    c=c+w(n)*(b2(n1)*w(n1)+b1(n)*w(n))
    c=1./cdsqrt(c)
    do 440 j=1,n
      440 v(j,nv)=w(j)*c
500 continue
    do 51 i=1,n
      c=cdsqrt(e(i))
      cr=dreal(c)
      ci=dimag(c)
      if(ci.gt.0.0d0.or.(ci.eq.0.0d0.and.cr.lt.0.0d0)) c=-c
51 e(i)=c

      return
      end

      subroutine prerayl (cr1,cr2,gr1,gr2,mr1,mr2,
1          oms,
2          nodes,
3          mdim2)

      implicit real*8 (a-h,o-z)
      real*8 mr1(mdim2),mr2(mdim2)
      complex*16 cr1(mdim2),cr2(mdim2),gr1(mdim2),gr2(mdim2)

```

```

do i = 1,nodes
  k1 = 2*i
  k2 = k1-1
  cr1(k2) = gr1(k2) - oms*mr1(k2)
  cr1(k1) = gr1(k1) - oms*mr1(k1)
  cr2(k2) = gr2(k2) - oms*mr2(k2)
  cr2(k1) = gr2(k1) - oms*mr2(k1)
end do

return
end

subroutine raylgh (a1,a3,b2,b4,c1,c3,
1      e,v,
2      a,v1,v2,u1,u2,r1,r2,s1,s2,
3      mvb,nn,
4      mdim2,mdim3,*)
c
c -----
c solves eigenvalue problem for rayleigh waves
c -----
c
implicit real*8 (a-h,o-z)
integer*4 mvb(mdim3)
complex*16 cf
complex*16 e(mdim2),v(mdim2,mdim2)
complex*16 r1(mdim2),r2(mdim2),ev,evs,ce,cd,dev,c,d
complex*16 a(mdim2*4),v1(mdim3),v2(mdim2),u1(mdim2),u2(mdim2)
complex*16 s1(mdim2),s2(mdim2)
complex*16 a1(mdim2),a3(mdim2),b2(mdim2),b4(mdim2)
complex*16 c1(mdim2),c3(mdim2)
data eps1/1.e-5/,eps2/1.e-10/

n1=nn-1
n2=nn-2
do 10 j=1,n2,2
  mvb(j)=j+3*nn
  i=j+1
10 mvb(i)=i+2*nn
  mvb(n1)=n1+nn
  xn=0.
  do 15 j=1,nn
    x=c1(j)/a1(j)
15 xn=xn+dabs(x)
  xn=dsqrt(xn/nn)
  c=dcmplx(xn,xn+xn)
  do 20 j=1,nn
    s1(j)=1.
    s2(j)=c
    v1(j)=s1(j)
    v2(j)=s2(j)
    r1(j)=0.
20 r2(j)=0.

```

```

ev=xn/nn
isw=0
kc=0
mc=0
400 kc=kc+1
do 50 n=1,nn
u1(n)=c1(n)*v1(n)
50 u2(n)=a1(n)*v2(n)
do 55 n=3,nn
l=n-2
u1(l)=u1(l)+c3(l)*v1(n)
u1(n)=u1(n)+c3(l)*v1(l)
u2(l)=u2(l)+a3(l)*v2(n)
55 u2(n)=u2(n)+a3(l)*v2(l)
if(isw.eq.1) go to 85
isw=0
cd=1.
x=cdabs(ev)/2.
ev=dcmplx(x,x+x)
go to 87
85 ev=conjg(ev)
isw=2
cd=1.
87 ik=0
do 200 it=1,100
evs=ev*ev
do 90 n=1,nn
a(n)=evs*a1(n)+c1(n)
a(n+nn)=ev*b2(n)
a(n+2*nn)=evs*a3(n)+c3(n)
a(n+3*nn)=ev*b4(n)
90 v2(n)=(u1(n)-u2(n)*ev)*cd
do 150 n=1,n1
i=n
j=n+nn
m=mvb(n)
do 120 l=j,m,nn
c=a(l)/a(n)
i=i+1
ji=i
do 110 k=l,m,nn
a(ji)=a(ji)-c*a(k)
110 ji=ji+nn
a(l)=c
120 v2(i)=v2(i)-c*v2(n)
150 v2(n)=v2(n)/a(n)
n=nn
if(cdabs(a(n)).eq.0.0d0) then
dev=dev*0.5
ev=ev-dev
goto 200
endif
v2(n)=v2(n)/a(n)

```

```

do 160 k=1,n1
n=n-1
i=n
j=n+nn
m=mvb(n)
do 160 l=j,m,nn
i=i+1
160 v2(n)=v2(n)-a(l)*v2(i)
ce=0.
do 170 n=1,nn
v1(n)=(v2(n)-v1(n)*cd)/ev
ce=ce-u1(n)*v1(n)+u2(n)*v2(n)
u1(n)=c1(n)*v1(n)
170 u2(n)=a1(n)*v2(n)
ce=ce*cd
do 180 n=3,nn
l=n-2
u1(l)=u1(l)+c3(l)*v1(n)
u1(n)=u1(n)+c3(l)*v1(l)
u2(l)=u2(l)+a3(l)*v2(n)
180 u2(n)=u2(n)+a3(l)*v2(l)
cd=0.
do 190 n=1,nn
190 cd=cd-u1(n)*v1(n)+u2(n)*v2(n)
dev=ce/cd
if(it.gt.15) dev=dev*0.5
ev=ev+dev
cf=cd
cd=cdsqrt(2./cd)
c=dev/ev
x=dabs(dreal(c))+dabs(dimag(c))
if(ik.eq.1.and.x.lt.eps2) go to 300
if(x.lt.eps1) ik=1
200 continue
write (*,*) ' failure to converge in 100 iteration steps'
return 1
300 e(kc)=ev
icr=0
x=dabs(dreal(ev))
y=dabs(dimag(ev))
z=x+y
if(y/z.lt.eps2) icr=1
if(x/z.lt.eps2) icr=2
if(icr.eq.1) e(kc)=dreal(ev)
if(icr.eq.2) e(kc)=dimag(ev)*(0.,1.)
do 310 n=1,nn
310 v(n,kc)=v2(n)*cd
c if the eigenvalue is real choose the sign such that
c the group velocity becomes positive
if(icr.ne.1) go to 316
x=(v1(1)*v1(1)+v1(2)*v1(2))*ev
if(x.gt.0.0d0) go to 316
e(kc)=-e(kc)

```



```

      do 315 n=2,nn,2
315 v(n,kc)=-v(n,kc)
c check the special orthogonality of the newly found eigenvector
c and the sum of the previously found eigenvector
316 ce=0.
      do 330 n=1,nn
330 ce=ce-r1(n)*u1(n)+r2(n)*u2(n)
      ce=ce*cd
      x=dabs(dreal(ce))+dabs(dimag(ce))
      if(x.lt.eps1) go to 335
      write (*,*) ' failure to find an orthogonal eigenvector'
      return 1
335 c=1./e(kc)
      do 340 n=1,nn
      r1(n)=r1(n)+v(n,kc)*c
340 r2(n)=r2(n)+v(n,kc)
c find a starting vector orthogonal to all eigenvectors found
c for the iteration toward the next eigenvector
      c=0.
      d=0.
      do 342 n=2,nn,2
      m=n-1
      c=c-u1(m)*s1(m)+u2(n)*s2(n)
342 d=d-u1(n)*s1(n)+u2(m)*s2(m)
      ce=2./cf
      c=c*ce
      d=d*ce
      do 343 n=2,nn,2
      m=n-1
      s1(m)=s1(m)-c*v1(m)
      s1(n)=s1(n)-d*v1(n)
      s2(m)=s2(m)-d*v2(m)
      s2(n)=s2(n)-c*v2(n)
      v1(m)=s1(m)
      v1(n)=s1(n)
      v2(m)=s2(m)
343 v2(n)=s2(n)
      if(icr+isw.eq.0) isw=1
      mc=mc+1
      if(mc.ge.nn) go to 350
      go to 400
c form vectors for displacement expansion
350 do 610 n=1,nn
      c=-1.
      x=dimag(e(n))
      if(x.le.0.) go to 600
      e(n)=-e(n)
      c=-c
600 do 610 j=2,nn,2
610 v(j,n)=v(j,n)*c

      return
      end

```

SUBROUTINE HANKEL(ZZ,H0,H1,IND)

```

C-----
C Computation of zero and first order Hankel functions
C
C ZZ - complex argument, -3.1415...LE.ARG(Z) .LE. 3.1415...
C H0 - Hankel function of IND'th kind (IND=1,2) and zero order
C H1 - Hankel function of IND'th kind (IND=1,2) and first order
C
C Written by G. Waas and E. Kausel
C-----
  IMPLICIT REAL*8 (A-H,O-Z)
  COMPLEX*16 Z,H0,H1,C,A,E,E2,ZH,P
  COMPLEX*16 G0,G1,ZZ
  Z=ZZ
  SG=1.D0
  IF(IND.EQ.1)SG=-1.D0
  X=DREAL(Z)
  Y=DIMAG(Z)*SG
  R=DSQRT(X*X+Y*Y)
  PHI=DATAN2(Y,X)
  IF(R.LE.10.D0)GO TO 6
C   Use asymptotic expansion for R > 10
  J=2.D0*R
  II=3
  H0=0.D0
  H1=0.D0
  IF(PHI.LT.1.57D0)GO TO 2
  II=0
  X=-X
  Z=-Z
  SG=-SG
  PHI=3.141592653589793D0-PHI
1  Y=-Y
  PHI=-PHI
  SG=-SG
  II=II+1
2  G0=2.D0*H0
  G1=2.D0*H1
  C=DCMPLX(0.D0,SG*0.125D0)/Z
  K=2
  P=C*C
  A=4.5D0*P
  P=7.5D0*P
  H0=1.D0+C+A
  H1=1.D0-3.D0*C-P
3  I=4*K
  K=K+1
  DI=I
  DK=K
  A=A*C*(DI+1.D0/DK)
  P=P*C*(DI-3.D0/DK)
  H0=H0+A

```

```

H1=H1-P
IF(DABS(DREAL(P))+DABS(DIMAG(P)).GT.1.D-16.AND.K.LT.J)GO TO 3
C=H0/H1*DCMPLX(0.D0,-SG)
AR=(0.785398163397448D0-X-PHI/2.D0)*SG
E=0.797884560802865D0/DSQRT(R)*DEXP(Y)*DCMPLX(DCOS(AR),DSIN(AR))
IF(X.NE.0.OR.PHI.GT.0.)GO TO 4
E=DCMPLX(0.D0,DIMAG(E))
4  H0=H0*E
   H1=H1*E*DCMPLX(0.D0,SG)
   H0=H0+G0
   H1=G1+H1
   GO TO (1,5,9),II
5  H1=-H1
   GO TO 8
C   Use ascending series for R <= 10
6  ZH=Z/2.D0
   C=-ZH*ZH
   E=DCMPLX(0.D0,.318309886183791D0)*SG
   E2=E*2.D0
   A=1.D0-E2*(0.577215664901533D0+DLOG(R/2.D0))+PHI*0.636619772367582
   $D0
   P=1.D0
   K=1
   H0=A
   H1=A+E*(1.D0-1.D0/C)
7  A=A+E2/K
   P=P*C
   H0=H0+A*P
   K=K+1
   P=P/(K*K)
   H1=H1+(A*K+E)*P
   IF(DABS(DREAL(P))+DABS(DIMAG(P)).GT.1.D-16) GO TO 7
   H1=H1*ZH
   IF(X.NE.0.OR.PHI.GT.0.)GO TO 8
   H0=DCMPLX(0.D0,DIMAG(H0))
   H1=DREAL(H1)
8  C=H0/H1
9  RETURN
   END

```

SUBROUTINE BESSEL (ZZ,J0,J1)

```

C-----
C Computation of zero and first order Bessel functions
C
C ZZ - complex argument, -3.1415...LE.ARG(Z) .LE. 3.1415...
C
C Written by E. Kausel
C-----
IMPLICIT REAL*8 (A-H,O-Z)
COMPLEX*16 Z,ZZ,C,P,A,A0,A1,B0,B1,J0,J1
Z = ZZ
X = DREAL(Z)
Y = DIMAG(Z)

```

```

R = DSQRT (X*X + Y*Y)
IF (R.LE.10.D0) GO TO 30
C
C   Use asymptotic expansion for R > 10
C
PHI = DATAN2 (Y,X)
L = 0
IF (X.GE.0.D0) GO TO 10
L = 1
Z = -Z
PHI = PHI - 3.14159265358793D0 * DSIGN (1.D0,PHI)
X = -X
Y = -Y
10  J = 2.D0*R
    C = (0.D0,-0.125D0)/Z
    K = 2
    P = C*C
    A = 4.5D0*P
    P = 7.5D0*P
    A0 = C
    B0 = 1.D0 + A
    A1 = -3.D0*C
    B1 = 1.D0 - P
20  I = 4*K
    K = K+1
    DI = I
    DK = K
    A = A*C * (DI + 1.D0/DK)
    P = P*C * (DI - 3.D0/DK)
    A0 = A0 + A
    A1 = A1 - P
    I = 4*K
    K = K+1
    DI = I
    DK = K
    A = A*C * (DI + 1.D0/DK)
    P = P*C * (DI - 3.D0/DK)
    B0 = B0 + A
    B1 = B1 - P
    IF (DABS(DREAL(P))+DABS(DIMAG(P)).GT.1.D-16 .AND. K.LT.J) GO TO 20
    CC = DCOS (X)
    S = DSIN (X)
    SS = S + CC
    CC = S - CC
    TH = DTANH (Y)
    CH = 0.56418958354776D0 * DCOSH (Y)/DSQRT (R)
    S = PHI/2.D0
    A = CH * DCMLPX (DCOS(S),-DSIN(S))
    J0 = B0 * DCMLPX (SS,-CC*TH)
    J0 = J0 + A0*DCMLPX (-SS*TH,CC)
    J1 = B1 * DCMLPX (CC,SS*TH)
    J1 = J1 - A1*DCMLPX (CC*TH,SS)
    IF (L.EQ.1) J1=-J1

```

```
C = J0/J1
J0 = J0*A
J1 = J1*A
RETURN
C
C   Use ascending series for R <= 10
C
30  A = Z/2.D0
    C = -A*A
    J0 = 1.D0
    J1 = 1.D0
    P = 1.D0
    K = 1
40  P = P*C
    J0 = J0+P
    K = K + 1
    DK = K
    P = P/DK
    J1 = J1 + P
    P = P/DK
    IF ( DABS (DREAL(P)) + DABS (DIMAG(P)) .GT. 1.D-16) GO TO 40
    J1 = J1*A
c   C = J0/J1
    RETURN
    END
```